Weighing supermassive black holes with molecular gas kinematics

Mark David Smith

Jesus College

University of Oxford

A thesis submitted for the degree of

Doctor of Philosophy

Trinity Term 2020

To the greater glory of God,
and in loving memory of
Geoffrey Weir
and
Gwendrah Smith

Acknowledgements

'No man is an island, entire of itself...'

– John Donne, Devotions upon Emergent Occasions, 1624

Throughout my research and the preparation of this text, I have received the support of many to whom I give my thanks, particularly:

My parents, Geoff and Sandra Smith: who have supported and encouraged me through times good and bad, and who enabled me to pursue my every interest, broadening my horizons and forming me into the person I am today.

Imogen Rhodes, my fiancée, for her love and unflagging support over the past four years, and with whom I look forward to sharing the new post-thesis age!

The other members of my family: grandparents David and Gwendrah Smith, Geoff and Judith Weir, and my sister Claire, each of whom have inspired me.

Martin Bureau, my supervisor, without whose steady support I'd have gone round in circles even more frequently than I did, who surrendered his Christmas break to support my first observing trip, and whose incisive 'red pen treatment' dramatically improved my writing.

Tim Davis, co-PI of the WISDOM team, whose readiness to assist with even the most obscure technical problems never failed.

Roger Davies and John Magorrian, who stepped in to provide additional support during Martin's sabbatical in the 2018-19 academic year.

My other colleagues in the WISDOM team, particularly Michele Cappellari, for assistance in modelling the stellar potentials of many galaxies, Lijie Liu, for plentiful advice on the cold ISM, and Eve North, working in parallel in Cardiff.

Judith Brown, whose sound advice and counsel put into perspective many of the experiences of the last years.

The parishioners of St. Mary Magdalene's Church, Woodstock, among whom it has been a pleasure to live for the last three years.

Finally, the community of Jesus College, which formed me as both scholar and tutor, and particularly my undergraduate tutors who told me that I was 'bloody-minded' enough to stay the course! How right they were...

The work in this thesis was supported by a Science and Technology Facilities Council (STFC) DPhil studentship under grant ST/N504233/1. Travel to the IRAM 30-m telescope at Christmas 2018 was funded by the European Union's Horizon 2020 research and innovation programme under grant agreement No. 730562 [RadioNet].

Abstract

Supermassive black hole (SMBH) masses correlate tightly with various properties of their host galaxies, implying close co-evolution. However, the mass measurements underpinning this conclusion have large uncertainties and are limited by selection biases. With the advent of modern millimetre/sub-millimetre interferometers, molecular gas dynamics are now suitable tracers of the SMBH-dominated regions of galaxy potentials.

In this thesis, I present new mass measurements for the SMBHs in the nuclei of the local elliptical galaxies NGC 524 and NGC 7052. These measurements exploit exceptionally high angular resolution observations of carbon monoxide (CO) J=2−1 emission using the Atacama Large Millimeter/sub-millimeter Array (ALMA). I refine earlier dynamical modelling methods, allowing for non-axisymmetric gas distributions and accounting for previously underestimated formal uncertainties when fitting models with very large numbers of constraints. The measurement in NGC 524 is consistent with an earlier stellar dynamical measurement, while that in NGC 7052 shows that an earlier gas dynamical measurement underestimated the SMBH mass (possibly by neglecting pressure support). The dynamical models of these galaxies also reveal a small inflow/warp in NGC 524, and that the central hole in NGC 7052 is consistent with the region within which tidal forces disrupt molecular clouds.

Using spatially-integrated CO spectra from both single-dish telescopes and interferometers I further show a correlation exists between large-scale CO emission line widths and SMBH masses. This new correlation is no less tight than most, allowing it to be used to estimate SMBH masses in the absence of the (often harder to obtain) data required to exploit tighter correlations.

Finally, I discuss the dynamical features revealed in new ALMA observations of 11 other SMBH mass measurement candidate galaxies, and estimate the SMBH masses in the three most promising.

This thesis demonstrates the potential of molecular gas dynamics to advance our understanding of SMBH–host coevolution, and indicates the next steps in understanding the molecular contribution to AGN fuelling and feedback.

Contents

List of Figures

List of Tables

1 Introduction

Contents

1.1 Massive dark objects

In 1784, the Rector of St Michael's Church at Thornhill, in the West Riding of Yorkshire, the Reverend John Michell, wrote to his friend Henry Cavendish to suggest a new method to measure the masses of stars. In his letter, he proposed that light - believed at that time to consist of fast-moving corpuscles - would be slowed by the gravity of a star, and that, by measuring the magnitude of this braking effect, it would be possible to determine the mass of the star. Moreover, he postulated the existence of so-called 'dark

stars', so massive that the light corpuscles would be totally retarded and fall back into the stars. Assuming an object with solar density, and applying a classical treatment, he estimated that such a dark star should have a radius of $500\,\mathrm{R}_\odot$, and hence a mass of $12.5 \times 10^7\,\mathrm{M}_\odot$. In a strikingly prescient conclusion, he went on to postulate that such 'dark stars' could perhaps be detected by their dynamical influence on (emitting) orbiting bodies (Michell, 1784).

Soon afterwards, the French polymath Pierre-Simon Laplace, apparently independently (Montgomery et al., 2009), asserted a similar phenomenon would occur for a star of radius $250\,\mathrm{R}_\odot$ and density four times that of the sun (and hence a mass of $6 \times 10^7\,\mathrm{M}_\odot$; Laplace 1796, 1799). Both Laplace's and Michell's treatments are based on a classical calculation of the escape velocity, with Laplace imposing the apparently arbitrary condition $R = 250 R_\odot$ to determine the necessary density and Michell assuming solar density to determine the radius. Neither appears to have conceived of the alternative, a compact object with very high density, allowing the light to be emitted from a much smaller radius, and hence a much smaller mass.

However, within eighty years, James Clerk Maxwell and others would show that light propagates as an electromagnetic wave, at a speed fixed in vacuum determined by the physical constants ϵ_0 and μ_0, the permittivity and permeability of free space, respectively (Faraday, 1846; Weber & Kohlrausch, 1856; Kirchhoff, 1857; Maxwell, 1865). Further evidence from, for example, the Michelson-Morley experiment (Michelson & Morley, 1887), indicated that that the classical treatment of light assumed by Michell and Laplace was erroneous. In 1905, Albert Einstein developed what would become known as the 'special' theory of relativity, postulating that the speed of light is the same in all reference frames (Einstein, 1905). It would take the later 'general' theory of relativity to reconcile the action of gravity with the motion of light.

1.1.1 Black holes in a general relativistic framework

The Einstein field equations, describing gravitation in the general theory of relativity, were presented in Einstein (1916). Shortly before his death in the Great

War, Karl Schwarzschild identified the first non-trivial exact solution, for a non-rotating uncharged spherically-symmetric mass distribution (Schwarzschild, 1916; Droste, 1917). The space-time interval for a point-mass solution in spherical polar coordinates (t, r, θ, ϕ) is

$$ds^2 = -\left(1 - \frac{2GM}{c^2 r}\right) c^2 dt^2 + \left(1 - \frac{2GM}{c^2 r}\right)^{-1} dr^2 + r^2 d\theta^2 + r^2 \sin^2\theta d\phi^2 \quad , \quad (1.1)$$

where G is the gravitational constant, c is the speed of light and M the mass.

The most notable feature of this solution is the singularity that occurs at $r = 2GM/c^2$. The interpretation of this singularity was contentious, with Schwarzschild originally proposing a coordinate transformation $r \to r' = (r^3 - (2GM/c^2)^3)^{1/3}$ to shift it to occur at $r' = 0$. Alternative transformations were proposed (e.g. Eddington, 1924; Lemaître, 1933; Penrose, 1965), but it took until 1958 for David Finkelstein to provide a clear explanation that the singularity formed 'a perfect unidirectional membrane: causal influences can cross it but only in one direction' (Finkelstein, 1958). This is, of course, the now popularly understood phenomenon of light being unable to escape such an object. It is worth reinforcing the point that while Schwarzschild's solution is valid outside any spherically-symmetric, non-rotating and uncharged mass distribution, for almost all physical objects (excluding black holes) the size of the object greatly exceeds the radius of the singularity. The latter has become known as the 'Schwarzschild radius' or 'event horizon', and is given by

$$R_{\text{Sch.}} \equiv \frac{2GM}{c^2} \quad . \quad (1.2)$$

The Schwarzschild solution was generalised into a family of solutions allowing for the possibility of a net charge and non-zero angular momentum (Reissner, 1916; Weyl, 1917; Nordström, 1918; Kerr, 1963; Newman & Janis, 1965; Newman et al., 1965). It transpires that these metrics are sufficient to fully characterise all the black-hole solutions, since the no-hair theorem demonstrates that no other property of in-falling matter has an effect observable by an external observer (e.g. Israel, 1967, 1968; Carter, 1971). A black hole can thus be totally characterised by its mass, charge, and angular momentum (plus position and velocity in an

arbitrary frame). A further extended general-relativistic discussion of black hole phenomena is beyond the scope of this thesis.

1.1.2 Black holes as gravitationally-collapsed objects

Both Michell and Laplace postulated dark-star masses that exceeded $10^7\,\mathrm{M}_\odot$, assuming that the density of such objects should be comparable to the volume-averaged solar density (Michell, 1784; Laplace, 1799). However, we now know of significantly denser objects, white dwarfs (Stoner, 1929; Anderson, 1929) and neutron stars (Baade & Zwicky, 1934; Zwicky, 1939). The minimum mass that can form a black hole is determined by the maximum density that can be stabilised against gravitational collapse, and thus these denser objects indicate that black holes can be formed significantly below $10^7\,\mathrm{M}_\odot$.

While stellar densities are determined by the balance of gravitational forces with pressure (e.g. Schwarzschild, 1906; Eddington, 1916), compact objects must be stabilised by degeneracy pressure (Pauli, W., 1925; Pauli, 1940; Ehrenfest, 1959; Dyson & Lenard, 1967; Lenard & Dyson, 1968) or nuclear forces (Tolman, 1939; Oppenheimer & Volkoff, 1939; Douchin & Haensel, 2001). The limiting mass that can be supported is determined by the equation of state, which for a white dwarf is known, yielding a critical mass of $\approx 1.4\,\mathrm{M}_\odot$ (Chandrasekhar, 1931, 1935). Although the neutron star equation of state is not known, attempts to constrain the maximum mass suggest a limit of $2-4\,\mathrm{M}_\odot$ (Salgado et al., 1994; Lattimer & Prakash, 2001; Özel & Freire, 2016). Thus compact objects with dynamical masses greater than $\gtrsim 5\,\mathrm{M}_\odot$ are now classified as black holes.

1.1.3 Evidence for black holes in the universe

Black-hole phenomena were, until very recently, essentially impossible to observe directly, due to the very small spatial scales concerned and the fact that, by definition, a black hole is non-luminous. To formally prove that an astrophysical object is a black hole, one needs to show that its extent is smaller than its Schwarzschild radius. Indirect evidence can be provided by demonstrating that the lower-bound

on the density exceeds that of nuclear matter (approximately $10^{17}\,\mathrm{kg\,m^{-3}}$) thereby excluding a neutron star. However, circumstantial evidence is offered by other observations (e.g. Shahbaz, 1999; Ho, 1999; Casares, 2007; Narayan & McClintock, 2013). These observations suggest there exist two classes of black holes - 'stellar-mass black holes' (typically ranging from $10-100\,\mathrm{M_\odot}$), and 'supermassive black holes' (SMBHs; of order $10^6 - 10^{10}\,\mathrm{M_\odot}$). Reasons for the absence of observational evidence for 'intermediate-mass black holes' will be discussed further in Section 1.3.3.

Although this thesis is only concerned with SMBH, brief mention can be made of the observational evidence for stellar-mass black holes. Early x-ray observations discovered a population of bright sources within the Milky Way. The high energies required to account for this emission, and its rapid variability, were explained by accretion on to a compact object within an interacting binary (e.g. Shklovskii, 1967). Further observations identified candidate binaries containing unseen massive primaries, with radial velocity variations indicating masses consistent with a black hole (e.g. Bolton, 1972, 1975; Webster & Murdin, 1972). The discovery in 1989 of a binary (V404 Cyg) with a $6.3 \pm 0.3\,\mathrm{M_\odot}$ compact object provided firm evidence for massive compact objects, consistent with expected stellar mass black holes (e.g. Życki et al., 1999a,b).

Turning to supermassive black holes, perhaps the most compelling non-dynamical evidence for their existence came from the unification of high-redshift quasars (e.g. Schmidt, 1963) with nuclear radio activity (e.g. Hargrave & Ryle, 1974), as initially postulated by Lynden-Bell (1969), and developed by Lynden-Bell & Rees (1971). Both phenomena required efficient highly-energetic processes to power the observed luminosities, and accretion onto a collapsed mass was the most credible solution. As Lynden-Bell wrote 'we would be wrong to conclude that such massive objects in space-time should be unobservable... we have been observing them indirectly for many years' (Lynden-Bell, 1969). Further evidence is offered by the rapid variability observed in active galactic nuclei (AGN), indicating the emission originates from a region only light-hours across.

A second piece of evidence is offered by the implausibly large central stellar mass-to-light ratios (or gradients) required to account for the observed velocities of gas or stars in the central parts of galaxies, even in cases where Keplerian motion is not observed (i.e. the scale within which the SMBH dominates the potential is not resolved; e.g. Goodman & Lee 1989; Richstone et al. 1990; van der Marel et al. 1997). In the absence of colour gradients that would indicate changing stellar populations, these mass-to-light ratio gradients must be explained by low-luminosity or non-luminous mass, such as stellar remnants or substellar objects (e.g. Ho, 1999). Maoz (1998) argued that such clusters have lifetimes much shorter than the age of the corresponding galaxy, and thus are implausible explanations, therefore leaving central SMBHs as the most likely explanation.

A third piece of evidence are the broad line widths observed in galactic nuclei, as would be expected from motions close to SMBHs. Unresolved observations of Fe Kα emission in the nucleus of MCG-6-30-15 revealed a line width exceeding $10^5\,\mathrm{km\,s^{-1}}$ ($0.33\,c$), indicating that the emission must originate from within $10\,R_{\mathrm{Sch.}}$ of a central SMBH (Tanaka et al., 1995).

Taken together these pieces of evidence made a compelling case for the existence of astrophysical black holes even before mass measurements are considered. The last five years have provided two other pieces of evidence from new observational facilities. Detections of gravitational waves from merging stellar-mass black holes at the Laser Interferometer Gravitational-Wave Observatory (LIGO) in 2017 (Abbott et al., 2017a,b,c), and the now famous image of a SMBH 'shadow' from the Event Horizon Telescope (EHT; Event Horizon Telescope Collaboration et al. 2019a), compellingly make the case for astrophysical black holes.

1.2 Weighing supermassive black holes

THE general principle behind measuring SMBH masses is to resolve spatial scales on which the SMBH dominates the potential using a dynamical tracer. Before 2013, three tracers were commonly used: stars, ionised gas and masers. The use of any spatially-resolved dynamical tracer requires that the

observations resolve spatial scales on which the SMBH has a detectable contribution to the galactic potential, often (slightly inaccurately) equated with the SMBH sphere of influence, this latter defined as

$$R_{\rm SoI} \equiv \frac{GM_{\rm BH}}{\sigma_*^2} \ , \tag{1.3}$$

where $M_{\rm BH}$ is the SMBH mass and σ_* the central stellar velocity dispersion.

Beyond the local universe, within which it is possible to resolve $R_{\rm SoI}$, Virial estimates have been made using the reverberation mapping technique to estimate the size of the broad line region (BLR) and the associated unresolved line width.

The Milky Way and the galaxy M87 are special cases. In our own galaxy the orbits of individual stars can be mapped both spatially and temporally with great accuracy, allowing very precise measures of the SMBH mass. The EHT was able to spatially resolve the 'shadow' of the central SMBH in M87 at 1.3 mm. The measurement of the radius of this shadow (corrected for general relativistic effects) enables the SMBH mass to be directly inferred.

Finally, gravitational wave detectors at LIGO and Virgo have enabled measurements of the masses of pairs of merging stellar mass black holes (and their merger products). Future gravitational wave detectors, such as the *Laser Interferometer Space Antenna* (*LISA*) will be sensitive to the low-frequency gravitational waves emitted by merging SMBHs.

1.2.1 Milky Way

The compact radio source Sagittarius A* (Sgr A*) was discovered in 1971 using the National Radio Astronomical Observatory interferometer (Balick & Brown, 1974). Although a larger radio source (Sgr A) had previously been detected in 1931 by Karl Jansky (Jansky, 1933a,b,c), this new source was found to be less than $0\farcs1$ (5×10^{-3} pc) in extent. It was swiftly identified with the phenomenon of nuclear radio activity observed in other galaxies, for which accretion onto a SMBH had already been proposed as the central engine (e.g. Lynden-Bell, 1969; Lynden-Bell & Rees, 1971).

The prospect of a central mass concentration was supported by very broad emission line widths, originally from infrared observations of Ne II that could penetrate the central dust extinction (Wollman et al., 1977; Lacy et al., 1979, 1982; Serabyn & Lacy, 1985; Genzel et al., 1985). However, for the reasons discussed in Section 1.2.3, these were not considered conclusive, and further evidence from stellar kinematics was sought (e.g. Rieke & Rieke, 1988; Sellgren et al., 1990; Krabbe et al., 1995; Haller et al., 1996).

The most dramatic advance was provided by the measurement of the stellar velocity field on light-day scales, followed by the discovery of a compact cluster of tracer stars (Forrest et al., 1987; Allen et al., 1990; Krabbe et al., 1991), and finally the measurement of the proper motions, radial velocities, and accelerations of these individual stars (e.g. Genzel et al., 1996; Genzel & Eckart, 1999; Genzel et al., 2000; Ghez et al., 1998, 2000, 2003, 2005; Schödel et al., 2003). As these were monitored over a period of two decades, they provided steadily tighter constraints on both the distance to and the mass of Sgr A*, ultimately yielding the most precise measurement of any SMBH at that time, $M_{\rm BH} = 4.1^{+0.6}_{-0.6} \times 10^6\,{\rm M}_\odot$ (Ghez et al., 2008; Gillessen et al., 2009). In May 2018, observations captured the perihelion of star S2, which passed within 120 AU ($\approx 5\,R_{\rm Sch.}$) of the SMBH (e.g. Gravity Collaboration et al., 2018).

Isolating the motions of individual stars in the Milky Way was possible as the SMBH is nearly three orders of magnitude nearer than other galaxies. Individual stars can be isolated in the outer parts of nearby galaxies (e.g. in M31; Dalcanton et al. 2012), however the higher densities in the central regions lead to crowding and confusion. It is unlikely that the exquisite angular resolutions required to apply this method to other galaxies will ever be attained significantly beyond the local group.

1.2.2 Stellar dynamics

In most galaxies, individual stars cannot be resolved in the central parts, but kinematic information from an unresolved (i.e. integrated) population still constrains the galactic potential. Line-of-sight velocity, velocity dispersion and higher-order line-of-sight velocity distribution moment maps can be created from observations of

the absorption lines in the integrated spectra of the unresolved stellar population (e.g. Kormendy, 1988a,b; Dressler & Richstone, 1988; Kormendy & Richstone, 1995). These stellar kinematics are the result of stars on a variety of orbits, moving in the gravitational potential of the galaxy and which can be modelled using the Jeans (collisionless Boltzmann) equations (Jeans, 1915, 1922; Binney & Tremaine, 2008).

The first attempts to use stellar kinematics to measure the SMBH mass in M87 were made in 1978 (Young et al., 1978; Sargent et al., 1978). In the following years, more sophisticated methods, including using Schwarszchild orbit-superposition (e.g. Schwarzschild, 1979; van der Marel et al., 1998; Cretton et al., 1999) and Jeans (e.g. Magorrian et al., 1998; Cretton & van den Bosch, 1999; Cappellari, 2008) modelling became widespread. Both methods attempt to fit the observations with dynamical models to determine the potential (typically assuming it to be axisymmetric). In parallel, the increasing availability of integral field spectrographs (to replace earlier long-slit spectrographs) and adaptive optics on larger telescopes enabled both new mass measurements in more distant galaxies and improved constraints on nearby objects (e.g. Verolme et al., 2002; Cappellari & McDermid, 2005; Krajnović et al., 2005; van de Ven et al., 2008).

As stars form an essentially collisionless fluid, they are significantly less susceptible to non-gravitational forces than gas measurements. However, since observations measure only the line-of-sight projections of the velocities and dispersions, the solutions can be degenerate in anisotropic cases, requiring the imposition of additional constraints (i.e. additional assumptions). Template mismatch (particularly for galaxies with multiple stellar populations) and dust contamination can make deriving the kinematics from observed spectra more challenging, meaning that this method has been preferentially applied to early-type galaxies (as these mostly host uniformly-old stellar populations and little dust).

The future of stellar dynamics is likely to be improved by the next generation of large ground-based optical telescopes with new adaptive optics systems and improved integral field spectrographs (such as the European Extremely Large Telescope and Thirty Meter Telescope), and by the launch of the *James Webb*

Space Telescope. These facilities will be able to resolve scales significantly closer to SMBHs than previously possible.

1.2.3 Ionised-gas dynamics

A nuclear disc of ionised gas can be used to probe the SMBH-dominated region of a galaxy. Gas molecules in (quasi-)circular motion around the SMBH rotate at a velocity set by the balance between gravitational and centrifugal forces:

$$v_{\rm c}^2 = \frac{GM_{<r}(r)}{r} \ , \tag{1.4}$$

where $v_{\rm c}$ is the circular velocity at, and $M_{<r}(r)$ the mass enclosed by, a radius r. Emission-line kinematics can be extracted from spectroscopic observations by direct line-profile fitting, providing measurements of the mean line-of-sight velocity and velocity dispersion at the observed r (although generally the higher-order moments are less well constrained than for stellar observations as the intrinsically-smaller line widths are poorly sampled). If a sufficiently small radius is observed, $M_{<r}(r) \approx M_{\rm BH}$, and the radial velocity profile can thus be fit to yield the SMBH mass.

Harms et al. (1994) published the first SMBH mass measurement exploiting ionised gas, observing the ionised-gas disc of M87 (Ford & Butcher, 1979; Ford et al., 1994) using the *Hubble Space Telescope* (*HST*) Faint Object Spectrograph (FOS). Gaussian line-profile fits to these observations extracted the Doppler shifts of the Hβ, [O I], [O III] and [S II] emission lines at six positions over the gas disc, from which the integrated mass profile could be inferred (taking into account the disc inclination and position angle).

Slit-based spectroscopy provides a valuable upgrade on single-pointing observations (e.g. Macchetto et al., 1997). A slit placed along a galaxy's kinematic major axis provides a full rotation curve in a single observation, rather than a single spectrum of the integrated light within the aperture. This not only provides significantly more constraints, allowing a more precise SMBH mass measurement, but it also enables the identification of and correction for pointing errors (or inaccurate astrometry) along the slit axis. However, if the slit is misaligned from the disc kinematic major

axis at the smallest radii (as could occur if there is an undiagnosed warp), or if the slit is not accurately centred in the orthogonal direction, projection effects can still lead to a biased SMBH mass measurement.

HST can probe angular scales down to 0.″05, an angular resolution only recently attained with adaptive optics systems on ground-based observatories. This has meant that ionised gas, when observed by *HST*, is an ideal tracer for the less massive SMBHs present in spiral galaxies (that have large ionised-gas reservoirs but faint optical continua, making absorption-line kinematic measurements difficult).

However, ionised gas is particularly susceptible to non-gravitational forces (and non-circular motions), that can provide additional support against gravity, thereby potentially leading to underestimated SMBH masses (e.g. Häring-Neumayer et al., 2006). Early results (e.g. van der Marel & van den Bosch 1998; see Chapter 3) indeed took account only of rotational support (i.e. an emission line's Doppler-shifted centroid), neglecting pressure support (evidenced by broad emission line widths). Furthermore, the rotational support is quantified through the line-of-sight projection of the gas velocities only, so it and the SMBH masses are degenerate with the discs' inclinations, constraining only $M_{\rm BH}/\sin i$. Inclination constraints can be obtained from e.g. images of the dust disc, but the tightest constraints are necessarily derived for highly-inclined discs, with very large uncertainties on the SMBH masses for face-on galaxies.

Modern integral-field spectrographs improve ionised-gas kinematic measurements, further reducing the uncertainties associated with slit positioning and providing significantly more constraints on the nuclear potential. The seeing limit implies that the *HST* was for many years the only option to resolve $R_{\rm SoI}$ in a significant number of galaxies, but in recent years adaptive optics on large ground-based telescopes have become increasingly competitive. Future large telescopes will enable many more measurements to be made, for instance, the E-ELT is expected to attain angular resolutions near its diffraction limit of 0.″004 (although it remains to be seen if the proposed adaptive optics systems will realise this goal). With comparable or higher angular resolutions than could be attained with the *HST* and the larger collecting

area dramatically shortening observation times, ground-based observations are likely to dominate the future of gas dynamical measurements.

1.2.4 Maser dynamics

Maser emission from the nuclei of active galaxies has provided the tightest constraints on SMBH masses so far. 22 GHz emission from H_2O clouds results in small but bright radio sources that can be detected and whose positions can be determined with great accuracy using very long baseline interferometry (VLBI). As these sources are generally very close to the SMBHs, they typically exhibit orderly Keplerian rotation, enabling SMBH mass measurements to be made in a manner similar to that for ionised gas.

The first maser SMBH mass measurement was made in the galaxy NGC 4258 using the Very Long Baseline Array, yielding a mass of $4 \times 10^7\,M_\odot$ within a radius of 0.13 pc (Miyoshi et al., 1995; Greenhill et al., 1995). The inferred minimum density provided much stronger evidence of a massive dark object than the larger-scale stellar and gas measurements. Further studies in more objects have yielded similarly tight constraints, although it appears that in general maser discs can have significant warps that need to be accurately modelled (e.g. Greenhill et al., 2003b). Recent results, such as those from the Megamaser Cosmology project, have provided increasing numbers of reliable mass measurements (e.g. Reid et al., 2009; Kuo et al., 2011; Gao et al., 2017; Zhao et al., 2018).

The key strength of maser-based SMBH mass measurements is the high angular resolutions achieved with radio VLBI. Probing sources so close to the SMBHs removes the uncertainties arising from other mass contributions, thus yielding the most precise extragalactic measurements. Additionally, dynamical mass measurements scale linearly with distance, and hence uncertainties on the distance directly and systematically propagate into uncertainties of the SMBH mass (although these are usually not quoted as they are well-understood). As VLBI observations also allow the proper motions of the masing clouds to be measured, they also allow accurate distances to be derived, thus removing this significant contribution to the

SMBH mass uncertainties (e.g. Gao et al., 2016). These advantages have made the sample of maser measurements the current 'gold standard'.

Having said that, maser emission is very rare, with detection fractions below 5% of even carefully-selected samples, and is only found in galaxies with nuclear activity (required to stimulate the maser emission; e.g. Braatz et al. 1996; Greenhill et al. 2003a). The prospects for dramatically expanding the maser sample are thus bleak, and they cannot provide an unbiased sample across the Hubble sequence.

1.2.5 Reverberation mapping

The formula linking the circular velocity v of a tracer at radius r to the mass of a SMBH is simple, $M_{\rm BH} \propto v^2 r$. In the previous sections, we have described the use of spatially-resolved observations to measure both r and v. However, an alternative approach has been taken in some distant active galaxies. The broad line region (BLR) of an AGN is well within the SMBH sphere-of-influence, and can thus be used to constrain its potential (e.g. Czerny & Hryniewicz, 2011).

The radius of the broad line region, $R_{\rm BLR}$, can be estimated using a temporally-varying flux from the AGN. A lag between variations of the AGN flux and variations of the BLR emission lines can be assumed to arise from the time light has taken to travel over the distance $R_{\rm BLR}$, that can thus be measured when these variations are temporally resolved ($R_{\rm BLR} = ct_{\rm lag}$; e.g. Blandford & McKee 1982; Clavel et al. 1991; Peterson et al. 1991; Dietrich et al. 1993; Maoz et al. 1993). Under this assumption, the SMBH mass is given by

$$M_{\rm BH} = f R_{\rm BLR} (\Delta V)^2, \tag{1.5}$$

where f is a constant of proportionality and ΔV the BLR emission line width (measured separately via optical spectroscopy). The concept was first demonstrated in the galaxy NGC 4151 (Gaskell, 1988), and many further studies followed (e.g. Gaskell, 1996; Wandel et al., 1999; Peterson & Wandel, 1999; Kaspi et al., 2000).

Although this technique appears to enable measurements in many galaxies in which the nuclear region cannot be spatially resolved, its inherent assumptions

limit its usefulness. The constant of proportionality (f) in Equation 1.5 encodes a variety of information, including the orientation of the BLR. Detailed studies of the BLR (true reverberation 'mapping') can enable the BLR geometry to be determined for individual objects. However, in most cases, the values of f used are derived from simple geometric models or *a posteriori* to ensure that reverberation mapping measurements recover the empirical correlations between SMBH mass and host galaxy properties discussed in Section 1.3 (e.g. Peterson & Horne, 2004; Peterson et al., 2004; Collin et al., 2006; Woo et al., 2015; Yu et al., 2019). This implies that these mass measurements are not independent tests of these correlations. Furthermore, once the uncertainties on f are taken into account, the uncertainties on the SMBH masses derived also become large (e.g. Mejía-Restrepo et al., 2018; Campitiello et al., 2020). On the other hand, the strengths of these measurements are the large number statistics available (when assuming f for an ensemble), and that they are possible in distant sources where spatially-resolved observations are not.

1.2.6 Gravitational waves

The detection of gravitational waves emitted by merging stellar-mass black holes at the two LIGO sites in 2017 (Abbott et al., 2017a,b,c) opened a new era for many fields of astronomy, with particular excitement at the potential for 'multi-messenger' observations. The relevant feature for this thesis is the ability to determine the 'chirp mass' of the merging pair, and subsequently the masses of each.

Existing ground-based gravitational wave detectors are only sensitive to frequencies in the 10 Hz to 10 kHz range (Martynov et al., 2016), suitable for detecting merging stellar-mass objects and potentially some intermediate-mass black holes (IMBHs), but not the lower frequencies expected from SMBH mergers (Matsubayashi et al., 2004), which will require *LISA*.

Predicted rates for IMBH mergers are of the order of tens of events per year across the entire universe (Matsubayashi et al., 2004; Rhook & Wyithe, 2005). *LISA* expects to detect ≈2 SMBH merger events per year (Salcido et al., 2016). These rates, if realised, could provide significant additional I/SMBH mass measurements

(albeit without the ability to target samples to address specific science questions), although localising them to their host galaxies will require additional detectors that are not currently planned.

1.2.7 M87 and the Event Horizon Telescope

The ultra-high angular resolution enabled by earth-diameter interferometry was used to image the 'shadow' of the SMBH in M87 (Event Horizon Telescope Collaboration et al., 2019a). The EHT comprises telescopes in Hawai'i, the Americas, the South Pole and Europe, including the Institut de Radioastronomie Millimétrique (IRAM) 30-m telescope and Atacama Large Millimeter/submillimeter Array (ALMA) used elsewhere in this thesis. These baselines lead to an angular resolution of ≈20 μarcsec at the observed 1.3 mm wavelength.

Ordinary inter-continental transmission lines do not provide sufficient data-rates to perform on-line correlations, as is the case at ALMA or the Jansky Very Large Array. Telescope output voltages were therefore synchronised with the rest of the array using Hydrogen masers and the Global Positioning System, and recorded to discs (Event Horizon Telescope Collaboration et al., 2019b). These data discs were then manually transported to high-performance computing facilities in the USA and Germany, where the complex visibilities were calculated (Event Horizon Telescope Collaboration et al., 2019c). From these data, images of the emission region around the putative SMBH were created by multiple teams using both standard interferometric techniques and a newer method to ensure the images were robust (Event Horizon Telescope Collaboration et al., 2019d).

The EHT results reveal an asymmetric ring of emission around the central black hole, originating from synchrotron emission near the event horizon (Event Horizon Telescope Collaboration et al., 2019e). The central void is caused by photons being captured by the SMBH's gravity, and its radius is thus proportional to the SMBH mass (it was found to be $\approx 10\, R_{\mathrm{Sch.}}$). The SMBH mass was thus inferred to be $M_{\mathrm{BH}} = 6.5 \pm 0.2 \times 10^9\, \mathrm{M}_\odot$ (Event Horizon Telescope Collaboration et al., 2019f), consistent with the most recent measurement using stellar dynamics (Gebhardt

et al., 2011) but inconsistent with that derived from ionised-gas dynamics (Walsh et al., 2013), most likely due to non-circular motions in the circumnuclear gas disc leading to the latter underestimating the SMBH mass (Jeter et al., 2019).

Although further EHT observations have been taken of Sgr A*, they have not yet been released. However, while the EHT observations are revolutionary, even with earth-diameter baselines, it will not be possible to resolve equivalent scales (in terms of $R_{\mathrm{Sch.}}$) in more than the few nearest galaxies, and thus these observations are not likely to provide significant numbers of new SMBH mass measurements.

1.3 The role of SMBHs in galactic evolution

NCE a significant number of SMBH masses had been measured, studies began to investigate the relationship between these central objects and the galaxies that host them. The patterns that were revealed led to dramatic shifts in our understanding of galaxy evolution.

A miscellany of SMBH mass correlations have been proposed (and subsequently challenged) over the last two decades, which broadly fall into two categories - an initial set of now well-established, very tight, correlations with properties of the galaxy bulge, and a later set of generally looser correlations with larger-scale components. The former set are widely agreed to indicate co-evolution between SMBHs and bulges. Disputes continue over the second group, particularly over whether the increased scatter (relative to SMBH-bulge correlations) implies any causal connection, or if they simply result from a general principle that larger galaxies contain larger structural components.

1.3.1 Bulge – SMBH scaling relations

As initial SMBH mass measurements were made in galaxies featuring a bulge, the first investigation (based on eight SMBH masses) was into whether SMBH masses correlate with bulge masses (Kormendy & Richstone, 1995). A close relation was found, where the ratio between SMBH mass and bulge luminosity/mass was

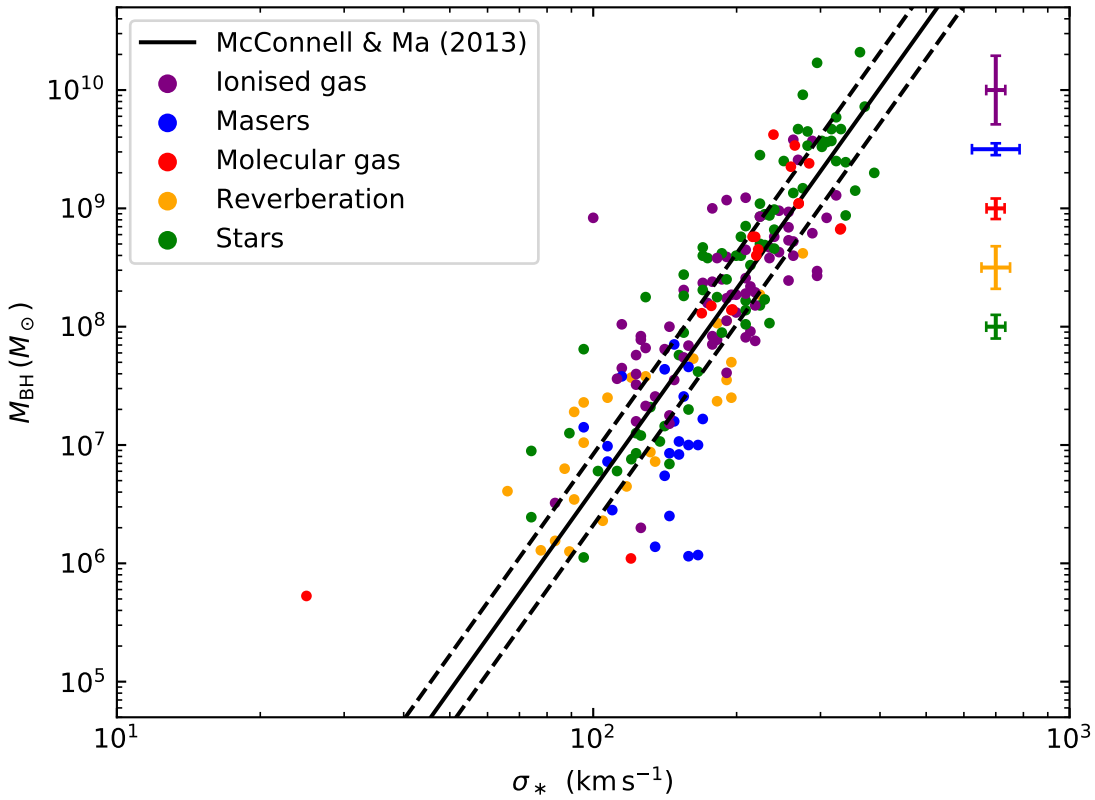

Figure 1.1: Correlation between SMBH mass ($M_{\rm BH}$) and stellar velocity dispersion averaged within $1R_{\rm e}$ (σ_*). Data points are robust SMBH mass measurements from the compilation of van den Bosch (2016), to which a few recent molecular gas measurements have been added (listed in Table 6.1). Colors indicate the method used to derive each SMBH mass. The representative error bars shown in the top-right corner indicate the median error in the measurements from each method excluding distance errors. The $M_{\rm BH}-\sigma_*$ relation of McConnell & Ma (2013) is shown by the black solid line, with the typical ±0.3 dex intrinsic scatter indicated by black dashed lines.

fixed at $\approx$0.003. Further work with an increased number of SMBH masses refined this correlation (Magorrian et al., 1998).

The most well-known, and to date tightest, correlation between SMBH mass and any property of the host galaxy is that with the stellar velocity dispersion within the half-light (effective) radius (σ_*). This correlation was initially brought to light by Ferrarese & Merritt (2000) and Gebhardt et al. (2000), with more recent studies estimating the intrinsic scatter at only $\approx$0.3 dex in SMBH mass (e.g. Gültekin et al., 2009b; Beifiori et al., 2012; McConnell & Ma, 2013; van den Bosch, 2016; Saglia et al., 2016). An updated version of the $M_{\rm BH}-\sigma_*$ correlation is shown in Figure 1.1.

Other correlations have been proposed with measures of the concentration of the bulge (e.g. Graham et al., 2001), particularly the Sérsic index (Graham & Driver, 2007). These have proven more contentious, with subsequent works finding no such correlation (Hopkins et al., 2007; Beifiori et al., 2012).

As a brief aside, Figure 1.1 offers a useful comparison of the SMBH mass measurement methods discussed in Section 1.2. At low σ_* (generally low-mass galaxies), the sample is dominated by reverberation mapping and maser measurements - consistent with a selection bias towards (mostly low-mass) active galaxies. At high σ_* (massive early-type galaxies), stellar dynamical measurements dominate, while ionised-gas measurements span the intermediate range. Molecular gas measurements thus far complement these techniques. The coloured error bars on the right indicate the median errors in each sample. The high precision of maser SMBH mass measurements is clearly apparent, as are the larger uncertainties in ionised-gas and reverberation mapping measurements.

1.3.2 Disc and halo correlations

The discovery of these SMBH-spheroid correlations sparked a flurry of searches for correlations with other parameters. The discovery of AGN (and by extension SMBHs) in bulge-less spiral galaxies (e.g. Satyapal et al., 2007, 2008) in turn indicates that a bulge is not essential for the formation and/or growth of a SMBH, and thus that there may be more fundamental correlations with other galaxy properties. However, these correlations have proved more controversial.

Ferrarese (2002) began the trend by showing that SMBH masses correlate with asymptotic (flat) rotation velocities measured from rotation curves at large radii. As these same rotation curves provide convincing evidence for dark matter haloes, it was thereby inferred that SMBH masses also correlate with halo masses. Following this result, Seigar et al. (2008) presented a correlation with the pitch angle of spiral arms, expected due to the known correlation between spiral arm tightness and (dark) mass concentration (e.g. Seigar et al., 2006). Ferrarese et al. (2006) similarly showed that SMBH masses are correlated with the total dynamical masses of their hosts.

Later studies cast doubt on these results. Kormendy et al. (2011) showed that SMBH masses do not correlate with galaxy discs (nor with disc-grown pseudo-bulges), and Kormendy & Bender (2011) that SMBH masses are only correlated with halo properties if a galaxy also hosts a bulge. In a systematic study of the intrinsic scatter in a number of correlations, Beifiori et al. (2012) further concluded that the large scatter of many of these relations indicates that SMBH masses correlate much better with bulge components than the entire galaxy (and better with baryonic matter than with dark haloes). However, recent works on spiral galaxies have sought to redeem these correlations (Davis et al., 2017b, 2018b, 2019b,c; Simmons et al., 2017), so the matter is not yet conclusively settled.

1.3.3 The growth of SMBH masses

That a SMBH, which only has a significant influence on the galactic potential within a very small central region, should co-evolve with much larger-scale properties of its host galaxy is a most surprising result. Two major models of SMBH growth have been proposed to explain this conundrum - either SMBHs grow by near-continuous, secular accretion, or they are stimulated into rapid but episodic growth by galaxy mergers. Both models reflect the underlying correlations indicating co-evolution with different structural components.

AGN observations provide evidence for accretion-driven SMBH growth, consistent with the hypothesis that SMBHs serve as the central engine of AGN emission. Gas accreted onto a galaxy can be transported to a central accretion disc by, for instance, torques exerted by galactic bars (and potentially bars-within-bars; e.g. Shlosman et al. 1989; Athanassoula 1992; Sellwood & Wilkinson 1993; Maciejewski et al. 2002; Combes 2008). Within the accretion disc, gas can lose angular momentum through viscous friction, allowing the gas to fall onto the central SMBH. Radiation emitted (radiative-mode feedback) and outflows and jets launched (kinetic-mode feedback) from this disc connect the small scales dominated by the SMBH potential to larger galactic scales (e.g. Fabian, 2012). By solving the 'cooling problem', whereby the high cooling rate of gas leads to simulated galaxies more luminous and

massive than observed, simulations have shown that this AGN feedback is essential to replicate multiple features of observed galaxies, such as the high-mass truncation of the galaxy luminosity function (e.g. Benson et al., 2003; McNamara & Nulsen, 2007).

An alternative scenario relies on the tight correlations with bulge properties. Galactic bulges appear to form in galaxy mergers (e.g. Toomre & Toomre, 1972; Combes, 2000; Mo et al., 2010), suggesting that these mergers are, in turn, key to SMBH mass growth. Mergers can have two compounding effects. First, the significant disruption to the galactic potential can dramatically enhance gas accretion onto the central regions, leading to rapid but episodic growth (e.g. Sanders et al., 1988; Hernquist, 1989; Di Matteo et al., 2005). Second, the central SMBHs of the merging galaxies can themselves merge.

The relative importance of these pathways remains disputed. Kormendy & Ho (2013) postulate a model in which secular accretion in bulgeless galaxies is too weak to lead to a correlation, with wet (i.e. gas-rich) major mergers playing the dominant role to grow SMBHs to large masses, before a 'maintenance mode' of AGN feedback inhibits star formation to truncate the galactic luminosity function. Merger averaging is invoked to reduce the observed intrinsic scatter to yield the tight correlations observed in elliptical galaxies. Krajnović et al. (2018) used a similar model to investigate variations in SMBH masses over the mass-size plane. Galaxies below a critical total stellar mass $M_{*,\mathrm{crit.}} \approx 2 \times 10^{11}\,\mathrm{M}_{\odot}$ were found to correlate most tightly with σ_*, but those above this mass were found to correlate increasingly tightly with total stellar mass. They suggest a model in which the galaxies below $M_{*,\mathrm{crit.}}$ increase their masses by accreting gas and forming stars while their SMBHs grow in tandem via secular accretion, but those above $M_{*,\mathrm{crit.}}$ grow principally by a sequence of dry (gas-poor) mergers, increasing their SMBH masses without significant change to the associated σ_*. This model is consistent with a broken power-law in the $M_{\mathrm{BH}}-\sigma_*$ relation, as indicated by the apparent saturation at high SMBH masses (see e.g. Figure 1.1).

A final piece of the puzzle is the origin of SMBHs in the early universe. It is generally accepted that relatively small black holes - of the order of a few to

a few tens of solar masses - were the initial seeds from which SMBHs grew (e.g. Volonteri, 2010). However, Eddington-limited accretion appears too slow to grow a stellar-mass black hole to the large black hole masses observed even in the early universe ($\gtrsim 10^9\,M_\odot$ at $z>6$; e.g. Willott et al. 2003; Barth et al. 2003), suggesting that either super-Eddington accretion occurred (e.g. Davies et al., 2011) or that the seeds from which SMBHs grow are larger (e.g. Madau & Rees, 2001; Volonteri et al., 2003; Begelman et al., 2006; Devecchi & Volonteri, 2009).

Regardless of the ultimate progenitors of the current SMBHs, any growth model implies the existence of black holes with intermediate masses (of order $10^4 - 10^6\,M_\odot$). However, the observational evidence for IMBHs is currently fairly weak (e.g. Mezcua, 2017). The lack of a secure detection, however, may be due to the biases in our BH mass measurement methods, all of which are towards the largest SMBHs - those with spatially-resolvable gravitational influences. Put simply, if IMBHs exist, we would not expect to detect them easily. We also principally look for black holes in the nuclei of galaxies, creating a further bias towards the large SMBHs that lurk there. It is likely that IMBHs are located outside of these nuclei, and thus searches for them will require large fields of view, at variance with the high spatial resolutions required to detect their gravitational influences.

1.4 Molecular gas as a tracer of SMBH potentials

The ATLAS^{3D} survey's molecular gas studies (Young et al., 2011; Davis et al., 2011, 2013a; Alatalo et al., 2013) showed that CO emission could be detected in a significant fraction of early-type galaxies, even though these galaxies were traditionally viewed as 'dead' (i.e. not star-forming). Spatially-resolved observations using interferometers showed that this molecular gas is typically found in regularly-rotating discs co-incident with nuclear dust features. This is consistent with the expectation that dust enhances molecule formation through surface reactions. These molecular gas discs bear a striking similarity to the ionised-gas discs used to measure SMBH masses (as described in Section 1.2.3), and hence it was realised that, if they continue kinematically undisturbed

to small galactic radii, within the regions in which the potentials are dominated by the central SMBHs, the dynamics of these discs could be used to measure the SMBH masses. This idea also relied on the fact that millimetre/sub-millimetre interferometers, such as the Combined Array for Research in Millimeter-wave Astronomy (CARMA) or the then newly-complete ALMA, would be capable of spatially-resolving emission lines on these scales.

1.4.1 NGC 4526: Proving the concept

CARMA observations of the early-type galaxy NGC 4526 enabled the first such measurement to be made. Davis et al. (2013b) generated simulated data cubes for a grid of SMBH masses and stellar mass-to-light ratios. The 'trace' (rotation curve) of each major-axis position-velocity diagram of the simulated cubes was then compared to the trace extracted from the observed data cube using the χ^2 statistic. This yielded a best-fitting SMBH mass of $M_{\rm BH} = 4.5^{+4.2}_{-3.0} \times 10^8\,{\rm M}_\odot$. Although the uncertainties are relatively large, this measurement demonstrated the potential of millimetre molecular gas observations to measure SMBH masses.

The greatest strengths of molecular gas dynamics for SMBH mass measurements are that suitable gas reservoirs exist in galaxies over the entire range of the $M_{\rm BH}$–σ_* relation, in both active and non-active galaxies, and the extended ALMA configurations can resolve angular scales inaccessible to even the *HST*, significantly increasing the number of potential targets.

Although in principle molecular gas measurements are susceptible to similar drawbacks to ionised gas, these are in general less significant. Turbulent motions can provide pressure support (that if neglected would lead to underestimated SMBH masses), but these motions are generally much smaller in molecular gas than in ionised gas. The derived SMBH masses are also strongly dependent on the inclinations of the gas discs, and hence the real constraints are on the quantity $M_{\rm BH}/\sin i$. Inclination uncertainties, and potential misalignments between the mid-planes of the stars and those of the gas discs, can thus lead to further

uncertainties (although interferometric data also lead to more accurate inclination determinations and warp diagnostics).

Davis (2014) studied the requirements to robustly derive SMBH masses from interferometric gas kinematics, considering the effects of channel width, spatial resolution and the depth of the galaxy's stellar potential on the accuracy of the derived masses. The key conclusions were that SMBH masses can be derived even from observations that only resolve a spatial scale of $\approx 2R_{\rm SoI}$ (although higher resolutions improve the precision), that a channel width of $\approx 15\,{\rm km\,s^{-1}}$ balances the requirements of sensitivity and spectral resolution, and that measurements are easier in galaxies with shallow stellar potentials. Davis (2014) also provided a figure of merit for SMBH mass measurements, based on the degree to which the gas velocities are enhanced by the SMBH above those expected from the stars. Although Davis (2014) intended for this figure of merit to be used to determine the required observational parameters (spatial and velocity resolution) to ensure the SMBH mass can be measured, as the stellar potential is not generally known *a priori*, a predicted $R_{\rm SoI}$ is usually adopted as the required angular resolution. In practice, observations that do not resolve $R_{\rm SoI}$ can still enable robust SMBH masses to be measured, as the SMBH still makes a detectable (and sometimes significant) contribution to the potential beyond $R_{\rm SoI}$ (e.g. Chapter 2).

1.4.2 Work by other groups

Following the Nature paper on NGC 4526, other groups around the world began using the same method in other galaxies. The first to publish was Onishi et al. (2015), using ALMA to observe HCN gas in the spiral galaxy NGC 1097, and performing the fit to the full position-velocity diagram, rather than simply the trace. This was quickly followed by a measurement in the early-type galaxy NGC 1332 (Barth et al., 2016a,b), based on a fit to the central (SMBH-dominated) region of the three-dimensional (3D) data cube. As the data were oversampled (as is usual, with a few spaxels across the synthesised beam), adjacent pixels were spatially

correlated, and thus the observed cube was rebinned to larger, independent, spaxels, to which the simulated cube was compared.

In parallel to the work of our own millimetre-Wave Interferometric Survey of Dark Object Masses (WISDOM) project described in Section 1.4.3, Boizelle et al. (2019) measured the SMBH mass in the elliptical galaxy NGC 3258, using both a flat disc and a tilted-ring model to fit a small warp. As the ALMA observations significantly resolved $R_{\rm SoI}$ (by $\approx$8 beams radially), they were able to test the sensitivity of their result to the assumed shape of the galactic mass profile. Extinction from the central dust disc (from which the CO emission originates) can bias the stellar light profile (and thus the associated mass profile if not corrected for). In the papers produced by our team, we have assumed either a (radially-) constant mass-to-light ratio, derived from gas motions at large radii within the molecular gas/dust disc (thereby effectively assuming the dust extinction is radially constant; e.g. Onishi et al. 2017; Davis et al. 2017a) or a mass-to-light ratio varying linearly with radius (e.g. Davis et al. 2018a; North et al. 2019), or we have attempted to correct the light profile for the extinction (Smith et al., 2019). Boizelle et al. (2019) showed that the stellar mass profile can be calculated independently from optical images, thereby avoiding this bias, provided the molecular gas observations reach resolutions at which the stellar contribution to the potential can be safely neglected (and thus the SMBH contribution disentangled).

Yoon (2017) performed simulations to better understand the systematic effects on SMBH masses derived from fitting position-velocity diagrams (rather than full cubes as adopted by WISDOM). Yoon (2017) used the radius at which the SMBH and stellar contributions to the potential are equal, $R_{\rm eqv}$, rather than $R_{\rm SoI}$ as the required angular resolution. Similarly to Davis (2014), Yoon (2017) concluded that a centrally-concentrated galaxy (with a high Sérsic index) requires a higher spatial resolution to resolve the SMBH-dominated scale, but the SMBH enhances the rotation velocities more at $R_{\rm eqv}$, allowing larger velocity channels to be used. Other systematics associated with fitting only the position-velocity diagram, including

the potential presence of neglected non-circular motions, were shown to bias the derived SMBH mass. This problem is mitigated by fitting the entire cube.

The CARMA observations used to measure the SMBH mass in NGC 4526 were later used to conduct a census of the giant molecular cloud (GMC) population in this galaxy (Utomo et al., 2015), the first in an early-type galaxy. The high spatial resolutions required for SMBH mass measurements generally imply that individual GMCs are spatially resolved, allowing their identification within the data cube and the extraction of cloud properties for the entire population. By comparison to the Milky Way GMCs, which follow Larson's relations (Larson, 1981), the GMCs in NGC 4526 are denser and more luminous, with internal rotation driven by the galactic shear. Utomo et al. (2015) thus demonstrated the opportunity to conduct spin-off studies of extragalactic GMCs (with nearly every SMBH dataset) with no additional telescope time required.

Further SMBH mass measurements from molecular gas kinematics were recently published in the elliptical radio galaxy NGC 1275 (Perseus A; Nagai et al., 2019) and the dwarf galaxy NGC 3504 (Nguyen et al., 2020). Both of these galaxies exhibit disturbed CO kinematics at large scales, but the gas appears to relax into regularly rotating discs close to the SMBHs. By contrast, an attempt by Combes et al. (2019) to simultaneously fit the major-axis position-velocity diagrams and velocity fields of seven late-type disc galaxies observed at $\approx$5 pc resolution found that the CO kinematics were strongly affected by non-circular motions, even well within the putative SMBH spheres of influence, and thus simplistic models were not good fits. These recent works demonstrate cases more challenging than the early-type galaxies previously studied, and unlocking these other galaxy populations will be key to fully exploit the potential of the molecular gas method.

1.4.3 The WISDOM project

The millimetre-Wave Interferometric Survey of Dark Object Masses (WISDOM) team was formed to exploit ALMA for SMBH mass measurements. Papers IV

(Smith et al., 2019), VI (Smith et al., 2021a) and VII (Smith et al., 2021b), in the WISDOM sequence were adapted to form the core of this thesis.

The first three papers in the WISDOM sequence, that preceded this thesis, made SMBH mass measurements in three early-type galaxies. WISDOM paper I (Onishi et al., 2017) used CARMA observations to measure the SMBH mass in NGC 3665. They compared the SMBH mass measured by fitting the full data cube to that measured by fitting only the rotation curve of the galaxy, finding consistent results. Rather than evaluating models for a limited number of model parameters (e.g. just the SMBH mass and stellar mass-to-light ratio), a Markov Chain Monte Carlo process was used to explore a larger set of variables. In Paper II, Davis et al. (2017a) measured the SMBH mass in NGC 4697 from ALMA observations, that also revealed a gas disc with abnormally low velocity dispersion (σ<3 km s^{-1}). Such low molecular gas velocity dispersions appear to be common in the early-type galaxies of the WISDOM survey, and have allowed us to neglect pressure support in dynamical models.

Paper III (Davis et al., 2018a) presented a study of the lenticular galaxy NGC 4429. The molecular gas disc turned out to have a central hole and thus Keplerian rotation was not detected. Nevertheless, the presence of a SMBH could still be inferred by enhanced gas rotation velocities at the inner edge of the disc, compared to those expected from the stellar mass alone, and thus an accurate SMBH mass was still derived. The gas velocities in the rest of the disc further required a stellar mass-to-light ratio gradient to be adequately fit by the model.

Concurrent with the work presented in this thesis, other work was pursued by the WISDOM team. Paper V (North et al., 2019) presented a SMBH mass measurement in the massive radio galaxy NGC 383, adopting several of the methods introduced in Smith et al. (2019). The linear resolution attained in the ALMA observations (0.″13 or ≈40 pc) resolved the (rather large) SMBH sphere of influence (by ≈7 beams radially), yielding a clear Keplerian central rotation signature. This angular resolution is equivalent to ≈140 000 $R_{\rm Sch.}$, and is thus among the best 'resolved' extragalactic SMBHs.

Liu et al. (2021) conducted a study of the GMCs in NGC 4429, using the observations of Davis et al. (2018a). The clouds identified were found to be less massive and less extended but denser than those in the Milky Way. Strong internal velocity gradients in individual clouds were shown to be the result of the strong gradient in the galactic potential; when taken into account, these indicate that the clouds are gravitationally unbound. This study further demonstrated that cloud properties can be strongly affected by rotational shear and tidal forces.

Having said all that, not all the WISDOM galaxies have a regularly rotating disc. Sub-parsec ALMA observations of the dwarf galaxy NGC 404 revealed a kinematically- and morphologically-complex outer ring, with an inner core of regularly rotating gas consistent with high rotational motions around an IMBH (Davis et al., 2020). Similarly, observations of the elliptical galaxy NGC 708 revealed a prominent non-circular feature superimposed on a rotating disc. North et al. (2021) analyse this feature, assuming it is an outflow, and estimate its mass and power. Although these quantities are sensitive to the assumptions adopted, they are consistent with a model in which the known AGN jet powers the outflow.

Future papers in the WISDOM series are planned to measure additional SMBH masses, further refine the software tools available, study the GMC properties of the full sample galaxies, and investigate the radial (streaming) flows seen in some sample galaxies.

1.5 Structure of this thesis

HIS thesis comprises four core chapters. Chapters 2 and 3 present measurements of the SMBH mass in the lenticular galaxy NGC 524 and the elliptical galaxy NGC 7052 respectively. Chapter 4 presents an empirical correlation between CO linewidths at large scales and central SMBH masses. Chapter 5 presents unpublished material on other galaxies observed and analysed as part of my work. Chapter 6 concludes by comparing the SMBH masses from the WISDOM project to those from other dynamical tracers, and anticipates the next steps for the WISDOM programme.

2

A molecular gas dynamical measurement of the supermassive black hole mass in NGC 524

Contents

The material in this chapter was originally published in the Monthly Notices of the Royal Astronomical Society, Volume 485, p.4359-4374.

2.1 Introduction

ALTHOUGH representing only a small fraction of its mass, the supermassive black hole (SMBH) now believed to lie at the heart of every galaxy has a major effect on its evolution. Observations over several decades have demonstrated the close relationship between the mass of a SMBH and various properties of its host galaxy (e.g. Magorrian et al., 1998; Ferrarese & Merritt, 2000; Gebhardt et al., 2000; Kormendy & Ho, 2013; McConnell & Ma, 2013), implying some form of co-evolution. The nature and explanation of these relationships remain disputed.

Aside from the aforementioned empirical correlations, the role of SMBHs in galaxy evolution has been explored extensively through theoretical work and simulations (e.g. Silk & Mamon, 2012; Naab & Ostriker, 2017). Accretion onto a SMBH is considered the most likely explanation for the nuclear activity observed in many galaxies (Lynden-Bell, 1969). Such activity can provide feedback, affecting the evolution of the galaxy. In particular, simulations have shown that the inclusion of feedback from accretion onto a SMBH reproduces a variety of observed galaxy properties (e.g. Meza et al., 2003; Vogelsberger et al., 2014), including the stellar mass function (e.g. Croton et al., 2006; Schaye et al., 2015) and metallicity (e.g. Choi et al., 2017). Most recently, observations have found correlations between SMBH masses and galaxy star formation histories, further emphasising the potential role of feedback on a galaxy's stellar mass assembly (Martín-Navarro et al., 2018).

Most empirical studies infer SMBH masses from correlations with more easily observed quantities; fewer carry out dynamical measurements based on the kinematics of orbiting material. The latter require high spatial and velocity resolution to disentangle the dynamical contribution of the dominant stellar mass from that of the SMBH in all but the innermost regions, and have historically been done using the velocities of stars, ionised gas or megamasers. Robust measurements are thus far available for only a relatively small number of galaxies (230 galaxies are listed in van den Bosch, 2016, of which $\approx$ 70 are upper limits).

In the millimetre-Wave Interferometric Survey of Dark Object Masses (WISDOM) project, we are developing a new alternative to the stellar and ionised gas dynamical tracers, through high spatial resolution measurements of the kinematics of molecular gas, available routinely with the Atacama Large Millimeter/Submillimeter Array (ALMA). This method was first demonstrated by Davis et al. (2013b), in which interferometric observations of the molecular gas disc in NGC 4526 allowed the measurement of the SMBH mass via dynamical modelling. Over the past few years, the technique has been characterised (Davis, 2014; Yoon, 2017) and applied to galaxies across the Hubble sequence, both active and inactive (Onishi et al., 2015; Barth et al., 2016c; Onishi et al., 2017; Davis et al., 2017a, 2018a).

In this chapter, we present an estimate of the SMBH mass at the centre of NGC 524, extending our previous techniques to account for its complicated gas distribution, and considering evidence for a kinematic warp in the disc. In Section 2.2, we introduce NGC 524 and previous studies of it. In Section 2.3, we discuss our observations, their calibration, reduction and imaging, and how they are optimised for our science goals. We then move on to make an estimate of the SMBH mass using our existing techniques in Section 2.4, and discuss the systemic uncertainties on our measurement. In Section 2.5 we modify our techniques by constraining the gas distribution directly using our data, demonstrating and validating a technique which will be needed for future studies of galaxies with complex gas distributions. Section 2.6 discusses the presence of a non-axisymmetric perturbation in the observed velocity field, and we conclude briefly in Section 2.7.

2.2 NGC 524

GC 524 is a nearly face-on early-type galaxy with a core stellar light profile (Faber et al., 1997). It has an I-band effective radius (R_e) of $51''$ and a stellar velocity dispersion within $1R_e$ of $\sigma_e = 220\,\mathrm{km\,s^{-1}}$(Cappellari et al., 2006, 2013a). It is classified as a fast rotator, with a specific angular momentum within $1R_e$ of $\lambda_{R_e} = 0.28$ (Emsellem et al., 2007). A regular central dust disc with flocculent spiral arms is visible in absorption in *Hubble Space Telescope*

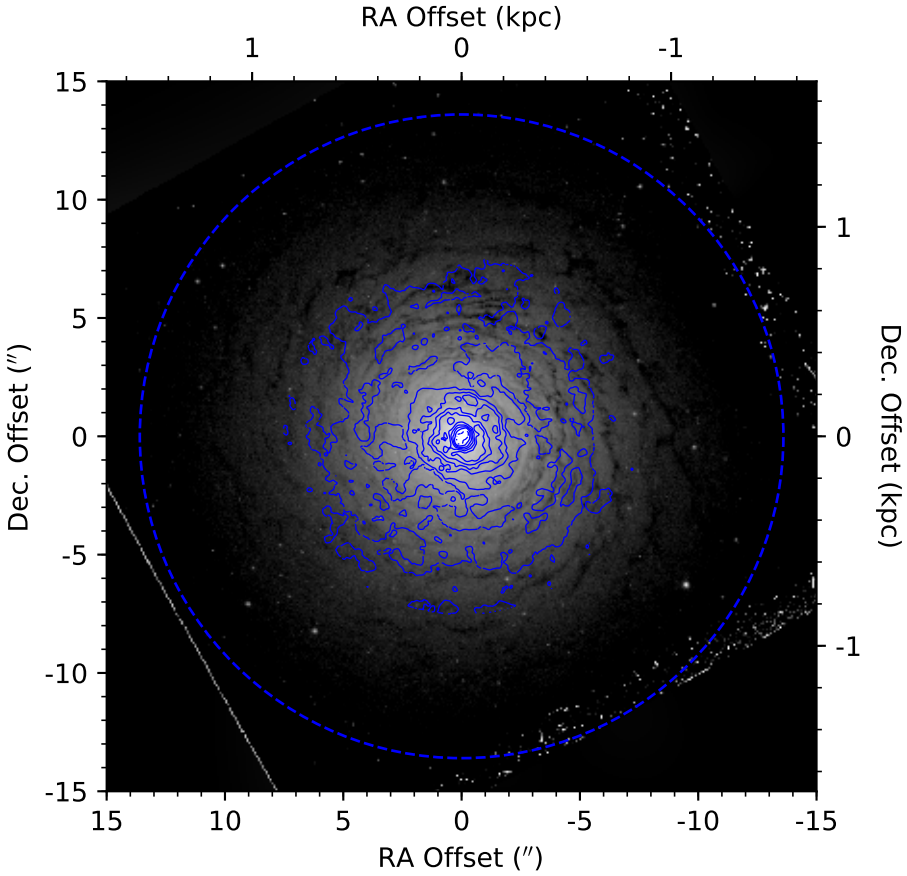

Figure 2.1: Unsharp-masked *HST* WFPC2/PC F555W image of NGC 524 (grey), overlaid with the molecular gas surface density (blue contours) at $5\,M_\odot\,pc^{-2}$, and then at 100, 200, 400, 600, 800, 1000, and $1200\,M_\odot\,pc^{-2}$ derived from our ALMA observations and assuming a CO-to-H_2 conversion factor $\alpha_{CO} = 4.3\,M_\odot\,(K\,km\,s^{-1})^{-1}\,pc^{-2}$. The ALMA primary beam is shown by the blue dashed circle.

(*HST*) images (Sil'chenko, 2000). Figure 2.1 shows an unsharp-masked *HST* WFPC2/PC F555W image, overlaid with blue contours indicating the distribution of CO gas in our ALMA data. Throughout this chapter we adopt a distance to NGC 524 of 23.3 ± 2.3 Mpc, as used in other studies, derived using the surface brightness fluctuation distance of Tonry et al. (2001) with the Cepheid zero-point of Freedman et al. (2001). At this distance, 1″ corresponds to 113 pc.

NGC 524's molecular gas has previously been observed in the ATLAS^{3D} project. Young et al. (2011) observed both the CO(2-1) and CO(1-0) lines with the Institut de Radioastronomie Millimétrique (IRAM) 30-m telescope, finding a double-horned profile typical of a rotating disc, and measuring a total molecular gas mass of

$M_{H_2} = (9 \pm 1) \times 10^7\,M_\odot$. In parallel, the disc was spatially-resolved using the Plateau de Bure Interferometer (PdBI; Crocker et al., 2011) in the CO(1-0) line, with a resolution of $2\farcs8 \times 2\farcs6$ ($320 \times 290\,pc^2$).

NGC 524 exhibits nuclear activity, and is revealed as a compact radio source at 5 GHz by the Very Large Array (VLA; Nyland et al., 2016) and Very Long Baseline Interferometry (VLBI; Filho et al., 2004). This is indicative of the presence of a SMBH, acting as the central engine of this activity through accretion. An earlier measurement of the SMBH mass was made by Krajnović et al. (2009), based on stellar kinematics obtained with the adaptive optics-assisted Gemini-North telescope. This galaxy therefore offers an important cross-check between the stellar and molecular gas dynamical techniques. Krajnović et al. (2009) concluded that the SMBH mass is $M_{BH} = 8.3^{+2.7}_{-1.3} \times 10^8\,M_\odot$ and the stellar mass-to-light ratio in the I-band is $M/L_I = 5.8 \pm 0.4\,M_\odot/L_{\odot,I}$, having assumed an inclination of 20° from Cappellari et al. (2006).

The radius of the sphere of influence of the SMBH, the approximate spatial scale within which the SMBH exceeds the stellar contribution to the potential, is defined as $R_{SOI} \equiv \frac{GM_{BH}}{\sigma^2}$, where σ is the stellar velocity dispersion. This is argued to be the relevant length scale for measuring the SMBH mass (e.g. Ferrarese & Ford, 2005; Davis, 2014). Using the Krajnović et al. (2009) black hole mass and the aforementioned stellar velocity dispersion, the expected sphere of influence radius is 73 pc ($0\farcs65$).

2.3 Data

2.3.1 Observations and data reduction

HE data presented here are combined observations of the ^{12}CO(2-1) line in NGC 524 from ALMA, using both the 12-m array and 7-m Atacama Compact Array (ACA; also known as the Morita array). Data were taken as part of the WISDOM project's observing programmes 2015.1.00466.S (PI: Onishi), 2016.2.00053.S (PI: Liu) and 2017.1.00391.S (PI: North). The 12-m data span baselines from 15 m to 1.3 km, providing the high spatial resolution required

for our project, and were taken in four tracks on the 26th March 2016, 17th July 2016, 2nd May 2017, and 16th September 2018. The ACA observations, on shorter baselines from 9 to 48 m and providing sensitivity to more extended gas structures, were taken in a single track on 25th June 2017. The total on-source time achieved was 2.2 hours with the 12-m array and 0.3 hours with the ACA.

For both arrays, a spectral window was positioned to observe the redshifted $J = 2$ to $J = 1$ transition of ^{12}CO at a velocity resolution of $\approx 1\,\mathrm{km\,s^{-1}}$ over a bandwidth of $\approx 2500\,\mathrm{km\,s^{-1}}$. Three additional spectral windows were positioned to observe the continuum emission, each with a bandwidth of 2 GHz and a lower spectral resolution.

The data were calibrated using the standard ALMA pipeline, and combined using the `Common Astronomy Software Applications` (`CASA`; McMullin et al., 2007) package.

2.3.2 Line data

To remove the continuum emission from the AGN, a linear fit was made to the line-free channels at both ends of the line spectral window and was subtracted from the *uv* plane using the `CASA` task `uvcontsub`. The remaining line data were imaged into an RA-Dec-velocity cube with a channel width of $15\,\mathrm{km\,s^{-1}}$. Baselines were weighted by the Briggs scheme with a robust parameter -1, weighting towards higher spatial resolution at the expense of sensitivity. The synthesised beam achieved was $0\farcs35 \times 0\farcs3$ at a position angle of 64°, a factor ≈ 7 improved spatial resolution compared to the Crocker et al. (2011) observations. This corresponds, at the distance of NGC 524, to a linear scale of $\approx 40 \times 30\,\mathrm{pc}$, so that the predicted radius of the SMBH sphere of influence is resolved with ≈ 2 synthesised beams. The pixel size adopted was $0\farcs1$, such that the beam was approximately Nyquist sampled. The cube size encompasses the array's primary beam spatially, and ≈ 15 channels on either side of the detected line spectrally, but not the entire bandwidth of the spectral window. The sensitivity achieved in the $15\,\mathrm{km\,s^{-1}}$channels is $0.5\,\mathrm{mJy\,beam^{-1}}$. The cube was cleaned interactively using a manually-defined mask to encompass regions of emission in each channel.

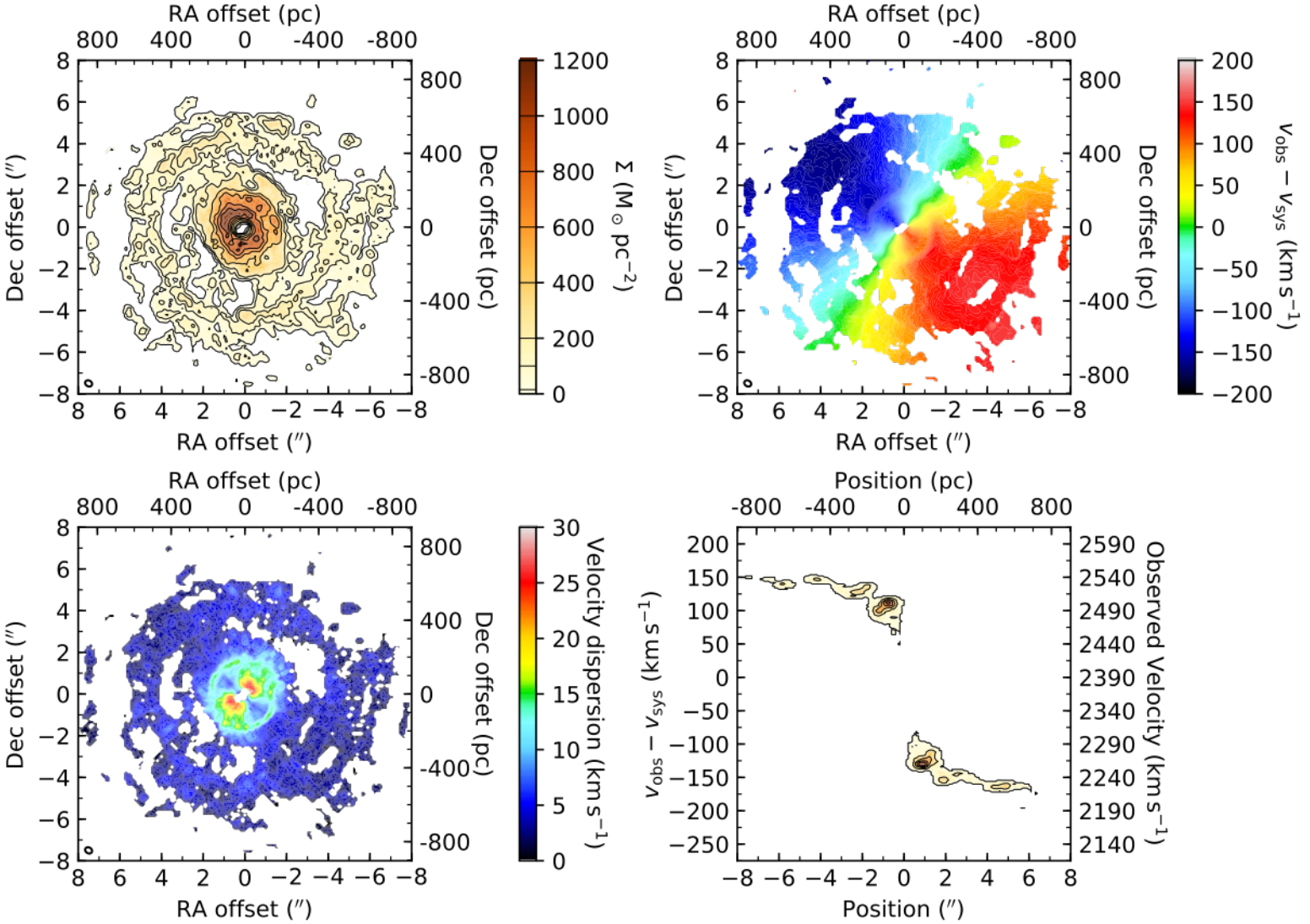

Figure 2.2: Moment maps of the ^{12}CO(2-1) emission in NGC 524, from our ALMA data. **Top-left:** Molecular gas surface density, assuming a CO-to-H_2 conversion factor $\alpha_{CO} = 4.3\,M_\odot\,(K\,km\,s^{-1})^{-1}\,pc^{-2}$. Black contours are from the level at which the noise was clipped, $5\,M_\odot\,pc^{-2}$, and then at 100, 200, 400, 600, 800, 1000, and $1200\,M_\odot\,pc^{-2}$. **Top-right:** Mean line-of-sight velocity. **Bottom-left:** Velocity dispersion. **Bottom-right:** Kinematic major-axis position-velocity diagram (PVD). In both right panels, v_{obs} is the observed line-of-sight velocity and $v_{sys} = 2390\,km\,s^{-1}$is the mean systemic velocity. The synthesised beam is shown in the bottom-left corner of each map. We note the presence of a central hole surrounded by a wide ring, from which the gas distribution falls off until a second, outer, ring. We also note the presence of a region of high velocity dispersions at a radius of $\approx 2''$, that correlates with a distortion in the velocity field. There is no evidence of a central Keplerian rise in the PVD, likely because of the central hole.

Table 2.1: Cube parameters.

Parameter	$2\,\mathrm{km\,s^{-1}}$ cube	$15\,\mathrm{km\,s^{-1}}$ cube
Image size (px)	800×800	800×800
Pixel scale ($''$/px)	0.1	0.1
Channels	400	50
Channel width ($\mathrm{km\,s^{-1}}$)	2	15
Velocity range ($\mathrm{km\,s^{-1}}$)	$2000 - 2798$	$2000 - 2735$
Synthesised beam ($''$)	0.35×0.3	0.35×0.3
Sensitivity ($\mathrm{mJy\,beam^{-1}}$)	1.0	0.5

A second cube was created from the same *uv* data with the same parameters but $2\,\mathrm{km\,s^{-1}}$ channels, reaching a sensitivity of $1.1\,\mathrm{mJy\,beam^{-1}}$. This provides the smaller channels required to constrain the gas velocity dispersion, if at the expense of sensitivity (see Section 2.4.4). The properties of both cubes are tabulated in Table 2.1.

Moment maps of the integrated flux, mean line-of-sight velocity, and velocity dispersion are shown in Figure 2.2. These were made using the smooth-masking method (Dame, 2011), whereby the cube is convolved spatially by a Gaussian of the synthesised beam size, is Hanning-smoothed spectrally, and is then clipped at some threshold. This defines a mask that is then applied to the original unsmoothed cube before the moment analysis.

While the molecular gas appears co-incident with the dust disc seen in optical images, a central hole can clearly be seen. This hole is slightly larger that the predicted sphere of influence of the SMBH, so that we are unlikely to capture the Keplerian rise in the rotation expected as the SMBH begins to exceed the enclosed stellar mass. Similar holes have been seen in smoothed-particle hydrodynamical simulations of the tidal disruption of molecular clouds in galactic nuclei (Trani et al., 2018), and in our observations of NGC 4429, but we were still able to obtain a good model of the gas kinematics and thus a good constraint on the SMBH mass (Davis et al., 2018a).

We additionally draw attention to the apparent distortion of the isovelocity contours at a radius of $\approx 2''$ (top-right panel of Figure 2.2). The position of this

distortion corresponds to that of the ring of increased velocity dispersions in the bottom-left panel of Figure 2.2. This feature is considered in detail in Section 2.6.

Interferometers resolve out flux due to the baselines incompletely sampling the *uv* plane. We initially try to ascertain how much flux has been recovered by comparing the integrated spectrum derived from our data with that of the IRAM 30-m telescope single-dish observations of Young et al. (2011), as shown in Figure 2.3. These single-dish observations collect all emission within the 10.″7 diameter primary beam. Our integrated flux map (top-left panel of Figure 2.2) however shows that the CO disc extends beyond this beam, and Figure 2.3 indeed shows that ALMA recovers more flux than the IRAM 30-m telescope. While this is encouraging, it is not a proof that all the flux is recovered by ALMA, as we now know that the single-dish spectrum necessarily underestimates the total flux. However, the inclusion of ACA baselines in our data should help to recover any missing flux, and gives a maximum recoverable scale of 29″. Since the disc shown in Figure 2.2 extends only across $\approx 16''$, well within the maximum recoverable scale, and the *uv* plane is well sampled from this scale to our spatial resolution, we conclude that it is likely that almost all flux has been recovered.

2.3.3 Continuum data

The continuum data, comprising the three other spectral windows and the line-free channels of the high-resolution spectral window (used for the line data), were also imaged. These spectral windows span 17 GHz, centred on 237.3 GHz, but only sample 7.5 GHz of this range due to gaps between the spectral windows. We do not detect continuum emission from the outer parts of the disc, but an unresolved source is detected at the centre of the galaxy, within the hole observed in the line emission. To localise this source, we create a continuum image using the multi-frequency synthesis option of the `TCLEAN` task in `CASA`. We use Briggs weighting with a robust parameter of -2, emphasising spatial resolution and achieving a synthesised beam of $0.''3 \times 0.''2$ with a sensitivity of 0.1 mJy beam^{-1}. We fit this source with a Gaussian using the `CASA` task `imfit`, and it is found to be unresolved,

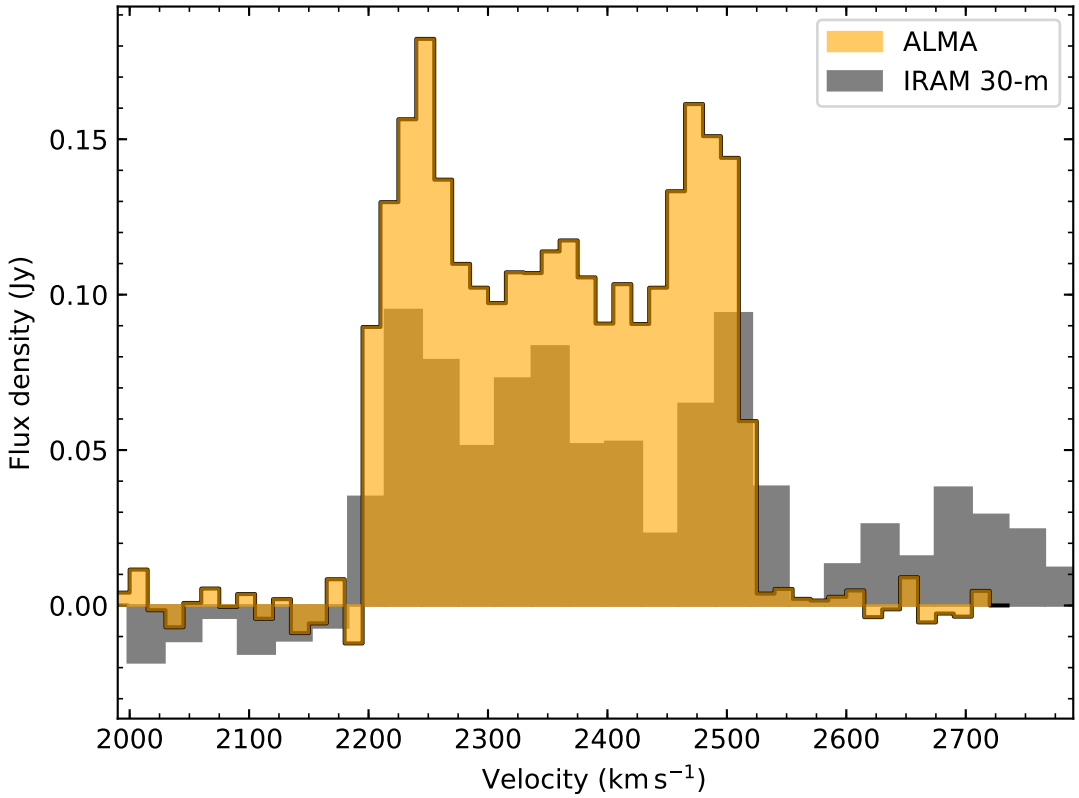

Figure 2.3: Spatially-integrated spectrum derived from our ALMA observations (orange shading) overlaid on an existing IRAM 30-m telescope spectrum (grey shading; Young et al., 2011). More flux is recovered with ALMA, likely the result of the wider ALMA primary beam, as our observations show that the CO disc extends beyond the 30-m beam. The IRAM 30-m velocities have been converted to the radio convention.

and centred at $01^{\mathrm{h}}24^{\mathrm{m}}47\overset{\mathrm{s}}{.}7448$, $+9°32'20\overset{''}{.}119$, consistent with the optical centre of the galaxy recorded in the NASA/IPAC Extragalactic Database[1] (NED). It has an integrated flux of 8.3 ± 0.1 mJy.

Central continuum emission has previously been observed at 3 mm using the PdBI and was shown to exceed that predicted from dust alone (Crocker et al., 2011), while at 5 GHz Filho et al. (2004) detected a compact radio source on a scale of milli-arcseconds (0.5 pc at our adopted distance of 23.3 Mpc). Together these are indicative of continuum emission from an active galactic nucleus (AGN). Our detection is consistent with these positions.

Unlike some of the previous WISDOM works, we do not present here a spectral energy distribution (SED) for this galaxy, since our source is compact. Archival

[1] http://ned.ipac.caltech.edu/

Table 2.2: Properties of the unresolved continuum source.

Parameter	Value
Right ascension	$01^{\rm h}\,24^{\rm m}\,47\overset{\rm s}{.}7448 \pm 0.0001$
Declination	$+9°32'20\overset{''}{.}119 \pm 0.001$
Integrated intensity	8.3 ± 0.1 mJy
Synthesised beam	$0\overset{''}{.}3 \times 0\overset{''}{.}2$
Sensitivity	$0.1\,\mathrm{mJy\,beam^{-1}}$

photometric data tabulated in NED show the similarly compact radio observations previously described and *Infrared Astronomical Satellite* (*IRAS*) observations at 100 µm and shorter wavelengths. The latter however trace thermal emission from dust on arcminute scales. Although a naïve approach to generating an SED shows that our detection appears to be in the Rayleigh-Jeans tail of this dust emission, we do not attempt to infer a dust temperature because of this difference in extent.

2.4 Model fitting

UR data allow us to measure the SMBH mass in NGC 524 by fitting the observed gas kinematics with those derived from a model of the galaxy's mass distribution. This procedure is discussed in detail in Davis et al. (2017a), and outlined here.

Within a Markov Chain Monte Carlo (MCMC) framework, we forward-model the observed data cube using the `Kinematic Molecular Simulation (KinMS)` tool[2] of Davis et al. (2013a), that produces simulated data cubes based on an input gas distribution, circular velocity curve and disc orientation. These simulated data cubes are generated by calculating the line-of-sight projection of the circular velocity for a large number of particles that represent the gas distribution. Additional velocity contributions can be added to account for the velocity dispersion and non-circular motions. The particles are then spatially and spectrally binned, and convolved by the synthesised beam to create a final simulated cube.

We initially assume that the SMBH is located at the position of the unresolved 1.3 mm continuum source (see Section 2.3.3). The fit is however allowed to vary

[2] https://github.com/TimothyADavis/KinMS

the exact kinematic centre of the galaxy from this position. We in fact find the centre is very strongly constrained to lie within a pixel of this location, and thus conclude the SMBH is at the kinematic centre of the galaxy's rotation.

The other inputs to our model describe the gas distribution, galaxy potential, and disc geometry. The latter is encapsulated in the overall spatial offsets previously described, a velocity offset, and the disc inclination and position angle relative to the observer. In the rest of this section, we thus discuss the remaining details of the model (gas distribution and galaxy potential), present the measurements, and estimate the associated uncertainties.

2.4.1 Gas distribution

In previous works in the WISDOM series, we have assumed some parametric function to describe the gas distribution - typically an exponential thin disc - and have fit the parameters defining this function to the observations as part of the MCMC framework. However, at the resolution achieved the presence of holes, rings and other complex gas morphological features affect our fits, significantly increasing the dimensionality of any model designed to reproduce them. There are two possible approaches to handle this. In this section, we fit our observations of NGC 524 with a coarse axisymmetric parameterisation of the gas distribution, accepting that this will necessarily miss some detailed features of the galaxy. Alternatively, we can directly sample the observed gas distribution to provide input particles to `KinMS`. We present this new method in Section 2.5.

In previous low-resolution observations of NGC 524, an exponential disc was sufficient to adequately describe its gas distribution (Davis & McDermid, 2017). However, our higher angular resolution data reveal a central hole. We therefore adopt an exponential surface density radial profile at large radii, truncated at the edge of a central hole:

$$I(r) \propto \begin{cases} 0 & r \leqslant R_{\rm trunc} \\ e^{-\frac{r}{R_0}} & r > R_{\rm trunc} \end{cases}, \tag{2.1}$$

where $R_{\rm trunc}$ is the central truncation radius and R_0 the scale length of the exponential disc, both of which are parameters in our MCMC fit. We continue to assume the disc is thin and axisymmetric. The central surface brightness of the exponential disc is not used in our model, instead the entire data cube is scaled to an overall integrated intensity, that is also a free parameter within our MCMC code.

2.4.2 Stellar mass

We parametrize the stellar mass distribution of NGC 524 using the multi-Gaussian expansion (MGE; Emsellem et al., 1994; Cappellari, 2002) of a *HST* Wide Field Planetary Camera 2 (WFPC2) F814W image at small radii, and a ground-based I-band image from the MDM observatory's 1.3-m McGraw-Hill Telescope at large radii. This MGE model was originally reported in Table B1 of Cappellari et al. (2006) and is reproduced in Table 2.3 of this work. This is the same model as that adopted in the prior stellar dynamical measurement of the SMBH mass (Krajnović et al., 2009). This model was made with no correction for extinction due to the flocculent dust disc in NGC 524, a correction we discuss in Section 2.4.7.3.

We assume the central MGE component, that is unresolved at our angular resolution, to correspond to optical emission from the AGN. It therefore should not contribute additional stellar mass to our model, and we exclude it. We will consider the effect of this choice in Section 2.4.7.3, including this component in the limiting case that all the emission is due to stellar light, and showing that it has a negligible effect on the best-fitting model.

The two-dimensional (2D) MGE parameterisation of the stellar light distribution is used to construct the circular velocity curve of the CO disc. The MGE model can be analytically deprojected to a three-dimensional (3D) distribution given a viewing angle (inclination). In our model, we assume axisymmetry and that the CO lies in the mid-plane of the stars, such that the inclination used to deproject the MGE is adopted from the CO disc (in principle a free parameter in our fit, in practice constrained to $\approx$20° as discussed in detail in Section 2.4.5).

Table 2.3: Deconvolved 2D MGE components of NGC 524, reproduced from Cappellari et al. (2006).

$\log_{10} I'_j$ ($L_{\odot,I}pc^{-2}$) (1)	$\log_{10} \sigma_j$ ($''$) (2)	q'_j (3)
*4.336	-1.762	0.95
3.807	-1.199	0.95
4.431	-0.525	0.95
3.914	-0.037	0.95
3.638	0.327	0.95
3.530	0.629	0.95
3.073	1.082	0.95
2.450	1.475	0.95
1.832	1.708	0.95
1.300	2.132	0.95

Notes: The table lists the central surface brightness (column 1), width (column 2), and axial ratio (column 3) of each Gaussian component. The innermost, unresolved Gaussian marked with a star is assumed to relate to emission from the AGN, and is thus omitted from our kinematic fits.

From this 3D light distribution, a mass distribution is obtained by multiplying by a spatially-constant mass-to-light ratio (M/L), another parameter included in our MCMC fit. Use of a constant M/L has been validated by previous kinematic and stellar population studies of NGC 524. Davis & McDermid (2017) fit the kinematics of earlier CO(1-0) PdBI observations (Crocker et al., 2011) using the Krajnović et al. (2009) SMBH mass, our adopted MGE model and a radially-varying mass-to-light ratio, concluding that an essentially flat dynamical mass-to-light ratio adequately reproduced the disc kinematics. This conclusion was further supported by a uniformly old stellar population.

Given this 3D mass distribution, the potential can be easily calculated by performing the one-dimensional integral given by Equation 12 of Cappellari (2002), and the circular velocity curve directly follows.

2.4.3 Bayesian parameter estimation

We use the Gibbs-sampling MCMC code `KinMS_MCMC`[3] with adaptive stepping to explore the parameter space. Assuming Gaussian errors, we use the chi-squared statistic as a metric of the goodness-of-fit of the model to the data:

$$\chi^2 \equiv \sum_i \left(\frac{\mathrm{data}_i - \mathrm{model}_i}{\sigma_i} \right)^2 = \frac{1}{\sigma^2} \sum_i (\mathrm{data}_i - \mathrm{model}_i)^2 \ , \tag{2.2}$$

where the sum is performed over all the pixels within the region of the data cube that the model fits, and σ is the rms noise as measured in line-free channels of the data cube, that we assume constant for all pixels. Samples are then drawn from the posterior distribution described by the the log-likelihood function $\ln P = -\chi^2/2$. Initially, the step size is adaptively scaled to ensure a minimum acceptance fraction is reached and the chain converges, before the entire chain is re-run at a fixed step size to sample the full posterior distribution. The final chain length is 3×10^5 steps, with the first 10% discarded as a burn-in phase.

To ensure the chain converges, we always set uniform priors within physical limits (see Table 2.4, columns 2 and 6), to constrain the range of parameter space the fit can explore. In particular, we draw attention to the prior boundaries on the disc inclination, where the lower bound is the lowest inclination for which the MGE can be analytically de-projected, and to the prior for the SMBH mass, that is uniform in logarithmic space rather than linear space.

2.4.3.1 Pixel-to-pixel correlations

As the product of interferometric observations is the source emission convolved by the synthesised beam, the latter oversampled in our data cube, adjacent pixels do not provide independent measures of the χ^2 value. In practice we therefore use a more general form of Equation 2.2, that includes the inverse of the covariance matrix describing pixel-to-pixel correlations (Barlow, 1989), as discussed in Davis et al. (2017a).

[3] https://github.com/TimothyADavis/KinMS_MCMC

The number of elements in this covariance matrix scales as the square of the number of spaxels included, rapidly becoming prohibitively expensive computationally. We therefore only fit the central $6\farcs4 \times 6\farcs4$ (720 pc × 720 pc) region of our cube. We previously predicted the sphere of influence of the SMBH to be only $0\farcs65$, so this region still provides a very large number of spaxels dominated by the stellar mass distribution, necessary to accurately constrain the stellar mass-to-light ratio.

2.4.3.2 Chi-squared uncertainties

As our data are noisy, the χ^2 statistic has an additional uncertainty associated with it, following the chi-squared distribution (Andrae, 2010). This distribution has a variance of $2(N - P)$, where N is the number of constraints and P the number of inferred parameters. For our data N is very large ($\approx 10^5$), so the variance becomes $\approx 2N$.

The traditional approach to inferring uncertainties in a single parameter using a χ^2 grid is to select the 1σ (68%) confidence interval as the contour within which $\Delta\chi^2 = 1$. However, as van den Bosch & van de Ven (2009) noted, this approach yields unrealistically small uncertainty estimates due to systematic effects, which can produce variations of χ^2 of the order of its formal error $\sqrt{2N}$. They proposed to increase the 1σ confidence interval to $\Delta\chi^2 = \sqrt{2N}$.

As we are using a Bayesian MCMC approach, rather than χ^2 contours, to achieve the same effect we need to scale the log-likelihood, as done by Mitzkus et al. (2017). This is done here by dividing the χ^2 of each model by $\sqrt{2N}$, which is identical to increasing the input errors (the noise in the cube) by $(2N)^{1/4}$, as in Mitzkus et al. (2017). This approach appears to yield physically credible formal uncertainties in the inferred parameters, whereas otherwise these uncertainties are unphysically small. Additionally, this remains a conservative estimate for the uncertainty on the SMBH mass, as the mass will be determined by only the innermost pixels, rather than the full N.

2.4.4 Gas velocity dispersion

We include in our model a non-zero velocity dispersion ($\sigma_{\rm gas}$), that will become large if the disc is not dynamically cold. We assume that this dispersion is spatially invariant, and only a small linear perturbation on the circular velocity field. Evidence for this is provided by the bottom-left panel of Figure 2.2, where in regions unaffected by beam smearing the velocity dispersions are uniformly less than $10\,{\rm km\,s^{-1}}$, and even in beam-smeared regions is $< 30\,{\rm km\,s^{-1}}$. This is to be compared to the typical (deprojected) rotation velocities ($v_{\rm rot}$) exceeding $400\,{\rm km\,s^{-1}}$.

The main data cube used for our SMBH measurement has channel widths of $15\,{\rm km\,s^{-1}}$, chosen to improve the signal-to-noise ratio of our data while still adequately probing the gas kinematics. However, as $\sigma_{\rm gas}$ is found to be less than a channel width, a better constraint on it can be derived by adopting narrower channels that resolve $\sigma_{\rm gas}$ spectrally. We thus opt to perform an initial fit using our cube with $2\,{\rm km\,s^{-1}}$channels, finding the best-fitting velocity dispersion, and then fixing this value for subsequent fits to our cube with $15\,{\rm km\,s^{-1}}$channels from which we derive the other model parameters. The best-fitting velocity dispersion is then $9.3\,{\rm km\,s^{-1}}$, fixed in all subsequent MCMC runs.

As suggested above, the low velocity dispersion implies $v_{\rm rot}/\sigma_{\rm gas} \approx 44$ (assuming $i = 20°$ and the velocity dispersion to be isotropic), indicating the disc is nearly perfectly rotationally supported. This is consistent with our assumption that the rotation curve is dominated by gravitational forces, and hence traces the galaxy potential.

2.4.5 SMBH mass

As stated above, following the initial fit, we perform a second fit over the 10 remaining parameters describing our model: SMBH mass, I-band mass-to-light ratio, gas disc scale length, truncation radius and an overall luminosity scaling, the disc position angle and inclination, and one offset in each of the three cube dimensions (RA, Dec., and velocity). Although most parameters are found to be within the priors, the disc inclination is not, with a best-fitting value of $19.^{\circ}9^{+4.^{\circ}9}_{-0.^{\circ}8}$,

where the uncertainties are the 99.7% confidence interval. However, the sample is truncated by the lower bound of the inclination prior. This prior is dictated by the MGE model described in Section 2.4.2, that cannot be deprojected below this inclination. It would be a mistake to ascribe to this minimum inclination a physical significance, since the Gaussian components themselves do not necessarily have physical significance (Cappellari, 2002). Thus we cannot be confident that the final chain is a true reflection of the posterior, as lower inclinations are not explored.

A very small modification to the MGE model allows us to remove this constraint. We circularise the MGE components using the transformation $[I'_j, \sigma_j, q'_j] \rightarrow [I'_j, \sigma_j\sqrt{q'_j}, 1]$, where I'_j, σ_j, and q'_j are respectively the surface brightness, width, and axis ratio of each Gaussian component, thereby avoiding the need to constrain the inclination prior (Cappellari et al., 2009). This transformation effects only a very small change to the MGE model, and ensures that the luminosity and peak surface brightness of each Gaussian is conserved. The priors for, and results of, this fit are shown in columns 2-5 of Table 2.4. We find a very weak constraint on the inclination, that has an asymmetric posterior and drives a very significant uncertainty in both the SMBH mass and stellar M/L_I derived (see Figure 2.4). Indeed, the effect of inclination is so strong that it over-rides the expected inverse correlation between SMBH mass and stellar mass-to-light ratio, that would otherwise conserve the total dynamical mass. This is shown by the positive covariance in the central panel of the left column of Figure 2.4. The covariance would be negative at fixed inclination, however as inclination varies the total dynamical mass varies with it, generating the apparent positive covariance in the 2D marginalisation that projects the posterior over inclination.

The effect varying inclination has on SMBH mass measurements can be easily understood by simple arguments. Since we do not directly observe the galaxy's rotation velocity $v_{\rm rot}$, but rather the line-of-sight projection $v_{\rm rot}\sin i$, the uncertainty associated with inclination will directly affect the black hole mass measurement. We can quantify this effect using a simple circular motion model:

$$M_{\rm BH} \propto v^2 \propto \left(\frac{v_{\rm obs}}{\sin i}\right)^2. \tag{2.3}$$

As $\sin i$ changes most rapidly at low inclinations it will be a major contributor to the uncertainty on the SMBH mass for the very low inclination disc of NGC 524. Using the circularised MGE model, we find an inclination of $15^\circ\,^{+8^\circ}_{-5^\circ}$, that from Equation 2.3 could change the SMBH mass by -0.4 to $+0.3$ dex. The median SMBH mass of the accepted models in the MCMC chain is $\log(M_{\rm BH}/{\rm M}_\odot) = 8.9 \pm 0.4$, indicating that almost all the uncertainty is due to the inclination uncertainty. The asymmetry of the posterior further means that the best-fit model and the median value of the 1-dimensional (1D) marginalisation are substantially different. The model with the maximum log-likelihood has an inclination of 20.6° and $\log(M_{\rm BH}/{\rm M}_\odot) = 8.6$.

Having said that, we can constrain the inclination using other information. A tilted-ring fit to the velocity field, as described in Section 2.6.2.2, yields an average inclination of 21°, with a standard deviation of 6°. Previously, assuming it is intrinsically circular, the dust disc seen in *HST* images was also found to lie at an inclination of $20 \pm 5^\circ$ (Cappellari et al., 2006). Since CO is commonly found co-incident with dust (e.g. Crocker et al., 2008, 2009, 2011; Young et al., 2008), this also provides information on the molecular gas disc inclination (Davis et al., 2011).

As giving our model extensive freedom to explore inclination does not lead to good constraints when using only our ALMA data, we re-run the fit with a fixed inclination of 20°, adopted from the above arguments. We also take the opportunity to fix the RA and Dec offsets to their previous best-fitting values to reduce the dimensionality of the model. The results of this fit are shown in columns 6-8 of Table 2.4, and in full corner plots in Figure 2.5. With the inclination uncertainty removed, we now obtain much tighter constraints on the SMBH mass and mass-to-light ratio. We then include the inclination uncertainty as a systematic uncertainty in Section 2.4.7.2.

Our best-fitting SMBH mass is thus $4.0^{+1.6}_{-1.5} \times 10^8\,{\rm M}_\odot$ (3σ formal uncertainties) with a reduced χ^2 of $\chi^2_{\rm red} = 1.84$. This yields a sphere of influence radius of 36 pc ($0\farcs31$) that, although marginally spatially resolved by our synthesised beam, is

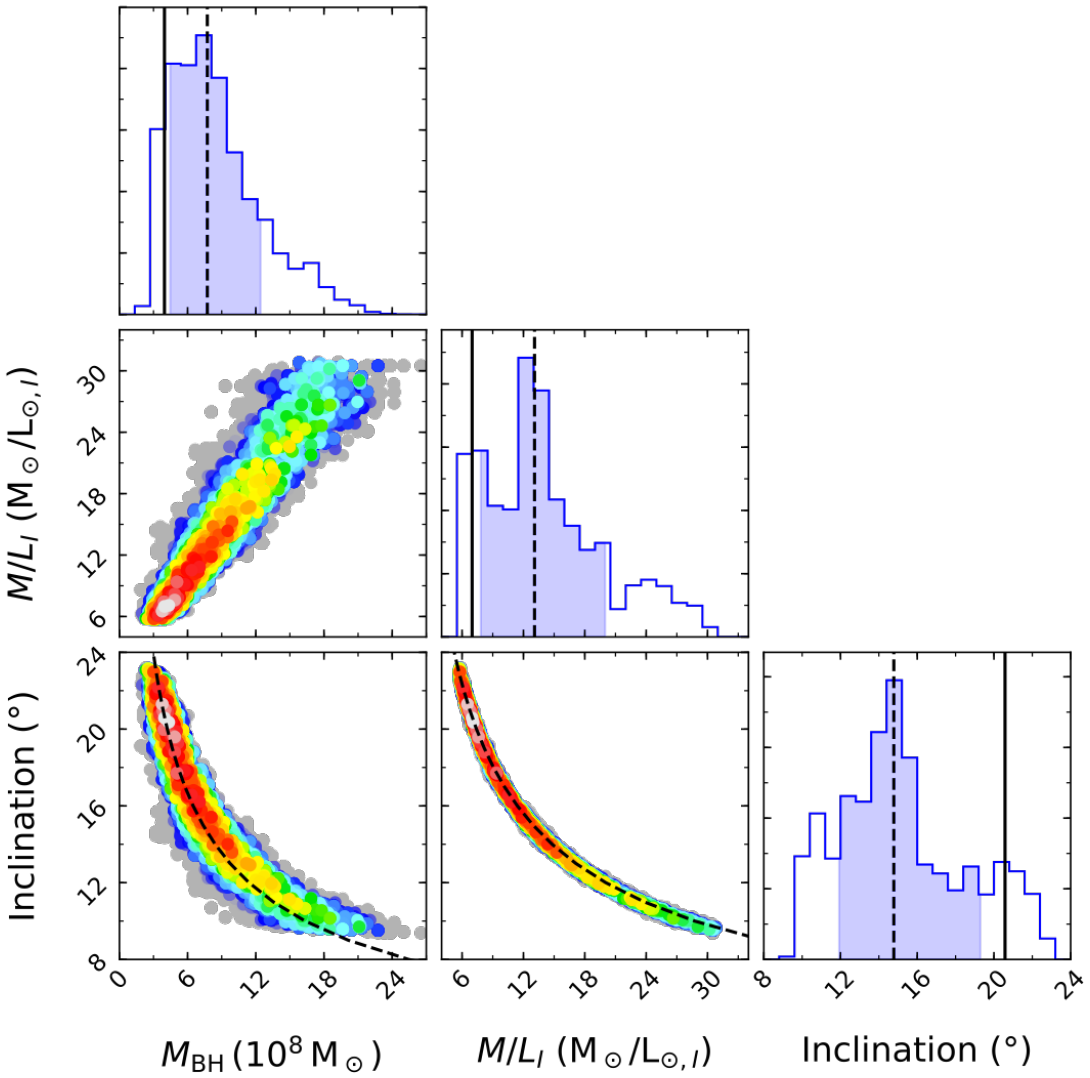

Figure 2.4: Corner plots showing the covariances between the three key model parameters, from a fit using the circularised MGE model permitting low inclinations. The inclination uncertainty is directly correlated with the uncertainties in both SMBH mass and stellar M/L_I. Each point is a realisation of our model, colour-coded to show the relative log-likelihood of that realisation, with white points the most likely and blue least. Grey points are realisations with $\Delta\chi^2 > \sqrt{2N}$ relative to the best-fitting model, and are even less likely. Black dashed lines on the scatter plots indicate the predicted effect a varying inclination has on the best-fitting values (following Equation 2.3). The data very closely follows these expected dependencies, showing that the uncertainties are dominated by the inclination. Histograms show 1D marginalisations of each parameter, with black lines denoting the median (dashed) and best-fitting (solid) values. We note that the asymmetry of the posterior means that the most likely value and median are different. The shaded region indicates the 68% confidence interval.

smaller than the hole observed in the CO gas. It is thus unsurprising that we do not see the Keplerian increase in the rotation curve in the very centre of the galaxy. The unusually large uncertainty in the SMBH mass compared to other CO measurements is also likely due to this limitation.

Our best-fitting mass-to-light ratio is $5.7 \pm 0.3\,M_\odot/L_{\odot,I}$ (3σ formal uncertainties). We will consider in Section 2.4.7.3 the effect our mass model has on the SMBH mass found.

2.4.6 Fit uncertainties

In subsection 2.4.3.2, we defined the fit confidence interval used in this work, whereby we modified the standard $\Delta\chi^2$ interval to include the uncertainty in the χ^2 value. As a sanity check of this definition, we make a second estimate of the uncertainties by bootstrapping. We select 16 sub-samples from our cube, constituted of half-cubes bounded by planes at fixed position angles. All planes are at regular angular intervals and pass through the previously established position of the SMBH. For each sample, we minimise the χ^2 defined in Equation 2.2 using `MPFIT` (Markwardt, 2009).

For each parameter, we define the overall best fit as the mean and the 1σ bootstrapped uncertainty as the standard deviation of all the best-fitting values across the 16 sub-samples. The uncertainties thus obtained are listed in Table 2.5. The best-fitting values are consistent with those estimated by the MCMC procedure, and the uncertainty estimates are reassuringly very similar. We are therefore confident that the uncertainties derived using our modified Bayesian approach described in Section 2.4.3.2 (and listed in Table 2.4) are reliable estimates of the true uncertainties, and we henceforth adopt them.

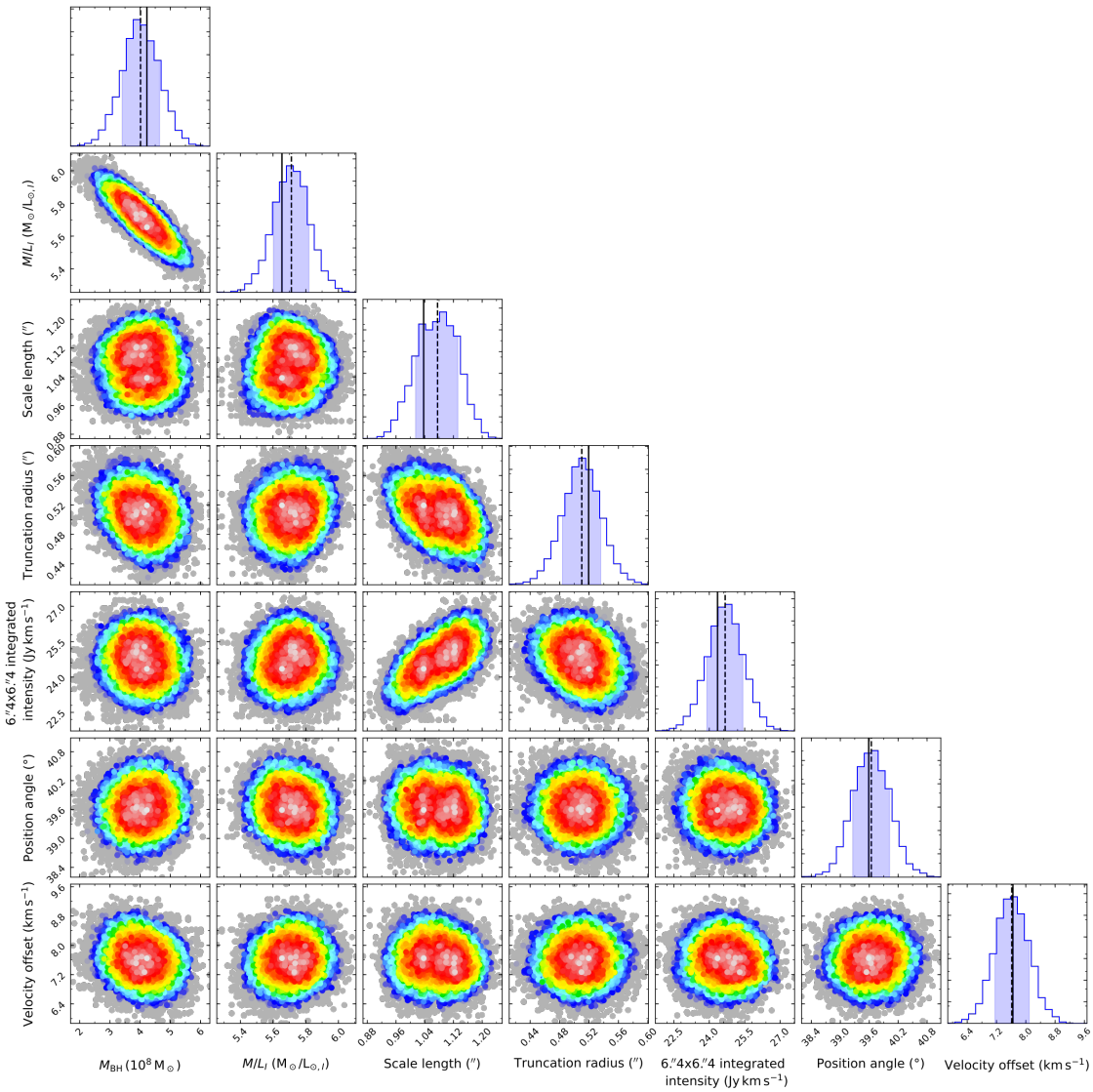

Figure 2.5: Corner plots showing the covariances between all model parameters, from an MCMC fit at fixed inclination. Each point is a realisation of our model, colour-coded to show the relative log-likelihood of that realisation, with white points the most likely and blue least. Grey points are realisations with $\Delta\chi^2 > \sqrt{2N}$ relative to the best-fitting model, and are even less likely. The only significant covariance is between the SMBH mass and the mass-to-light ratio, that corresponds to attributing the dynamical mass across the SMBH and stellar distribution. The weak covariances between integrated intensity, scale length and truncation radius are due to the integrated intensity being the normalisation of the surface brightness profile, and therefore dependent on the exact fits. Histograms show 1D marginalisations of each parameter, with black lines denoting the median (dashed) and best-fitting (solid) values. We note that the asymmetry of the posterior means that the most likely value and median are very slightly different. The shaded region indicates the 68% confidence interval.

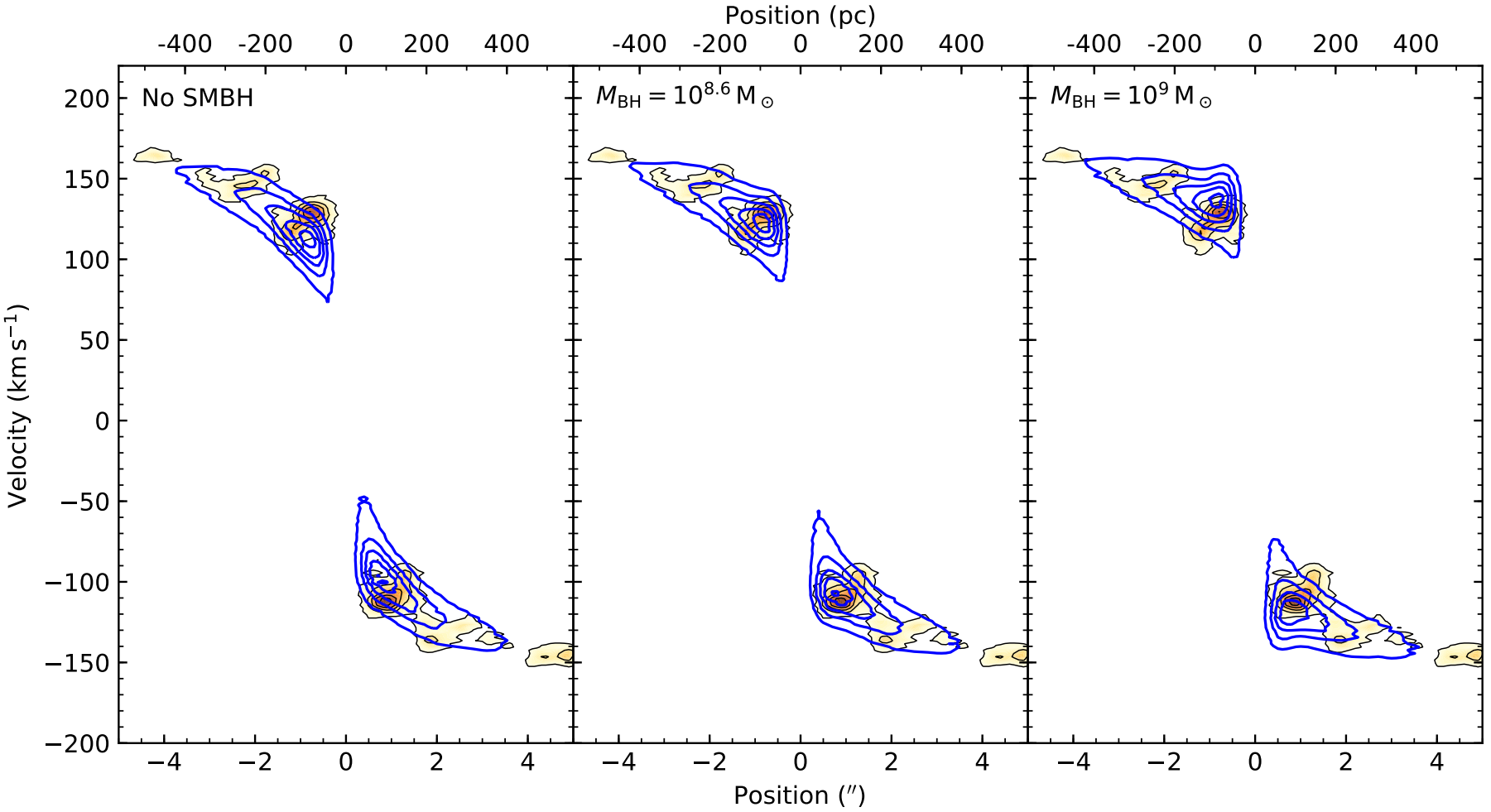

Figure 2.6: Model position-velocity diagrams along the kinematic major axis of the galaxy (blue contours), showing a model without a SMBH (left), with the best-fitting SMBH (centre) and with an overly large SMBH (right). These are overlaid on the observed PVD previously shown in Figure 2.2 (orange scales and contours). As can be seen at small radii, the line-of-sight velocities are enhanced compared to a stellar mass-only model, requiring additional central mass to fully account for them.

Table 2.4: Best-fitting model parameters, with associated formal uncertainties determined using the modified Bayesian sampling approach described in Section 2.4.3.2.

	Circularised MGE ($\chi^2_{\rm red} = 1.84$)				Fixed inclination ($\chi^2_{\rm red} = 1.84$)		
Parameter	Priors	Best fit	Median	3σ Error	Priors	Median	3σ Error
(1)	(2)	(3)	(4)	(5)	(6)	(7)	(8)
Mass model							
log(SMBH mass) ($M_\odot$)	5 → 16	8.60	8.89	±0.42	5 → 12	8.60	−0.21, +0.15
Stellar M/L_I ($M_\odot/L_{\odot,I}$)	1 → 10^7 ⋆	7.0	13.2	−7.4, +15.0	0.1 → 10	5.7	±0.3
Molecular gas geometry							
Scale length (″)	0.1 → 10	1.02	1.02	±0.1	0.1 → 10	1.1	±0.1
Truncation radius (″)	0 → 10	0.53	0.52	±0.07	0 → 10	0.51	±0.07
6.″4 × 6.″4 integrated intensity (Jy km s^{-1})	1 → 200	20.8	20.8	±1.5	1 → 200	24.7	−2.0, +1.9
Gas velocity dispersion (km s^{-1})	1 → 100	9.3	(fixed)	(fixed)	(fixed)	9.3	(fixed)
Viewing geometry							
Inclination (°)	0.1 → 90	20.6	14.8	−5, +8	(fixed)	20	(fixed)
Position angle (°)	0 → 359	39.9	39.6	±1	0 → 359	39.6	±1
Nuisance Parameters							
Centre RA offset (″)	−1 → 1	-0.12	-0.12	±0.04	(fixed)	−0.12	(fixed)
Centre Dec. offset (″)	−1 → 1	-0.05	-0.05	±0.04	(fixed)	−0.05	(fixed)
Centre velocity offset (km s^{-1})	−75 → 75	7.9	7.8	±1.5	−75 → 75	7.6	±1.2

Notes: The reduced chi–squared value given is that of the model with the best-fitting parameters for each MCMC chain. For the circularised MGE fit, the asymmetric posteriors shown in Figure 2.4 mean that the minimum chi-squared and the median of the 1D marginalisation of each parameter are not the same, so both are listed. In both fits, the gas velocity dispersion was fixed to the value found in an identical fit to our 2 km s^{-1}cube, using the priors listed in column 2. The prior for the mass-to-light ratio marked with a ⋆ is uniform in logarithmic-space for the free inclination fit, where it covers several orders of magnitude, but it is uniform in linear space for the fixed-inclination fit. This avoids unduly favouring high values.

2.4.7 Systematic uncertainties

Our SMBH mass estimate relies on our model being an appropriate model of the data. We thus consider in this section how robust our estimate is against a number of effects:

2.4.7.1 Distance

Dynamical SMBH mass estimates are systematically affected by the assumed distance (D) to the galaxy, with $M_{\rm BH} \propto D$. Here we have adopted a distance of 23.3 Mpc, from the surface brightness fluctuation work of Tonry et al. (2001), updated for the Cepheid photometric zero-point of Freedman et al. (2001). The formal uncertainty in this measurement is $\approx 10\%$, but since this is a simple normalisation, we follow standard practice and do not include it in our systematic uncertainty.

2.4.7.2 Inclination

We include in the SMBH mass uncertainty a contribution from inclination uncertainty, by adding the additional contribution predicted from Equation 2.3. For this purpose, we adopt as the inclination uncertainty at 20° the representative value of ±5° quoted by Cappellari et al. (2006). This is slightly more conservative than the uncertainty given by our tilted-ring model, but broadly consistent with the upper bound of the confidence interval from the MCMC fit without the circularised MGE where inclination was allowed to vary. At 25° inclination, Equation 2.3 implies a decrease in $\log(M_{\rm BH}/{\rm M}_\odot)$ of −0.18 dex, and at 15° an increase of +0.24 dex.

2.4.7.3 Mass model

Since the molecular gas disc has a central hole, we do not capture the Keplerian increase of the rotation velocities where the SMBH dominates the mass distribution. We therefore rely on the accuracy of our stellar mass model to constrain the SMBH mass, observing an enhancement of the velocities compared to those expected from the stellar mass alone.

Table 2.5: Uncertainties estimated by bootstrapping fits to subsets of the data.

Parameter	Best Fit	Uncertainty (3σ)
Mass model		
log(SMBH mass) ($M_\odot$)	8.61	$\pm$0.21
Stellar M/L_I ($M_\odot/L_{\odot,I}$)	5.73	$\pm$0.33
Molecular gas geometry		
Scale length ($''$)	1.16	$\pm$0.12
Truncation radius ($''$)	0.54	$\pm$0.12
$6''.4 \times 6''.4$ integrated intensity (Jy km s^{-1})	25.1	$\pm$6.2
Gas velocity dispersion (km s^{-1})	9.3	(fixed)
Viewing geometry		
Inclination ($^\circ$)	20	(fixed)
Position angle ($^\circ$)	39.6	(fixed)
Nuisance parameters		
Centre RA offset ($''$)	-0.12	(fixed)
Centre Dec. offset ($''$)	-0.05	(fixed)
Centre velocity offset (km s^{-1})	7.7	(fixed)

Notes: The best fitting value listed is the mean of the best-fitting values for each subset, while the uncertainty is 3 times the standard deviation of these values.

The I-band image used by Cappellari et al. (2006) to construct the MGE stellar light model discussed in Section 2.4.2 may be contaminated by dust extinction, although we expect the extinction in this band to be minimal. It is possible that this will only reduce the total flux without affecting the light distribution, in which case the derived M/L will simply be overestimated, and the SMBH mass derived will be unaffected. However, the flocculent dust distribution visible in *HST* images suggests that the extinction will be irregular. Although correcting for extinction can be challenging, we can make a first-order correction using the prescription of Cappellari et al. (2002). Using the *HST* Planetary Camera F555W and F814W images, we calculate the (V-I) colour for each pixel. We assume the galaxy has an intrinsic (V-I) colour that is a power-law in radius, fit from the dust-free region at the centre of the galaxy, where our CO map exhibits a hole. We then use a standard

galactic extinction law (Binney & Merrifield, 1998) to correct the I-band image for the colour excess in each pixel. This excess is most significant over the region from $0\farcs5$ to $4''$, diminishing at larger radii. We construct a new MGE model from this extinction-corrected image, and use this model as before to fit the ALMA data cube. Since we are only interested in whether the SMBH mass derived is changed, rather than a full MCMC chain, we only perform a chi-squared minimisation using `lmfit`[4]. We find that the SMBH mass is unchanged within our uncertainties, and therefore dust extinction is not a significant effect.

Since our mass model is based entirely on the I-band light emitted by the galaxy, we neglect any possible contribution to the potential by non-luminous matter. If this were distributed identically to the stellar mass, the only impact would be that an overestimated stellar M/L_I, with no effect on the SMBH mass or other model parameters. However, if centrally concentrated, some of the excess velocities would be attributed to the SMBH, leading us to systematically overestimate the SMBH mass.

Fortunately, on these small spatial scales we expect the stellar mass to dominate the potential. Our observations show that the molecular gas disc extends only to a radius $R \approx 8''$, whereas the I-band effective radius $R_{\mathrm{e},I} = 51''$ (Cappellari et al., 2006), and we can assume a negligible dark matter contribution over so small a fraction of the galaxy's volume. Figure 2.7 shows the mass enclosed within a sphere of radius R due to each significant contribution to the potential.

Another possible source of mass not considered previously is the interstellar medium (ISM). Interferometric observations of NGC 524 by Oosterloo et al. (2010) do not detect HI associated with the molecular gas disc, implying that the cold ISM is dominated by molecules. Young et al. (2011) observed NGC 524 with the IRAM 30-m telescope, in both CO(1-0) and CO(2-1), reporting a total molecular gas mass of $9 \times 10^7\,\mathrm{M}_\odot$ assuming a standard CO-to-H_2 conversion factor. However, this mass is spread across the entire disc. We can test if it is significant by comparing it with the total stellar mass present within the same volume, as estimated from

[4] DOI:10.5281/zenodo.1699739

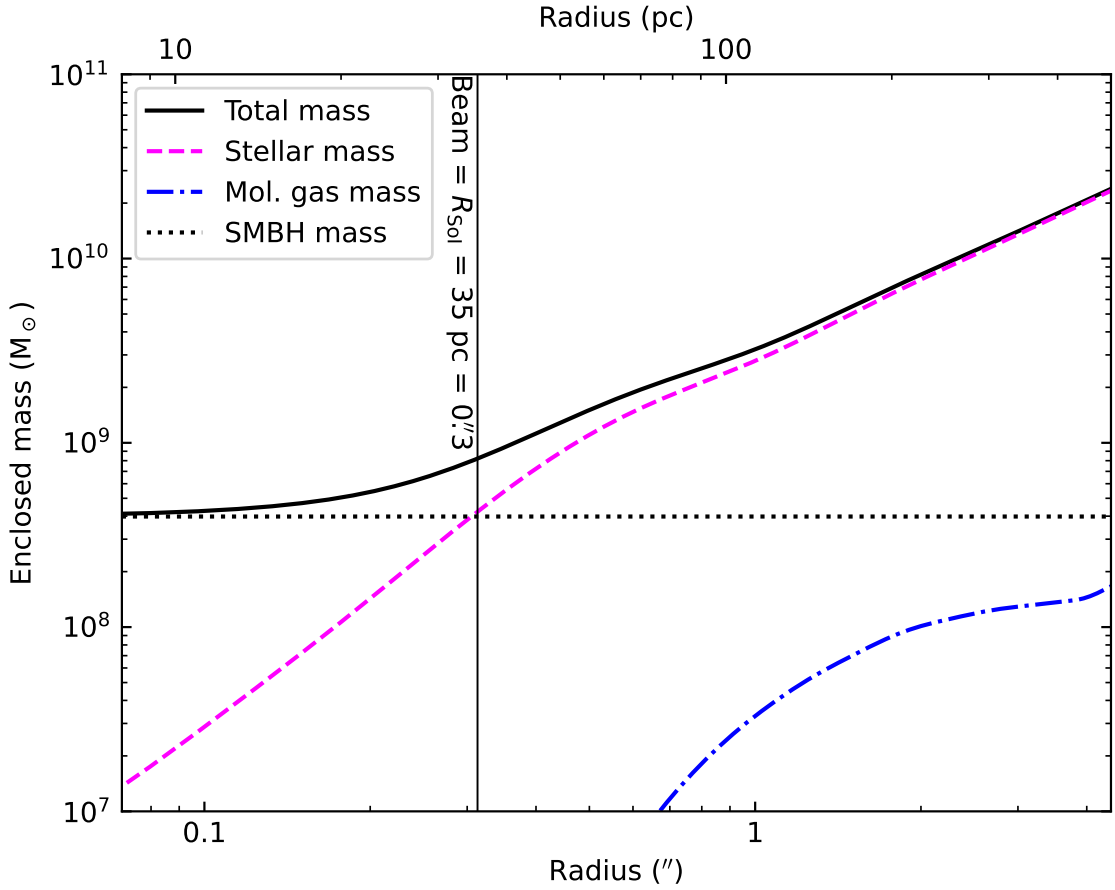

Figure 2.7: Radially-integrated mass profiles based on our best-fitting dynamical model of NGC 524. The total mass enclosed (black, solid) is the sum of contributions from stars (magenta, dashed), molecular gas (blue, dot-dashed) and the SMBH (black, dotted). At $R_{\rm SoI}$, the stellar mass enclosed is equal to the SMBH mass. The molecular gas mass is negligible at all radii.

our best-fitting model. This is calculated from the integral of the MGE model to the edge of the disc ($R = 8''$) and our best-fitting mass-to-light ratio, yielding a stellar mass of $6 \times 10^{10}\,{\rm M}_\odot$, thus dwarfing the cold ISM contribution. Additional evidence that we can neglect the molecular gas mass is provided by the presence of the central hole, indicating that the H_2 content around the SMBH is very low. We therefore conclude that the SMBH mass is not biased by the cold ISM at small radii.

In addition, we recall (from Section 2.4.2) that we *a priori* excluded the central MGE component (marked with a * in Table 2.3), arguing that it is likely due to emission from the AGN, and so should not contribute mass to our stellar distribution. It is however possible that the light in this component is in fact due to stars, that

would thus contribute mass to our model, indistinguishable from that of the SMBH as our observations do not resolve them. To test this, we re-fit our data cube fixing all parameters except the SMBH mass to their previous best-fitting values, and including this MGE component. We find no significant change in the best-fitting SMBH mass. This is unsurprising since, even integrated to the edge of the disc and using our best-fitting mass-to-light ratio, this MGE component contributes only $\approx 10^6\,\mathrm{M}_\odot$, or less than 1 per cent of the previously derived SMBH mass. This potential contribution is thus again dwarfed by both the SMBH mass and the stellar mass due to all the resolved MGE components.

Finally, we assumed that a constant mass-to-light ratio is appropriate across the entire disc. In the outer regions, this has been shown to be a good assumption by Davis & McDermid (2017), using the earlier lower-resolution observations of Crocker et al. (2011). In the very centre, as we do not detect the Keplerian signature of the SMBH, one could argue that a different M/L_I and thus mass distribution within the hole would obviate the need for a SMBH. To achieve this effect through additional stellar mass would require M/L_I to suddenly increase from 5.7 to ≈ 7. There is however no evidence of a commensurate change in the stellar population (Davis & McDermid, 2017). Additionally, the nuclear activity provides strong evidence for the presence of a SMBH, so we reject this argument.

2.4.8 Discussion

Having considered the sources of systematic uncertainty in Section 2.4.7, we conclude that the dominant sources of uncertainty are the poorly-constrained inclination and the distance adopted. The remaining uncertainties are the formal errors associated with the model fit. In Section 2.4.3.2, we argued that rescaling $\Delta\chi^2$ is required to yield physically reasonable formal uncertainties (and demonstrated that these uncertainties are consistent with those estimated by bootstrapping). We now combine the formal and inclination uncertainties to yield our final result.

We thus seek to combine our best-fitting SMBH mass at fixed-inclination, $M_{\mathrm{BH}} = 4.0^{+1.6}_{-1.5} \times 10^8\,\mathrm{M}_\odot$, where the uncertainties are 3σ formal errors, and the

uncertainty in the inclination, $20 \pm 5°$. For each model in the final MCMC chain, we draw an inclination from a Gaussian distribution with a 3σ width of 5°, and then use Equation 2.3 to transform the SMBH mass and stellar mass-to-light ratio to the new inclination. The final mass and uncertainty are then the median and 99.7% confidence intervals in the resultant distribution. Our resulting SMBH mass measurement is then $4.0^{+3.5}_{-2.0} \times 10^8\,\mathrm{M}_\odot$, where the uncertainty given is at the 3σ level.

This mass is approximately half that found by Krajnović et al. (2009) using stellar dynamics, but these results are consistent within the 3σ confidence intervals. The $M_{\mathrm{BH}}-\sigma_*$ relation of McConnell & Ma (2013) yields a SMBH mass estimate of $3.6^{+1.2}_{-1.0} \times 10^8\,\mathrm{M}_\odot$ (68% confidence interval including intrinsic scatter), compared to which our result is not only consistent, but also very similar. However, the uncertainties on our mass are larger than other CO dynamical measurements. This is due to the combination of the central hole, within which only ≈ 22 per cent of the dynamical mass is contributed by the SMBH, and the poor inclination constraints, the latter a result of the low inclination of the source.

Applying the same prescription to include the effect of inclination on the stellar $M/L_I = 5.7 \pm 0.3\ \mathrm{M}_\odot/\mathrm{L}_{\odot,I}$ (3σ formal uncertainties), we derive that $M/L_I = 5.7^{+3.9}_{-1.9}\,\mathrm{M}_\odot/\mathrm{L}_{\odot,I}$. In Section 2.4.7.3, we argued that an increase in the stellar M/L to $M/L_I = 7\,\mathrm{M}_\odot/L_{\odot,I}$ could obviate the need for a central SMBH, and at face value this inclination-adjusted result is now consistent with no SMBH. However, as we vary the inclination the SMBH mass also increases, so we still robustly recover an SMBH. Our M/L_I is comparable to the dynamical results of Cappellari et al. (2006) and Krajnović et al. (2009) and the stellar population analysis of Davis & McDermid (2017). It is however significantly higher than the latter's dynamical mass-to-light ratio ($M/L_I \approx 3.2\ \mathrm{M}_\odot/\mathrm{L}_{\odot,I}$), most likely as a result of the different inclination assumed. Using an equation analogous to Equation 2.3 to correct this dynamical mass-to-light ratio to the same inclination as the other works we find consistent results.

If our model fully explained our data, we would expect to find the χ^2 value of the best-fitting model to be $\nu \pm \sqrt{2\nu}$, where ν is the number of degrees of freedom

and $\nu \approx N$ due to the large number of data points. We in fact find our best fitting model has a larger χ^2, indicating there are features in the data unexplained by our relatively simple model. This will be common in the exquisite data available in the ALMA era. In the remainder of this chapter, we thus will explore features for which our simple model does not account.

2.5 Modelling complex molecular gas morphologies with `SkySampler`

UR high angular resolution ALMA data reveal an inner hole and much sub-structure in the molecular gas disc of NGC 524. In spite of crudely assuming a smooth gas distribution, we were still able to well-constrain the SMBH mass. Previous works on this galaxy used models with one fewer parameter to describe the disc morphology, lacking the truncation radius needed to account for the (then unresolved) central hole.

As ALMA reveals ever more substructures in the discs of many WISDOM targets, such coarse models will not remain appropriate. Yet in some of these, the velocity field still exhibits regular kinematics where gas is present to trace it, implying dynamical modelling is worth pursuing. We therefore face two options - either select arbitrarily complex models, adding free parameters until the gas distributions are well-described, or use the observed gas distributions as inputs to our models, thereby constraining the total flux at each location.

The latter option can be implemented by a simple modification of our existing methods. When we produce the `KinMS` model of the data cube, we generate a large number of particles with positions (r, θ) relative to the galaxy centre, such that the density of particles is proportional to the parameterised gas distribution function. We then calculate line-of-sight velocities based on the (axisymmetric) potential specified by our adopted mass model (usually, but not exclusively an MGE model of the stars). However, there is no reason why the gas distribution must be specifiable analytically by a small number of parameters, as we can define an arbitrary set of particle positions that satisfy any density distribution. As long as

this (non-axisymmetric) gas distribution is not a significant contributor to the total mass distribution, the assumption of axisymmetry for the potential will remain valid.

The method adopted to build such a model of the gas distribution is as follows. By integrating along the velocity axis of the data cube (i.e. creating a zeroth moment map), we obtain the desired spatial information on the distribution of the gas, independent from the kinematics. We then sample this image with a large number of particles. Were we to assume some particular inclination and position angle, we could now calculate the intrinsic (rather than projected) positions of the particles in the plane of the galaxy's disc. However, we actually include this deprojection step in our MCMC process, since in general we do not want to assume *a priori* a particular orientation of the gas disc. We thus supply these particles to `KinMS` using the `inClouds` variable, whereby a particle distribution can be manually specified rather than generated from an analytic radial profile. The particles are thereafter de-projected into the disc plane at each iteration within the MCMC framework (i.e. for each inclination and position angle), before line-of-sight velocities are calculated and the simulated cube generated using the same method as before.

However, the observations consist of the intrinsic gas distribution convolved by the beam, that is oversampled in the data cube. If we were to sample the cube directly, add the velocity field, and then apply the instrumental effects, we would effectively smear the data twice. We therefore sample instead a point source model of the gas distribution obtained from the `CLEAN` algorithm (Högbom, 1974). This model is already produced for every channel when imaging the data from *uv* plane visibilities, and we simply add the CLEAN components from all channels here, ignoring the velocity information. Sampling from the de-convolved cube ensures that our particles are placed at positions unbiased by beam smearing, creating a physically reasonable representation of the underlying intrinsic gas distribution. Beam smearing effects are then applied to each channel after the particle velocities are taken into account.

Our cube sampling code is implemented in Python in the software package `SkySampler`[5]. Having integrated along each spaxel, multiple particles are generated within each pixel, where the number generated is proportional to the intensity of the pixel. This allows us to reproduce emission in multiple channels. `SkySampler` also allows the use of other weighting schemes, so that, for example, the number of particles generated for each spaxel could be proportional to the width of the emission line in that spaxel.

2.5.1 Application to NGC 524

Although a good fit can be obtained to the NGC 524 data using the simple axisymmetric gas distribution given in Equation 2.1, we can also use the non-parametric distribution generated using SkySampler, allowing us to compare the two methods.

We thus re-run the fixed inclination MCMC fit with the `SkySampler` model of the gas distribution, that by construction replicates all the rings and holes in the data. Our best-fitting model has $\chi^2_{\rm red} = 1.82$. The improvement in $\chi^2_{\rm red}$ compared to the parametric model (for which $\chi^2_{\rm red} = 1.84$) might appear modest at first, but it reflects a significant change (roughly 6 times the variance) in the χ^2 value given the large number of pixels in the fit. The posterior is well-constrained, with all parameters consistent with those obtained assuming the parametric gas distribution. The resulting SMBH mass at fixed inclination is $M_{\rm BH} = 4.6^{+1.8}_{-1.3} \times 10^8\,{\rm M}_\odot$ (3σ formal uncertainties). The associated position-velocity diagram for the best-fitting model is shown in Figure 2.8 for comparison.

Although for NGC 524 the non-parametric method is not strictly required for our fit to converge, this new capability will be useful in sources with complex (non-axisymmetric) gas distributions, enabling us to make measurements without either forcing a coarse parametric model onto the data or requiring an excessive number of free parameters. The efficacy of this method to recover intrinsic source

[5] https://github.com/Mark-D-Smith/KinMS-skySampler

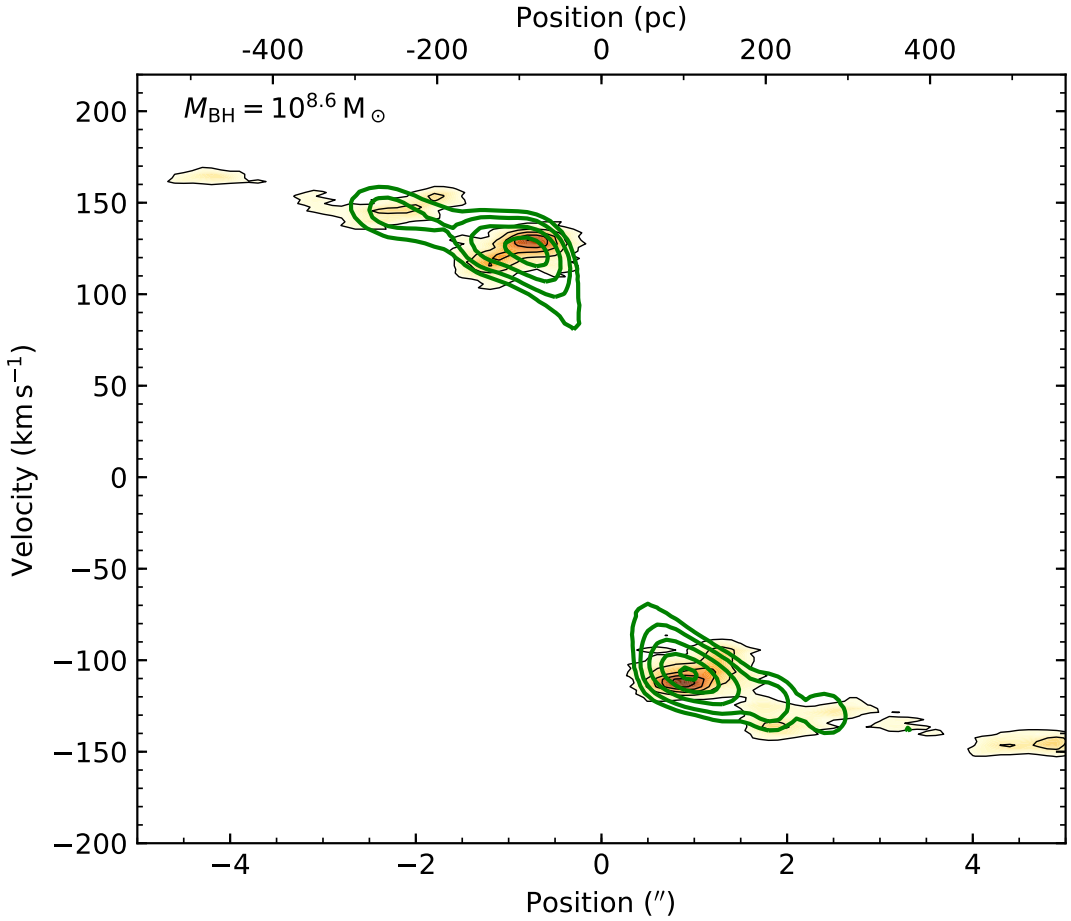

Figure 2.8: Kinematic major-axis position-velocity diagram for the best-fitting model using a non-parametric description of the gas disc morphology (green contours), overlaid on the observed PVD previously shown in Figure 2.2 (orange scale and contours). The model only extends to a 3.″2 radius due to the use of the covariance matrix (see Section 2.4.3.1). The SMBH mass and stellar mass-to-light ratio are consistent with those found using a simple parametric model of the gas distribution. The slight deviations of the model from the data at radii $\approx 2''$ are due to the feature described in Section 2.6.

distributions will be tested more formally on simulations in a future work of the WISDOM series (North 2020).

2.6 Non-circular motions

In this section we consider whether our data provide evidence for non-circular motions within the gas, and the effect these might have on the SMBH mass measurement.

The model presented in Section 2.4 assumes all gas is in circular motions, such that the observed velocities are the projection of only an azimuthal component

onto the line-of-sight. This appears a good assumption initially, as the observed velocity field shown in the top-left panel of Figure 2.2 appears smooth, with no significant motion along the minor axis (or equivalently a rather straight zero-velocity curve). However, as previously mentioned, the isovelocity contours at a radius $\approx 2''$ appear distorted, suggesting a purely circular model may be inappropriate. Further evidence for this is revealed by the residual velocity field (Figure 2.9), generated by subtracting the first velocity moment of a simulated cube (using the best-fitting parameters previously determined, but extending beyond the $6''.4 \times 6''.4$ fitting region) from the first velocity moment of the data shown in the top-left panel of Figure 2.2. A very clear spiral feature can be seen in the residuals, extending from the central hole with a peak amplitude of $\approx 15\,\mathrm{km\,s^{-1}}$. The systematic structure of these residuals suggests that the original model is not a complete representation of the data. However, we note that the characteristic magnitude of these residuals is only $\approx 10\%$ of the line-of-sight projection of the circular velocity curve, so they probably only trace a small perturbation on top of a dominant axisymmetric potential.

2.6.1 Observed velocity field

We first seek to correlate the distortions of the isovelocity contours and the ring of enhanced velocity dispersions (both visible in Figure 2.2) with the residual spiral structure shown in Figure 2.9. We initially guess that the increased velocity dispersions are due to beam smearing of tightly-spaced isovelocity contours. This broadens the distribution in a single spaxel, as emission in adjacent spaxels at slightly different velocities are blended together. This effect is already seen along the minor axis, where a large gradient in the velocity field as the radius approaches zero causes the isovelocity contours to bunch. Once these are convolved by the beam, emission is smeared over adjacent spaxels, broadening the observed lines.

The top panel of Figure 2.10 shows the spatial distribution of the observed velocity dispersion (coloured shading), and the predicted velocity dispersion from our best-fitting model cube (black contours), comprising the intrinsic velocity dispersion ($9.3\,\mathrm{km\,s^{-1}}$, as found in Section 2.4.4) and beam smearing of the circular velocity

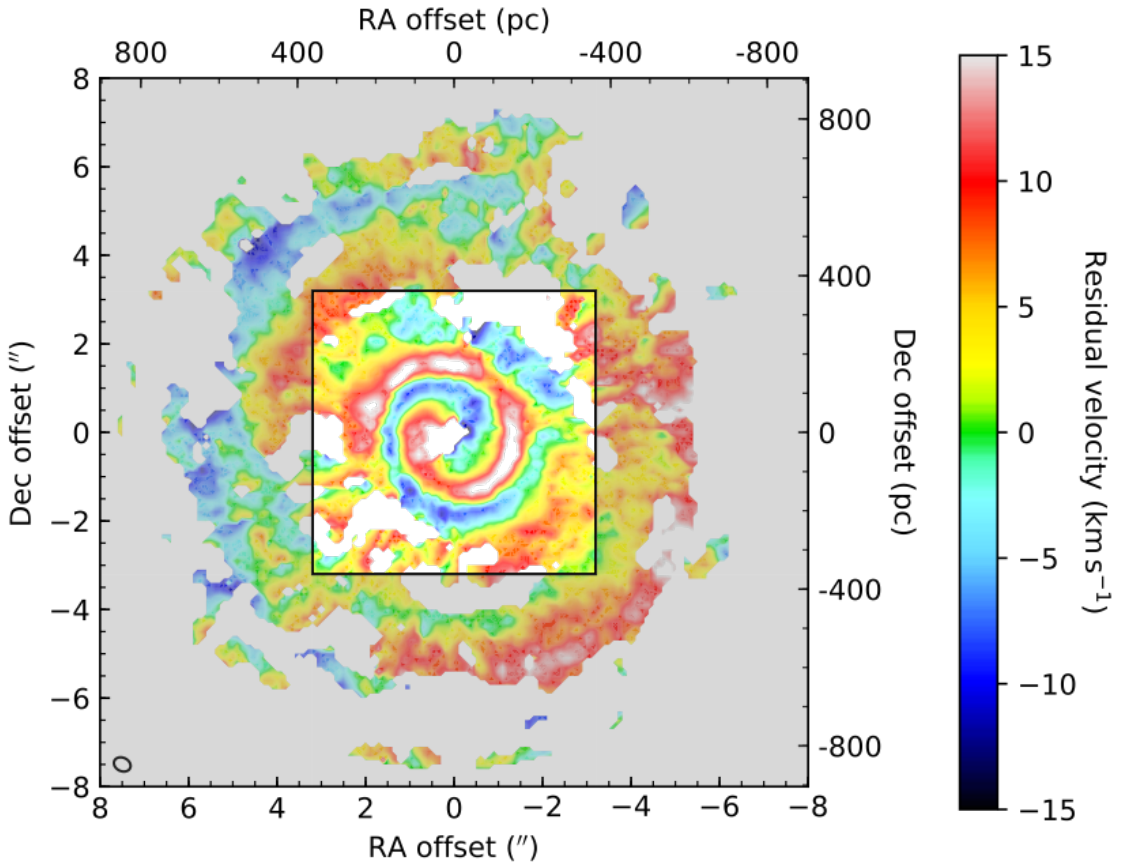

Figure 2.9: Residuals between the first moments (mean velocity fields) of the data cube and best-fitting model cube. The central box indicates the region within which the model was fit. The synthesised beam is shown in the bottom-left corner.

field. The velocity dispersions in the best-fitting model cube appear to closely match the enhanced velocity dispersion along the minor-axis, validating our assumption that this feature is due to beam smearing of the projected circular velocity field. However, the enhanced velocity dispersions across the major axis at $\approx 2''$ radius are not explained by beam smearing of the projected circular velocity field.

If the increased velocity dispersions at a radius $\approx 2''$ are caused by beam smearing of the two residual arms, the enhanced dispersions will lie between the peaks of the velocity residuals. We initially attempted to parameterise the spiral pattern and fit it with an additional velocity term with a phase described by an Archimedean or logarithmic spiral, but such fits do not match the data. We therefore attempted instead a non-parametric description of the spiral using the ridge-finding algorithm[6] of Steger (1998), to trace the peaks of the residual image. The residual

[6] DOI:10.5281/zenodo.845874

image was first manually masked to eliminate areas of low signal-to-noise ratios, retaining the principal spiral structure.

The bottom panel of Figure 2.10 again shows the spatial distribution of the observed velocity dispersion (coloured shading), and the velocity residual peaks (red- and blue-shifted arms) identified by the ridge-finding algorithm above. These remaining enhanced velocity dispersions are seen between the two spiral arms, and are on length scales consistent with the synthesised beam. We therefore attribute these enhanced velocity dispersions to beam-smearing of a non-axisymmetric/spiral perturbation in the velocity field.

2.6.2 Harmonic expansion

Having shown that the features identified in Figures 2.2 and 2.9 are due to a small perturbation on the circular velocity field, we now seek to characterise the nature of this perturbation. In particular, we wish to determine if it is evidence of non-circular motions (i.e. non-zero radial velocities), thereby potentially affecting our SMBH mass measurement. For this, we use the harmonics of the velocity field to separate the azimuthal and radial components of the observed line-of-sight velocities (e.g. Canzian, 1993; Schoenmakers et al., 1997; Spekkens & Sellwood, 2007).

We can write the general form of the line-of-sight velocities in terms of the radial and azimuthal components of the gas motion (restricting the motion to the disc plane in the thin disc approximation, and assuming axisymmetry):

$$\frac{v_{\rm los} - v_{\rm sys}}{\sin i} = \sum_{m=1}^{\infty} c_m(r)\,\cos(m\phi - \phi_0) + s_m(r)\,\sin(m\phi - \phi_0) \qquad (2.4)$$

where $\phi - \phi_0$ is the azimuthal phase of a point in the velocity field relative to the position angle ϕ_0 (the kinematic major axis). The $m = 1$ coefficient c_1 is then the rotation curve of the galaxy. All higher order terms could, in general, contribute kinematic support to the gas against gravity.

As expected, the phase dependence shows that azimuthal terms are zero along the minor axis, while radial terms are zero along the major axis. A single slit observation of the rotation curve, if not perfectly aligned with the major axis, could yield an

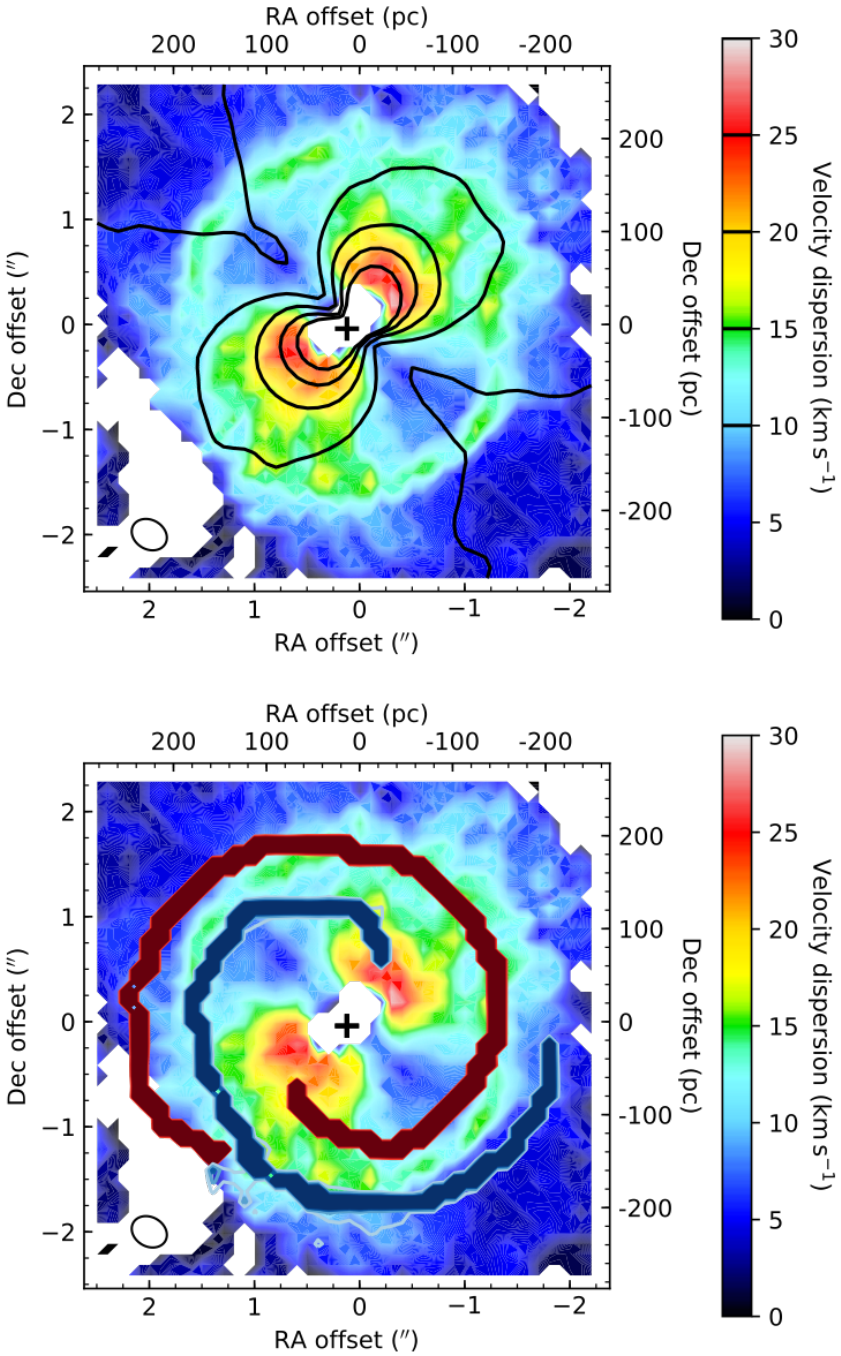

Figure 2.10: Top panel: Velocity dispersions measured in the best-fitting model data cube (black contours, at 5 km s^{-1} intervals from 10 km s^{-1} overlaid on the observed velocity dispersions (coloured shading). The model cube's velocity dispersions comprise the intrinsic dispersion (9.3 km s^{-1}, as found in Section 2.4.4) and beam smearing of the circular velocity field. Along the minor axis, the beam smearing accounts well for the observed velocity dispersions, but beam smearing of the model does not account for the excess dispersions along the major axis at $\approx 2''$ radius. **Bottom panel:** Red- and blue-shifted arms of the velocity residual shown in Section 2.9 (dark red and dark blue shading and contours), again overlaid on the observed velocity dispersions (coloured shading). The enhanced velocity dispersions on either side of the major axis appear consistent with beam smearing of the two spiral velocity perturbations detected. In both panels, the synthesised beam is shown in the lower-left corner, and the position of the SMBH with a black cross.

incorrect SMBH mass measurement due to artificially reduced velocities, even if no radial component is present. The addition of a radial velocity component will also modify the observed kinematics, affecting the resulting mass model. However, with 3D data and 2D kinematics, as in this work, this problem can be avoided, as the kinematic major axis can be well-determined empirically. The phase difference between the projection of the azimuthal and radial components further allows us to constrain the presence of any inflow/outflow through a harmonic analysis.

2.6.2.1 First-order term

To allow a first-order correction to be included in our models, we re-run the MCMC fit at fixed inclination while allowing an axisymmetric radial component of velocity, that is then projected as an additional contribution to the line-of-sight velocities. This adds one free parameter, the magnitude of this component, that we constrain within priors of $\pm 100\,\mathrm{km\,s^{-1}}$. Above such a magnitude, this contribution would almost equal the azimuthal component, and therefore be visually obvious in the velocity field. After running the MCMC chains as previously described, the best-fit solution is consistent with no radial flow, and the SMBH mass is unchanged.

2.6.2.2 Higher-order terms

Higher-order harmonic terms in Equation 2.4 are non-trivial to include in our forward-modelling process, adding many additional parameters to our model. However, higher order harmonics are routinely calculated for 2D velocity fields. Using the `Kinemetry` package[7] of Krajnović et al. (2006) and the observed velocity field (top-right panel of Figure 2.2), we fit higher order harmonics to ellipses at the fixed inclination and position angle determined by our MCMC model. The key results are shown in red in Figure 2.11.

The spiral feature highlighted in Figure 2.9 can also be seen in Figure 2.11 as the s_1 term, that from its definition in Equation 2.4 can be a radial flow. However, the best-fitting ellipse position angles are defined by minimising the s_1, s_3 and c_3 terms of the harmonic expansion (Krajnović et al., 2006). Thus the spiral feature

[7] http://davor.krajnovic.org/idl/#kinemetry

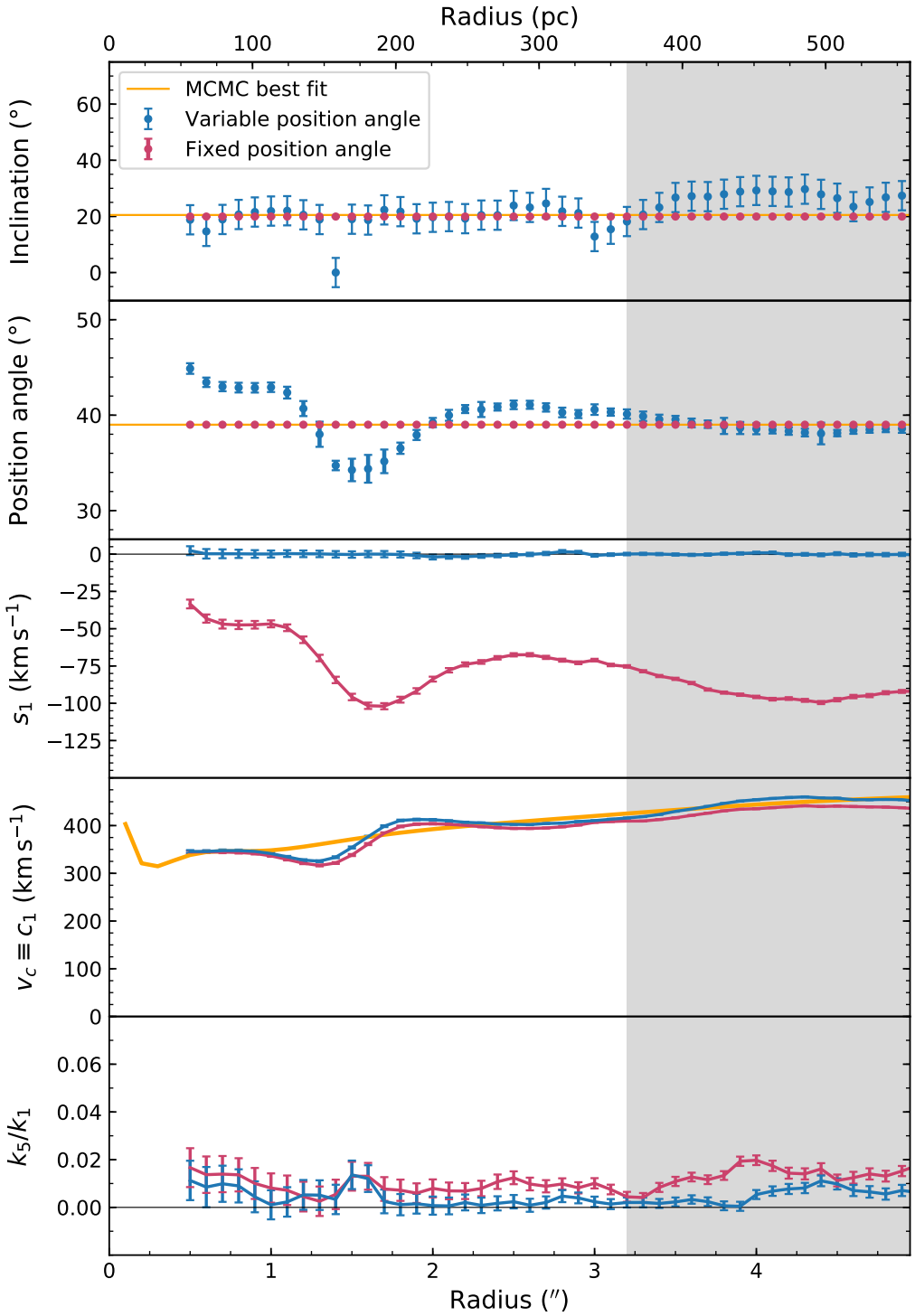

Figure 2.11: Best-fitting parameters of two harmonic expansions of the observed velocity field, evaluated on ellipses. In blue, the position angles are fit to the velocity field, whereas in red the position angles are fixed to the value used in the full cube fit. The orange line shows the equivalent parameter in the fixed-inclination MCMC fit, while the grey shading shows a radius of 3.″2 that approximates the boundary of the region fit in Section 2.4.5. **Top panel:** inclinations of the best-fitting ellipses, calculated from Equation 2.5. **Second panel:** position angles of the best-fitting ellipses. **Third and fourth panels:** first-order coefficients s_1 and c_1, as defined in Equation 2.4. **Lower panel:** higher-order deviations from ordered motion ($k_n \equiv \sqrt{c_n^2 + s_n^2}$).

could also be described as a position angle warp, a possibility not explored in this harmonic expansion nor in the MCMC fits. The degeneracy between a radial flow and a position angle warp in a tilted-ring harmonic expansions of 2D velocity fields was recently also identified and extensively discussed in Sylos Labini et al. (2019).

To explore the possibility of a position angle warp, we therefore re-run the harmonic expansion in a tilted-ring fit, shown in blue in Figure 2.11, permitting the model to freely choose both the axial ratio and the position angle of each ring. The inclinations of these rings are calculated from their axial ratios using

$$\cos i \equiv \sqrt{\frac{q^2 - q_0^2}{1 - q_0^2}} \ , \tag{2.5}$$

where q is the axial ratio of the best-fitting ellipses and q_0 is the intrinsic axial ratio of an edge-on galaxy. Since we assume the CO is distributed in a thin disc, the intrinsic axial ratio is $q_0 = 0$, and Equation 2.5 reduces to $\cos i = q$. The rings have a mean inclination of 21° and standard deviation of 6°, as previously discussed in Section 2.4.5.

Allowing for a position angle warp leaves no spiral structure after subtracting the first-order harmonics from the observed velocity field. The k_5 term ($k_n \equiv \sqrt{c_n^2 + s_n^2}$), the first harmonic that does not determine the parameters of the ellipses, remains small. This suggests that there is no significant radial flow present in the velocity field.

With no significant radial component contributing to the velocity field, we now need to consider what effects the position angle warp may have on the SMBH mass measured. Figure 2.11 shows that the position angle varies radially before settling to the value of $\approx 39°$ found by the MCMC fit. Centrally, the position angle peaks at $\approx 45°$. Such a position angle mismatch would mean that the observed central line-of-sight velocities are under-estimates of the true circular velocities, and so we could under-estimate the SMBH mass. Combining Equations 2.3 and 2.4, we find that the SMBH mass will scale with position angle as:

$$M_{\rm BH} \propto v^2 \propto \left(\frac{v_{\rm obs}}{\cos \phi} \right)^2 . \tag{2.6}$$

The position angle warp could thus, at most, increase our SMBH mass by 0.08 dex. The actual effect will be smaller than this, since the SMBH mass will be constrained not merely by the central annulus but by all spaxels - the central few providing the strongest constraints. We therefore test the effect of this warp on the SMBH mass measurement by running an additional MCMC chain with the position angle fixed to that found from kinemetry. There is no significant change of the best-fitting SMBH mass, nor of its uncertainties.

2.7 Conclusion

SING high angular resolution ALMA observations of CO(2-1) in the galaxy NGC 524, we have identified a compact 1.3 mm continuum source, that we find to be spatially consistent with the previously identified compact radio source in this galaxy. Line emission arises from a central molecular gas disc in regular rotation; this disc has a central hole and exhibits a small distortion to the isovelocity contours over the central 2.″5. We showed this distortion can be interpreted as either a position angle warp or evidence for radial flow using a harmonic expansion of the velocity field.

We forward-modelled the kinematics of the gas in the observed cube to measure the SMBH mass. Although the hole prevents us from observing the expected Keplerian increase in the central velocities, we nevertheless obtain a measurement of the supermassive black hole mass of $4.0^{+3.5}_{-2.0} \times 10^8\,\mathrm{M}_\odot$, where the uncertainties stated are at the 3σ level and include the formal error and the uncertainty in the inclination. The model also yields a stellar mass-to-light ratio of $5.7^{+3.9}_{-1.9}\,\mathrm{M}_\odot/\mathrm{L}_{\odot,\mathrm{I}}$, with uncertainties dominated by the inclination. The formal uncertainties alone in M/L_I are consistent with other results.

The CO disc has a degenerate inclination, so we assumed the gas is coincident with the observed dust, and adopt the inclination previously established from the dust morphology (Cappellari et al., 2006), that is consistent with a tilted-ring fit to the 2D kinematics from our data. This yielded a good fit to the data, but we subsequently included the effects of this inclination uncertainty in our

adopted uncertainties by a Monte Carlo method. The formal uncertainties in our measurement take into account the uncertainty in the χ^2 minimum, and are estimated by bootstrapping and the MCMC process itself, both giving consistent results. The overall uncertainty is dominated by the poorly-constrained inclination.

We also tested whether our result is robust against the gas distribution assumed. The axisymmetric centrally-truncated exponential disc assumed in our original model is only a coarse representation of the underlying morphology, so we introduced a new method to generate a model gas distribution directly from the observations. This model distribution is then kinematically deprojected to model the observed cube. We found no significant change in the best-fitting SMBH mass, but this method will be useful for analysing future observations with complex gas distributions.

Our SMBH mass is consistent with, but half that found using stellar kinematics by Krajnović et al. (2009). It is consistent, and in fact very similar to, that predicted with the $M_{\rm BH}-\sigma_*$ relation of McConnell & Ma (2013).

3

Molecular gas measurement of the supermassive black hole mass in the elliptical galaxy NGC 7052

Contents

The material in this chapter has been published in the Monthly Notices of the Royal Astronomical Society, Volume 503, p.5984-5996.

3.1 Introduction

SUPERMASSIVE black holes (SMBHs) are characterised by just a few properties: their masses, spins and charges. A SMBH mass can be measured by either spatially- or temporally-resolving a dynamical tracer of the central potential. The last three decades of studies have demonstrated that

SMBH masses correlate tightly with a wide variety of properties of their host galaxies, including the stellar velocity dispersion (e.g. Gebhardt et al., 2000; Ferrarese & Merritt, 2000), bulge mass and/or luminosity (e.g. Kormendy & Richstone, 1995; Magorrian et al., 1998), total luminosity (e.g. Kormendy & Gebhardt, 2001) and Sérsic index (e.g. Graham et al., 2001). These correlations are sufficiently tight to imply (potentially self-regulating) co-evolutionary processes. However, the relative importance of these processes remains unknown.

Molecular gas emission has proved to be a suitable tracer of SMBH potentials (e.g. Davis et al., 2013b) for galaxies across the Hubble sequence, including those hosting an active galactic nucleus (AGN). Our millimetre-Wave Interferometric Survey of Dark Object Masses (WISDOM) exploits the high angular resolution available from modern interferometers to spatially-resolve CO emission on SMBH-dominated scales. In previous papers in this sequence, we have presented new SMBH measurements (Davis et al., 2017a, 2018a; Onishi et al., 2017; Smith et al., 2019; North et al., 2019), explored a correlation between CO line width and SMBH mass (Smith et al., 2021a), and studied the properties of the cold molecular interstellar medium at very high resolution in local galaxies (Liu et al., 2021).

In this chapter, we use new high-resolution observations of the galaxy NGC 7052 to measure its central SMBH mass. In Section 3.2, we describe the properties of our target galaxy. Section 3.3 describes the Atacama Large Millimeter/submillimeter Array (ALMA) observations, their calibration and imaging. The dynamical model we fit to our observations is described in Section 3.4, and we discuss our results in Section 3.5. We conclude briefly in Section 3.6. Throughout this chapter, velocities are given in the radio convention.

3.2 NGC 7052

NGC 7052 is an isolated elliptical radio galaxy (Figure 3.1, left panel) in the Vulpecula constellation, located at $21^{\mathrm{h}}18^{\mathrm{m}}33^{\mathrm{s}}, +26°26'49''$. Its total stellar mass is $5.6 \times 10^{11}\,\mathrm{M}_{\odot}$ (Pandya et al., 2017), among the most massive galaxies in the local universe, and as such is included in the MASSIVE

sample of such galaxies (Ma et al., 2014). The near-infrared effective (i.e. half-light) radius (R_e) is 14.″7 (Ma et al., 2014). The galaxy is kinematically classified as a slow-rotator according to the criterion by Emsellem et al. (2011), based on the projected stellar angular momentum λ_e (spin parameter) averaged within one effective radius ($\lambda_e = 0.15$; Veale et al. 2017). Throughout this chapter, we adopt the distance used in the MASSIVE survey, from Hubble flow, $D = 69.3$ Mpc. At this distance, 1″ corresponds to 336 pc.

Radio jets have been mapped in NGC 7052 on arc-minute scales at 1.5 and 5 GHz using the Very Large Array (VLA; Parma et al. 1986) and Westerbork Synthesis Radio Telescope (WSRT; Fanti et al. 1977), respectively. The radially-declining profile of this emission indicates the galaxy is an Fanaroff-Riley Class I source (FR-I; Capetti et al., 2000, 2002).

X-ray emission from the galaxy has been detected and extensively studied (e.g. Donato et al., 2004; Mulchaey & Jeltema, 2010; Goulding et al., 2016). Memola et al. (2009) used *Chandra* observations to separate the contribution of the AGN from that of the spatially-unresolved X-ray binaries, determining an AGN X-ray luminosity of $L_{\mathrm{AGN,X}} \approx 10^{33}$ W.

Optical images from the *Hubble Space Telescope* (*HST*) reveal that the centre of NGC 7052 harbours a prominent nuclear dust disc with a dust mass of $\approx 10^4\,\mathrm{M}_\odot$ (Nieto et al., 1990), shown here in extinction in Figure 3.1 (right panel). This dust disc has a semi-major (-minor) axis of 1.″94 (0.″67) (van der Marel & van den Bosch, 1998). Assuming the dust disc has no intrinsic thickness yields an inclination estimate of $70 \pm 2°$. Although the dust disc is very prominent to the north-west of the nucleus, it does not appear to significantly obscure the nucleus itself (Capetti et al., 2000). It is not orthogonal to the radio emission (Capetti & Celotti, 1999).

Despite being an early-type galaxy, NGC 7052 hosts a significant molecular gas reservoir with a total mass of $2.3 \times 10^9\,\mathrm{M}_\odot$ (Wang et al., 1992, converted to $\alpha_{\mathrm{CO}} = 4.3\,\mathrm{M}_\odot\,(\mathrm{K\,km\,s^{-1}})^{-1}\,\mathrm{pc}^{-2}$). Warm gas makes up only a very small proportion of the galaxy's mass budget, totalling only $4 \times 10^3\,\mathrm{M}_\odot$ (estimated from the Hβ luminosity) over the central 1.7 kpc radius (Pandya et al., 2017).

HST Faint Object Spectrograph (FOS) observations of the Hα and [N II] emission lines along the major axis have been modelled to measure the SMBH mass. Although the ionised gas kinematics in the centre of the galaxy are dominated by turbulent motions (exceeding 400 km s^{-1}), van der Marel & van den Bosch (1998) determined a SMBH mass of $3.9^{+2.7}_{-1.5} \times 10^8$ M$_\odot$ (corrected to our adopted distance), robustly excluding models without a central SMBH. Although the most precise SMBH mass measurements so far have been achieved by tracing maser emission very close to the SMBHs with very long baseline interferometry (VLBI; e.g. Miyoshi et al. 1995; Kuo et al. 2011; Gao et al. 2017), no 22 GHz maser emission was detected in NGC 7052 with the Effelsberg 100-m telescope (Braatz et al., 1996).

The sphere of influence of the SMBH, the approximate physical scale at which the SMBH dominates the gravitational potential, is given by $R_{\rm SoI} \equiv GM_{\rm BH}/\sigma_*^2$, where G is the gravitational constant, $M_{\rm BH}$ the SMBH mass and σ_* the central stellar velocity dispersion. Using the distance-corrected SMBH mass from van der Marel & van den Bosch (1998) and the stellar velocity dispersion of NGC 7052 $\sigma_* = 284$ km s^{-1} (Ma et al., 2014), we estimate $R_{\rm SoI} = 21$ pc (0.″06).

3.3 ALMA observations

NGC 7052 was observed with the ALMA 12-m array as part of the WISDOM project 2018.1.00397.S. An extended ALMA configuration was used to provide baselines of 40 m–5.9 km, in two tracks on 8th and 9th August 2018, each on-source for 21 minutes. The former track failed the on-line ALMA quality assessment check (known as QA0) due to large residuals in the phase calibration, and therefore the second track was taken. Manual calibration was performed on the first track by the United Kingdom ALMA Regional Centre, recovering much of the data for further use. The second track was automatically calibrated by the ALMA pipeline, and one antenna (DA45) was subsequently manually flagged due to an amplitude error.

To better sample the *uv* plane and thus recover any large-scale structure, additional observations were taken with a compact ALMA configuration and with

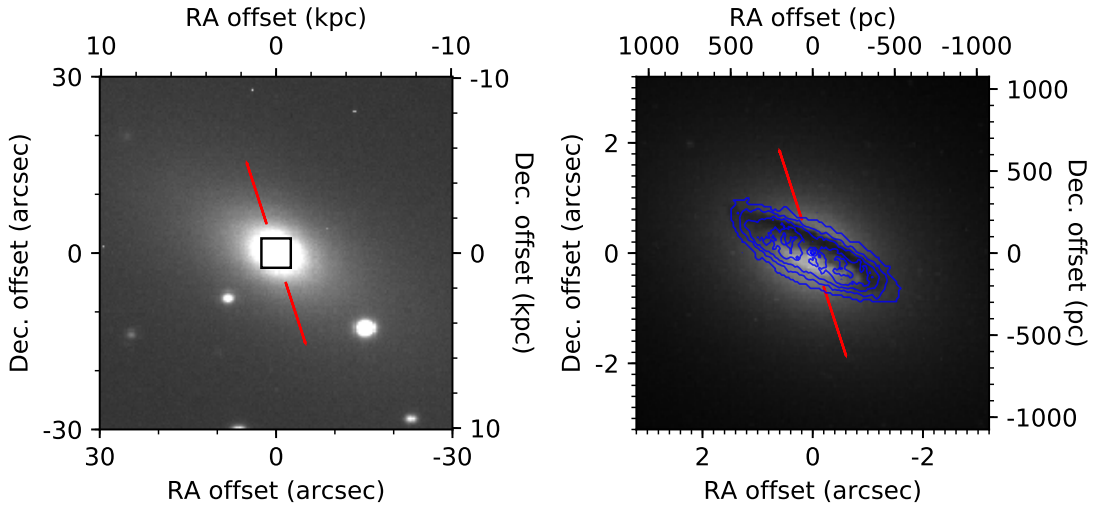

Figure 3.1: Left panel: Jakobus Kapteyn Telescope V-band image of NGC 7052 (greyscale), showing the large-scale morphology of NGC 7052. The black central box is the area shown in the right panel. **Right panel:** Unsharp-masked *HST* WFPC2/PC F814W image of NGC 7052 (greyscale; van der Marel & van den Bosch 1998), showing the central dust disc. Overlaid are the H_2 surface density contours (blue) inferred from our ALMA observations, assuming a CO-to-H_2 conversion factor $\alpha_{CO} = 4.3\,M_\odot\,(K\,km\,s^{-1})^{-1}\,pc^{-2}$. The contours are from the level at which the noise was clipped, $15\,M_\odot\,pc^{-2}$, and then at 4000, 8000, 12 000, and $16\,000\,M_\odot\,pc^{-2}$. Spatial offsets are relative to the 1.3 mm continuum source position listed in Table 3.2. The red lines in each panel indicate the 6 cm radio emission axis (Condon et al., 1991).

the 7-m Atacama Compact Array (ACA). The additional 12-m track on 31st October 2018 covered baselines 15 m–1.4 km and was on-source for 5 minutes. The ACA track was taken in programme 2016.2.00046.S, was observed on 21st August 2019, covered baselines 9 – 45 m, and was on-source for 32 minutes. Both of these tracks were automatically calibrated by the ALMA pipeline.

The properties of these four observing tracks are listed in Table 3.1. Combining all four tracks together yields continuous baseline coverage from 9 m to 5.9 km, corresponding to sensitivity to angular scales from 0.″06 to 36″. The dust disc visible in optical images of NGC 7052 has a major- (minor-)axis diameter of ≈4″ (≈1″). Assuming the CO is co-spatial with the dust disc, we therefore expect to recover all the emitted flux.

Two spectral setups were used. For all 12-m array observations, a 1.875 GHz bandwidth spectral window with a channel width of ≈1 MHz was placed over the

^{12}CO(2-1) emission line. At this frequency, this corresponds to a $\approx$2400 km s^{-1} velocity range and $\approx$1 km s^{-1} channels. The ACA observations used a slightly different receiver configuration, with one 2 GHz ($\approx$2600 km s^{-1}) bandwidth spectral window and 500 kHz ($\approx$0.7 km s^{-1}) channels. In both cases, the remaining three 2 GHz bandwidth spectral windows were placed to detect continuum emission.

3.3.1 Continuum images

The calibrated observations were concatenated using the `Common Astronomy Software Applications (CASA)` package (McMullin et al., 2007), and an image of the 1.3 mm continuum was made using the `CASA` task `tclean` in multi-frequency synthesis mode. The continuum spectral windows and line-free channels of the line spectral window were used. The image was made using Briggs weighting with a robust parameter of 0, balancing angular resolution and sensitivity. An approximately point-like continuum source was detected and fit with a two-dimensional (2D) Gaussian using the `CASA` task `imfit`. The properties of this continuum image and of the detected continuum source are listed in Table 3.2.

3.3.2 Line images

A linear fit to the continuum spectral windows and line-free channels of the line spectral window was subtracted from the *uv*-plane data using the `CASA` task `uvcontsub`. The continuum-subtracted data were then concatenated, imaged and cleaned using the 'cube' mode of the `tclean` task and adopting Briggs weighting with robust=0. The properties of the resulting image cube are listed in Table 3.3.

Table 3.1: Properties of the four observing tracks.

Track	Date	Array	Baseline range	On-source time	Calibration
`uid_A002_Xc39302_X5d57`	21st August 2017	7-m	9 m–45 m	32 min	Pipeline
`uid_A002_Xd44a99_X974`	31st October 2018	12-m	15 m–1.4 km	5 min	Pipeline
`uid_A002_Xdfcc3f_X1c7a`	8th August 2019	12-m	40 m–5.9 km	21 min	Manual
`uid_A002_Xdfdbea_X598`	9th August 2019	12-m	40 m–5.9 km	21 min	Pipeline; antenna DA45 flagged

Table 3.2: Parameters of the continuum image and the detected 1.3 mm continuum source.

Image property	Value
Image size (pix)	512×512
Image size (arcsec)	10.24×10.24
Image size (pc)	3440×3440
Pixel scale (arcsec pix^{-1})	0.02
Pixel scale (pc pix^{-1})	6.72
1σ sensitivity (μJy beam^{-1})	80
Synthesised beam (arcsec)	0.12×0.09
Synthesised beam (pc)	38×27
Source property	**Value**
Right ascension	$21^{\mathrm{h}}18^{\mathrm{m}}33\overset{\mathrm{s}}{.}0433 \pm 0\overset{\mathrm{s}}{.}0001$
Declination	$+26°26'49\overset{''}{.}242 \pm 0\overset{''}{.}003$
Integrated flux (mJy)	22.3 ± 1.5
Deconvolved size (arcsec)	$(0.07 \pm 0.02) \times (0.05 \pm 0.03)$
Deconvolved size (pc)	$(22 \pm 6) \times (16 \pm 9)$

Table 3.3: Parameters of the CO line cube.

Image property	Value
Image size (pix)	512×512
Image size (arcsec)	10.24×10.24
Image size (pc)	3440×3440
Pixel scale (arcsec pix^{-1})	0.02
Pixel scale (pc pix^{-1})	6.72
Velocity range (km s^{-1})	$4035 - 5235$
Channel width (km s^{-1})	15
1σ sensitivity (mJy beam^{-1})	0.5
1σ sensitivity (M$_\odot$ pc^{-2})	15
Synthesised beam (arcsec)	0.13×0.10
Synthesised beam (pc)	41×30

The molecular gas distribution, mean line-of-sight velocity field, velocity dispersion field, and kinematic major-axis position-velocity diagram (PVD) are shown in Figure 3.2. These were made with the masked-moments method (Dame, 2011), whereby the cube is convolved spatially by the beam and Hanning-smoothed spectrally, pixels that exceed a noise threshold are included in a mask, and this mask is then applied to the original cube. This method selects only areas of structured emission in the original cube and excludes regions with no significant emission, thus producing improved moment maps.

The CO gas in NGC 7052 is distributed in a regularly rotating disc, coincident with the dust disc (Figure 3.1, right panel). The total molecular gas mass is $1.8 \times 10^9\,\mathrm{M}_\odot$, assuming $\alpha_{\mathrm{CO}} = 4.3\,\mathrm{M}_\odot\,(\mathrm{K\,km\,s^{-1}})^{-1}\,\mathrm{pc}^{-2}$. This is very similar to the single-dish measurement of Wang et al. (1992), further evidence that we have not resolved out significant flux. The CO surface density peaks along the major axis at $\approx 0\farcs5$ on either side of the centre, rapidly decreasing toward the nucleus and more slowly outward. In the very centre of the galaxy is a small hole, where the gas surface density is below our sensitivity limit of $15\,\mathrm{M}_\odot\,\mathrm{pc}^{-2}$.

In principle, such a hole could be an artefact caused by projecting the cube onto an image. Indeed, the mask could exclude gas close to the SMBH where the line-of-sight velocity distribution becomes very broad, causing emission to be spread over many channels (and therefore fall below our sensitivity limit in

any given channel). However, we have checked that a manually-defined mask including all channels within the hole does not recover any more emission. Another possibility is that a few channels showing absorption against the continuum source contribute negative flux in this region (once continuum subtracted), reducing the sum. There is however no evidence of such absorption features in the spectra within the hole. To further exclude the possibility that erroneous continuum-subtraction has created the hole, we made a second data cube from the observations without first subtracting the continuum. The hole was still visible in this cube, the continuum source not being sufficiently extended to fill the void. Having excluded these two explanations, we conclude that the hole is genuine and astrophysical in origin. We discuss it further in Section 3.5.5.

Such holes appear to be common in the galaxies studied in the WISDOM survey. Typically, they have spatial extents similar to those of the SMBH spheres-of-influence, occasionally preventing the detection of the central Keplerian rotation (e.g. Davis et al., 2018a; Smith et al., 2019). In such cases we have nevertheless been able to measure the SMBH masses, as the SMBH's presence still enhances the gas velocities above those expected from the stars alone.

The kinematic major-axis PVD (Figure 3.2, bottom-right panel) shows a rotation curve that rises towards the centre at radii $r < 0\farcs5$, as would be expected from Keplerian rotation around a compact mass. The signature is most prominent on the north-east side of the galaxy (positive velocities), albeit only in the faintest contour, while it is only marginally visible on the south-west side (negative velocities), due to the slight asymmetry of the CO disc. Additional evidence for the enhanced velocities due to the presence of a central mass concentration is given by the shape of the PVD envelope. The gas remains at high velocities to very small radii ($\approx$250 km s^{-1} at $0\farcs2$ or 70 pc), before falling very steeply. In the absence of a central mass concentration, a shallower central decline would be expected.

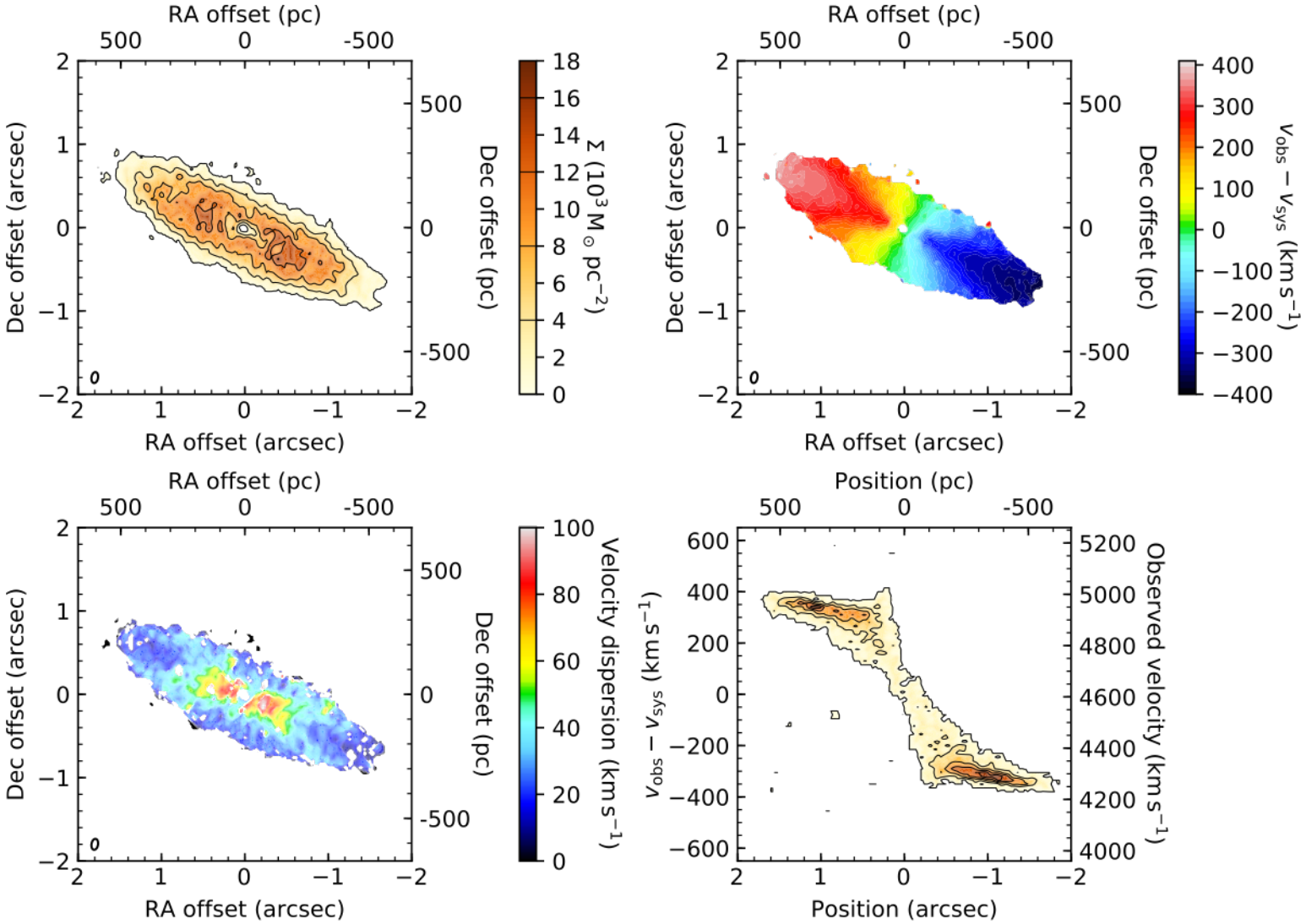

Figure 3.2: Moment maps of the ^{12}CO(2-1) emission in NGC 7052 centred on the compact continuum source. **Top-left:** Molecular gas surface density (orange scale and black contours), assuming a CO(2-1)/CO(1-0) line ratio of unity and a CO(1-0)-to-H_2 conversion factor $\alpha_{CO} = 4.3\,M_\odot\,(K\,km\,s^{-1})^{-1}\,pc^{-2}$. Black contours are from the level at which the noise was clipped, $15\,M_\odot\,pc^{-2}$, and then at 4000, 8000, 12 000 and 16 000 $M_\odot\,pc^{-2}$. **Top-right:** Mean line-of-sight velocity. **Bottom-left:** Observed line-of-sight velocity dispersion. **Bottom-right:** Kinematic major-axis position-velocity diagram (PVD; orange scale and black contours). In both right panels, v_{obs} is the observed line-of-sight velocity and $v_{sys} = 4610\,km\,s^{-1}$ is the galaxy systemic velocity in the radio convention. The maps show the synthesised beam in their bottom-left corners.

The velocity dispersion map (Figure 3.2, bottom-left panel) indicates that the gas at the edge of the disc is dynamically cold ($\sigma_{\rm gas}$<30 km s^{-1}). As the gas density increases, the dispersion also increases, but in the centre of the disc it is likely that the line-of-sight velocity dispersion is dominated by (beam) smearing of closely-spaced isovelocity contours. This suggests that the molecular gas remains dynamically cold throughout the disc, in contrast to the strong gradients observed in ionised gas (van den Bosch & van der Marel, 1995). We will further test this conclusion using our dynamical modelling in Section 3.4.

3.4 Dynamical modelling

DYNAMICAL modelling of NGC 7052 was carried out using the same methods as discussed in the preceding chapter, so we provide only a rough outline of our procedures here, before discussing in greater detail features of the model unique to this case.

Simulated data cubes were constructed from dynamical models of the molecular gas disc in NGC 7052 using the `IDL` version of the `Kinematic Molecular Simulation (KinMS)` tool[1] (Davis et al., 2013a). These were fit to the observed data cube using a Markov-chain Monte-Carlo (MCMC) method with a custom Gibbs sampler (`KinMS_mcmc`[2]). `KinMS` generates a set of particles at positions replicating a specified surface brightness profile, it assigns to each particle the circular velocity expected at its radius from a specified profile (although every particle is also assigned an additional random velocity, depending on the velocity dispersion selected by the user, that is not taken into account dynamically), it projects these velocities along the line of sight, and places the particle into a data cube. This cube is then convolved spatially by the synthesised beam to replicate instrumental effects.

The circular velocity at every radius is calculated (using the IDL procedure `MGE_CIRCULAR_VELOCITY`[3]) from the SMBH mass and a model of the stellar mass distribution. This stellar contribution is derived from a multi-Gaussian expansion

[1] https://github.com/TimothyADavis/KinMS
[2] https://github.com/TimothyADavis/KinMS_mcmc
[3] http://purl.org/cappellari/software

(MGE; Emsellem et al. 1994; Cappellari 2002) of a *HST* Wide Field Planetary Camera 2 (WFPC2) Planetary Camera (PC) F814W image (originally presented in van der Marel & van den Bosch 1998) assuming a radially-constant mass-to-light ratio. This model is explained in further detail in Section 3.4.1, listed in Table 3.4, and shown in Figure 3.3.

In addition to these three dynamical parameters (SMBH mass, stellar mass-to-light ratio and gas velocity dispersion), and two specifying the disc orientation relative to the observer (inclination and position angle), we also allow the model to vary four 'nuisance' parameters. The kinematic centre of the galaxy can have small spatial and velocity offsets with respect to the location of the aforementioned continuum source and the galaxy systemic velocity, and we let the surface brightness function have an arbitrary overall scaling.

3.4.1 Stellar potential

To minimise the impact of extinction from the dust disc on our MGE model of the F814W image, we mask the north-western side of the dust disc, that appears to be in the foreground. We nevertheless include the central 9×9 pixels to robustly constrain the stellar light in the galactic centre.

The MGE model consists of the deconvolved central intensity (I'), width (σ) and apparent flattening (q') of a sequence of 2D Gaussians that accurately replicate the observed light distribution. We convert these components to physical units ($L_{\odot,I}\,\mathrm{pc}^{-2}$) adopting a zero-point of 21.1 and an I-band Solar luminosity of 5.34 (Willmer, 2018), both in ST magnitudes. These components are listed in Table 3.4 and the fit is shown in Figure 3.3. The dust disc is evident in the distortions to the (otherwise elliptical) isophotes.

The MGE components describing the stellar light distribution can be converted into a mass distribution by multiplying by a mass-to-light ratio, another free parameter of our fits. Assuming an inclination, the stellar light (or mass) distribution can be analytically deprojected into a three-dimensional (3D) distribution, and the circular velocity resulting from this distribution can be calculated.

Table 3.4: Deconvolved 2D MGE components of a model of the *HST* F814W image of NGC 7052.

$\log_{10}\left(\frac{I'_j}{\mathrm{L}_{\odot,I}\,\mathrm{pc}^{-2}}\right)$	$\log_{10}\left(\frac{\sigma_j}{\mathrm{arcsec}}\right)$	q'_j
(1)	(2)	(3)
4.49	−1.76	0.73
3.93	−0.23	0.77
3.67	0.14	0.69
3.56	0.60	0.71

Notes: The table lists the central surface brightness (column 1), width (column 2) and axial ratio (column 3) of each de-convolved Gaussian component.

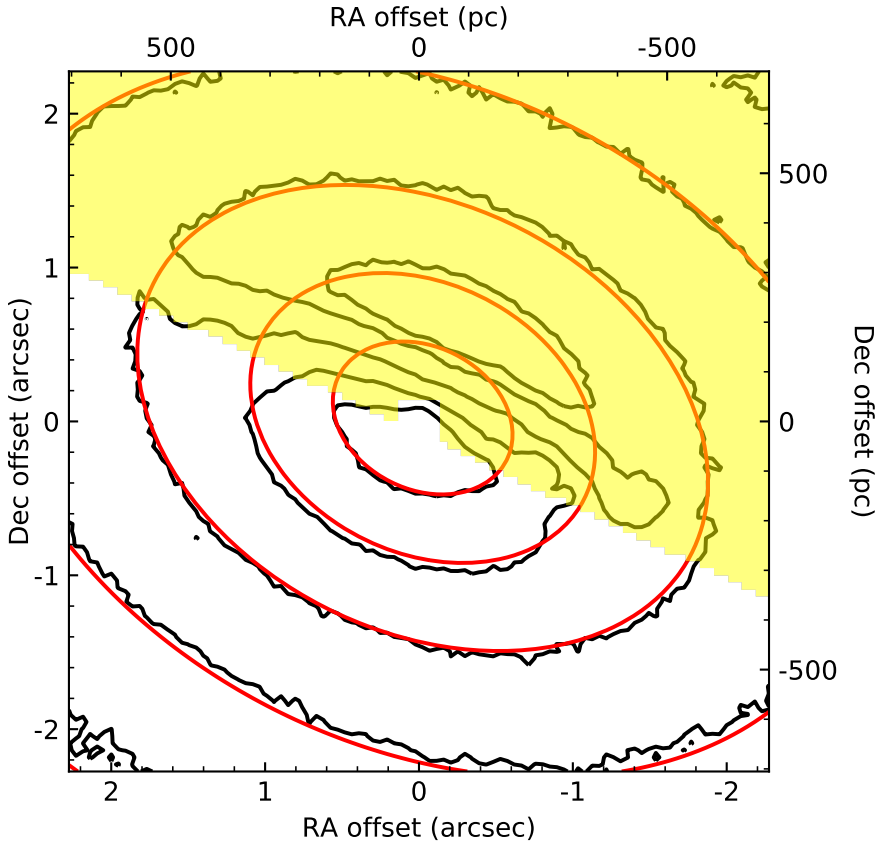

Figure 3.3: *HST* WFPC2/PC F814W image of NGC 7052 (black contours), overlaid with our MGE model (red contours). The north-western side of the image is masked (yellow) to exclude the foreground dust disc, but we retain the central 9×9 pixels.

We will ultimately find that the stellar mass contribution to the potential within the central few resolution elements is negligible, and thus does not affect the best-fitting SMBH mass. This is corroborated by the spatially-resolved central Keplerian rotation curve, indicating that the central potential is dominated by a compact mass. In consequence, any extinction of the dust disc in the background of the south-eastern side of the galaxy does not significantly bias the inferred SMBH mass.

3.4.2 Molecular gas geometry

In previous works in this series, we have commonly parametrized the molecular gas distribution using an axisymmetric exponential disc. The extremely high angular resolutions achieved with ALMA have however revealed that many objects host a central hole, that we have typically included using an additional central truncation. However, many galaxies have a molecular gas distribution which cannot be described by such a simple function. Smith et al. (2019) presented a new approach, using the `SkySampler` tool[4] to infer the de-convolved projected gas distribution (once re-convolved by the synthesised beam this distribution is equivalent to the top-left panel of Figure 3.2), deproject this distribution into the disc plane under the thin disc assumption, and then calculate the associated line-of-sight velocities for the distribution as before. By construction, the model matches the observed gas distribution. The gas distribution therefore offers no constraint on the model parameters, but `SkySampler` allows us to remove a few degrees of freedom from the model.

We adopt this approach for NGC 7052. The molecular gas disc appears to peak along the major axis at a radius of $\approx 0\farcs5$, before declining toward the centre of the galaxy (and outward). Attempting a fit using an exponential disc and central truncation failed to adequately reproduce the observed gas distribution. For our final fit, we instead built a `SkySampler` model of the gas distribution from the projected `CLEAN` components, thus avoiding over-smoothing our model.

3.4.3 Bayesian inference and priors

The MCMC fit to our data explores the posterior probability distribution of our model, given by Bayes' theorem. Assuming uniform (maximum-ignorance) priors, and that our data has a Gaussian noise distribution constant for all pixels, the posterior is then proportional to the log-likelihood ($\ln P \propto -0.5\,\chi^2$), where the

[4] https://github.com/Mark-D-Smith/KinMS-skySampler

chi-squared goodness-of-fit statistic is given by

$$\chi^2 \equiv \sum_i \left(\frac{\mathrm{data}_i - \mathrm{model}_i}{\sigma_i} \right)^2 = \frac{1}{\sigma^2} \sum_i (\mathrm{data}_i - \mathrm{model}_i)^2 \ , \tag{3.1}$$

where the sum is performed over all the pixels within the region of the data cube that the model fits, and σ is the rms noise measured in line-free channels of the data cube.

Due to the very large number of constraints when fitting the entire 3D data cube, the ordinary assumption that the 1σ (67%) confidence interval corresponds to $\Delta\chi^2 \equiv \chi^2 - \chi^2_{\mathrm{min}} = 1$ (where χ^2_{min} is the absolute χ^2 minimum across all parameters explored) yields unrealistically small formal uncertainties. We therefore rescale the standard $\Delta\chi^2$ by a factor $\sqrt{2(N-P)} \approx \sqrt{2N}$, where N is the number of constraints and $P = 9$ is the number of parameters in the model. This effectively rescales the uncertainties associated with our model parameters. This approach has been used in previous works of this series (e.g. Smith et al., 2019; North et al., 2019) and other works encountering the same problem (e.g. van den Bosch & van de Ven, 2009; Mitzkus et al., 2017). Smith et al. (2019) showed that this correction yields formal uncertainties that are consistent with those found by a bootstrap approach, and are thus more credible.

However, since adjacent pixels in our observations are not independent (i.e. the observations are spatially convolved by the synthesised beam), failing to correct for pixel-to-pixel covariances would lead to underestimating the uncertainties. In previous works, we have corrected Equation 3.1 accordingly. The disadvantage of using this correction is that we need to introduce the inverse covariance matrix (with N^2 elements) to the calculated deviations, and in consequence can only fit a relatively small region of the cube. However, this correction is negligible compared to the $\sqrt{2N}$ rescaling described above, and so we neglect it in this work. This enables us to fit the entire molecular gas disc, rather than only some smaller central region as was previously necessary.

Finally, we impose physical bounds on each parameter to ensure the chain converges in a finite time, and that it does not explore unphysical regions of parameter space. Assuming maximal ignorance, we adopt uniform priors for all

parameters except $M_{\rm BH}$ (see Table 3.5). As the SMBH mass can potentially span many orders of magnitude, we adopt instead a prior that is uniform in log-space for this single parameter, thus avoiding unduly favouring large values.

3.4.4 Best-fitting model

We ran our MCMC chain for 100 000 steps, discarding the first 10 000 steps as a burn-in. Our best-fitting model cube replicates the observed gas disc well. Figure 3.4 shows the 2D marginalisation of each pair of input parameters, and the 1D marginalisation (histogram) of each parameter. As can be seen, all the 1D posteriors are approximately Gaussian, indicating the MCMC chain is well-converged. The coloured points in the 2D marginalisations indicate the log-likelihood of each model. The colour scale indicates points within $\Delta\chi^2 < \sqrt{2N}$ with white points the most likely (the best fitting model is also shown by a solid black line in each histogram) and blue points the least likely. Grey points are realisations with $\Delta\chi^2 > \sqrt{2N}$ relative to the best-fitting model, and are even less likely. Slight asymmetries in the posterior, resulting from the highly non-linear model, imply that the median value of each parameter is slightly different from the best-fitting model. However, these are consistent within the formal uncertainties for all parameters. The elliptical coloured contours also indicate that the posterior is well-sampled and well-converged.

The only significant physical covariance is the well-known one between the SMBH mass and the stellar mass-to-light ratio, equivalent to the conservation of total dynamical mass. The three offset parameters (right ascension, declination and velocity) are also correlated, as the gas disc is systematically distributed along a single plane in the cube. A small perturbation to one parameter will thus also change the other two to remain in this plane.

The best-fitting and median value and formal uncertainties of each model parameter are listed in Table 3.5. The best-fitting SMBH mass is $2.5 \pm 0.3 \times 10^9\,\mathrm{M}_\odot$ and $M/L_{\rm I} = 4.6 \pm 0.2\,\mathrm{M}_\odot\,\mathrm{L}_{\odot,I}^{-1}$, where both uncertainties are the 3σ (97%) confidence level.

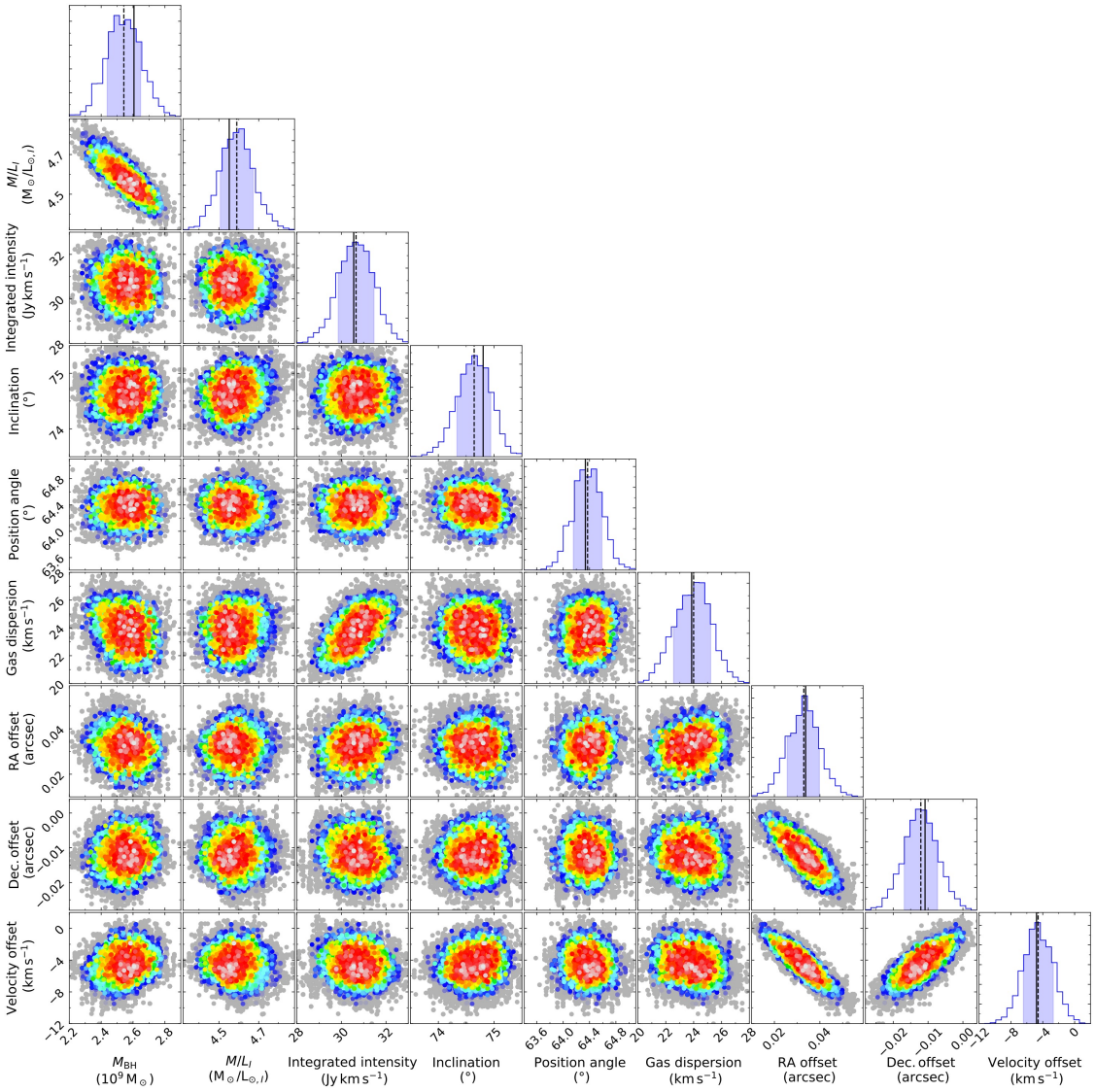

Figure 3.4: Corner plots showing the covariances between all model parameters, from our MCMC fit. Each point is a realisation of our model, colour-coded to show the relative log-likelihood of that realisation. Coloured points are within $\Delta\chi^2 < \sqrt{2N}$ with white points the most likely and blue points the least likely. Grey points are realisations with $\Delta\chi^2 > \sqrt{2N}$ relative to the best-fitting model, and are even less likely. The only significant physical covariance is between the SMBH mass and the mass-to-light ratio, that corresponds to attributing the same dynamical mass differently across the SMBH and stellar distribution. The covariances between the RA, Dec and velocity offsets correspond to moving the kinematic centre of the galaxy in three dimensions within a plane, and these offsets are much smaller than the resolution of our data. Each histogram shows the 1D marginalisation of a model parameter, the black lines denoting the median (dashed) and best-fitting (solid) values. The shaded region indicates the 68% confidence interval. We note that the slight asymmetries of the posteriors imply that the most likely (best-fitting) and median value are very slightly different.

Table 3.5: Best-fitting model parameters, with associated formal uncertainties.

Parameter (1)	Priors (2)	Best fit (3)	Median (4)	1σ error (5)	3σ error (6)
Mass model:					
SMBH mass ($10^9\,\mathrm{M}_\odot$)	$10^5 \rightarrow 10^{12}$	2.61	2.54	0.11	0.31
Stellar M/L_I ($\mathrm{M}_\odot/\mathrm{L}_{\odot,\mathrm{I}}$)	$1 \rightarrow 10$	4.55	4.59	0.08	0.24
Molecular gas disc:					
$2\farcs5 \times 2\farcs5$ integrated intensity ($\mathrm{Jy\,km\,s^{-1}}$)	$1 \rightarrow 200$	30.6	30.7	0.8	2.3
Gas velocity dispersion ($\mathrm{km\,s^{-1}}$)	$1 \rightarrow 100$	23.9	24.0	1.3	3.6
Viewing geometry:					
Inclination ($^\circ$)	$60 \rightarrow 89$	74.8	74.6	0.3	0.9
Position angle ($^\circ$)	$0 \rightarrow 359$	64.3	64.4	0.2	0.6
Nuisance Parameters:					
Centre RA offset ($''$)	$-0.1 \rightarrow 0.1$	0.034	0.033	0.007	0.021
Centre Dec. offset ($''$)	$-0.1 \rightarrow 0.1$	-0.011	-0.012	0.005	0.014
Centre velocity offset ($\mathrm{km\,s^{-1}}$)	$-75 \rightarrow 75$	-4.8	-4.6	1.9	5.4

Notes: Column 1 lists the input parameters of our dynamical model of NGC 7052. Column 2 lists the range of values allowed for each parameter, between which we adopt a uniform prior, except for the SMBH mass for which the prior is uniform in log-space. Column 3 lists the best-fitting value of each parameter, while column 4 lists its median value after marginalising over all other parameters. Columns 5 and 6 list the 1σ (67%) and 3σ (99.7%) confidence intervals of each parameter.

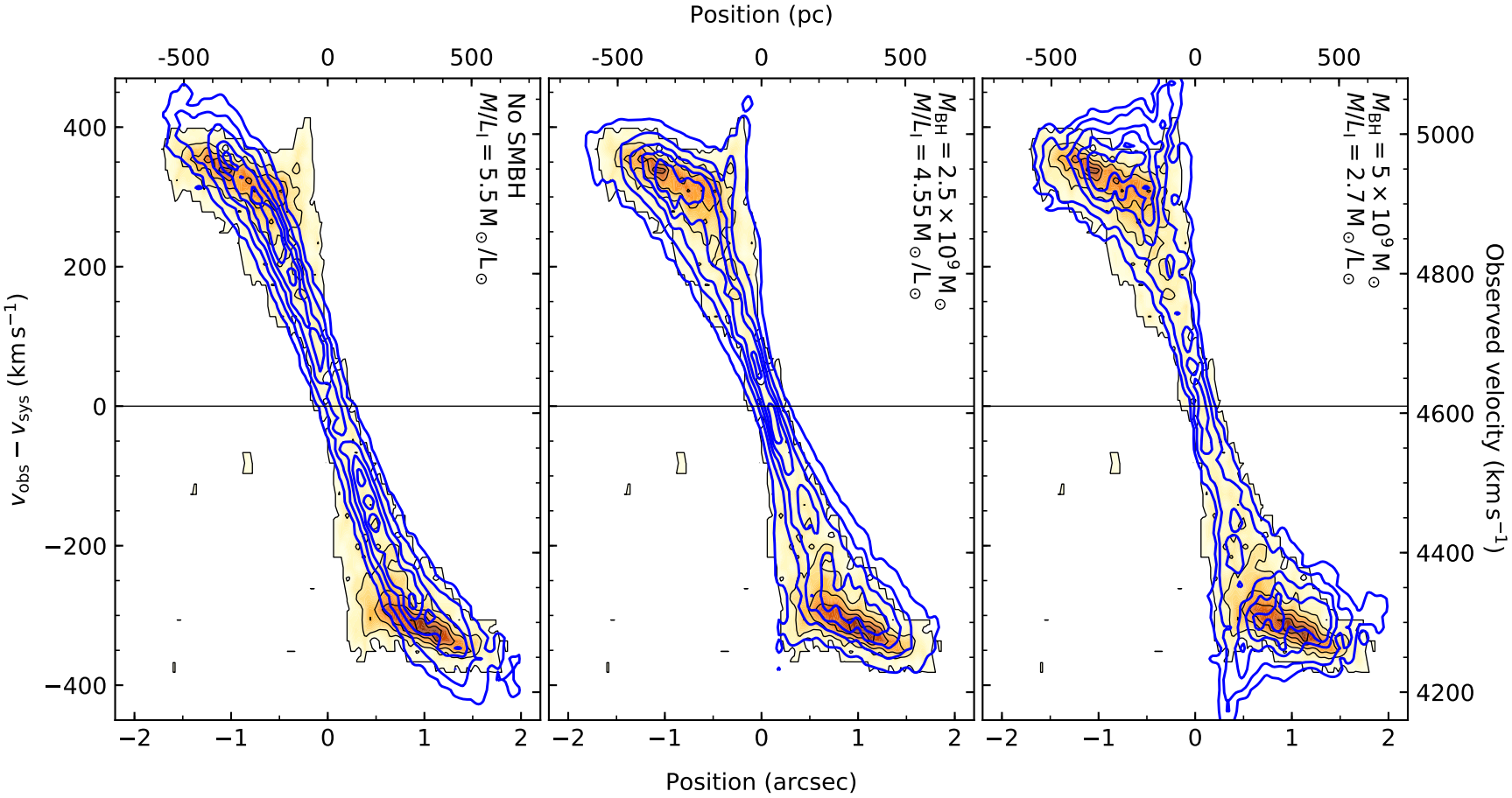

Figure 3.5: Model position-velocity diagrams along the kinematic major axis of NGC 7052 (blue contours), showing a model without a SMBH (left), with the best-fitting SMBH (centre) and with an overly large SMBH (right). These are overlaid on the observed PVD (orange scales and black contours). The line-of-sight velocities at small radii are enhanced compared to those of a stellar mass-only model, thus requiring additional central mass to fully account for them.

3.5 Discussion

3.5.1 Best-fitting mass model

THE quality of our best-fitting model is easy to assess from a kinematic major-axis PVD, as shown in Figure 3.5, although it should be noted that our fit was performed to the entire data cube, not only to this PVD. The left panel shows a fit to the observed data cube assuming no SMBH. To attempt to account for the high velocities observed at small radii, the fit adopts a larger $M/L_{\rm I}$, however this is clearly not a good match to the observations. The right panel shows another fit assuming a SMBH mass larger than that found in our best model. The fit attempts to compensate by reducing $M/L_{\rm I}$, however again this yields a poor fit. The central panel clearly shows that our best model recovers the observed Keplerian rotation within the central region dominated by the SMBH, and the asymmetry of this signature on either side of the disc. Since the only non-axisymmetric feature of our model is the gas distribution, it is clear that the observed asymmetry is the result of the lack of gas to properly sample the Keplerian rise on the south-western (negative velocities) side of the disc, rather than evidence of disturbed motions.

The velocity field residuals, obtained by subtracting the model velocity field from the observed velocity field shown in the top-right panel of Figure 3.2, show no spatial structure that would indicate organised non-circular motions (as were found in e.g. Smith et al. 2019). In addition, the very low velocity dispersions indicate that the gas velocities are dominated by circular motion. Throughout the disc, $v/\sigma \approx 15$ (where v is the deprojected velocity and σ the intrinsic velocity dispersion), indicating that the gas is rotationally-supported.

In principle, the stellar mass-to-light ratio can vary across the galaxy, tracing changes of the stellar population (e.g. Davis & McDermid, 2017; Davis et al., 2018a). No such variation is required to adequately fit our data, but as always a sudden change in the mass-to-light ratio in the centre of the galaxy could obviate the need for a SMBH. There is no photometric evidence to support such a change, and the variation required would be unphysically large - a factor of $\approx$50.

3.5.2 Systematic uncertainties

SMBH mass uncertainties due to the inclination scale as $M_{\rm BH} \propto 1/\sin^2 i$ (e.g. Smith et al., 2019). The molecular gas disc in NGC 7052 is reasonably highly inclined (i≈70°). At low inclinations, the inclination uncertainty can dominate the SMBH mass uncertainty. At the highest inclinations, other effects become important, such as the inability to resolve non-axisymmetric structures, the disc's intrinsic thickness along any line of sight, and potentially the gas optical depth, all of which inhibit the accuracy of a dynamical model. The gas disc of NGC 7052 has very small inclination uncertainties which make only a very small contribution to the total $M_{\rm BH}$ uncertainty budget. Indeed, simulations suggest that i≈70° appears to be an optimal inclination for accurately recovering SMBH masses from molecular gas kinematics (Davis 2014; North 2020).

Inaccuracies in the mass model adopted can, in general, bias the recovered SMBH mass, as an incorrect share of the dynamical mass is assigned to the SMBH. Beside the SMBH, our mass model includes only a contribution from the stellar mass distribution, and it neglects both gas and (dark) halo contributions. However, the relevant length scale on which these contributions matter is that traced by the CO disc, that extends only to a radius of ≈1.″5. Over such a small scale, dark matter likely makes a negligible contribution to the overall mass budget. Contributions from warm gas ($10^{3.6}\,{\rm M}_\odot$; Pandya et al. 2017) and the dust disc ($10^4\,{\rm M}_\odot$; Nieto et al. 1990) are similarly negligible. Naturally, if any of these components were radially distributed identically to the stellar mass, their only effect would in any case be to change the derived dynamical mass-to-light ratio. A radially-varying distribution would lead to a mass-to-light ratio gradient, but it would require a significantly centrally-concentrated mass distribution to substantially affect $M_{\rm BH}$.

Figure 3.6 shows the enclosed mass within spheres of increasing galactic radius from our best-fitting model, with the contributions from the SMBH, stars and molecular gas indicated. Separately indicated are the radii corresponding to the synthesised beam and $R_{\rm SoI}$, the latter using our $M_{\rm BH}$ and $\sigma_* = 284\,{\rm km\,s^{-1}}$(Ma et al., 2014). As is clearly seen, the SMBH dominates the galactic potential

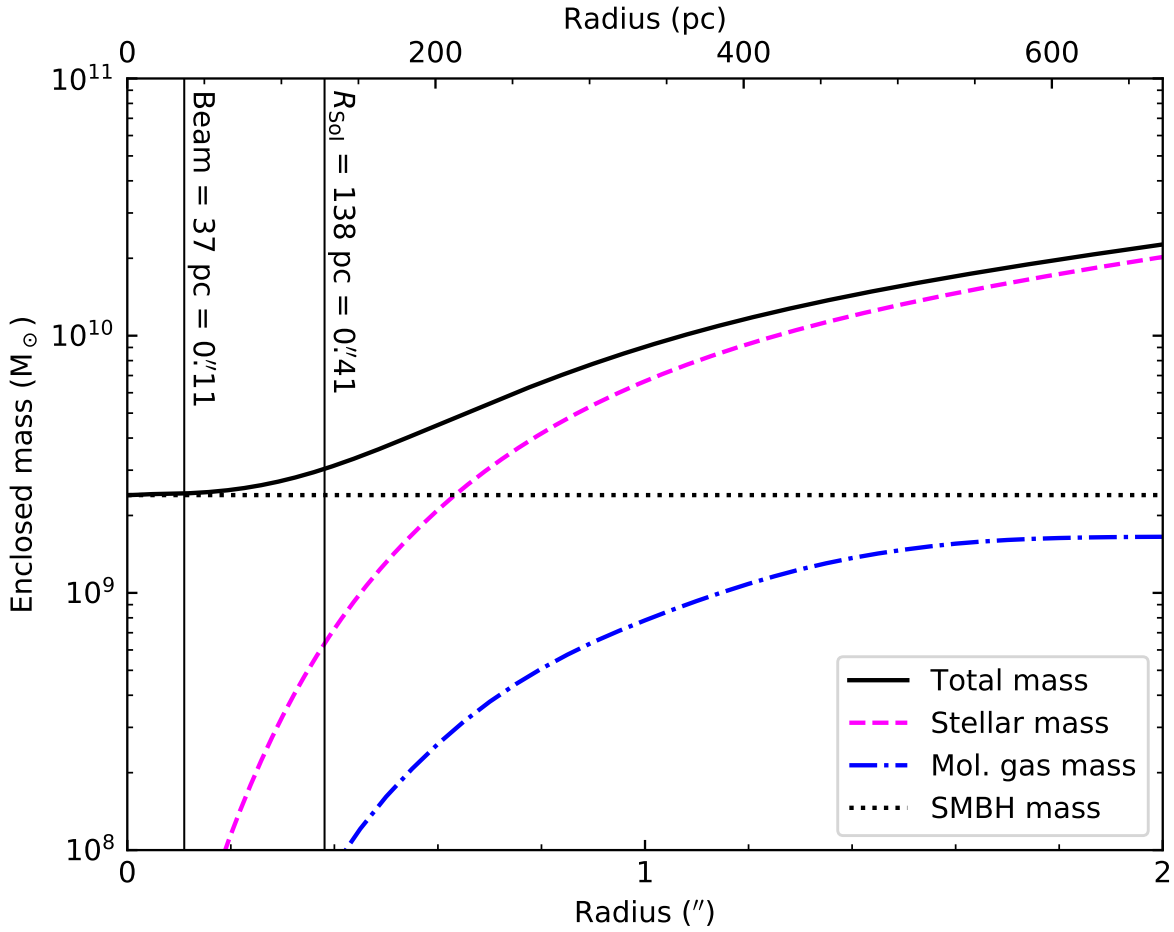

Figure 3.6: Cumulative mass function of NGC 7052, showing the relative contributions from the SMBH (black dotted line), molecular gas (blue dot-dashed line) and stars (violet dashed line). The total enclosed mass is shown by the solid black line. The physical scales of the synthesised beam and SMBH sphere of influence (assuming our measured SMBH mass and a stellar velocity dispersion $\sigma_* = 284\,\mathrm{km\,s^{-1}}$) are indicated by vertical black lines. The molecular gas mass contribution is negligible at all radii.

not only within its nominal sphere of influence, but up to ≈0.″6 (≈200 pc). We thus resolve this region radially with approximately 6 beams. The molecular gas contribution is negligible at all radii.

We note that the radius at which the SMBH and stars have equal contributions ($R_{\rm eq}$) is around 60% larger than the nominal SMBH sphere of influence. This is not necessarily concerning, as typical early type galaxies have $R_{\rm eq}$ slightly larger than $R_{\rm SoI}$ (Yoon, 2017).

Next, we consider the accuracy of our adopted stellar mass model. Although the MGE model appears to match well the *HST* F814W image over the centre of the galaxy (Figure 3.3), this region is strongly affected by dust. Dust attenuation is

expected to decrease the observed flux, and hence cause us to attribute too little mass to the stellar contribution, potentially overestimating $M_{\rm BH}$. We argue that this effect can be safely disregarded here, as it has been carefully mitigated. Firstly, we adopted the *HST* F814W image of the galaxy to build our stellar light model. We masked the north-western side of the dust disc, where it is in the foreground. Adopting this relatively long wavelength, and masking the foreground dust, will reduce the extinction. Secondly, as we have argued previously, an erroneous stellar light profile can be corrected by an appropriate change to the mass-to-light ratio. Thus, inferring the mass-to-light ratio from beyond the dust disc and assuming it is radially constant would significantly bias our results if no correction was made for dust extinction. However, our stellar mass-to-light ratio is determined purely by the CO kinematics, that only extends across the dust disc. Assuming the extinction due to this disc does not vary dramatically, the effect on the stellar light model will be compensated by an associated change in the mass-to-light ratio. In Section 3.5.1, we have further shown that there is no evidence for a mass-to-light ratio gradient, that would be a consequence of a substantial deviation of the photometrically-derived stellar light profile and the dynamically-derived mass profile.

In any case, due to the very high spatial resolution of our data, we probe well into the SMBH-dominated regime, where the stellar contribution is small (see Figure 3.6). We therefore conclude that any remaining uncertainties in our stellar light model will not significantly bias our SMBH mass.

Finally, the adopted distance to NGC 7052 sets the scale of our dynamical model. The inferred SMBH mass scales linearly with distance, since $M_{\rm BH} \propto v^2 R \propto D$, where v is the velocity of a particle at radius R (as we observe an angular radius, the physical radius scales with the assumed distance).

We have adopted a distance of 69.3 Mpc for consistency with the MASSIVE survey (Ma et al., 2014). This distance is calculated from the observed recession velocity and the flow model of Mould et al. (2000) assuming a current Hubble constant $H_0 = 70\,{\rm km\,s^{-1}\,Mpc^{-1}}$. Although Ma et al. (2014) do not quantify the uncertainty of this distance, the Hubble flow distances listed in the NASA/IPAC

Extragalactic Database[5] have a typical uncertainty of 7%. As is standard practice, we do not include this uncertainty in our quoted dynamical SMBH mass measurement, and the results herein are simply corrected to any adopted distance.

3.5.3 Gas velocity dispersion

The observed line-of-sight velocity dispersions observed in molecular gas are comprised of an intrinsic (turbulent) velocity dispersion, broadened by beam smearing of mean velocity gradients. Typical molecular gas intrinsic velocity dispersions are very small (often $<10\,\mathrm{km\,s^{-1}}$; e.g. Davis et al. 2017a, 2018a; Smith et al. 2019).

van der Marel & van den Bosch (1998) found that the Hα velocity dispersion of NGC 7052 decreased with increasing radius, with a central peak of $400\,\mathrm{km\,s^{-1}}$ falling to $70\,\mathrm{km\,s^{-1}}$ by a radius of $\approx 1''$. Although enhanced central dispersions are expected by Doppler broadening close to the central SMBH, a model excluding an intrinsic velocity dispersion gradient was inconsistent with their observations (van den Bosch & van der Marel, 1995). In their dynamical models, they found that an exponentially-decaying intrinsic (turbulent) velocity dispersion was required to account for the above variation, of the form

$$\sigma(R) = \sigma_0 + \sigma_1 e^{-R/R_\mathrm{t}}\,, \tag{3.2}$$

where R_t is the scale length of the (turbulent) velocity dispersion and σ_0 and σ_1 parametrize the radial variation. Their best-fitting dynamical model yielded $\sigma_0 = 60\,\mathrm{km\,s^{-1}}$, $\sigma_1 = 523\,\mathrm{km\,s^{-1}}$ and $R_\mathrm{t} = 0\farcs11$. The very small scale length implies that although the central amplitude is large, the dispersion is dominated at almost all radii by the (rather large) constant term.

Our best-fitting model described in Section 3.4 assumed a radially-constant velocity dispersion. For comparison, we performed another fit allowing the velocity dispersion to vary with radius according to Equation 3.2. This model is visibly inferior to that found assuming a constant dispersion, but the best-fitting SMBH mass is consistent with our previous result. We therefore conclude that no intrinsic

[5] http://ned.ipac.caltech.edu

velocity dispersion gradient is required to account for our observations, and our derived SMBH mass is robust.

3.5.4 Comparison with ionised gas

van der Marel & van den Bosch (1998) used H α and [N II] emission observed with the *HST* Faint Object Spectrograph to measure the central SMBH mass of NGC 7052, and found $M_{\rm BH} = 3.9^{+2.7}_{-1.5} \times 10^8\,{\rm M}_\odot$ (corrected to our adopted distance). Our measurement is not consistent with this result.

As a check, we performed another fit to our observations, with the SMBH mass set to that found by van der Marel & van den Bosch (1998) from warm gas kinematics. The major-axis PVD of the model with the maximum log-likelihood is shown in Figure 3.7 (left panel), overlaid on our ALMA data. Clearly, the model severely underestimates the molecular gas velocities at small radii, as would be expected from imposing a SMBH mass one-quarter of that required.

This can be partially compensated for by allowing a mass-to-light ratio gradient. We thus include a gradient in yet another model by calculating the circular velocity as before, but assuming $M/L_I = 1\,{\rm M}_\odot/{\rm L}_{\odot,I}$, and then multiplying this function at each radius by $\sqrt{M/L_I(R)}$ (Davis & McDermid, 2017; Davis et al., 2018a). We adopt a linearly-varying mass-to-light ratio that flattens beyond 2″. The best-fitting model is shown in Figure 3.7 (right panel), and has a central mass-to-light ratio of $6.9\,{\rm M}_\odot/{\rm L}_{\odot,I}$, returning to $4.6\,{\rm M}_\odot/{\rm L}_{\odot,I}$ (our best-fitting spatially-constant M/L_I) at 2″. Although as expected the M/L gradient increases the central velocities, the model is still inferior to that presented in Section 3.5.1. As we discussed in Section 3.5.2, a discrete increase in the mass-to-light ratio at very small (spatially-unresolved) scales can always mimic a SMBH signature, but there is no physical reason to expect such a change. We therefore conclude here that such a mass-to-light ratio gradient is disfavoured, and hence that the $M_{\rm BH}$ measurement of van der Marel & van den Bosch (1998) is excluded by our data.

The main advantages of our molecular gas observations over those used by van der Marel & van den Bosch (1998) are as follows. First, our observations trace the

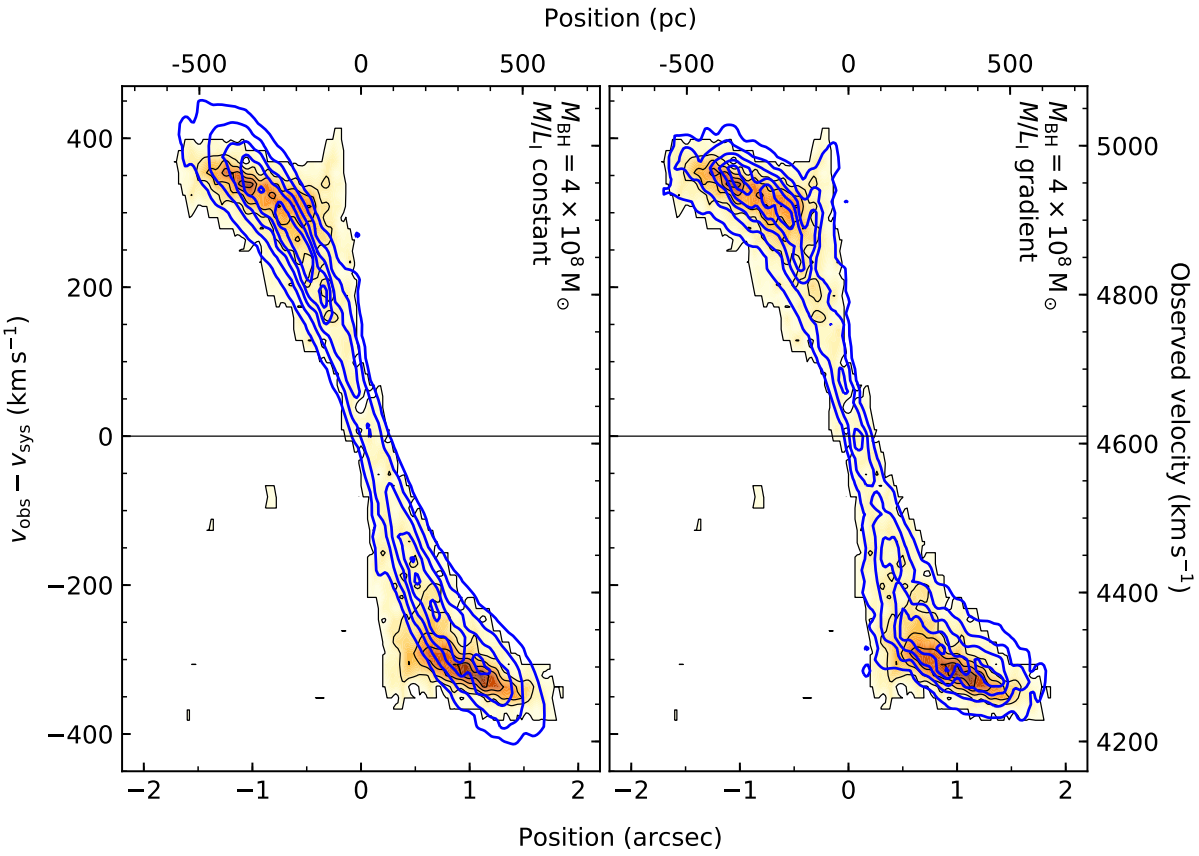

Figure 3.7: Model position-velocity diagrams along the kinematic major axis of the galaxy (blue contours), showing the best-fitting models with the SMBH mass fixed to that of van der Marel & van den Bosch (1998), with either a radially-constant mass-to-light ratio (left), or a mass-to-light ratio gradient (right). These are overlaid on the observed PVD (orange scales and contours). Although allowing a mass-to-light ratio gradient helps to enhance gas velocities at small radii, this model remains inferior to that described in Section 3.4.4.

entire gas disc, rather than only a few discrete locations along the major axis (the galactic radii of which can themselves have significant uncertainty due to pointing uncertainty). By fitting the entire gas disc, we have many more constraints on the observed kinematics (and the uncertainty on their locations), and hence on the mass distribution throughout the central region of the galaxy. Second, all gas dynamical measurements can be affected by non-gravitational forces and non-circular motions. The very low velocity dispersions of our CO gas indicate that these are negligible (while warm ionised gas is likely to be more significantly affected). As outlined in Section 3.5.3, van der Marel & van den Bosch (1998) required a significant central velocity dispersion to adequately fit their observations, attributed to turbulence and neglected in the dynamical model. If this dispersion instead corresponds to

(some component of) pressure support, the fit will necessarily underestimate the SMBH mass. It should be further noted that more recent *HST* Space Telescope Imaging Spectrograph observations indicate the presence of a separate dynamical component (perhaps a broad-line region; Noel-Storr et al. 2003, 2007; Verdoes Kleijn et al. 2006) that may exhibit significantly different ionised-gas kinematics to the extended gas detected by the FOS.

A similar case of a rotating warm gas disc with a strong velocity dispersion gradient is found in Centaurus A. Häring-Neumayer et al. (2006) explored the sensitivity of SMBH mass predictions from dynamical models to the inclusion of the velocity dispersion gradient as component of the dynamical support. They found that a cold disc assumption could underestimate the SMBH mass by a factor of ≈3 in their case, with respect to a model including the velocity dispersion gradient. Although the degree to which the lack of this support can underestimate the SMBH mass will vary between discs, this evidence suggests that their lack of dynamical pressure support in the warm gas disc could be the reason for the disagreement between the SMBH mass measurement of van der Marel & van den Bosch (1998) and our (cold molecular gas) model.

The $M_{\rm BH}-\sigma_*$ relation of McConnell & Ma (2013) predicts $M_{\rm BH} = 1.5^{+2.1}_{-0.9} \times 10^9\,{\rm M}_\odot$ (assuming $\sigma_* = 284\,{\rm km\,s^{-1}}$, and including 0.38 dex of intrinsic scatter) for NGC 7052. Our result is in excellent agreement with this prediction, whereas the ionised gas measurement of van der Marel & van den Bosch (1998) is significantly below it. The significant differences across SMBH masses derived via different dynamical tracers thus continues to demonstrate the need for robust cross-checks between all techniques. Further SMBH mass measurements using molecular gas offer the prospect of determining the intrinsic scatter in the SMBH-host galaxy scaling relations with measurements from a single technique across the entire Hubble sequence.

3.5.5 Tidal accelerations and molecular cloud stability in the galactic centre

The molecular gas discs of many galaxies in the WISDOM sample exhibit central holes at small radii (e.g. Davis et al., 2018a; Smith et al., 2019), including NGC 7052. These ≈100 pc holes have been revealed for the first time by the exceptionally high angular resolutions required for SMBH measurements. The typical extents of these features are roughly consistent with the SMBH spheres-of-influence, suggesting that they may have a dynamical origin.

One dynamical mechanism that could give rise to depleted molecular gas surface densities at the centre of galaxies is the tidal disruption of gas clouds. It is generally believed that molecular gas forms in these clouds, due to the outer layers of the clouds shielding their centres from ultraviolet radiation that would otherwise photo-dissociate the molecules, and due to the high densities increasing the number of collisions that can form molecules (and those with dust grains that can enhance molecule formation through surface reactions; Binney & Merrifield 1998). Strong shear or tidal acceleration could exceed the self-gravity of such clouds, disrupting them and exposing the molecules to photo-dissociation, or preventing the formation of clouds entirely. This would in turn inhibit the formation of stars near an SMBH (e.g. Sarzi et al., 2005).

Liu et al. (2021) considered the effect of external gravity on the morphology and confinement of giant molecular clouds. In their formalism, spatial variations of the external gravitational potential can contribute to either keeping clouds bound or to disrupting them, depending on the sign of $T - 2\Omega^2$, where

$$T(R) \equiv -R \frac{d\Omega^2(r)}{dr}\bigg|_R \tag{3.3}$$

is the tidal acceleration in the radial direction and Ω is the orbital angular velocity (v/R; see Appendix A of Liu et al. 2021, particularly their equations A9 and A14-A25). These quantities are shown in the bottom panel of Figure 3.8. Uncertainties in each are estimated by propagating the uncertainties in our model parameters via Monte Carlo methods.

Our model indicates that $T - 2\Omega^2$ changes sign at $0\farcs50 \pm 0\farcs09$ and is positive (thus disrupting the clouds) within this radius. This position is consistent with the peak of the gas distribution (Figure 3.8, top panel). If other contributions to the energy budgets of clouds at these radii are negligible (or, more likely, are finely balanced by gravity), then the central gas deficit could be the result of tidal accelerations disrupting the clouds. We cannot directly measure these other contributions in NGC 7052, and thus cannot robustly test this hypothesis.

Entirely different explanations are of course possible, such as the central AGN contributing a very large number of photons and thus dissociating the molecules in the centre (and hence suggesting that the size of the hole is proportional to the optical depth), or the central molecular gas being better traced by other CO transitions or higher density tracers.

3.6 Conclusions

HIGH angular resolution observations from the Atacama Large Millimetre/submillimetre Array (ALMA) and Atacama Compact Array (ACA) were used to make a 1.3 mm continuum image and a ^{12}CO(2-1) cube of the elliptical galaxy NGC 7052. We detect a compact continuum source at the optical centre of the galaxy, assumed to correspond to emission from the active galactic nucleus. The CO data reveal a dynamically cold ($\sigma \approx 20\,\mathrm{km\,s^{-1}}$) rotating disc coincident with a prominent dust disc visible in *Hubble Space Telescope* (*HST*) images. The ALMA observations resolve a physical scale of $0\farcs11$ (37 pc), smaller than the central region over which the galactic gravitational potential is dominated by the central supermassive black hole (SMBH).

We constructed a dynamical model of NGC 7052 to constrain the SMBH mass. We estimated the stellar contribution to the potential by multiplying a multi-Gaussian expansion of a *HST* WFPC2/PC F814W optical image by a spatially-constant mass-to-light ratio. The model was fit to the central $2\farcs56 \times 2\farcs56$ region of the ALMA data cube within a Markov Chain Monte Carlo framework. The best-fitting SMBH mass is $2.5 \pm 0.3 \times 10^9\,\mathrm{M}_\odot$ and the I-band mass-to-light ratio

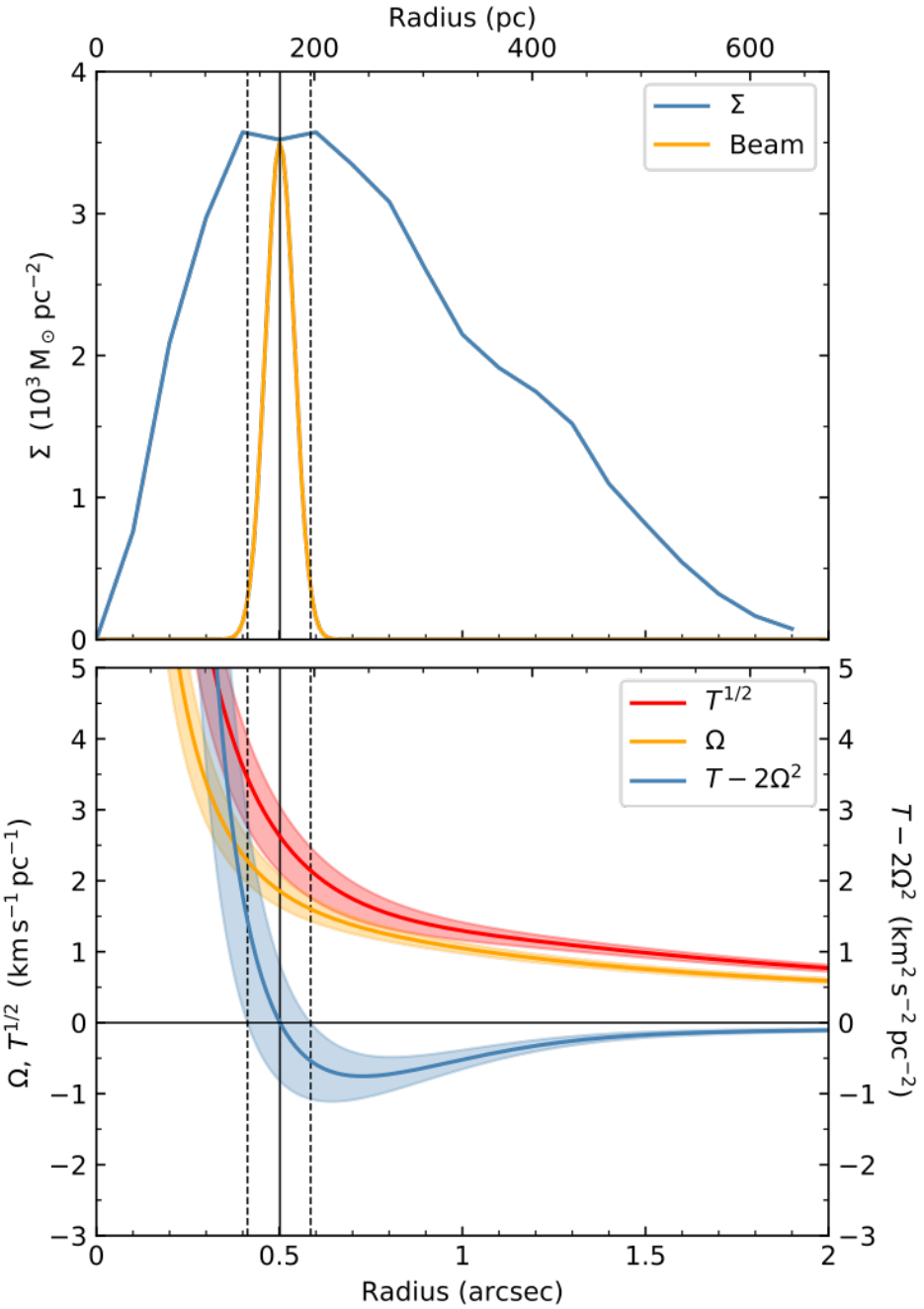

Figure 3.8: Top panel: Azimuthally-averaged molecular gas surface density radial profile (Σ; blue solid line), overlaid with our synthesised beam (orange solid line) centred at $0\farcs5$. **Bottom panel:** Orbital angular velocity (Ω, orange solid line), tidal acceleration per unit length in the radial direction (T, red solid line) and the function $T - 2\Omega^2$ (blue solid line), all calculated from our dynamical model. Coloured envelopes around each line indicate the $\pm 3\sigma$ confidence intervals. $T - 2\Omega^2$ is positive within $0\farcs50 \pm 0\farcs09$, indicated by a black vertical line (with 3σ confidence intervals indicated by black dashed vertical lines) in both panels. This matches well the maximum of the surface density profile, and thus the radius within which the molecular gas density rapidly decreases.

is $4.6 \pm 0.2\,\mathrm{M}_{\odot}/\mathrm{L}_{\odot,\mathrm{I}}$ (3σ confidence intervals). We exclude the possibility of a physically-motivated mass-to-light ratio gradient.

This SMBH mass measurement is substantially larger than that found previously using *HST* Faint Object Spectrograph observations of ionised gas by van der Marel & van den Bosch (1998). The key difference is that the molecular gas disc is dynamically cold even very close to the SMBH, whereas the warm gas kinematics of van der Marel & van den Bosch (1998) show large velocity dispersion gradients. Our observations strongly exclude their previous measurement. We suggest that the difference in our SMBH mass measurement may be due to the fact that they do not include dynamical pressure support in their models.

The peak molecular gas surface density occurs at a radius of $\approx 0\farcs5$, the surface density slowly declining towards the centre of the galaxy (and outward). This peak corresponds to the radius within which the external gravitational potential acts to tidally disrupt molecular gas clouds. We suggest that if this effect dominates the self-gravity of clouds, it is likely that the central molecular gas depletion is the result of tidal forces preventing the formation of molecular clouds.

Our SMBH measurement once more demonstrates the power of the molecular gas kinematics method to measure SMBH masses, and the important role ALMA can play to understand the dynamics of molecular gas in the central regions of galaxies. The steadily increasing sample of such masses will soon allow us to constrain the $M_{\mathrm{BH}}-\sigma_{*}$ relation over several orders of magnitude in SMBH mass with a single method.

4

Exploring the relation between supermassive black hole mass and galaxy rotation with molecular gas

Contents

The material in this chapter was originally published in the Monthly Notices of the Royal Astronomical Society, Volume 500, p.1933-1952.

4.1 Introduction

SUPERMASSIVE black holes (SMBHs) are found in the centres of almost all massive galaxies. They are now believed to play an instrumental role in the evolution of their hosts, a conclusion drawn from the tight correlations, spanning multiple orders of magnitude, between the SMBH masses and large-scale host properties (for reviews, see e.g. Kormendy & Ho 2013; Graham 2016). This is surprising given that, in almost all galaxies following these correlations, the SMBH only dominates the gravitational potential on very small spatial scales ($\lesssim$100 pc), and it has a negligible gravitational influence on the scales on which the host properties are measured. Nevertheless, these tight correlations have been used to argue that each SMBH coevolves with its host, invoking mechanisms such as active galactic nucleus (AGN) feedback (e.g. Croton et al., 2006; Bower et al., 2006; Vogelsberger et al., 2014), major merger-enhanced accretion (e.g. Sanders et al., 1988; Cattaneo et al., 1999; Di Matteo et al., 2005), and simple merger averaging (e.g. Peng, 2007; Hirschmann et al., 2010; Jahnke & Macciò, 2011). The relative importance of these mechanisms remains under dispute (e.g. Kormendy & Ho, 2013; Simmons et al., 2017).

The millimetre-Wave Interferometric Survey of Dark Object Masses (WISDOM) project aims to use the high angular resolutions achievable with the latest large millimetre/sub-millimetre interferometers to probe the environments around SMBHs. Principally, the survey is measuring SMBH masses using molecular gas kinematics, as the interferometers can resolve spatial scales dominated by the SMBHs (Davis et al., 2013b; Onishi et al., 2017; Davis et al., 2018a; Smith et al., 2019, 2021b; North et al., 2019). Other groups have also used the same method to constrain SMBH masses (e.g. Onishi et al., 2015; Barth et al., 2016a,c; Boizelle et al., 2019; Ruffa et al., 2019b; Nagai et al., 2019; Nguyen et al., 2020). In addition to measuring SMBH masses, the same data can be used to investigate the physical state of the molecular gas and study giant molecular clouds (Utomo et al., 2015; Liu et al., 2021). In this chapter, we use relatively low-resolution CO observations to investigate a

correlation between deprojected integrated CO line widths and SMBH masses, that we propose could be a useful estimator of SMBH masses.

4.1.1 Dynamical signatures of SMBH–baryonic matter correlations

The tightest known correlations are those between the SMBH mass and properties of the host galaxy's bulge - stellar velocity dispersion (σ_*; e.g. Ferrarese & Merritt 2000; Gebhardt et al. 2000), mass or luminosity ($M_{\rm bulge}$ and $L_{\rm bulge}$; e.g. Kormendy & Richstone, 1995; Magorrian et al., 1998; Marconi & Hunt, 2003; Häring & Rix, 2004). These host quantities are measures of the stellar mass-dominated central potential of the bulge.

The $M_{\rm BH}-\sigma_*$ relation has traditionally been viewed as the tightest correlation, with an intrinsic scatter of only $\approx$0.3 dex (e.g. Gebhardt et al., 2000; Beifiori et al., 2012; Saglia et al., 2016). The velocity dispersions used for these investigations are usually taken from spectra integrated within 1 effective radius ($R_{\rm e}$), although the effects of finite instrumental apertures can affect this scale.

Correlations also exist between the SMBH mass and other properties of the host galaxy. One of the simplest such properties is the total stellar mass ($M_{*,\rm tot}$; Davis et al. 2018b). Although originally the total stellar mass (and the disc component in late-type galaxies, LTGs) was thought not to correlate with SMBH mass (Kormendy & Gebhardt, 2001; Kormendy et al., 2011), recent works have indicated there is a correlation, albeit one weaker than $M_{\rm BH}-\sigma_*$ (e.g. Beifiori et al., 2012; Läsker et al., 2014; Savorgnan & Graham, 2016; Mutlu-Pakdil et al., 2018) with 0.66 dex scatter (Davis et al., 2018b). This allows total stellar mass (or luminosity) to be invoked as a convenient proxy for SMBH mass where the dynamical σ_* is unavailable or hard to measure.

The total stellar mass/luminosity can also be linked to a dynamical quantity via the shape of the rotation curve, as indicated for spirals by the Tully-Fisher relation (Tully & Fisher, 1977). Such rotation curves are observed from the line-of-sight projected velocities of (rotating) dynamical tracers (e.g. Pease 1918; Burbidge

et al. 1959; Rubin & Ford 1970, see Sofue & Rubin 2001 for a review), and have been extensively used to study the structure of galaxies. Each galactic rotation curve is a probe of the gravitational potential, from the SMBH-dominated central region (occasionally spatially-resolvable with modern high-resolution observations; e.g. Greenhill et al., 1995; Gao et al., 2017; North et al., 2019), through a stellar-mass dominated regime, to outer parts dominated by a putative dark halo. A rotation curve can be decomposed into contributions from these components of the galactic potential (e.g. Martinsson et al., 2013). Disc galaxies often exhibit rotation curves that are (almost) flat over most of the stellar-dominated regimes and into the halo-dominated regimes, providing evidence for the 'disc-halo conspiracy' (e.g. van Albada & Sancisi, 1986; Williams et al., 2009). The rotation curves of some elliptical and lenticular galaxies peak within $1\,R_{\rm e}$ before declining with increasing radius, some then flattening in the outer parts (e.g. Noordermeer et al., 2007; Cappellari et al., 2013a).

4.1.2 CO kinematics as a baryonic matter tracer

Both $M_{*,\rm tot}$ and σ_* are widely known to correlate with the spatially-integrated line width of neutral hydrogen (H I; e.g. Whitmore et al. 1979; Courteau et al. 2014; Serra et al. 2016). However, each has also been linked to the line width of CO. Throughout this discussion, for simplicity, we refer to the spatially-integrated width of an emission line as ΔV, with a subscript denoting the emitting atom/molecule, irrespective of the method by which this line width has been measured. Later in this chapter, we will introduce alternative notation (W_{50}) to refer specifically to the width of a CO emission line measured by fitting a particular line profile (see Section 4.3.1).

4.1.2.1 CO Tully-Fisher relation

The Tully-Fisher relation (TFR), relating the asymptotic velocity of a rotationally-supported disc to its host galaxy's absolute magnitude, is widely used to measure distances to extragalactic sources. For the last two decades, since initial proposals by Dickey & Kazes (1992) and Sofue (1992), millimetre-wave emission from CO

molecules has been used as an alternative to radio H I or optical Hα emission to trace the asymptotic rotation velocity (e.g. Ho, 2007b; Davis et al., 2011, 2016; Tiley et al., 2016; Topal et al., 2018; Tiley et al., 2019), including in early-type galaxies (ETGs) where such rotationally-supported CO discs are still reasonably common (e.g. Davis et al., 2013a).

Although CO discs do not usually extend as far as neutral hydrogen discs, they have been found to extend to the flat part of the rotation curve in ≈70% of CO-rich ETGs (Davis et al., 2013a), and they appear to be present in most LTGs (e.g. Leung et al. 2018; Levy et al. 2018). The potential at the radii probed by CO, however, is still dominated by the stellar component (Cappellari et al., 2013a), and thus CO gas does not trace the same halo-dominated potential as H I. We discuss this in further detail in Section 4.1.3.

Nevertheless, Davis et al. (2019c) combined the CO TFR of Tiley et al. (2019) with the $M_{\rm BH}-M_{*,\rm tot}$ correlation of Davis et al. (2018b) to predict $M_{\rm BH} \propto \Delta V_{\rm CO}^{12.2\pm2.1}$. For spiral galaxies, the disc-halo conspiracy enables the replacement of the CO line widths in the Tiley et al. (2019) TFR with those of H I. The same argument cannot be made for ETGs, as we discuss in Section 4.1.4. In a sample of 48 spiral galaxies with dynamically-measured SMBH masses and H I line widths, Davis et al. (2019c) obtained a relation of $M_{\rm BH} \propto \Delta V_{\rm H\,I}^{10.62\pm1.37}$, consistent with their prediction. Notably, both the predicted and the observed relation are substantially steeper than found in earlier works (e.g. Beifiori et al., 2012; Sabra et al., 2015).

4.1.2.2 H I and CO line widths correlations with σ_*

A correlation between spatially-integrated H I emission line widths and stellar velocity dispersions was initially suggested for disc galaxies by Whitmore et al. (1979) and Whitmore & Kirshner (1981), where a constant $\Delta V_{\rm H\,I}/\sigma_* \approx 1.7$ was observed in local S0 and spiral galaxies (using velocity dispersions from spectra integrated within a fixed 3″ aperture). This ratio has since been shown to vary substantially with redshift and morphology (e.g. Cresci et al., 2009). The most accurate $\Delta V_{\rm H\,I}-\sigma_*$ correlation for ETGs was obtained using spatially-resolved

rotation curves from the ATLAS^{3D} survey. Serra et al. (2016) found a linear relation, $\Delta V_{\rm H\,I}/\sigma_* = 1.33$, and 12% total scatter consistent with the measurement errors. We must once more emphasise that these correlations physically correspond to a correlation between a halo property and a property measured on baryon-dominated scales, discussed further in Section 4.1.4.

In addition to that of large-scale H I, other emission line widths on smaller spatial scales have been proposed to potentially correlate with σ_*. Nelson & Whittle (1999) showed for a sample of Seyfert galaxies that the full-width at half-maximum (FWHM) of the nuclear [O III] emission correlates with its σ_* when the latter is measured on a similar scale, with $\Delta V_{\rm [O\,III]}/\sigma_* = 2.35$. Nelson (2000) later adopted this relation to use the [O III] FWHM as a proxy for σ_* to investigate the $M_{\rm BH}$–σ_* relation among active galaxies, for which there were few σ_* measurements available.

Shields et al. (2006) proposed the use of the CO line width as a proxy for σ_* to study whether the $M_{\rm BH}$–σ_* relation was already in place in a sample of quasars at redshifts $2 < z < 6$ (since [O III] is out of the optical window at these redshifts), assuming similarly that $\Delta V_{\rm CO}/\sigma_* = 2.35$. Although Shields et al. (2006) thereby concluded that $M_{\rm BH}$–σ_* does not hold at high redshifts, a subsequent analysis by Wu (2007) showed that by de-projecting $\Delta V_{\rm CO}$ and assuming the quasars were viewed almost face-on, the CO line widths could be brought into agreement with the local $M_{\rm BH}$–σ_* relation. In his analysis of Seyfert galaxies, Wu (2007) found a steeper $\Delta V_{\rm CO}$–σ_* correlation than Shields et al. (2006) had assumed, $\Delta V_{\rm CO}/(\sin i\,{\rm km\,s^{-1}}) = (-67.16 \pm 80.18) + (3.62 \pm 0.68)(\sigma_*/{\rm km\,s^{-1}})$, where i is the inclination of the CO disc. Although this relation still has substantial scatter, it dramatically outperforms the simpler approximation of Shields et al. (2006).

4.1.3 What part of the rotation curve do spatially-integrated CO line widths trace?

The spectral profile of a broad spatially-integrated emission line is dominated by Doppler-broadening, and thus tells us about the kinematics of the galaxy rather than the physical state of its emitting gas. Thus both H I and CO line

widths trace the rotation curve. However, as hinted at above, these emission lines originate from very different regions of the galaxy. H I emission primarily traces the outer parts, where the rotation curve is typically very flat and the potential dominated by non-luminous matter.

In contrast, CO emission typically extends to only $\approx 0.5\,R_{\rm e}$ (Davis et al., 2013a), emphatically in baryon-dominated regions. It thus traces the depth of the central, stellar, potential in a manner similar to σ_*. As previously discussed (Section 4.1.2.1), in LTGs this distinction is made smaller by the disc-halo conspiracy. However, this conspiracy is not known to hold in ETGs (Young et al., 2008; Cappellari et al., 2013a). Furthermore, ETG rotation curves are not ubiquitously flat in their outer parts, with recent kinematic modelling indicating that the rotation curves often decline (from some maximum) with increasing radius, such that the asymptotic velocities traced by H I are typically $\approx$25% lower than those found by central tracers at $0.2\,R_{\rm e}$ (Serra et al., 2016), as previously found in early-type disc galaxies (Noordermeer et al., 2007). This indicates the existence of an inner maximum in the rotation curve (hereafter $V_{\rm max}$). The ATLAS$^{\rm 3D}$ survey constructed Jeans Anisotropic Models (JAMs) of ETGs, and from these generated a rotation curve for each object. Cappellari et al. (2013a) showed that both the outer asymptotic circular velocity and $V_{\rm max}$ correlate tightly with σ_*, the latter with an intrinsic scatter of only 7%.

However, if one simply measures the width of an emission line, it is not trivial to identify which of these two velocities (asymptotic circular velocity or $V_{\rm max}$) is traced by CO emission (e.g. Noordermeer & Verheijen, 2007). Lavezzi & Dickey (1997) have argued that the shapes of the emission line profiles can be used to select those that reach beyond $V_{\rm max}$, i.e. the profiles must be 'boxy' or 'sharp-edged'. With different specific implementations, this criterion is now widely used in the absence of spatially-resolved emission (e.g. Davis et al., 2011; Tiley et al., 2016; Topal et al., 2018).

However, even when $V_{\rm max}$ has not been reached such profiles can also be produced by sharply-truncated discs. Modern interferometric observations have revealed populations of (potentially low-surface brightness) CO discs in ETGs that are truncated at the edge of the associated circumnuclear dust discs (e.g. Barth et al.

2016c; Boizelle et al. 2017; Davis et al. 2018a; Boizelle et al. 2019). It is worth noting that some of these galaxies have nearly-flat rotation curves within the $V_{\rm max}$ defined by luminous mass models, due to the contribution of the central SMBHs, also leading to double-horned profiles, but spatially-resolved observations are nevertheless essential to determine which scales the CO emission probes.

4.1.4 Rotation curves, haloes, and SMBHs

Following the discovery of the first SMBH mass-host property correlations, studies began to investigate whether the underlying coevolution was with the bulge, or whether a more fundamental correlation existed with another structural component. Particular interest revolved around the halo mass, with the asymptotic value of the rotation curve invoked as a suitable observable proxy. Initial work by Ferrarese (2002) and later Pizzella et al. (2005) appeared to show a non-linear relationship between the SMBH and (dark) halo masses. However, this was really a correlation between the rotation velocity and σ_* of each galaxy, and it relied on invoking the $M_{\rm BH}-\sigma_*$ relation and the assumption that the asymptotic rotation velocity measured correlates with the (dark) halo mass.

The later analysis of Kormendy & Bender (2011) showed that there was no correlation unless the galaxy also hosted a classical bulge - thus the apparent correlation was merely an 'indirect result of the rotation curve conspiracy'. Moreover, they argued that a loose correlation between these parameters cannot be taken to imply coevolution - on the simple principle that a larger galaxy contains larger structural components. Kormendy et al. (2011) went on to challenge the assumption that σ_* closely traces $M_{\rm BH}$ in pseudobulges, and hence the inference that haloes drive the growth of SMBHs.

Nevertheless, interest in these correlations has not subsided, not least because although weak correlations should not be taken as implying co-evolution, they can enable simple observable proxies to be used as estimators of SMBH masses. Davis et al. (2018b), for instance, suggested that their $M_{*,\rm tot}$ correlation is 'beneficial

for estimating $M_{\rm BH}$ from pipeline data or at higher redshift, conditions that are not ideal for the isolation of the bulge'.

However, we must be cautious. In Section 4.1.2.2 we argued that the spatially-integrated width of a CO line traces the baryonic component of a galaxy, since CO emission does not extend to halo-dominated scales. Moreover, since it is unclear whether the disc-halo conspiracy holds in lenticulars (or an analogous relation in ellipticals), we argue that the discussion in this chapter of a correlation between CO line widths and SMBH masses should not be taken as implying anything about SMBH-halo coevolution.

4.1.5 A CO perspective on rotation curve correlations

The discussion in Sections 4.1.1 and 4.1.2 implies that it is reasonable to investigate a correlation between the deprojected, spatially-integrated CO line widths of galaxies, tracing their rotation curves within the baryon-dominated regions, and their SMBH masses. Such a correlation may prove an alternative to the $M_{\rm BH}-\sigma_*$ relation. To this end, we fit double-horned emission line profiles to new and archival CO observations of galaxies to measure their line widths. We then show that these CO line widths correlate sufficiently well with the SMBH masses to be used as proxies to estimate SMBH masses. We also contribute to the extensive literature on CO line width correlations with σ_*, by finding a reasonably tight correlation.

This chapter exploits three recent improvements: (1) we use only the most robust SMBH masses measured dynamically, (2) we derive our tightest relation with spatially-resolved, high spectral resolution and high signal-to-noise ratio (SNR) CO observations from the Atacama Large Millimetre/sub-millimetre Array (ALMA) and other interferometers (and show the negative impact of instead using unresolved single-dish spectra) and (3) we fit our spatially-integrated CO emission lines with 'Gaussian double-peak' line profiles, that have been shown to recover well the intrinsic line widths (Tiley et al., 2016).

In Section 4.2, we describe the observational data used in this study. New observations made as part of this study are described in the Appendix to Smith

et al. (2021a). Section 4.3 goes on to measure the CO line widths and explore correlations. In Section 4.4, we discuss the conclusions that can be drawn from this study and the limitations of the sample used. We conclude in Section 4.5.

4.2 Data

SMBH masses have been measured in around 200 local galaxies over the last three decades, using a variety of dynamical tracers of the galaxies' central potentials. These results, as compiled in van den Bosch (2016), are used as the starting point for this work, to which a few more recent measurements are added. In addition to robust measurements, there are also a large number of upper limits, principally from ionised gas. In this work, we exclude such upper limits, leaving a parent sample of 196 galaxies with well-constrained SMBH masses. As most SMBH mass measurements require spatially-resolved tracers, these objects are typically well-studied local galaxies. Almost all have now been observed in CO using single-dish telescopes (though only 75 were detected), and 73 have been observed with interferometers (of which 58 were detected).

Investigating a correlation with CO line widths requires that we are able to recover these widths precisely. This is of particular importance since, while among massive galaxies the asymptotic rotation velocities span less than one order of magnitude ($100 - 500\,\mathrm{km\,s^{-1}}$), the corresponding SMBH masses vary over four ($10^6 - 10^{10}\,\mathrm{M_\odot}$). Thus, a comparatively small uncertainty of a few tens of $\mathrm{km\,s^{-1}}$ in a line width will translate to a large uncertainty in the predicted SMBH mass. The significance of this potentially large line width uncertainty is somewhat mitigated by the fact that even a dynamically-measured SMBH mass can exhibit a relatively large uncertainty.

The data required to constrain the line widths need to be of high quality to obtain robust line width measurements. Available observations comprise (intrinsically spatially-integrated) spectra from single-dish telescopes and spatially-resolved data cubes from either interferometers or mosaics of multiple pointings by single-dish telescopes. Although spatially-resolving the CO is formally unnecessary to measure

spatially-integrated line widths, resolved observations offer multiple advantages. First, we can verify that the molecular gas discs are in ordered rotation, and thus that the line widths truly measure the depths of the potentials. Second, the achieved sensitivities are generally significantly higher, due to the arrays' larger total collecting areas compared to single dishes, and the similar (or longer) integration times. Third, the use of smaller individual antennae leads to array primary beams that are much larger than those of single-dish telescopes, avoiding the data potentially missing some emission at large galactic radii. Pointing errors for single-dish telescopes can also cause extended emission to be missed, leading to erroneously asymmetric (and potentially artificially narrowed) line profiles. Such pointing errors are trivially diagnosed with spatially-resolved images, and are in any case generally unimportant due to the large primary beams. This is particularly important for our sample, as the galaxies used are all sufficiently local (and thus extended on the sky) that their SMBH masses could be measured by resolving spatial scales on which the SMBHs dominate the potentials. These advantages are countered by the significantly higher complexity in obtaining, calibrating and imaging interferometric observations, although modern observing, data reduction and data analysis pipelines have now somewhat mitigated this challenge. For these reasons, observations that spatially resolve the CO discs are preferable.

Although spatially-resolved observations are to be preferred, such observations are not available for most galaxies. We therefore divide our objects into two samples, galaxies with respectively spatially-resolved and unresolved CO observations. We fit both samples using identical procedures, and in Section 4.4.1 discuss the negative effects of using unresolved data.

From the parent sample of 196 candidate galaxies, we obtain CO spectra as described in Sections 4.2.1 and 4.2.2. The final samples are selected from these observations, applying the criteria discussed in Sections 4.2.1, 4.2.2 and 4.3.1. Finally, a few galaxies that are clear outliers are excluded, and these are justified in Section 4.4.3. Table 4.1 lists the number of galaxies that remain after each selection criterion is applied.

Table 4.1: Sample size after applying each selection criterion.

Selection criterion	Spatially-resolved sample	Spatially-unresolved sample	Section
(1)	(2)	(3)	(4)
Observed	73	162	4.2.1/4.2.2
CO detected	58	75	4.2.1/4.2.2
Regular rotation*	37	–	4.2.1
Boxy profile	29	53	4.1.3, 4.2.1/4.2.2
Accepted fit	27	24	4.3.1
Not omitted	25	21	4.4.3

Notes: Column 1 lists each selection criterion applied to the samples, described in the main text. Column 2 lists the number of galaxies with spatially-resolved observations that remain after each criterion is applied, while Column 3 lists the corresponding number of galaxies with unresolved observations. Column 4 lists the section(s) in which each criterion is discussed. The criterion marked with a * only applies to the spatially-resolved sample.

4.2.1 Spatially-resolved CO observations

Data cubes (right ascension, declination, and velocity) are produced from either interferometric observations or by mosaicking multiple pointings of a single-dish telescope. We obtain such cubes from the ALMA archive, the Berkeley-Illinois-Maryland Association Survey of Nearby Galaxies[1] (BIMA-SONG; Helfer et al., 2003) and the ATLAS^{3D} survey[2] (Alatalo et al., 2013). ALMA observations have been calibrated and imaged automatically either by the ALMA pipeline or manually by ALMA Regional Centre staff, and the cubes used are those provided on the archive, with the exception of observations taken by our own WISDOM programme and its precursor studies, for which the data reduction and calibration (and the properties of the data cubes) are described in the associated papers (Davis et al., 2013b; Onishi et al., 2017; Davis et al., 2017a, 2018a; Smith et al., 2019; North et al., 2019; Smith et al., 2021b). BIMA-SONG and ATLAS^{3D} data cubes are used as provided on the associated websites. We visualise each cube and manually select only those that appear to show overall rotation, leaving 37 galaxies.

[1] https://ned.ipac.caltech.edu/level5/March02/SONG/SONG.html
[2] http://www-astro.physics.ox.ac.uk/atlas3d/

We then convert each data cube into a spectrum by integrating each channel over the two spatial dimensions. The emission in any given channel typically extends over only a few pixels, with the remainder populated by noise. To simply sum all pixels together blindly would needlessly include all this noise in our sum, degrading the sensitivity of the resultant spectrum. We can do better by summing only the pixels contained within a mask encompassing all the emission.

Such a mask can be generated using the 'smooth-masking' technique (Dame, 2011), originally developed to make high-quality moment maps. Each cube is first smoothed spatially by the beam and Hanning-smoothed spectrally. Pixels with values exceeding a noise threshold in the smoothed cube are included in the mask; we use a threshold of 5 times the rms noise measured in the original cube. The mask is then applied to the original, unsmoothed cube, and should encompass all high-surface brightness pixels, assumed to correspond to real emission, as well as small regions around them that may include lower surface brightness emission. An integrated spectrum is then produced by summing all pixels included in the mask.

The resulting spectra are of generally significantly higher quality than those obtained by single-dish telescopes. However, the uncertainty on the total flux in each channel must be considered carefully. In a normal single-dish spectrum, we can simply measure the rms noise in line-free channels, and assume that it is constant across the full bandpass. However, in integrated spectra derived from data cubes, the uncertainty in each channel is instead a function of the number of pixels included in the mask in that channel. We estimate this in each channel by assuming the noise to be Gaussian with standard deviation $\sigma_{\rm px}$. The sum of $N_{\rm mask}$ normal random variables is then $\sigma_{\rm px}\sqrt{N_{\rm mask}}$, where $N_{\rm mask}$ is the number of pixels in the mask in that channel. This formalism is only valid in channels where the mask is non-zero.

In channels where the mask is zero (i.e. $N_{\rm mask} = 0$), both the integrated flux and the estimated uncertainty would be zero. There may however be real emission below the detection threshold. We assume that such emission would be distributed on a spatial scale comparable to those in other channels, and adopt the mean number of pixels in the non-zero channels of the mask ($\langle N_{\rm mask}\rangle$) as the representative spatial

scale over which undetected emission would be distributed. The uncertainty is thus given by $\sigma_{\rm void} = \sigma_{\rm px}\sqrt{\langle N_{\rm mask}\rangle}$, and it is therefore constant for line-free channels.

The resulting spectra are all visually inspected, and those that do not have a boxy line profile are rejected. This can occur even when the dynamics appear to exhibit overall rotation (e.g. if the CO distribution does not sample the velocity field well). Applying this criterion leaves 29 galaxies with spatially-resolved CO observations.

4.2.2 Unresolved sample

Line widths can also be measured directly from the spectra obtained in single-dish observations. Such observations are simpler than spatially-resolved observations, but typically have lower SNRs. The other challenge with these spectra in local galaxies is the relatively small primary beams of the large telescopes used, that may not extend far enough into the galaxies to reach the flat parts of their rotation curves in single pointings. For these reasons, there are two concerns with the line widths obtained from the objects in this unresolved galaxy sample: the uncertainties are larger fractions of the channel width than those estimated for the resolved sample galaxies, and we cannot be certain whether the line widths measured encompass the full widths of the rotation curves.

The literature contains single-dish CO observations in two forms. Most commonly, spectra are shown in figures only, with the quantitative information needed for other astronomers to use the data rarely available. We then use the public tool `GraphClick`[3] to manually digitise these figures, obtaining flux measurements by interpolating from the axis scales.

These data are given variously in the antenna ($T_{\rm A}^*$), radiation ($T_{\rm R}^*$) and main beam ($T_{\rm mb}$) temperature scales. For the sake of homogeneity, we transform them all to the same flux density scale (Jy) as the spectra obtained for our resolved galaxy sample, using observatory-specific appropriate beam efficiencies listed in Table 4.2. We assume that the emission is point-like and do not account for the spatially-varying responses of the telescopes. This would be valid only if the gas is centrally concentrated. As we have argued above, and discuss further in Section

[3] http://www.arizona-software.ch/graphclick/

4.4.1, the relatively small extents of the beams compared to the very large extents of these local galaxies imply this assumption may be invalid. With no *a priori* information on the gas distributions, however, we cannot make more appropriate conversions. Moreover, since this is a spectrally-constant conversion, any change will not affect the line widths measured, the only quantities used in this chapter.

For all spectra except those of Maiolino et al. (1997) (for which a direct conversion from $T_{\rm R}^{*}$ is provided), we therefore first convert from $T_{\rm mb}$ or $T_{\rm R}^{*}$ to $T_{\rm A}^{*}$ using the efficiencies in Table 4.2, and then convert from $T_{\rm A}^{*}$ to flux densities using

$$S\,({\rm Jy}) = \frac{2k_{\rm B}}{\eta_{\rm A}}\,\frac{4}{\pi D^2}\,T_{\rm A}^{*}\,, \tag{4.1}$$

where $k_{\rm B}$ is Boltzmann's constant, $\eta_{\rm A}$ the telescope aperture efficiency (relating the geometric area of the telescope dish to its effective area) and D the telescope diameter.

In addition to observations published by other authors, we acquired new observations at the Institut de Radioastonomie Millimétrique (IRAM) 30-m telescope under programme 191-18 and at the Onsala Space Observatory (OSO) 20-m telescope under programme 2018-04a. Fifty-one galaxies were observed with the IRAM 30-m telescope, of which twenty-two were detected. Nine were observed at the OSO 20-m telescope, and four detected. These observations are described in detail in the Appendix to Smith et al. (2021a), and the spectra are shown in the supplemental material.

Combining observations from the literature and from our programmes, there are unresolved CO detections of 75 of the galaxies in our parent sample. Those without a boxy line profile are rejected, leaving 53 galaxies. Estimates of the noise levels in all these spectra are obtained from the emission-free channels at either end of the CO lines, and are assumed to be spectrally constant.

4.3 Results

We discussed in Section 4.1.2.1 the role of the CO Tully-Fisher relation to interpret our proposed CO line width–SMBH mass correlation. However, different methods of measuring the CO line width from a

Table 4.2: Adopted conversions from literature units to fluxes, assuming point sources.

Telescope	CO line	Conversions
IRAM 30-M	CO(1-0)	$T_{\rm A}^* = 0.78\,T_{\rm mb}$
		$S_{\rm Jy} = 5.98\,T_{\rm A}^*$
	CO(2-1)	$T_{\rm A}^* = 0.63\,T_{\rm mb}$
		$S_{\rm Jy} = 7.73\,T_{\rm A}^*$
NRAO 12-M	CO(1-0)	$T_{\rm R}^* = 0.91\,T_{\rm mb}$
		$S_{\rm Jy} = 35\,T_{\rm R}^*$

spectrum have been proposed. The simplest scheme is simply to adopt the width at which the observed flux first falls below some fraction of the maximum (e.g. Davis et al., 2011). Using 20% of the maximum flux appears to yield a tighter CO TFR correlation (Ho, 2007b), but 50% would be preferable at low SNRs where a smaller fraction cannot be accurately determined. This approach can be particularly unreliable with very low SNR spectra, where although the line can be visually identified as a consistently-positive sequence of channels, the line edges are ill-defined. A profile fit to the line is therefore now generally preferred. This latter method also allows spectra with anomalous line shapes to be rejected when poorly fit by a suitably physically-motivated profile.

4.3.1 Line-width measurements

Tiley et al. (2016) investigated appropriate choices of line profiles and determined that the 'Gaussian double peak' profile, consisting of a quadratic function bounded by half-Gaussian wings, gave the most reliable line width measurements with least sensitivity to SNR and inclination. We therefore adopt the full-width at half-maximum (FWHM; equivalent to the 50% criterion defined above) of such a profile as our measure of the line width, fitting each spectrum with the Tiley et al. (2016) function

$$f(v) = \begin{cases} A_{\rm G} \times e^{\frac{-[v-(v_0-w)]^2}{2\sigma^2}} & v \leqslant v_0 - w \\ A_{\rm C} + a(v-v_0)^2 & v_0 - w \leqslant v \leqslant v_0 + w \\ A_{\rm G} \times e^{\frac{-[v-(v_0+w)]^2}{2\sigma^2}} & v_0 + w \leqslant v \end{cases}, \tag{4.2}$$

where $A_{\rm G}$ (the flux of each peak), $A_{\rm C}$ (the flux of the central extremum), v_0 (the velocity of the central extremum), w (the velocity half-width of the quadratic function) and σ (the velocity width of both half-Gaussian functions) are all free parameters, and a is determined by the continuity conditions at $v_0 \pm w$. The corresponding line width at the half-maximum is then given by

$$W_{50} = 2(w + \sigma\sqrt{2\ln 2}) \, . \tag{4.3}$$

We remind the reader that the notation W_{50} is used to refer specifically to a CO line width measured by fitting this line profile, as distinct to $\Delta V_{\rm CO}$, which was used to refer to CO line widths irrespective of the method used to measure them. We note that in cases for which $A_{\rm C} > A_{\rm G}$, this equation will not yield the FWHM, yielding instead slightly broader line widths. We describe below that galaxies for which $A_{\rm C} > (3/2)A_{\rm G}$ (those that would be most affected by this effect) are in any case rejected for not being double-horned profiles, and in the few cases where this condition occurs in the remaining galaxies this broadening effect is negligible due to the sharp edges of the spectral lines and $A_{\rm C}$ being only very slightly greater than $A_{\rm G}$.

The fits are performed using the Python package `lmfit`[4], minimising the chi-squared statistic:

$$\chi^2 = \sum_i \left(\frac{\text{data}_i - \text{model}_i}{\sigma_i} \right)^2 , \tag{4.4}$$

where i denotes each velocity bin (i.e. channel) of the spectrum, and σ_i is the uncertainty on the flux at each velocity bin as described in Section 4.2. Each spectrum is fit 30 times, with initial conditions selected randomly from a uniform distribution within reasonable physical limits, to ensure a global minimum is found. The fit with the smallest reduced chi-square is then selected as the best-fitting solution. The associated line width and uncertainty is then estimated from the uncertainties on σ and w (determined by the `lmfit` routines) through Monte Carlo methods: (σ, w) pairs are generated as normal random variables with means

[4] https://lmfit.github.io/lmfit-py/

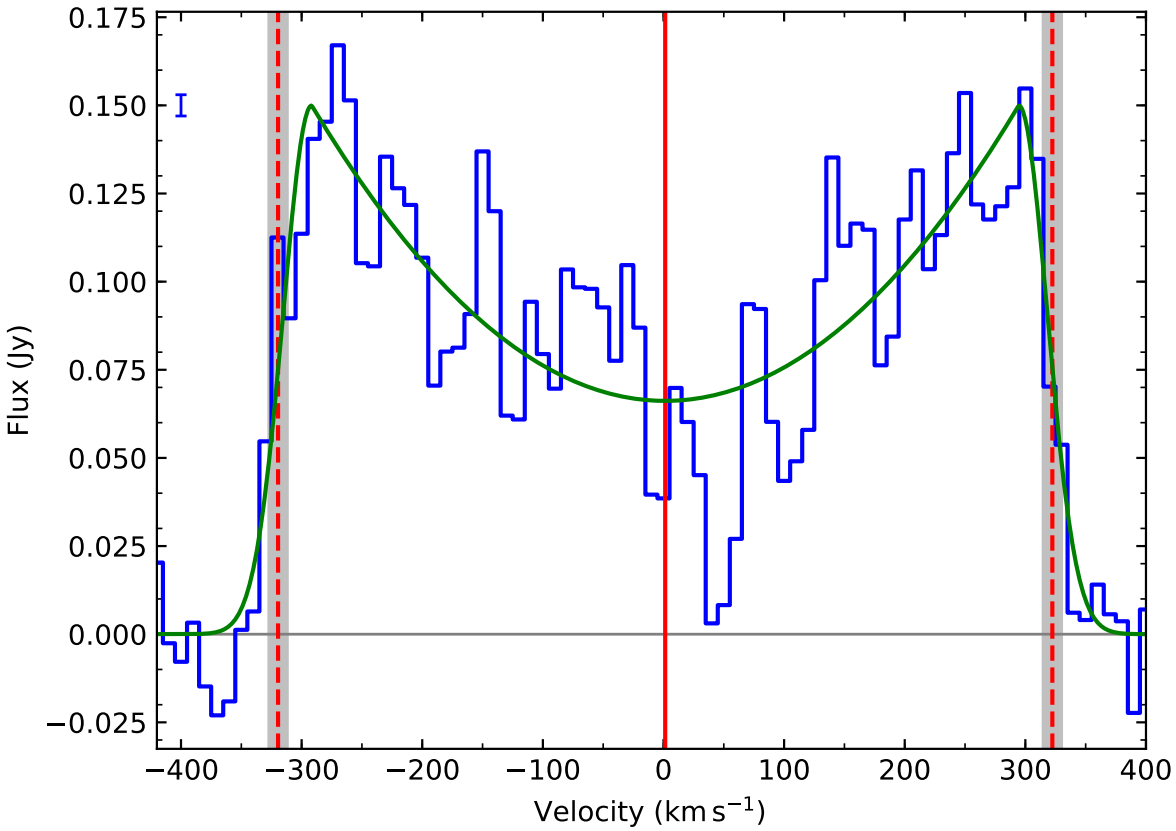

Figure 4.1: Example Gaussian double peak profile fit (green) overlaid on a spectrum synthesised from the CARMA data cube of NGC3665 (blue). The mean noise estimate ($\pm 1\sigma$) is shown in the top-left corner. The red vertical lines are at v_0 (solid) and bound W_{50} (dashed), defined in Equation 4.3, while the grey bands indicate the 67% confidence interval in W_{50}. Fits to the other spectra of spatially-resolved galaxies are shown in an extended version of this figure in the supplemental material to Smith et al. (2021a). The original data cube had already had the galaxy's systemic velocity subtracted.

given by the best-fitting (σ, w) and standard deviations obtained from the `lmfit`-derived uncertainties. The corresponding W_{50} are then calculated from Equation 4.3, and the median and standard deviation adopted as the best-fitting line width and uncertainty respectively.

We also investigated the systematics affecting our line width measurements. We generate 150 realisations of the best-fitting model with random normally-distributed noise of magnitude equal to the noise in the data added to each. Each realisation is then fit by the same Gaussian double peak profile using the parameters best-fitting the data as initial conditions. The standard deviations of the distributions of line widths from these fits are comparable to the uncertainties estimated by `lmfit`

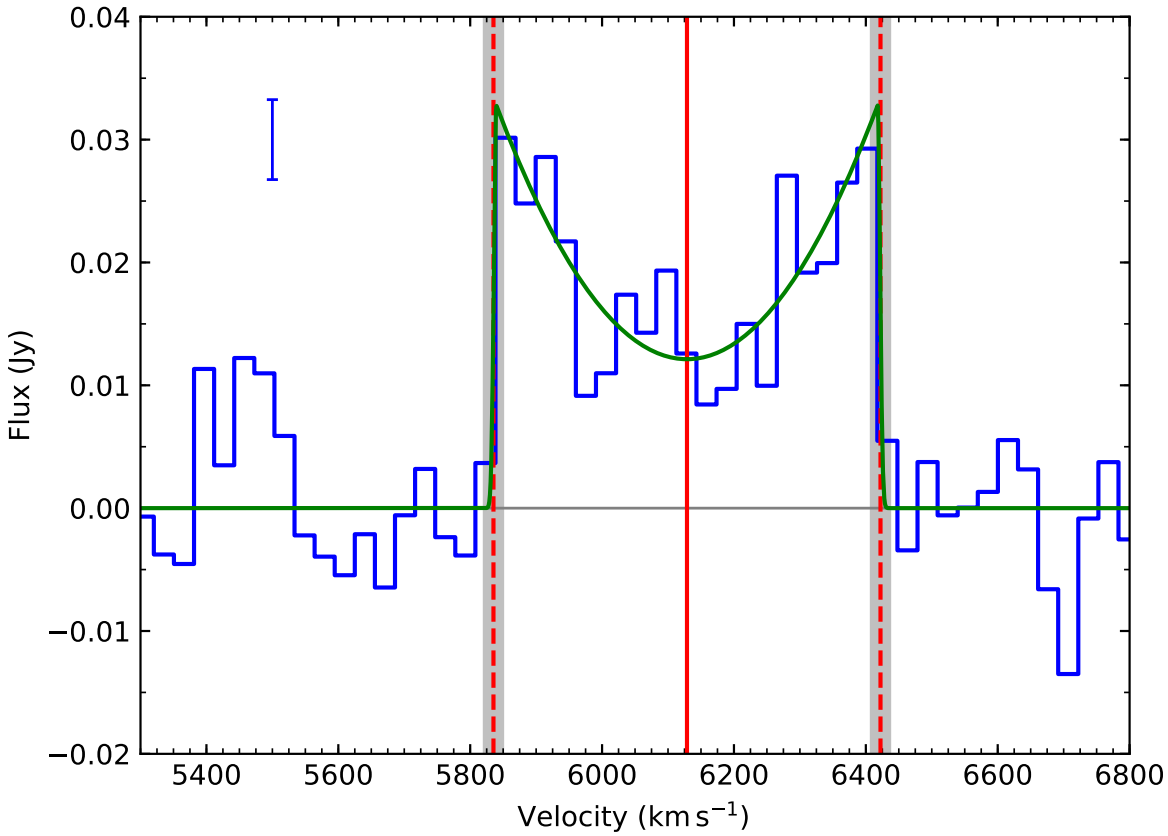

Figure 4.2: Example Gaussian double peak profile fit (green) overlaid on the IRAM 30-m spectrum of NGC 1497. The mean noise estimate ($\pm 1\sigma$) is shown in the top-left corner. The red vertical lines are at v_0 (solid) and bound W_{50} (dashed), defined in Equation 4.3, while the grey bands indicate the 67% confidence interval in W_{50}. Fits to the other spectra of unresolved galaxies are shown in an extended version of this figure in the supplemental material to Smith et al. (2021a). The velocity axis is the observed velocity, such that v_0 (red vertical line) is the galaxy's systemic velocity.

for the spectra in our unresolved sample, but they are much smaller (and also much smaller than the channel width) for our spatially-resolved sample due to the much higher signal-to-noise ratios. This suggests that reducing the noise in the spectra of the unresolved sample would yield smaller line width uncertainties, whereas adopting smaller channel widths will yield the greatest improvement for galaxies in the spatially-resolved sample.

Since not all profiles are well-reproduced by a Gaussian double peak profile, we also fit each profile with a simple Gaussian. We immediately reject a spectrum if either the Gaussian profile has a lower reduced χ^2 or the Gaussian double peak profile has $A_{\rm C} > (3/2)A_{\rm G}$, the latter corresponding to the flux at the centre of the

spectrum being at least 50% higher than that of the bounding half-Gaussians, in which case one might more naturally fit the spectrum with a single Gaussian (e.g. Tiley et al., 2016). Both criteria correspond to a violation of the 'boxy' criterion outlined previously, and imply that the observed CO gas is unlikely to have reached the flat part of the rotation curve.

Finally, every spectrum is manually inspected to ensure a good fit was achieved. This leaves final samples of 27 galaxies with spatially-resolved observations and 24 galaxies with unresolved observations that satisfy our selection criteria. These galaxies, and the associated line width measurements, inclinations and SMBH masses, are listed in Tables 4.3 and 4.4, respectively. Example profile fits to interferometric and single-dish observations are shown in Figures 4.1 and 4.2 respectively, and all data and associated fits are shown in extended versions of these figures in the supplemental material to Smith et al. (2021a).

Since we observe the line-of-sight projection of each line width, rather than the intrinsic width, we de-project W_{50} determined by the fit by $\sin i$. Uncertainties in the inclination, which can be significant, are propagated by Monte Carlo sampling as before. The inclinations are determined either from fits to dust features or the resolved CO discs in the literature, ellipse fits to dust discs in archival *Hubble Space Telescope* (*HST*) images, or, where the other methods are not possible, by using the apparent flattenings of the $25\,\mathrm{mag\,arcsec^{-2}}$ B-band isophotes and assuming morphology-dependent intrinsic thicknesses as given in HyperLEDA[5]. Davis et al. (2011) discuss the relative merits (and dangers) of using these methods to infer the inclination of a molecular gas disc. Where the B-band isophotes are used, the uncertainties in both the apparent flattenings and the morphological T-types listed in HyperLEDA are propagated into the inclination uncertainties by Monte Carlo sampling. This approach does not work for the face-on galaxy NGC 4388, which appears to be flatter than the inferred intrinsic thickness given its morphological classification, so we adopt a typical inclination uncertainty of 5°. We note this has a negligible effect on the deprojected line width.

[5]The formula for this inclination and for the assumed intrinsic thickness is given online at https://leda.univ-lyon1.fr/leda/param/incl.html

Table 4.3: CO data, best-fitting line widths and host galaxy properties for our spatially-resolved galaxies. All galaxies listed have a well-determined CO line width, but one (NGC 5055) is excluded from the final correlations. This omission is justified in Section 4.4.3.

Name	T-type	CO transition	W_{50} ($\mathrm{km\,s^{-1}}$)	Inclination (°)	$\log(M_{\rm BH}/\mathrm{M}_\odot)$	SMBH method	Notes
(1)	(2)	(3)	(4)	(5)	(6)	(7)	(8)
Circinus	3.3	1-0[1]	337.0 ± 3.0	78 ± 1[2] (M)	6.06 ± 0.10[3]	masers	$M_{\rm BH}-\sigma_*$ outlier
NGC 383	-2.9	2-1[4]	522.0 ± 3.7	38 ± 4[4] (M)	9.62 ± 0.07[4]	CO	
NGC 524	-1.2	2-1[5]	292.4 ± 13.8	20 ± 5[6] (D)	8.60 ± 0.30[5]	CO	
NGC 1332	-2.9	2-1[7]	884.8 ± 4.8	84 ± 1[8] (M)	8.82 ± 0.04[7]	CO	
NGC 1386	-0.7	1-0[9]	373.6 ± 1.8	68 ± 2[10] (D)	6.07 ± 0.29[11]	masers	$M_{\rm BH}-\sigma_*$ outlier
NGC 3081	0.0	2-1[12]	285.6 ± 10.9	46 ± 10[12] (D)	7.20 ± 0.30[13]	ionised gas	
NGC 3245	-2.1	2-1[14]	579.2 ± 2.6	63 ± 1[15] (K)	8.28 ± 0.11[15]	ionised gas	
NGC 3258	-4.3	2-1[16]	609.6 ± 12.0	45 ± 5[16] (M)	9.35 ± 0.01[17]	CO	
NGC 3504	2.1	2-1[18]	215.4 ± 10.4	62 ± 3[18] (M)	7.01 ± 0.07[18]	CO	Omitted
NGC 3557	-4.9	2-1[19]	431.3 ± 19.1	56 ± 1[19] (M)	8.85 ± 0.01[19]	CO	
NGC 3607	-3.2	2-1[20]	542.6 ± 8.9	48 ± 6[21] (D)	8.14 ± 0.16[22]	stars	
NGC 3627	3.1	1-0[23]	389.1 ± 13.1	61 ± 1[24] (D)	6.93 ± 0.05[25]	stars	
NGC 3665	-2.1	2-1[26]	641.9 ± 15.4	70 ± 1[26] (M)	8.76 ± 0.10[26]	CO	
NGC 4258	4.0	1-0[23]	388.1 ± 20.4	68 ± 4[27] (B)	7.58 ± 0.03[28]	masers	
NGC 4303	4.0	2-1[29]	121.0 ± 6.9	21 ± 10[30] (M)	6.51 ± 0.74[31]	ionised gas	
NGC 4429	-0.8	1-0[32]	543.9 ± 11.1	66.8 ± 0.2[33] (M)	8.18 ± 0.08[34]	CO	
NGC 4459	-1.6	1-0[34]	382.8 ± 14.5	46 ± 2[35] (D)	7.84 ± 0.09[36]	ionised gas	
NGC 4526	-1.9	2-1[37]	692.3 ± 5.9	79 ± 3[37] (M)	8.65 ± 0.12[37]	CO	
NGC 4697	-4.5	2-1[38]	435.7 ± 2.8	76 ± 1[38] (M)	8.11 ± 0.06[38]	CO	
NGC 4736	2.3	1-0[23]	236.5 ± 5.9	35 ± 10[39] (K)	6.78 ± 0.12[40]	stars	FP outlier
NGC 4826	2.2	1-0[23]	327.8 ± 3.1	60 ± 3[21] (D)	6.05 ± 0.12[40]	stars	FP outlier
NGC 5005	4.0	1-0[23]	574.3 ± 15.6	69 ± 5[10] (D)	8.27 ± 0.23[13]	ionised gas	

Table 4.3: (continued) CO data, best-fitting line widths and host galaxy properties for our spatially-resolved galaxies. All galaxies listed have a well-determined CO line width, but one (NGC 5055) is excluded from the final correlations. This omission is justified in Section 4.4.3.

Name	T-type	CO transition	W_{50} ($\mathrm{km\,s^{-1}}$)	Inclination (°)	$\log(M_{\mathrm{BH}}/\mathrm{M}_\odot)$	SMBH method	Notes
(1)	(2)	(3)	(4)	(5)	(6)	(7)	(8)
NGC 5055	4.0	1-0[23]	363.2 ± 4.7	59 ± 2[10] (D)	8.70 ± 0.90[41]	ionised gas	$M_{\mathrm{BH}}-\sigma_*$ outlier; omitted
NGC 5248	4.0	1-0[23]	241.6 ± 5.9	54 ± 4[21] (D)	6.30 ± 0.38[13]	ionised gas	
NGC 6861	-2.7	2-1[16]	995.9 ± 6.2	71 ± 5[21] (D)	9.30 ± 0.08[42]	stars	
NGC 7052	-4.9	2-1[43]	712.7 ± 10.2	75 ± 5[43] (M)	9.41 ± 0.05[43]	ionised gas	
NGC 7331	3.9	1-0[23]	528.5 ± 8.2	70 ± 4[27] (B)	8.02 ± 0.18[13]	ionised gas	

Notes: Column 1 lists the name of each galaxy contained in the final sample of spatially-resolved galaxies. The morphological classification on the numerical Hubble scale from HyperLEDA is listed in Column 2. Spatially-resolved observations of the CO transition listed in Column 3 were integrated within a mask to obtain a spectrum. Column 4 lists the (line-of-sight projected) line width and associated uncertainty measured from a Gaussian double peak line profile fit to this spectrum. Column 5 lists the inclination of the CO disc and in parentheses the method used to measure it (D - dust morphology, M - molecular gas morphology/kinematics, B - *B*-band apparent flattening, K - other kinematics). Column 6 lists the dynamically-measured SMBH mass using the tracer cited in Column 7. Column 8 contains other notes about certain galaxies. Footnotes in column 3 indicate the source of the CO observations, and those in columns 6 and 7 the source of the measurement, as follows. **References:** (1) Zschaechner et al. (2016), (2) Curran et al. (1998), (3) Greenhill et al. (2003b), (4) North et al. (2019), (5) Smith et al. (2019), (6) Cappellari et al. (2006), (7) Barth et al. (2016a), (8) Barth et al. (2016c), (9) Zabel et al. (2019), (10) this work, from a *HST* WFPC2 F606W image, (11) Braatz et al. (1997), (12) Ramakrishnan et al. (2019), (13) Beifiori et al. (2012), (14) ADS/JAO.ALMA#2017.1.00301.S, (15) Barth et al. (2001), (16) Boizelle et al. (2017), (17) Boizelle et al. (2019), (18) Nguyen et al. (2020), (19) Ruffa et al. (2019b), (20) ADS/JAO.ALMA#2015.1.00598.S, (21) this work, from a *HST* WFPC2 F814W image, (22) Gültekin et al. (2009a), (23) Helfer et al. (2003), (24) Casasola et al. (2011), (25) Saglia et al. (2016), (26) Onishi et al. (2017), (27) HyperLEDA, (28) Herrnstein et al. (2005), (29) Sun et al. (2018), (30) Schinnerer et al. (2002), (31) Pastorini et al. (2007), (32) Alatalo et al. (2013), (33) Davis et al. (2018a), (34) Davis & McDermid (2017), (35) Young et al. (2008), (36) Sarzi et al. (2001), (37) Davis et al. (2013b), (38) Davis et al. (2017a), (39) Bosma et al. (1977), (40) Kormendy et al. (2011), (41) Blais-Ouellette et al. (2004), (42) Rusli et al. (2013) and (43) Smith et al. (2021b).

Table 4.4: CO data, best-fitting line widths and host galaxy properties for our spatially-unresolved galaxies. All galaxies listed have well-determined CO line widths, but a few are excluded from the final correlations. These omissions are justified in Section 4.4.3.

Name	T-type	CO transition	W_{50} ($\mathrm{km\,s^{-1}}$)	Inclination (°)	$\log(M_{\rm BH}/\mathrm{M}_\odot)$	SMBH method	Notes
(1)	(2)	(3)	(4)	(5)	(6)	(7)	(8)
3C120	-1.7	1-0[1]	526.3 ± 38.1	65 ± 5[2] (B)	7.73 ± 0.15[3]	reverberation	
Ark 120	-5.0	1-0[4]	371.5 ± 30.9	49 ± 5[5] (D)	8.05 ± 0.17[6]	reverberation	
Mrk 590	1.0	1-0[6]	223.9 ± 7.5	26 ± 8[2] (B)	7.55 ± 0.18[8]	reverberation	
NGC 383	-2.9	1-0[9]	534.0 ± 15.4	38 ± 4[10] (M)	9.62 ± 0.07[10]	CO	
NGC 524	-1.2	1-0[11]	310.2 ± 54.5	20 ± 5[12] (D)	8.60 ± 0.30[13]	CO	
NGC 541	-3.6	2-1[9]	271.0 ± 43.2	32 ± 5[14] (D)	8.59 ± 0.34[15]	ionised gas	Omitted
NGC 1068	3.0	1-0[16]	288.8 ± 24.2	35 ± 8[2] (B)	6.92 ± 0.25[17]	masers	
NGC 1497	-2.0	1-0[4]	587.0 ± 28.2	85 ± 5[18] (M)	8.63 ± 0.19[15]	ionised gas	
NGC 1667	5.0	1-0[16]	408.6 ± 17.7	40 ± 8[2] (B)	8.20 ± 0.23[15]	ionised gas	
NGC 1961	4.2	1-0[4]	429.5 ± 8.0	46 ± 7[2] (B)	8.29 ± 0.34[15]	ionised gas	
NGC 2273	0.9	1-0[19]	348.8 ± 43.3	58 ± 4[2] (B)	6.93 ± 0.04[20]	masers	
NGC 2911	-2.0	1-0[4]	549.5 ± 41.1	63 ± 5[2] (B)	9.09 ± 0.29[15]	ionised gas	
NGC 3384	-2.6	2-1[21]	172.0 ± 24.8	62 ± 5[22] (K)	7.03 ± 0.21[23]	stars	Omitted
NGC 3665	-2.1	1-0[11]	632.7 ± 41.5	70 ± 1[24] (M)	8.76 ± 0.09[24]	CO	
NGC 3862	-4.8	1-0[9]	212.1 ± 13.7	15 ± 15[25] (D)	8.41 ± 0.37[15]	ionised gas	Omitted
NGC 4388	2.8	1-0[16]	304.6 ± 26.9	90[2] (B)	6.86 ± 0.04[20]	masers	
NGC 4429	-0.8	1-0[11]	521.7 ± 14.8	66.8 ± 0.2[26] (M)	8.17 ± 0.03[26]	CO	
NGC 4459	-1.6	1-0[27]	387.3 ± 50.2	46 ± 2[12] (D)	7.84 ± 0.09[28]	ionised gas	
NGC 4486	-4.3	1-0[9]	421.3 ± 47.1	42 ± 5[29] (K)	9.58 ± 0.10[30]	ionised gas	
NGC 4526	-1.9	1-0[27]	673.8 ± 30.1	79 ± 3[31] (M)	8.65 ± 0.29[31]	CO	
NGC 4593	3.0	1-0[16]	368.1 ± 34.4	35 ± 6[2] (B)	6.86 ± 0.21[32]	reverberation	

Table 4.4: (continued) CO data, best-fitting line widths and host galaxy properties for our spatially-unresolved galaxies. All galaxies listed have well-determined CO line widths, but a few are excluded from the final correlations. These omissions are justified in Section 4.4.3.

Name	T-type	CO transition	W_{50} ($\mathrm{km\,s^{-1}}$)	Inclination (°)	$\log(M_{\mathrm{BH}}/\mathrm{M}_\odot)$	SMBH method	Notes
(1)	(2)	(3)	(4)	(5)	(6)	(7)	(8)
NGC 5548	0.4	1-0[16]	212.8 ± 31.0	41 ± 6[2] (B)	7.70 ± 0.13[33]	reverberation	
NGC 7052	-4.9	1-0[9]	683.7 ± 81.5	75 ± 1[34] (M)	9.41 ± 0.05[34]	CO	
UGC 3789	1.6	1-0[35]	271.1 ± 33.1	43 ± 5[2] (B)	6.99 ± 0.09[20]	masers	

Notes: Column 1 lists the name of each galaxy contained in the final sample of spatially-unresolved galaxies. The morphological classification on the numerical Hubble scale from HyperLEDA is listed in Column 2. Column 3 indicates the CO transition observed. Column 4 lists the (line-of-sight projected) line width and associated uncertainty measured from a Gaussian double peak line profile fit to this spectrum. Column 5 lists the inclination of the CO disc and in parentheses the method used to measure it (D - dust morphology, M - molecular gas morphology/kinematics, B - *B*-band apparent flattening, K - other kinematics). Column 6 lists the dynamically-measured SMBH mass using the tracer (or via a Virial estimate for reverberation mapping) listed in Column 7. Column 8 contains other notes about certain galaxies. Footnotes in column 3 indicate the source of the CO observations, and those in columns 6 and 7 the source of the measurement, as follows. **References:** (1) Evans et al. (2005), (2) HyperLEDA, (3) Kollatschny et al. (2014), (4) this work, IRAM project 191-18, (5) this work, from a *HST* ACS/HRC F550M image, (6) Doroshenko et al. (2008), (7) Bertram et al. (2007), (8) Peterson et al. (2004), (9) Ocaña Flaquer et al. (2010), (10) North et al. (2019), (11) Young et al. (2011), (12) Cappellari et al. (2006), (13) Smith et al. (2019), (14) this work, from a *HST* WFPC2 F814W image, (15) Beifiori et al. (2012), (16) Maiolino et al. (1997), (17) Lodato & Bertin (2003), (18) Davis et al. (2016), (19) Heckman et al. (1989), (20) Kuo et al. (2011), (21) Welch & Sage (2003), (22) Cappellari et al. (2013a), (23) Schulze & Gebhardt (2011), (24) Onishi et al. (2017), (25) this work, from a *HST* WFPC2 F606W image, (26) Davis et al. (2018a), (27) Combes et al. (2007), (28) Sarzi et al. (2001), (29) Ford et al. (1994), (30) Walsh et al. (2013), (31) Davis et al. (2013b), (32) Barth et al. (2013), (33) Kovačević et al. (2014), (34) Smith et al. (2021b) and (35) this work, OSO 20-m project 2018-04a.

4.3.2 Correlation fits

Given our derived line widths, and the associated SMBH masses and stellar velocity dispersions, we now investigate the correlations between these parameters. We use the `HYPER-FIT` package (Robotham & Obreschkow, 2015) via its web interface[6] to fit both line width to SMBH mass and line width to stellar velocity dispersion. `HYPER-FIT` seeks to maximise the likelihood function that takes into account the multivariate Gaussian uncertainties on each data point, and allows for the possibility of intrinsic scatter. The use of this approach, in contrast to the traditional forward and/or reverse fits used in many Tully-Fisher relation works (e.g. Tiley et al., 2016), allows us to include the significant uncertainties on both $M_{\rm BH}$ and W_{50}, and to minimise the scatter orthogonal to the best-fitting line (rather than only the vertical or horizontal scatter).

To reduce the covariance between the slope and the intercept, and the error in the intercept, we follow the approach of Tremaine et al. (2002), as is now common practice, and translate the data to bring the median line width closer to zero. We therefore translate the line widths by 2.7 dex and fit the general function

$$y = a\left[\log\left(\frac{W_{50}}{\sin i\,\mathrm{km\,s^{-1}}}\right) - 2.7\right] + b\,, \tag{4.5}$$

where the variable y is an observable quantity - for this work either the SMBH mass or the stellar velocity dispersion. We also determine the total scatter as the root-mean-square deviation (along the y-axis) of the data from the best-fitting relation assuming zero measurement errors. Anticipating that the principal application for these relations will be estimating $M_{\rm BH}$ from a measured $\Delta V_{\rm CO}$, we use the projection of the intrinsic scatter onto the y-axis to quantify the tightness of each fit.

We omit from the fits a small number of galaxies that, although having well-constrained SMBH masses and sufficiently double-horned line profiles to yield a robust measurement of W_{50}, are nevertheless not considered sufficiently reliable to use. These are indicated in Tables 4.3 and 4.4 and are discussed in detail in Section 4.4.3.

[6] http://hyperfit.icrar.org/

Table 4.5: Best-fitting correlations, based on HYPER-FIT fits of Equation 4.5.

Dataset	Count	a	b	Total scatter	Intrinsic scatter
(1)	(2)	(3)	(4)	(5)	(6)
SMBH mass ($y \equiv \log[M_{\rm BH}/{\rm M}_\odot]$; Figure 4.3):					
Resolved data	25	8.5 ± 0.9	7.5 ± 0.1	0.6	0.5 ± 0.1
Unresolved data	21	10.5 ± 2.3	7.6 ± 0.2	0.9	0.8 ± 0.2
All data	39	9.2 ± 1.1	7.6 ± 0.1	0.7	0.7 ± 0.1
Resolved ETGs	16	8.7 ± 1.7	7.4 ± 0.3	0.6	0.6 ± 0.2
Unresolved ETGs	12	12.7 ± 4.1	7.3 ± 0.5	0.8	0.7 ± 0.3
All ETGs	21	10.0 ± 2.1	7.4 ± 0.3	0.8	0.7 ± 0.2
Resolved LTGs	9	10.0 ± 3.5	7.7 ± 0.2	0.5	0.4 ± 0.1
Unresolved LTGs	9	12.0 ± 9.4	7.8 ± 0.5	1.3	1.3 ± 1.0
All LTGs	18	10.2 ± 2.8	7.7 ± 0.3	0.8	0.8 ± 0.3
Stellar velocity dispersion ($y \equiv \log[\sigma_*/{\rm km\,s^{-1}}]$; Figure 4.4):					
Resolved data	25	1.1 ± 0.1	2.20 ± 0.02	0.09	0.09 ± 0.02
Unresolved data	21	0.9 ± 0.2	2.22 ± 0.02	0.09	0.08 ± 0.02
All data	39	1.1 ± 0.1	2.21 ± 0.02	0.10	0.10 ± 0.01
Resolved ETGs	16	1.0 ± 0.2	2.22 ± 0.03	0.08	0.07 ± 0.02
Unresolved ETGs	12	0.9 ± 0.3	2.22 ± 0.04	0.06	0.06 ± 0.02
All ETGs	21	1.0 ± 0.2	2.23 ± 0.03	0.08	0.07 ± 0.01
Resolved LTGs	9	1.0 ± 0.5	2.17 ± 0.05	0.11	0.10 ± 0.04
Unresolved LTGs	9	0.8 ± 0.6	2.21 ± 0.04	0.11	0.11 ± 0.04
All LTGs	18	1.1 ± 0.4	2.20 ± 0.04	0.12	0.11 ± 0.03

Notes: Column 1 lists each sample of galaxies, Column 2 the number of galaxies in that sample. Columns 3 and 4 list the parameters a and b, respectively, measured by fitting Equation 4.5 to the data of that sample with HYPER-FIT. Column 5 lists the total scatter, defined as the root-mean-square deviation along the y-axis between the data and the best-fitting relation, of that sample. Column 6 lists the intrinsic scatter, projected along the y-axis, of that sample.

Table 4.5 lists the results of our fits for both relations (discussed in Sections 4.3.3 and 4.3.4) and for two-different morphologically-selected sub-samples (ETGs and LTGs), in addition to our spatially-resolved and unresolved galaxy samples (and all data/galaxies taken together; see Section 4.4.1). Seven galaxies are included in both the resolved and unresolved samples, as there are both interferometric and single-dish observations available. The fits for 'all' galaxies use the line width with the smaller uncertainty only, almost always from the resolved observations.

In the following two subsections, we present our results for each correlation and

evidence for a morphological dependence. In Section 4.4, we describe the impacts of using spatially-resolved or unresolved data, compare our results with other host property correlations, and explore the implications of the $\Delta V_{\rm CO}-M_{\rm BH}$ correlation.

4.3.3 The $\Delta V_{\rm CO}-M_{\rm BH}$ correlation

Figure 4.3 shows the $\Delta V_{\rm CO}-M_{\rm BH}$ correlation of all our data and the best-fitting relation derived using only the galaxies with spatially-resolved observations. This is the tightest correlation we find, with

$$\log\left(\frac{M_{\rm BH}}{\rm M_\odot}\right) = (8.5\pm0.9)\left[\log\left(\frac{W_{50}}{\sin i\,\rm km\,s^{-1}}\right)-2.7\right]+(7.5\pm0.1)\,, \qquad (4.6)$$

with a total scatter in the $\log M_{\rm BH}$ direction of 0.6 dex, dominated by the intrinsic scatter of 0.5 dex.

The most significant systematic deviations from this fit are when we restrict the sample to LTGs. When we consider only the spatially-resolved LTGs, the slope steepens to 10.0 ± 3.5, in agreement with the results of Davis et al. (2019c) from H I and invoking the disc-halo conspiracy. The sample of unresolved LTGs do not adequately constrain the relation's slope, and exhibit a much higher total (and intrinsic) scatter. We discuss this deviation further in Section 4.4.1.

4.3.4 The $\Delta V_{\rm CO}-\sigma_*$ correlation

Figure 4.4 shows the $\Delta V_{\rm CO}-\sigma_*$ correlation using our data and the stellar velocity dispersions compiled by van den Bosch (2016). These velocity dispersions are those available in the literature that most closely approximate the dispersion within $1\,R_{\rm e}$.

We find that the dispersions are consistent with a linear relationship between CO line width and σ_* for all sub-samples. The best-fitting relation, from the sample of spatially-resolved observations of galaxies of all morphologies, is

$$\log\left(\frac{\sigma_*}{\rm km\,s^{-1}}\right) = (1.1\pm0.1)\left[\log\left(\frac{W_{50}}{\sin i\,\rm km\,s^{-1}}\right)-2.7\right]+(2.20\pm0.02)\,. \qquad (4.7)$$

There is a systematic trend of the intrinsic scatter with morphology, ETGs having an intrinsic scatter of 0.07 ± 0.02 dex in the $\log\sigma_*$ direction, whereas LTGs have 0.10 ± 0.04 dex.

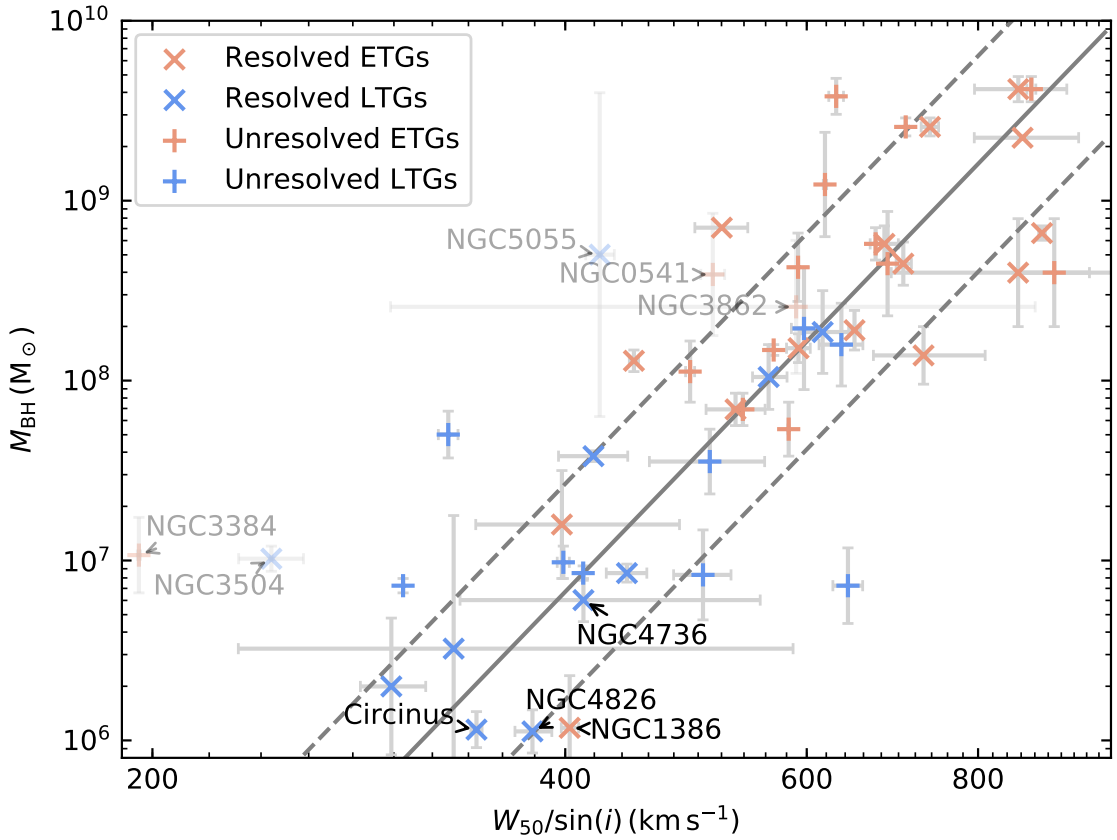

Figure 4.3: Correlation between deprojected line width ($W_{50}/\sin i$) and SMBH mass ($M_{\rm BH}$) for our sample galaxies. Colours indicate whether a galaxy is classified as early- (red) or late-type (blue), while the markers indicate whether it belongs to our spatially-resolved (×) or unresolved (+) sample. Some galaxies appear in both samples, and hence appear twice on this plot at the same $M_{\rm BH}$. Labelled galaxies are discussed in Section 4.4.3. The tightest correlation determined from the resolved sample is indicated by the dark grey solid line, with the 1σ intrinsic scatter indicated by the dashed dark grey lines. Error bars are shown in pale grey. Faded galaxies are excluded from the correlation fits.

The most recent works investigating $\Delta V_{\rm H\,I}-\sigma_*$ have also found morphologically-varying results. In ETGs, Serra et al. (2016) found a linear relation with total scatter of 12%, whereas in late-type spirals Davis et al. (2019c) excluded a linear relation, obtaining $\sigma_* \propto \Delta V_{\rm H\,I}^{1.55\pm0.25}$. This accords with the early work of Ho (2007a), that indicated that $\Delta V/\sigma_*$ varies systematically with Hubble-type, albeit with less compelling data. The literature on the $\Delta V_{\rm CO}-\sigma_*$ has not considered a potential morphological variation systematically.

We, however, find no significant deviation from a linear relation for either early- or late-type galaxies. This is perhaps surprising, as using the disc-halo conspiracy

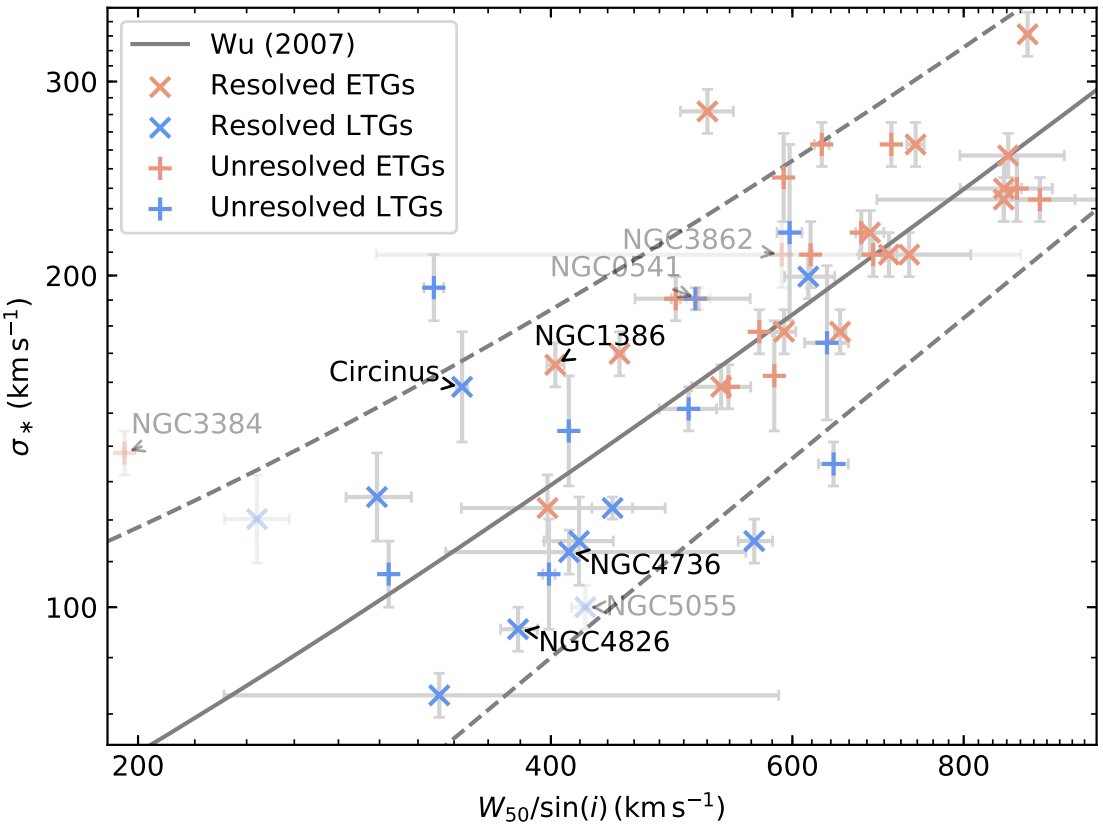

Figure 4.4: Correlation between deprojected line width ($W_{50}/\sin i$) and stellar velocity dispersion (σ_*) for our sample galaxies. Colours indicate whether a galaxy is classified as early- (red) or late-type (blue), while the markers indicate whether it belongs to our spatially-resolved ($\times$) or unresolved ($+$) sample. Some galaxies appear in both samples, and hence appear twice on this plot at the same σ_*. Labelled galaxies are discussed in Section 4.4.3. The best-fitting correlation found by Wu (2007) amongst local Seyfert galaxies is indicated by the solid dark grey line, with the 1σ intrinsic scatter indicated by the dashed dark grey lines. Error bars are shown in pale grey. Faded galaxies are excluded from the correlation fits.

for LTGs to equate $\Delta V_{\rm CO} = \Delta V_{\rm H\,I}$, the results of Davis et al. (2019c) would predict otherwise. The small intrinsic scatter for ETGs agrees with the results from JAM modelling of Cappellari et al. (2013a), that indicate a tight correlation between the rotation curve at these scales and σ_*.

4.4 Discussion

In this section we first discuss the benefits of using spatially-resolved rather than unresolved observations. We then evaluate the biases associated with our sample, account for the galaxies excluded from our fits, and finally discuss the utility of our correlations for estimating SMBH masses.

4.4.1 Spatially-resolved vs unresolved observations

In Section 4.2 we outlined the advantages of using spatially-resolved observations of the CO emission instead of single-dish observations. These advantages are clear in our results.

First, the spatially-resolved observations have much higher sensitivities. Since the uncertainties on our line width measurements are derived from Monte Carlo fits to simulated data with noise characteristic of the real spectra, these improved sensitivities lead to smaller line width uncertainties (of order $1 - 10\,\mathrm{km\,s^{-1}}$ rather than $10 - 50\,\mathrm{km\,s^{-1}}$), that are also smaller fractions of the channel widths. This in turn leads to best-fitting correlations with systematically smaller uncertainties. While present, the effect on the total scatters (dominated by the intrinsic scatters) is less significant.

Second, spatially-resolved kinematics enable improved sample selection, ensuring that galaxies with disturbed kinematics can be omitted more robustly. This reduces the measured intrinsic scatters in our $\Delta V_{\mathrm{CO}} - M_{\mathrm{BH}}$ and $\Delta V_{\mathrm{CO}} - \sigma_*$ correlations when only resolved observations are used.

Third, the relatively small primary beams of large single-dish observations (e.g. $22''$ for the IRAM 30-m telescope at ^{12}CO(1-0)) mean that observations may not reach the flat parts of the rotation curves of nearby galaxies. In spatially-resolved observations, not only do we benefit from the larger primary beams of the smaller individual antennae (e.g. $55''$ for ALMA's 12-m dishes at ^{12}CO(1-0)), but pointing errors can also be straightforwardly diagnosed.

We briefly note that, in addition to the primary beam, another spatial scale generally relevant for interferometric observations is the maximum resolvable scale, i.e. the largest spatial structure to which an array configuration is sensitive, set by the shortest baseline of the array. However, CO emission is generally patchy, and thus most of it generally remains detectable even when only an extended array configuration is used. In addition, as the emission of a rotating disc extends only over a small spatial scale in any given channel (typically of the order of the disc

minor axis along one direction only), we are likely to recover (most of) it all the way to the flat part of the rotation curve, provided the emission extends that far.

We have also argued that a sharp-edged double-horned line profile arises from an emitting exponential disc that reaches the flat part of the rotation curve. However, such a profile can also occur if the disc is sharply truncated, whether the flat part is reached or not. If such a disc is truncated before the flat part, the measured line width will be strictly narrower than would be found if the disc extended further. Similarly, if the primary beam is too compact to reach the flat part, the measured line width will be artificially narrowed.

In each spatially-resolved sample galaxy, we can easily assess whether the CO emission reaches the flat part of the rotation curve by examining the kinematic major-axis position velocity diagram, and thus straightforwardly determine whether the primary beam is too small to recover all of the emission. For each of our spatially-unresolved sample galaxies, we assess this issue as follows. As low-J CO emission generally follows dust, the extent of the dust disc in *HST* optical images can be assumed to be the same as that of the CO emission. Although some of these galaxies have dust extending to larger radii than would be reached by the primary beams of our single-dish telescopes, we have verified that these galaxies do not exhibit systematically narrower line profiles. However, the galaxies with the smallest dust extents ($\lesssim 0.02\,R_{25}$, where R_{25} is the radius of the $25\,{\rm mag\,arcsec^{-2}}$ B-band isophote listed in HyperLEDA) are biased to narrower line widths. We therefore exclude them from this sample.

Notwithstanding the concerns described above, we do not find a statistically-significant difference between the correlations determined from the spatially-resolved and unresolved samples, and Figure 4.3 further indicates that the unresolved ETGs follow the relation of all resolved galaxies closely; the significant outliers are all sufficiently explained in Section 4.4.3 as resulting from observations of CO emission that may not reach the flat part of the rotation curve. The only substantial discrepancy is found for the $\Delta V_{\rm CO}-M_{\rm BH}$ relation using unresolved LTGs, with a much greater uncertainty in the slope (and to a lesser extent in the zero point)

and significantly larger intrinsic scatter than those of all resolved data and ETGs. These galaxies are likely to be preferentially affected by the aforementioned issues, as they are systematically nearer and have more slowly rising rotation curves. It is therefore unsurprising that we find greater uncertainties in their best-fitting parameters and a larger intrinsic scatter. Interestingly, the spatially-resolved LTG sample, for which we can exclude galaxies with disturbed kinematics, actually exhibits a slightly smaller intrinsic scatter.

For all the reasons discussed above, we conclude that spatially-resolved observations are to be preferred when calibrating (and using) the $\Delta V_{\rm CO}-M_{\rm BH}$ correlation. We further suggest that the improvements offered by the use of spatially-resolved observations have wider applicability, particularly when calibrating the CO TFR. Interferometric observations in the ALMA era will therefore allow sample selections significantly more robust than was previously possible, with associated improvements of the accuracy of the slopes, zero-points and intrinsic scatters of the determined relations.

4.4.2 Selection biases

Our sample was selected from galaxies with dynamically-measured SMBH masses in the literature and CO observations, and thus cannot be considered a statistically-representative sample of galaxies. Shankar et al. (2016) discussed the biased population of galaxies with dynamical SMBH mass measurements, due to the need to resolve the scales on which the SMBH dominates the potential. Additionally, the SMBH mass measurements and CO observations are highly heterogenous, being derived using different dynamical tracers and resolving different physical scales for the former, and with different primary beams, spectral resolutions and sensitivities for the latter.

The heterogenous CO observations have all been homogenised following the prescriptions discussed in Sections 4.2.1 and 4.2.2. These procedures do not bias our conclusions regarding the correlations, but the selection of only sharp-edged

double-horned profiles arguably limits the applicability of the correlations to similar CO spectra only.

The SMBH masses used in this chapter are drawn from the large variety of measurements available in the literature. Due to the differing selection criteria, very few SMBH mass measurements have been cross-checked with multiple tracers and/or methods, and those that have suggest mass measurements can vary by factors of 2–4 (e.g. Kormendy & Ho, 2013). Figure 4.5 shows the variety of mass measurement methods used. Maser dynamics are, in principle, the most precise method as masers probe the spatial scales closest to the SMBHs, while the uncertainty in the scaling factor used in reverberation mapping (f; meant to account for the broad-line region geometry and line-of-sight velocity dispersion anisotropy) implies these measurements are generally the least reliable (e.g. Pancoast et al., 2014; Mejía-Restrepo et al., 2018; Campitiello et al., 2020). The associated SMBH mass uncertainties are taken into account by the `HYPER-FIT` routine, so that lower-quality measurements do not bias our results. Although it would be preferable to use homogeneously-measured SMBH masses, to impose this requirement would excessively reduce the sample size.

The $M_{\rm BH}-\sigma_*$ relation is the tightest known correlation between SMBH mass and host property, and it is customarily interpreted as indicating the primary co-evolutionary path for SMBH growth. Galaxies that are outliers on the $M_{\rm BH}-\sigma_*$ plane are therefore likely to have had unusual evolutionary pathways, and it is unlikely they will follow other host–SMBH correlations. Since we argued in Section 4.1.2 that the CO line width of a galaxy traces the same baryonic matter as σ_*, any galaxy that genuinely deviates from the $M_{\rm BH}-\sigma_*$ relation is also likely to deviate from the $\Delta V_{\rm CO}-M_{\rm BH}$ relation. Galaxies consistent with only one of these relations may be genuine outliers, or may indicate one of the quantities has been incorrectly measured.

Figure 4.6 shows the $M_{\rm BH}-\sigma_*$ relation for our sample galaxies. A few galaxies are clearly outliers and are discussed in Section 4.4.3. The remainder of the sample galaxies all follow the empirical $M_{\rm BH}-\sigma_*$ relation and are not significantly biased in their distribution in the $M_{\rm BH}-\sigma_*$ plane. We do not, however, sample

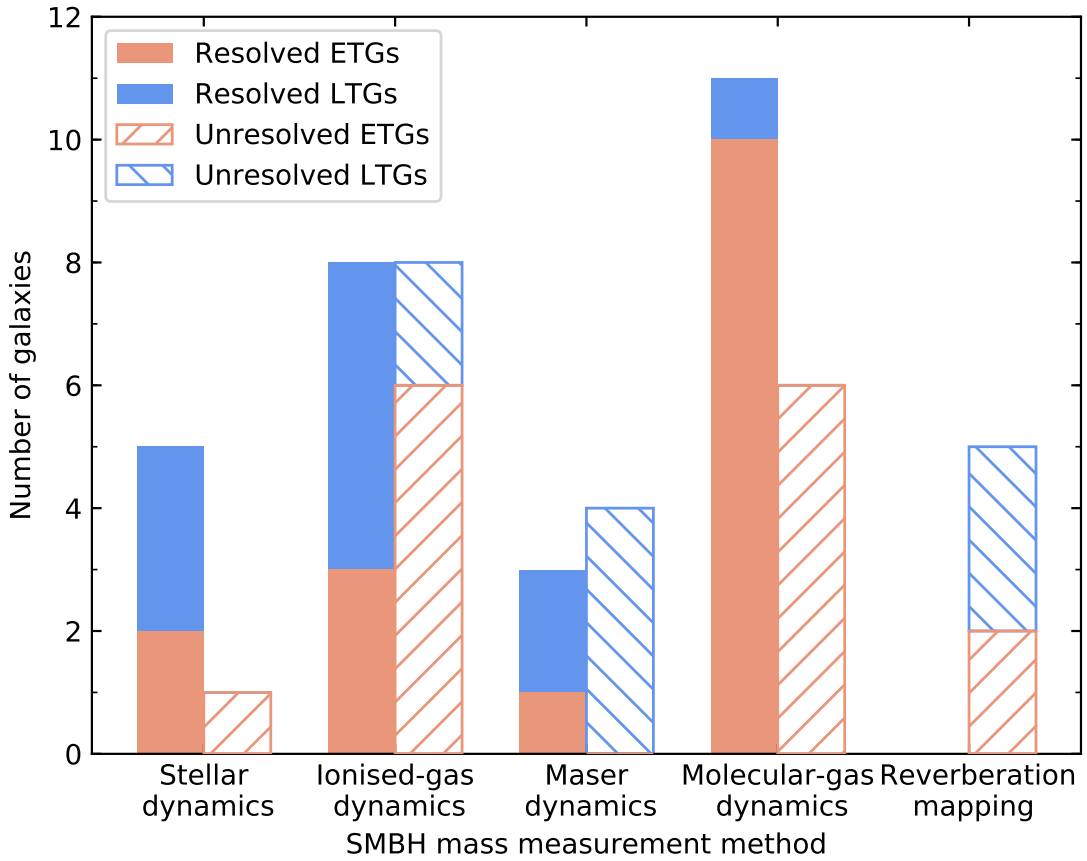

Figure 4.5: SMBH mass measurement methods of our sample galaxies. Early-type galaxies are shown in red, late-type galaxies in blue. The spatially-resolved sample is shown in solid colour, the unresolved sample as hatched areas. Galaxies appear in both resolved and unresolved samples for a given method where both interferometric and single-dish observations exist.

the significant population of galaxies with $\sigma_* < 100\,\mathrm{km\,s^{-1}}$, for which very few SMBH masses are available, and that appear to deviate from the $M_{\mathrm{BH}}-\sigma_*$ relation (e.g. van den Bosch, 2016).

Our samples are necessarily biased towards CO-bright galaxies. The CO content of a galaxy varies with morphology, the latest representative surveys finding that only about 20−30% of ETGs host detectable molecular gas reservoirs (Combes et al., 2007; Young et al., 2011). However, this detection rate is independent of mass, size and environment, suggesting that CO-rich ETGs are 'normal' ETGs (Davis et al., 2019a). CO emission is also detected in ≈85% of LTGs (Young et al., 1995; Saintonge et al., 2017). As a result, our samples encompass a wide range of morphologies, as shown in Figure 4.7.

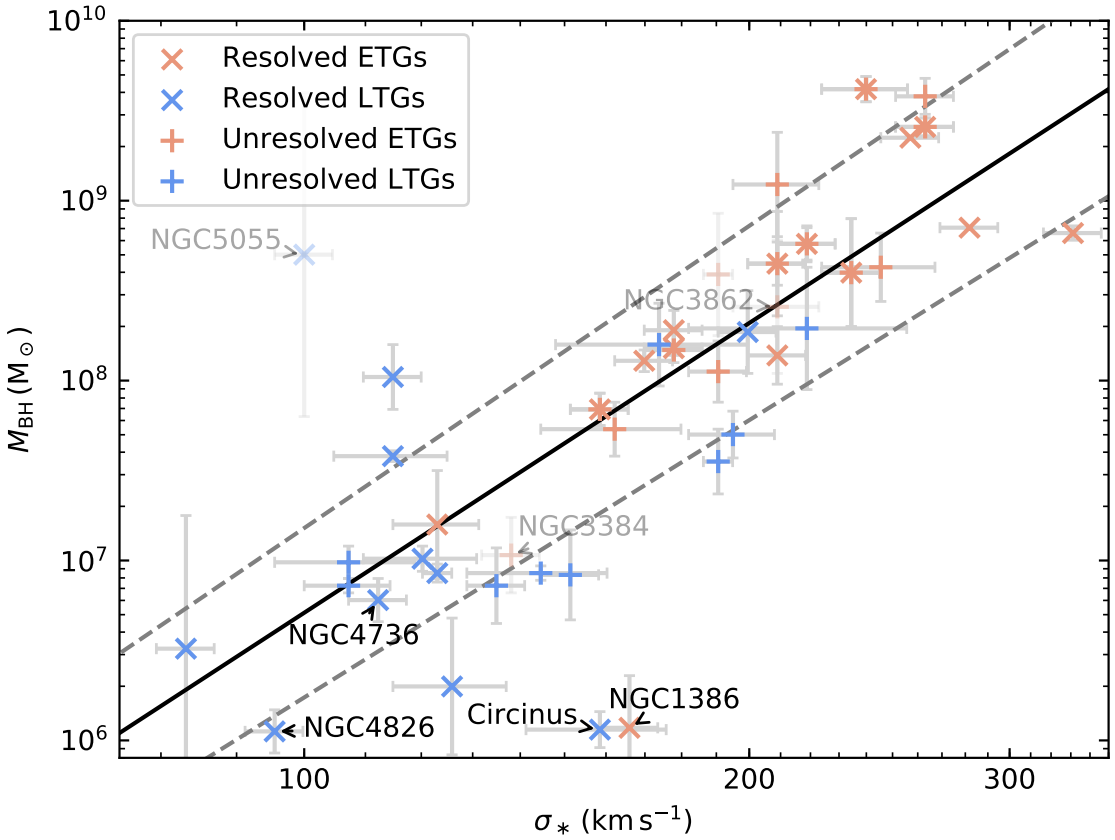

Figure 4.6: Correlation between stellar velocity dispersion (σ_*) and SMBH mass (M_{BH}) for our sample galaxies. Colours indicate whether a galaxy is classified as early- (red) or late-type (blue), while the markers indicate whether it belongs to our spatially-resolved (×) or unresolved (+) sample. Some galaxies appear in both samples, and hence are indicated with both symbols superimposed. The $M_{BH}-\sigma_*$ relation found by van den Bosch (2016) is indicated by the solid black line, with the 1σ intrinsic scatter indicated by the dashed dark grey lines. Labelled galaxies are discussed in Section 4.4.3. Error bars are shown in pale grey. Faded galaxies are excluded from the correlation fits.

In Sections 4.3.3 and 4.3.4 we discussed whether our results depend on galaxy morphology. We adopted the HyperLEDA morphological classifications on the numerical Hubble scale, and classified galaxies with T-types less than or equal to 0 as ETGs and the others as LTGs. The morphological type distribution of our sample is illustrated in Figure 4.7 by colour and the solid vertical line.

Our samples are thus necessarily limited by the existing biases in the SMBH masses that have been measured, and to galaxies with CO emission. Nevertheless, we do not find evidence of a systematic deviation in the $\Delta V_{CO}-M_{BH}$ correlation as a function of morphology, but do caution that this issue requires further study

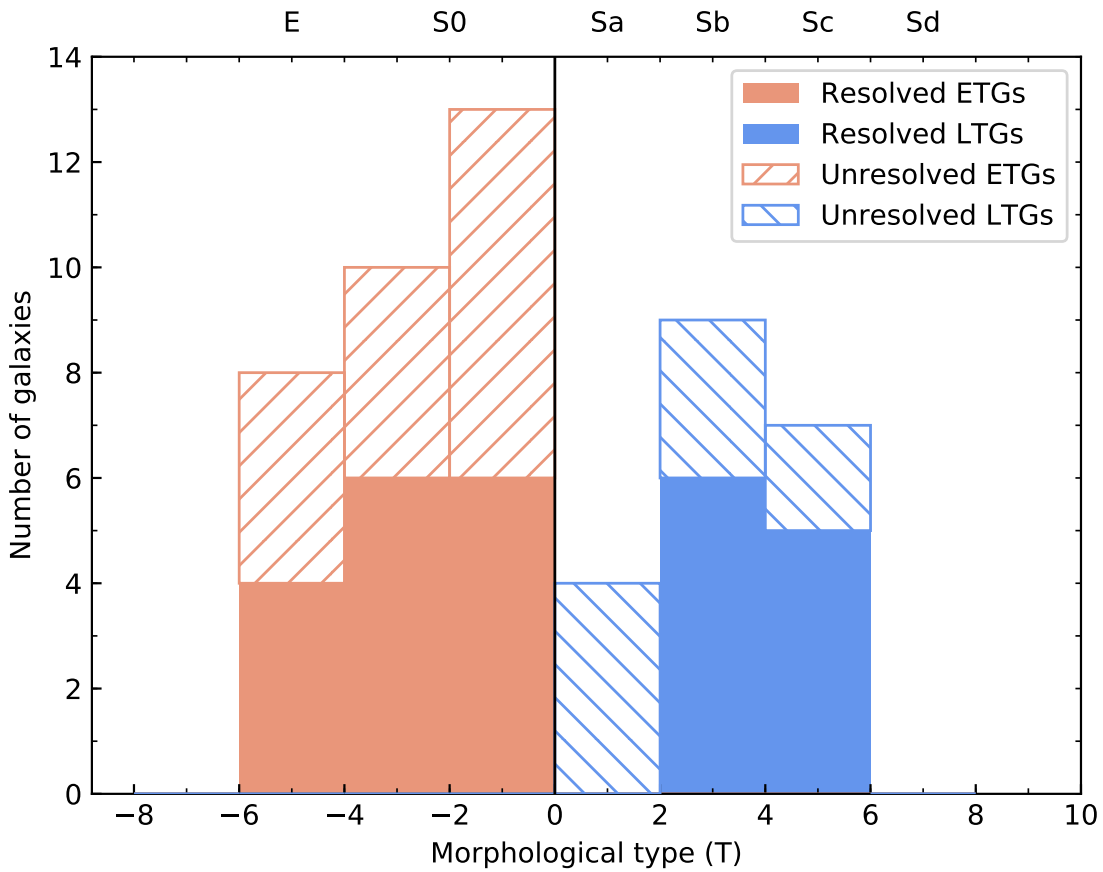

Figure 4.7: Morphological type distribution of our sample galaxies, according to the numerical Hubble type listed in HyperLEDA, with $T \leqslant 0$ classified as early type and $T > 0$ as late type.

going beyond the coarse classification used here.

4.4.3 Outliers

We have excluded a few galaxies from our fits even though they have well-resolved and sharp-edged CO lines and dynamically-measured SMBH masses. Each of these is indicated in Tables 4.3 and 4.4 and is discussed below.

Three galaxies in our samples are known to be outliers in the $M_{\rm BH}-\sigma_*$ relation: Circinus, NGC 1386 and NGC 5055. The former two galaxies have SMBH measurements too small for their associated velocity dispersions by about an order of magnitude. However, they are consistent with our $\Delta V_{\rm CO}-M_{\rm BH}$ relation, their positions on the $\Delta V_{\rm CO}-\sigma_*$ relation (Figure 4.4) compensating. For Circinus, Davis et al. (2019c) find a similar behaviour using $\Delta V_{\rm H\,I}$, and suggest its central

stellar velocity dispersion may be anomalous. We therefore elect to include both galaxies in our fits.

NGC 5055 has a SMBH mass measurement too large by around two orders of magnitude compared to that predicted from either the $M_{\rm BH}-\sigma_*$ relation or our $\Delta V_{\rm CO}-M_{\rm BH}$ correlation. This mass is based on Fabry-Perot spectroscopy taken at the Canada-France-Hawaii Telescope (Blais-Ouellette et al., 2004), in which the central 300 pc exhibits dual velocity components, one consistent with the overall galactic rotation, the other with a counter-rotating disc (from which the SMBH mass is derived) or a bipolar outflow. As this SMBH mass is suspect (see Graham, 2008), we exclude this object from our fits.

We also omit the dwarf galaxy NGC 3504, which is an outlier from the $\Delta V_{\rm CO}-M_{\rm BH}$ relation. As the only dwarf galaxy in the sample it would otherwise have a disproportionate effect on the determined slope and scatter, and dwarfs do not appear to follow the other SMBH–host galaxy property correlations (see e.g. Figure 1 of van den Bosch 2016).

In the unresolved sample, we omit NGC 541, NGC 3384 and NGC 3862. NGC 541 has the most compact dust disc of the galaxies observed, extending to only 0.01 R_{25}, and a narrow line width consistent with our discussion in Section 4.4.1. There is no dust disc visible in NGC 3384, but the CO line width is very narrow. NGC 3862 has a dust disc of only 0.02 R_{25} that is also nearly face-on, implying that the inclination uncertainties are very large.

NGC 4736 and NGC 4826 are both outliers from the fundamental plane and were therefore excluded from previous fundamental plane parameter – SMBH mass correlations (van den Bosch, 2016). However, they appear consistent with both correlations investigated in this chapter, and with the $M_{\rm BH}-\sigma_*$ relation, so they are included in this work.

Finally Mrk 590, NGC 524 and NGC 4303 all have inclinations below 30°. Studies of the Tully-Fisher relation exclude galaxies at such low inclinations (e.g. Tully & Fisher, 1977; Pierce & Tully, 1988; Davis et al., 2011; Tiley et al., 2016; Topal et al., 2018). This is because customary approaches to measuring inclination,

such as fitting ellipses to features assumed to be intrinsically circular, respond only weakly to varying inclinations at $i \approx 0°$, but the line-of-sight projected velocity responds strongly ($v_{\rm los} \propto \sin i$). In our work, we allow these galaxies to remain (and omit to label them in Figures 4.3, 4.4, and 4.6) as the large uncertainties have been propagated through, and thus these galaxies have low statistical weights.

4.4.4 Comparison with other correlations

The best-fitting correlations for our samples (Table 4.5) can be compared to the extensive literature on other correlations. Correlations between $\Delta V_{\rm H\,I}$ at halo scales and either $M_{\rm BH}$ or σ_* have already been discussed in Sections 4.3.3 and 4.3.4, so we only briefly summarise these findings before considering other correlations.

We find a close correlation between $\Delta V_{\rm CO}$ and $M_{\rm BH}$, as would be expected from the simple arguments presented in Section 4.1.2. We find a steeper slope for LTGs than for ETGs; the LTG result is in agreement with the slope and intrinsic scatter found using H I line widths (Davis et al., 2019c). When computing a single relation for galaxies of all morphologies, we obtain an intrinsic scatter of 0.5 ± 0.1 dex, identical to that found using H I in the equivalent sample of Beifiori et al. (2012).

We find a linear $\Delta V_{\rm CO} - \sigma_*$ correlation regardless of galaxy morphology. For ETGs, this agrees with the H I results of Serra et al. (2016), even though we cannot assume a baryon-halo conspiracy holds. However, contrary to us, Davis et al. (2019c) exclude a linear relation in LTGs. Wu (2007) fit a linear relation to local Seyferts, leading to larger uncertainties in the coefficients, but did not estimate the scatter. We fit the line widths measured by Wu (2007), that are also FWHM but are not based on profile fits, with Equation 4.5, yielding the best-fitting parameters $a = 0.71 \pm 0.12$ and $b = 2.21 \pm 0.02$, with a total scatter of 2.1 dex, of which the intrinsic scatter is 0.13 ± 0.02 dex. The total scatter is dominated by the large uncertainties of the sample stellar velocity dispersions. Our intrinsic scatters are similarly small, although we do not have a Seyfert galaxy sample to directly compare.

The tightest correlations between SMBH masses and host properties have intrinsic scatters comparable to ours. The careful analysis of Kormendy & Ho

(2013) showed that for classical bulges and ellipticals, the $M_{\rm BH}$–σ_* relation has an intrinsic scatter of 0.29 dex. Using a less rigorously selected and larger sample of galaxies, Beifiori et al. (2012) determined a total scatter of 0.41 ± 0.06 dex, dominated by the intrinsic scatter of 0.36 ± 0.07 dex. Our tightest correlation is for spatially-resolved galaxies, with a total scatter of 0.6 dex, that is also dominated by the intrinsic scatter of 0.5 dex.

The other major bulge correlations are those with bulge luminosity and mass. Beifiori et al. (2012) determined intrinsic scatters of 0.58 ± 0.11 dex and 0.46 ± 0.07 dex, respectively, while Kormendy & Ho (2013) found 0.3 dex and 0.28 dex, respectively. Our results are thus comparably tight to the bulge correlations.

Looser $M_{\rm BH}$–host property correlations, including those with Sérsic index (Graham & Driver, 2007; Davis et al., 2017b), spiral arm pitch angle (Seigar et al., 2008; Davis et al., 2017b) and total galaxy light or mass (Jahnke et al., 2009; Bennert et al., 2010; Merloni et al., 2010; Davis et al., 2018b), have also been proposed and investigated over the last two decades. Beifiori et al. (2012) investigated several of these, finding typical intrinsic scatters of $0.5 - 0.6$ dex, similar to or slightly larger than our results.

We therefore conclude that the correlations we have probed are at least no worse than many of the correlations well-established in the literature. However, our $M_{\rm BH}$–$\Delta V_{\rm CO}$ correlation is not so tight as to outperform those commonly used to estimate SMBH masses. In the absence of a measurement of σ_*, and where a bulge decomposition is either too difficult or too laborious, use of the CO line width is thus a competitive estimator of a galaxy's SMBH mass.

4.4.5 Utility for estimating SMBH masses

To illustrate the use of CO line widths as SMBH mass estimators, we construct a SMBH mass function (see review by Kelly & Merloni 2012) from the Tiley et al. (2016) sample of 207 CO(1-0) line widths, that were measured in a manner identical to that in this work. These observations were originally obtained as part of the COLD GASS survey (Saintonge et al., 2011), with the IRAM 30-m

telescope. The sample is purely mass-selected to be representative of galaxies in the local universe with $\log(M_*/\mathrm{M}_\odot) > 10$, that corresponds to $M_{\mathrm{BH}} \gtrsim 10^{6.8}\,\mathrm{M}_\odot$ using the correlation of Beifiori et al. (2012). The Tiley et al. (2016) sample also contains some galaxies below $10^{10}\,\mathrm{M}_\odot$, that were later published in the extended COLD GASS survey (xCOLDGASS; Saintonge et al. 2017), but are not necessarily statistically-representative of these galaxies. Removing the galaxies with stellar masses less than $10^{10}\,\mathrm{M}_\odot$ makes only a marginal change to the derived SMBH mass function (and this only at $M_{\mathrm{BH}} < 10^{6.8}\,\mathrm{M}_\odot$), even though it makes a substantial change to the expected distribution of galaxies in a volume-limited sample.

The parent COLD GASS sample was selected to be flat in $\log(M_*)$, although the need for robust double-horned profiles implies that the sample of Tiley et al. (2016) does not exactly match this criterion (see the top panel of Figure 4.8). Nevertheless, we need to weight the sample to match a representative galaxy stellar mass function. We adopt the approach described by Catinella et al. (2018), whereby we assume the local galaxy stellar mass function of Baldry et al. (2012), predict the number of galaxies in a volume-limited sample of equal size in 0.2 dex stellar mass bins, and weight the SMBH masses predicted from the CO line widths by the ratio of these predictions to the actual number of galaxies in each bin. The estimated SMBH mass function is shown in the lower panel of Figure 4.8.

The mass function estimated from our correlation shows good agreement with that estimated by Shankar et al. (2009) from the AGN luminosity function assuming a fixed radiative efficiency $\eta = 0.065$ and bolometric-to-Eddington luminosity ratio $L_{\mathrm{bol}}/L_{\mathrm{Edd}}$=0.45. Significant deviations occur at SMBH masses greater than $10^9\,\mathrm{M}_\odot$, but we note that each populated bin at $M_{\mathrm{BH}} > 10^9\,\mathrm{M}_\odot$, in addition to the $10^{8.2} - 10^{8.4}\,\mathrm{M}_\odot$ bin that lies substantially below the Shankar et al. (2009) results, is based on only a single galaxy and therefore has a large associated uncertainty. In addition, the SMBH masses in the sample used for our $\Delta V_{\mathrm{CO}} - M_{\mathrm{BH}}$ correlation poorly sample these most massive SMBHs (see e.g. Figure 4.3). Furthermore, for $M_{\mathrm{BH}} > 10^{10}\,\mathrm{M}_\odot$, the $M_{\mathrm{BH}}-\sigma_*$ relation appears to saturate (e.g. Gültekin et al., 2009b; McConnell & Ma, 2013; Krajnović et al., 2018). We have no SMBH in this

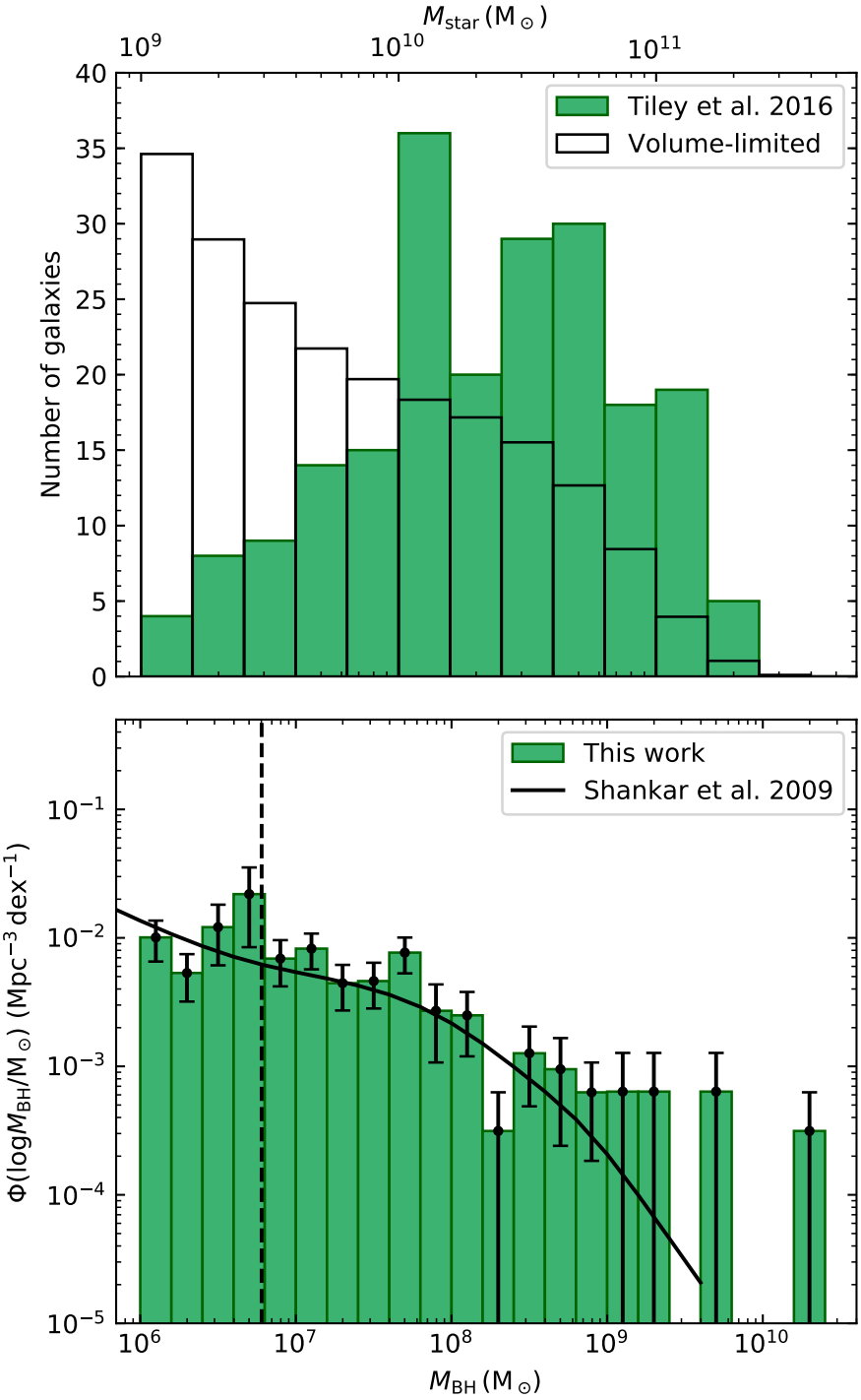

Figure 4.8: Top panel: Galaxy stellar mass function of the Tiley et al. (2016) sample drawn from COLD GASS (green histogram), and of a purely volume-limited sample of equal size following the galaxy stellar mass function of Baldry et al. (2012) (black histogram). **Bottom panel:** Local SMBH mass function derived from the Tiley et al. (2016) sample and our $\Delta V_{CO} - M_{BH}$ correlation (green histogram) and that determined by Shankar et al. (2009) from the local AGN luminosity function (solid black line). Error bars are given by the square-root of the sum of the squared weights. The vertical dashed line indicates the SMBH mass corresponding to the 10^{10} M$_\odot$ stellar mass limit of the COLD GASS sample, assuming the correlation of Beifiori et al. (2012), below which we expect our sample to be incomplete.

regime in our sample, and so cannot determine whether our correlation continues to hold or not at these masses.

Naturally, estimating a SMBH mass function requires a very careful analysis of potential biases in the underlying sample; that is beyond the scope of this thesis. We highlight the morphological biases in the CO detection fraction, and the integration limit of the COLD GASS sample of $M_{\rm H_2}/M_* = 0.015$, as factors we have not controlled for here. Nevertheless, the agreement with the Shankar et al. (2009) result is encouraging, particularly since their result arises from accretion physics and a photometric measurement while ours arises from dynamical measurements.

4.5 Conclusions

CO line emission has previously been used as a tracer of the central parts of galaxy rotation curves, including for the Tully-Fisher relation. The CO discs typically do not extend to halo-dominated radii, and thus in any given galaxy the width of the CO line probes the stellar potential, analogously to the central stellar velocity dispersion σ_*. Although in a LTG one might suppose that the 'disc-halo conspiracy' implies that the CO line width measures a flat rotation velocity equivalent to that measured with neutral gas, the same has not been shown for ETGs. The CO line width has however previously been used as a proxy for the stellar velocity dispersion, that is often hard to measure and is strongly affected by both dust extinction and finite apertures.

In this chapter, we proposed a correlation between SMBH masses and CO line widths. We investigated this correlation using two samples of galaxies with CO line emission. The first is comprised of galaxies with synthesised spectra from spatially-resolved observations, with generally very high signal-to-noise ratios (SNRs). These spectra were constructed by summing emission within a mask defined from a smoothed version of the original data cube. The second sample is comprised of galaxies with single-dish observations, either from the literature or from new observations conducted at the IRAM 30-m and OSO 20-m telescopes. All the galaxies used have robust dynamical SMBH mass measurements.

Each CO line width was measured as the FWHM of a profile fit using a Gaussian double peak profile, that has been previously shown to recover well the intrinsic widths of noisy double-horned spectra arising from rotating discs. The line width uncertainties were estimated by Monte Carlo sampling from the determined parameter uncertainties.

We find a good correlation of the CO line widths with both SMBH masses and the central stellar velocity dispersions. There is some evidence that the SMBH mass correlation is steeper for LTGs, without increased scatter. However, the stellar velocity dispersion correlation exhibits a higher intrinsic scatter for LTGs than for ETGs. Using only the spatially-resolved sample yields tighter correlations, and we suggest that the lower SNRs and less robust selection of unresolved observations account for this.

The tightest correlation is found from our spatially-resolved sample as

$$\log\left(\frac{M_{\rm BH}}{\rm M_\odot}\right) = (8.5\pm0.9)\left[\log\left(\frac{W_{50}}{\sin i\,\rm km\,s^{-1}}\right)-2.7\right]+(7.5\pm0.1)\,, \qquad (4.8)$$

with a total scatter of 0.6 dex in the log $M_{\rm BH}$ direction, dominated by the intrinsic scatter of 0.5 dex. This intrinsic scatter is comparable to those found for other popular host property–SMBH mass correlations, and it is not dramatically worse than the 0.3 dex of intrinsic scatter in the SMBH masses conventionally adopted for the $M_{\rm BH}-\sigma_*$ relation.

We applied our adopted correlation to the CO line widths measured in the COLD GASS survey as part of previous CO Tully-Fisher relation studies, thereby estimating the galaxies' SMBH masses, and constructed a local SMBH mass function, correcting for the original sample's bias in stellar mass. We showed that our SMBH mass function thus derived is consistent with that estimated from the local AGN luminosity function.

We suggest that our correlation has significant value to estimate SMBH masses where the conventional proxies are unavailable. The CO observations required are simple to make and avoid the need for complicated bulge-disc decompositions. We have further shown that the use of resolved CO observations to generate synthesised

spectra dramatically improves the line width measurements. We also suggest that substantial improvements could be made in the CO Tully-Fisher relation by using (low-resolution) interferometric observations, such as those available with the Atacama Compact Array, as these observations allow more robust sample selection and the high SNRs yield significantly smaller line width measurement uncertainties.

5

Molecular gas dynamics in SMBH mass measurement candidates

Contents

5.1 Introduction

ALAXIES observed with the Atacama Large Millimeter/submillimeter Array (ALMA) as parts of the millimetre-Wave Interferometric Survey of Dark Object Masses (WISDOM) project form multiple sub-samples, each designed to address different questions pertaining to galaxy-SMBH co-evolution. The galaxies from these sub-samples most promising for a SMBH mass measurement were studied in the first papers of the WISDOM series. Notable sub-samples include spiral galaxies (ALMA programmes 2015.1.00466.S, 2016.1.00839.S and 2017.1.00277.S), maser galaxies (2016.1.01553.S), high-mass galaxies (2017.1.00904.S and 2017.1.00397.S), dwarf galaxies (2017.1.00572.S) and galaxies in under-sampled regions of the mass-size plane (2015.1.00419.S, 2016.1.00437.S and 2017.1.00391.S). When observations are delivered by the ALMA staff, members of the WISDOM

team produce 'quick-look' maps that show the CO emission and velocity field of each galaxy, to diagnose whether the molecular gas is regularly rotating and whether an obvious SMBH signature is detected. Galaxies with these features are then prioritised, and full analyses of two of these were presented in Chapters 2 and 3. In this chapter, we present additional observations reduced and imaged in this 'quick-look' manner in the course of this thesis, we discuss the dynamical features present, and we make rough estimates of the SMBH masses where possible.

In Section 5.2 we discuss general aspects of the data reduction of all these galaxies. In Section 5.3 we present the three maser galaxies observed in an attempt to cross-check molecular gas-derived SMBH masses. In Section 5.4 we discuss the significant non-circular motions observed in the spiral galaxy NGC 4501 (M88), and in Section 5.5 we present observations from our ALMA programme to probe the highest SMBH masses. We conclude briefly in Section 5.6.

5.2 Observations and data calibration

ALMA observations of the galaxies discussed in this chapter were obtained through a variety of programmes during Cycles 4–7 (2015–2019). Details of each observing track, including the observing date, on-source integration time, baseline lengths and calibration are tabulated in Table 5.1. Each galaxy was observed using a variety of configurations of the 12-m array to ensure adequate *uv*-plane coverage, and complementary shorter baseline observations were obtained for some galaxies using the 7-m Atacama Compact Array (ACA). The spectral set-ups mirror those used in Chapters 2 and 3, with three continuum spectral windows and one spectral window covering the ^{12}CO(2-1) emission line. The data were calibrated either automatically by the ALMA pipeline or manually by staff at one of the ALMA Regional Centres before delivery to the WISDOM team. Some antennae with calibration errors were subsequently manually flagged, as listed in Table 5.1.

The calibrated data were then restored (i.e. imaged) using the `Common Astronomy Software Application` (`CASA`; McMullin et al. 2007). Channels containing line emission were identified from the spectra for each track. The line-free channels

(including the three continuum spectral windows) from all tracks were then combined and imaged to measure the 1.3 mm continuum. In most cases, a single compact source was detected and fit with a two-dimensional (2D) Gaussian using the `CASA` task `imfit`, to measure the integrated flux and constrain the intrinsic size of the source. The exceptions are the galaxies NGC 3393, in which multiple compact sources were detected and fit, and NGC 5765b and Mrk 567, in which no continuum emission was detected.

The continuum emission was then fit in the *uv* plane over the full line-free bandwidth and subtracted from the line spectral window for each observing track individually. The continuum-subtracted *uv* data from all the tracks were then combined and imaged into a single data cube. The raw channels ($\approx$1 km s^{-1}) were then averaged into broader channels of 10 or 15 km s^{-1}, sufficient to resolve almost all the dynamical features in these galaxies while dramatically improving sensitivity.

The continuum images and CO line data cubes were all imaged with Briggs weighting, with a robust parameter (normally 0.5) selected to balance spatial resolution and sensitivity. Pixel scales were selected to over-resolve the synthesised beam by a factor of typically 3–5. Images and data cubes were then cleaned within a manually-defined mask to depths of 2–3 times the noise in a single channel.

Two-dimensional projections of the data cubes were made using the masked-moments method, to avoid including large numbers of noise-dominated pixels in the moment images. For each galaxy, a mask was generated by first convolving the cube spatially by the synthesised beam, then Hanning-smoothing it spectrally. All pixels above a given threshold (usually $0.6-0.8$ times the noise in the original cube) were then included in the mask, which was applied to the original unsmoothed cube. The gas distribution (moment 0), mean line-of-sight velocity field (moment 1) and line-of-sight velocity dispersion (moment 2) maps were then calculated from this masked cube. These maps are shown in figures throughout this chapter. Kinematic major-axis position-velocity diagrams (PVDs) were also constructed by applying a pseudo-slit across the masked cube. These are shown for the galaxies discussed in Sections 5.4 and 5.5.

Table 5.1: Observing track properties.

Galaxy	Programme	Track	Date	Array	Baseline range	On-source time	Calibration
NGC 1194	2016.1.01553.S	uid_A002_Xb9c01c_X1931	24th Oct. 2016	12-m	18 m – 1.8 km	21 min	Pipeline
NGC 3393	2015.1.00086.S*	uid_A002_Xb28642_X9219	3rd May 2016	12-m	15 m – 630 m	28 min	Manual
	2016.1.01553.S	uid_A002_Xbfdb60_X6921	2nd May 2017	12-m	15 m – 1.1 km	20 min	Pipeline
NGC 5765b	2016.1.01553.S	uid_A002_Xc04da7_X88f3	15th May 2017	12-m	15 m – 1.1 km	22 min	Pipeline
NGC 4501	2015.1.00466.S	uid_A002_Xacdf75_X2601	17th Nov. 2015	12-m	83 m – 16.2 km	10 min	Manual
		uid_A002_Xacf797_X14d9	20th Nov. 2015	12-m	16 m – 16.2 km	10 min	Manual
		uid_A002_Xad2439_X2ff7	27th Nov. 2015	12-m	68 m – 14.3 km	10 min	Manual
		uid_A002_Xb1cc39_X272a	15th Apr. 2016	12-m	15 m – 600 m	2 min	Pipeline
		uid_A002_Xb54d65_X2531	12th Jul. 2016	12-m	15 m – 870 m	2 min	Pipeline
	2016.2.00053.S	uid_A002_Xc26103_X1fdc	20th Jul. 2017	7-m	9 m – 45 m	20 min	Pipeline
Frl 49	2017.1.00904.S	uid_A002_Xd21a3a_X503	17th Sep. 2018	12-m	15 m – 1.4 km	5 min	Pipeline; (1)
		uid_A002_Xdee82d_X7bed	17th Jul. 2019	12-m	90 m – 8.5 km	5 min	Pipeline; (2)
Frl 1146	2016.2.00046.S	uid_A002_Xc19d6f_X2e00	2nd Jul. 2017	7-m	9 m – 48 m	16 min	Pipeline
	2017.1.00904.S	uid_A002_Xd23397_X4424	20th Sep. 2018	12-m	15 m – 1.4 km	7 min	Pipeline
Mrk 567	2016.2.00046.S	uid_A002_Xc2d675_X735	30th Jul. 2017	7-m	8 m – 43 m	18 min	Pipeline
	2017.1.00904.S	uid_A002_Xd271e2_X9c84	26th Sep. 2018	12-m	15 m – 1.4 km	5 min	Pipeline
		uid_A002_Xdfcc3f_X2edc	8th Aug. 2019	12-m	40 m – 5.9 km	5 min	Pipeline
NGC 3862	2015.1.00598.S	uid_A002_Xb41687_X865	10th Jun. 2016	12-m	15 m – 700 m	10 min	Pipeline
	2016.2.00046.S	uid_A002_Xc3c940_X202a	26th Aug. 2017	7-m	9 m – 49 m	20 min	Pipeline
	2016.2.00053.S	uid_A002_Xc39302_X3b83	20th Aug. 2017	7-m	9 m – 49 m	21 min	Pipeline
	2018.1.00397.S	uid_A002_Xe07f3e_X1410c	27th Aug. 2019	12-m	38 m – 3.6 km	37 min	Pipeline
NGC 4061	2015.1.00598.S	uid_A002_Xb41687_Xb2e	11th Jun. 2016	12-m	15 m – 700 m	10 min	Pipeline
	2016.2.00046.S	uid_A002_Xc43aa5_X3e43	5th Sep. 2017	7-m	9 m – 49 m	10 min	Pipeline
	2016.2.00053.S	uid_A002_Xc3a8fe_X275d	22nd Aug. 2017	7-m	9 m – 49 m	21 min	Pipeline
	2018.1.00397.S	uid_A002_Xe03886_X7606	19th Aug. 2019	12-m	40 m – 3.2 km	28 min	Pipeline
		uid_A002_Xe03886_Xd75e	20th Aug. 2019	12-m	40 m – 3.4 km	28 min	Pipeline

Table 5.1: (continued) Observing track properties.

Galaxy	Programme	Track	Date	Array	Baseline range	On-source time	Calibration
NGC 4261	2016.2.00046.S	`uid_A002_Xc39302_X3dc6`	20th Aug. 2017	7-m	9 m – 49 m	18 min	Pipeline
	2017.1.00301.S*	`uid_A002_Xc94c38_Xd353`	19th Jan. 2018	12-m	15 m – 1.4 km	30 min	Pipeline
	2018.1.00397.S	`uid_A002_Xe02ab0_Xc3`	16th Aug. 2019	12-m	40 m – 3.6 km	5 min	Pipeline
NGC 5995	2017.1.00904.S	`uid_A002_Xc6ff69_X441f`	19th Nov. 2017	12-m	90 m – 8.5 km	5 min	Pipeline
		`uid_A002_Xd21a3a_X60c`	17th Sep. 2018	12-m	15 m – 1.4 km	5 min	Pipeline
		`uid_A002_Xdf0444_X2e0`	17th Jul. 2019	12-m	90 m – 8.5 km	5 min	Pipeline

Notes: ALMA programme numbers indicated by a * are archival observations not taken by the WISDOM team. Groups of galaxies separated by double lines are discussed in separate sections and originate in different proposals. (1) Antenna DA55 was manually flagged due to an amplitude error. (2) Antennae DA45, DA47, DA53, DA59, DV06 and DV20 were manually flagged due to amplitude errors.

Table 5.2: Maser galaxy properties.

Name	Right Ascension[1] (J2000)	Declination[1] (J2000)	Distance (Mpc)	SMBH mass (10^7 $M_\odot$)	$\sigma_\star$ (km s^{-1})	$R_{\rm SoI}$ (pc)	$R_{\rm SoI}$ ($''$)	Morphology	Activity
NGC 1194	$03^h03^m49\overset{s}{.}1$	$-\ 1°\,06'\,13\overset{''}{.}5$	53.2 ± 3.2[1,2]	6.5 ± 0.3[2]	148 ± 26[3]	12.8	0.05	SA0[1]	Sy1.9[4]
NGC 3393	$10^h48^m23\overset{s}{.}5$	$-25°\,09'\,43\overset{''}{.}4$	56.2 ± 3.9[1]	3.1 ± 0.2[5]	148 ± 11[3]	6.1	0.022	SBa[1]	Sy2[4,6]
NGC 5765b	$14^h50^m51\overset{s}{.}5$	$+\ 5°\,06'\,52\overset{''}{.}1$	126 ± 12[7]	4.6 ± 0.4[7]	162 ± 17[8]	7.5	0.012	Sab[1,9]	Sy2[10]

References: (1) NASA/IPAC Extragalactic Database (2) Kuo et al. (2011) (3) Greene et al. (2010) (4) Véron-Cetty & Véron (2006) (5) Kondratko et al. (2006) (6) Baumgartner et al. (2013) (7) Gao et al. (2016) (8) Greene et al. (2016) (9) Pjanka et al. (2017) (10) Toba et al. (2014)

Table 5.3: Maser galaxy and NGC 4501 data properties.

Galaxy property:	NGC 1194	NGC 3393	NGC 5765b	NGC 4501
Morphology	S0	Sa	Sab	Sb
Systemic velocity ($\mathrm{km\,s^{-1}}$)	3970	3680	8075	2240
Distance (Mpc)	53.2 ± 3.2	56.2 ± 3.9	126 ± 12	16.5 ± 1
Velocity dispersion ($\mathrm{km\,s^{-1}}$)	150 ± 25	150 ± 10	160 ± 20	158 ± 5
Continuum image property:				
Image size (px)	500×500	512×512	512×512	2048×2048
Pixel scale ($''$/px)	0.1	0.1	0.1	0.01
Robust weighting	-0.5	-0.5	-0.5	0.5
Sensitivity ($\mu\mathrm{Jy\,beam^{-1}}$)	43	20	168	20
Synthesised beam ($''$)	0.26×0.20	0.44×0.35	0.33×0.23	0.046×0.028
Continuum source property:				
Right ascension (J2000)	$03^{\mathrm{h}}03^{\mathrm{m}}49^{\mathrm{s}}.1084 \pm 0^{\mathrm{s}}.0002$	See Table 5.4	–	$12^{\mathrm{h}}31^{\mathrm{m}}59^{\mathrm{s}}.1526 \pm 0^{\mathrm{s}}.0006$
Declination (J2000)	$-1°6'13''.482 \pm 0''.002$	–	–	$14°25'13''.20 \pm 0''.01$
Deconvolved size (milliarcsec)	–	–	–	780×610
Integrated flux (mJy)	1.61 ± 0.08	–	<0.5[1]	40 ± 1
CO(2-1) cube property:				
Spatial size (px)	500×500	512×512	512×512	4096×4096
Pixel scale ($''$/px)	0.1	0.1	0.1	0.01
Robust weighting	2	-0.5	-0.5	0.5
Sensitivity ($\mathrm{mJy\,beam^{-1}}$)	0.45	0.42	1.2	0.4
Synthesised beam ($''$)	0.3×0.23	0.45×0.35	0.33×0.27	0.045×0.028
Velocity range ($\mathrm{km\,s^{-1}}$)	3500 – 4490	3000 – 4390	7500 – 8490	1800 – 2685
Channel width ($\mathrm{km\,s^{-1}}$)	10	10	10	15
CO(2-1) property:				
Integrated flux ($\mathrm{Jy\,km\,s^{-1}}$)	12.2 ± 0.5	70.8 ± 0.8	87 ± 2	1127 ± 9
Molecular gas mass ($\log[M_{\mathrm{mol}}/\mathrm{M}_\odot]$)	8.56 ± 0.02	9.37 ± 0.01	10.16 ± 0.02	9.508 ± 0.004
Disc diameter ($''$)	–	25×24	–	26×8
Disc diameter (pc)	–	6800×6500	–	2080×640
Disc inclination ($°$)	–	17	–	72

Notes: (1) This upper limit assumes an unresolved continuum source at 3σ significance.

5.3 Maser galaxies

INCE ALMA resolves spatial scales that cannot be resolved using existing optical instruments (as would be required to obtain SMBH masses with stellar or ionised-gas dynamics), masers are the only tracers suitable for cross-checking molecular gas measurements. Three galaxies with maser emission were thus observed to attempt to cross-check our molecular gas SMBH masses against those derived from maser kinematics. These galaxies were all observed at intermediate angular resolutions in programme 2016.1.01553.S, to verify whether suitable molecular gas discs exist before higher-resolution follow-up. The three galaxies selected were NGC 1194, NGC 3393 and NGC 5765b. These galaxies are all accessible from ALMA, have SMBH spheres of influence sufficiently large to be resolvable with ALMA's longest baselines, and are free from strong molecular gas outflows that would otherwise contaminate the velocity fields. The general properties of these targets, morphologies, activity classifications, maser-derived SMBH mass measurements, and predicted spheres of influence are listed in Table 5.2.

To complement the ALMA observations, single-dish observations of the ^{12}CO(2-1) and ^{12}CO(3-2) emission lines were acquired with the James Clerk Maxwell Telescope (JCMT), to determine if the interferometer resolved out any flux. These observations were provided to the author by the programme Principal Investigator, and therefore extensive details of the observational procedures are not provided here. The spectra were rebinned from a raw resolution of 0.65 km s^{-1} to 10 km s^{-1} per channel to match our ALMA data. A linear baseline fit to line-free regions was then subtracted from each spectrum. The spectra were converted from antenna temperatures to flux densities ($S = 15.6\,T_{\rm A}^{\star}/\eta_A$) adopting the JCMT aperture efficiency of $\eta_A = 0.52$ at both frequencies. These JCMT spectra are compared to integrated spectra synthesised from the ALMA observations in the bottom-right panels of Figures 5.1, 5.3 and 5.5.

5.3.1 NGC 1194

NGC 1194 is a highly-inclined S0 galaxy at a distance of 53.2 ± 3.2 Mpc (Kuo et al. 2011). Maser emission was detected by the Very Long Baseline Array and Green Bank Telescope, and found to be oriented in a slightly-warped thin disc with outer and inner radii of 1.3 and 0.5 pc, respectively. The dynamics of this disc were modelled to derive a SMBH mass (Kuo et al., 2011). The complex line shapes found by X-ray observations have been controversially interpreted as evidence for a SMBH binary (Vasylenko et al., 2015) or more conventionally a warped disc (Fedorova et al., 2016). Greene et al. (2014) presented infrared integral-field spectrograph observations from the Keck telescope, finding spatially-resolved but patchy H_2 2.12 μm emission, with asymmetric velocities interpreted as central non-circular motions.

Our ALMA observations observations reveal a similarly patchy CO distribution along the optical major axis, consistent with the orientation of the maser disc. Although there is CO emission in the galactic nucleus, it is weak and high angular resolution follow-up observations to resolve the SMBH sphere of influence would require impractically longer integrations (≈450 hours). The large-scale CO velocities are consistent with those found by H I observations (Sun et al., 2013). There is no compelling evidence for non-circular motions in the CO velocity field, but the integrated line profile is asymmetric due to the gas distribution. The gap in the CO gas to the south-east of the galactic nucleus appears to be real, rather than an artefact of the data reduction or a result of our masking. It seems probable that the gas distribution follows the patchy H_2 distribution found by Greene et al. (2014).

The JCMT observations only targeted the ^{12}CO(2-1) emission line as the expected CO(3-2) line intensity was too small to be detected. The JCMT primary beam exceeds the field of view shown in Figure 5.1, so all the CO(2-1) emission should have been included. However, the JCMT observations did not achieve sufficient sensitivity to detect this emission.

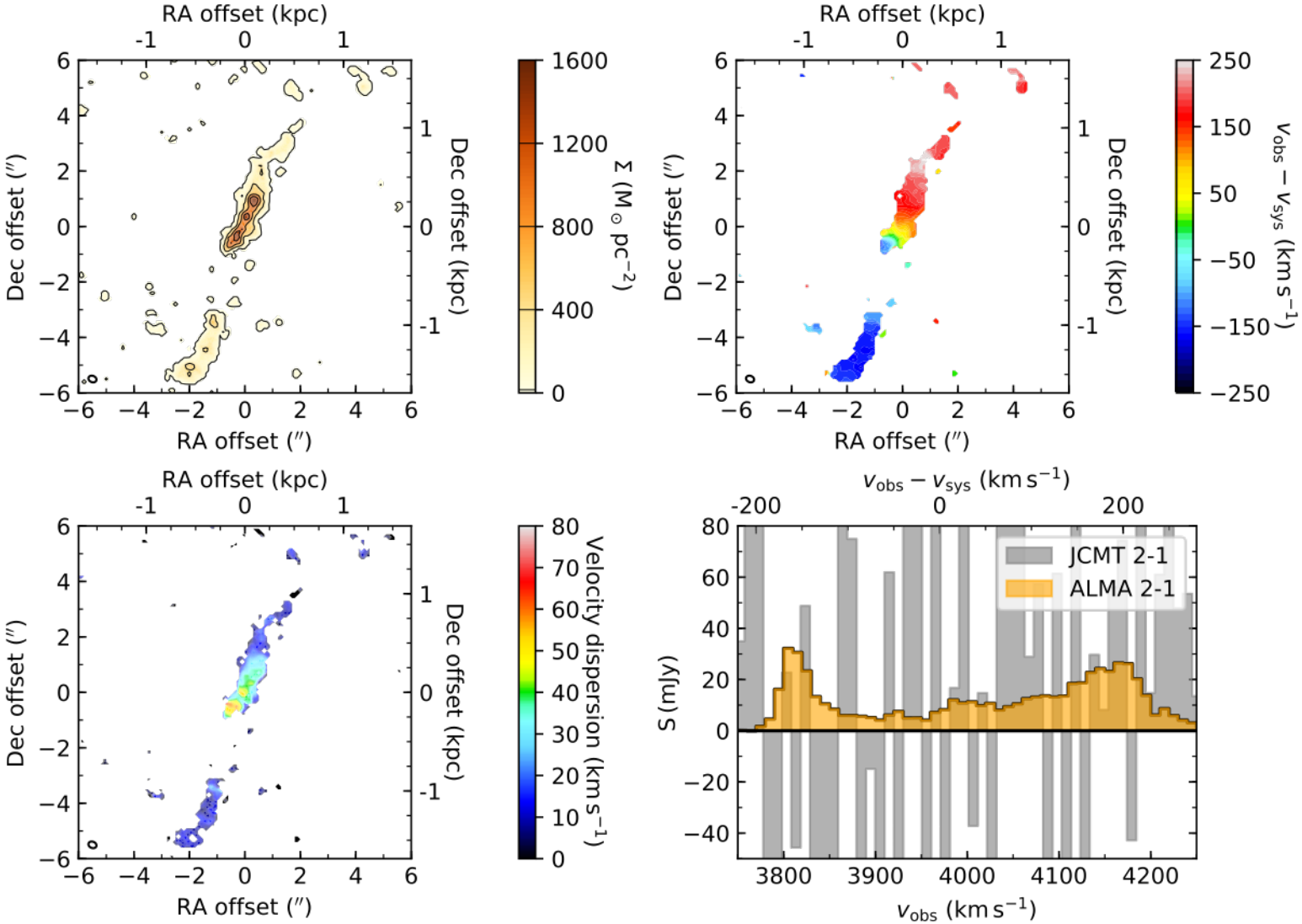

Figure 5.1: Moment maps of the ^{12}CO(2-1) emission of NGC 1194, from our ALMA observations. **Top-left:** Molecular gas surface density, assuming a CO-to-H_2 conversion factor $\alpha_{CO} = 4.3\,M_\odot\,(K\,km\,s^{-1})^{-1}\,pc^{-2}$. Black contours are from the level at which the noise was clipped, $15\,M_\odot\,pc^{-2}$, and then at 400, 800, 1200 and $16\,000\,M_\odot\,pc^{-2}$. The JCMT primary beam at CO(2-1) encloses the entire region shown. **Top-right:** Mean line-of-sight velocity. **Bottom-left:** Line-of-sight velocity dispersion. **Bottom-right:** Integrated spectra, synthesised from our ALMA (orange), and JCMT (greyscale) observations at CO(2-1), although the latter did not reach a sensitivity sufficient to detect the emission. In both right panels, v_{obs} is the observed line-of-sight velocity and $v_{sys} = 3970\,km\,s^{-1}$ is the mean systemic velocity of the galaxy. The synthesised beam is shown in the bottom-left corner of each map.

5.3.2 NGC 3393

NGC 3393 is a nearby spiral galaxy featuring a large-scale stellar bar and radio jet (Alonso-Herrero et al., 1998; Cooke et al., 2000). The existence of a nuclear bar has also been posited (e.g. Jungwiert et al., 1997). The NASA/IPAC Extragalactic Database lists a distance of 52 Mpc and the galaxy covers an angular scale of 1′. The presence of two compact X-ray sources separated by ≈ 130 pc gave rise to the suggestion that there are two SMBHs in the nuclear region (Fabbiano et al., 2011). Subsequent analysis however determined that the radio, near-infrared, optical and radio nuclear emission are all consistent with a single point source, and statistical noise in the X-ray data can give rise to the erroneous conclusion of a dual SMBH system (Koss et al., 2015). H_2O maser emission was discovered by the NASA Deep Space Network (Kondratko et al., 2006), mapped with very long baseline interferometry, and modelled to obtain a central mass of $3.1 \pm 0.2 \times 10^7\,M_\odot$ (Kondratko et al., 2008a).

While our observations were in the ALMA queue, marginally lower-resolution (0.″5) observations were carried out and published by Finlez et al. (2018). They discussed the central molecular gas kinematics extensively, concluding that they are perturbed by the presence of the bar and interactions with the jet. In particular, they determined that the CO emission does not adequately probe the region around either of the two postulated SMBHs. Our analysis of this object is therefore restricted only to the continuum (see Figure 5.2) and to a comparison between the ALMA and JCMT observations (see Figure 5.3).

Our 1.3 mm continuum image reveals two sources at the centre of the field, separated by $\approx 1''$ (approximately 2.5 synthesised beams). We verified that these are not artefacts from improperly combining the two observing tracks by imaging each track separately, recovering the same two sources in both images. We fit these sources with Gaussian components using the `CASA` task `imfit`, determining the properties listed in Table 5.4. Our NE and SW sources correspond respectively to component A and B of Koss et al. (2015). They are therefore attributed to the nuclear component and one jet lobe, respectively, and hereafter we refer to the NE source as the nuclear

component. The nuclear component is spatially resolved along one axis at our resolution for the first time, with a deconvolved size of 380 ± 50 mas. Both Koss et al. (2015) and Finlez et al. (2018) detected an additional north-east source, that the latter determined to have an integrated 1.3 mm flux of 0.08 mJy. It is therefore significantly fainter than the other two sources. Koss et al. (2015) suggested that the reduced flux in this component (and increased flux in the SW component) is the result of Doppler-boosting of the receding (approaching) jet. We do not detect this NE component in our observations as they have a lower signal-to-noise ratio than that of the Finlez et al. (2018) observations (due to the higher angular resolution).

Using our integrated-flux measurements and those at 8.4 and 4.9 GHz from Koss et al. (2015), we fit a power law of the form $S \propto \nu^{\alpha}$ (Figure 5.2), and determine that the nuclear component has a spectral index $\alpha = -0.23 \pm 0.02$ and the SW component (jet lobe) $\alpha = -0.901 \pm 0.004$. Although our image does not detect the third source, by adopting the flux measured by Finlez et al. (2018) we measure a spectral index $\alpha = -0.93 \pm 0.04$. This is very similar to the spectral index of the SW component in our data, confirming it is likely that they both arise from the same emission mechanism. The indices are also comparable to those of other nuclei/jets (e.g. Hovatta et al., 2014).

The JCMT CO(2-1) spectrum shows good agreement with the ALMA integrated spectrum at velocities exceeding 3650 $\mathrm{km\,s^{-1}}$, but below this threshold does not reveal the same gas as ALMA. The ALMA velocity field indicates that this could be accounted for if the JCMT beam were centred $\approx 3''$ north of the galactic centre, thereby missing the southern material. Integrating over the velocity range $3650 - 3800\,\mathrm{km\,s^{-1}}$, where the two spectra appear to match, we estimate the fraction of flux recovered by the interferometer to be $\approx$100%, indicating that although the interferometric observations are missing baselines shorter than 15 m, very little, if any, flux is resolved out. The CO(3-2) JCMT observations appear to be systematically offset from the ALMA CO(2-1) data by $\approx 75\,\mathrm{km\,s^{-1}}$. We speculate that this higher-energy transition may be more perturbed by the jet interaction, leading to the offset, but have not reliably ascertained the origin of this offset.

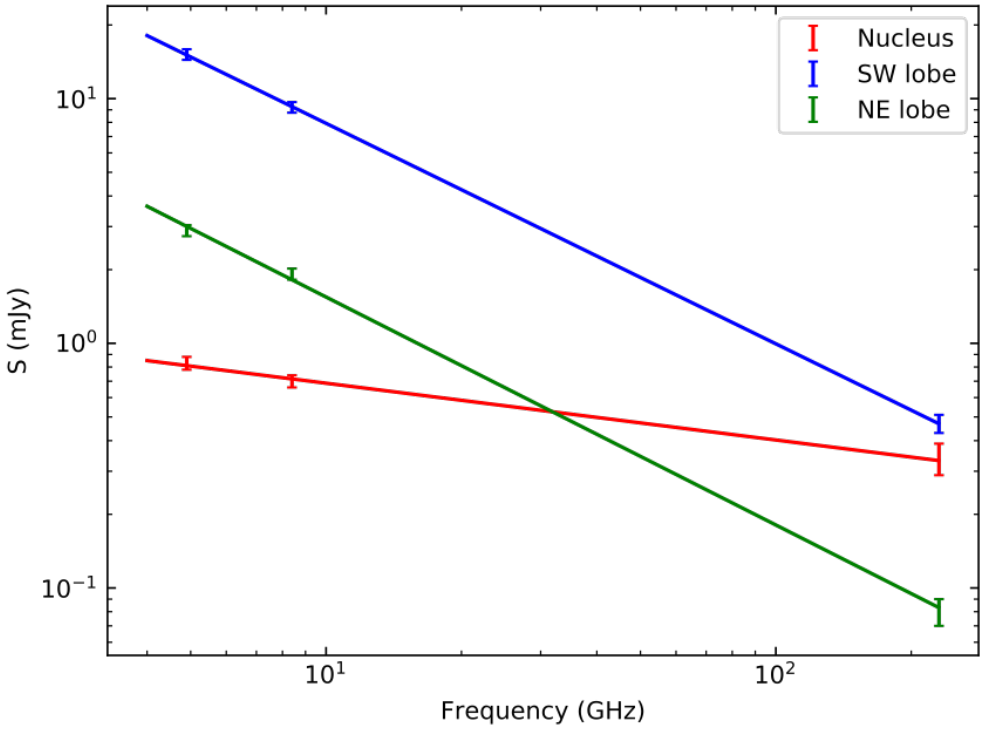

Figure 5.2: Radio-millimetre continuum fluxes of the three components identified in NGC 3393 (colour-coded), from VLA observations at 4.9 GHz and 8.4 GHz (Koss et al., 2015) and our ALMA 230 GHz data. For the NE lobe, we adopt the 1.3 mm flux measured by Finlez et al. (2018), as we do not detect this component in our data. A power-law fit to each component is overlaid in matching colour.

Table 5.4: NGC 3393 1.3 mm continuum point source properties.

Component	Property	Value
SW	RA (J2000)	$10^{\rm h}48^{\rm m}23\overset{\rm s}{.}4040 \pm 0\overset{\rm s}{.}0007$
	Dec. (J2000)	$-25°09'44\overset{''}{.}06 \pm 0\overset{''}{.}01$
	Integrated flux (μJy)	470 ± 40
	Spectral index[1] (α)	-0.901 ± 0.004
Nucl.	RA (J2000)	$10^{\rm h}48^{\rm m}23\overset{\rm s}{.}466 \pm 0\overset{\rm s}{.}0013$
	Dec. (J2000)	$-25°09'43\overset{''}{.}49 \pm 0\overset{''}{.}02$
	Integrated flux (μJy)	339 ± 50
	Major axis[2] (mas)	380 ± 50
	Spectral index[1] (α)	-0.23 ± 0.02
NE	Integrated flux (μJy)	80[3]
	Spectral index[1] (α)	-0.93 ± 0.04

Notes: (1) The spectral indices quoted for NGC 3393 are based on cross-identifying the three components with those in VLA observations by Koss et al. (2015), and fitting a power law of the form $S \propto \nu^{\alpha}$. (2) This component is resolved along one axis, and the size listed is deconvolved by the synthesised beam. (3) Flux taken from Finlez et al. (2018), as this component was not detected in our data.

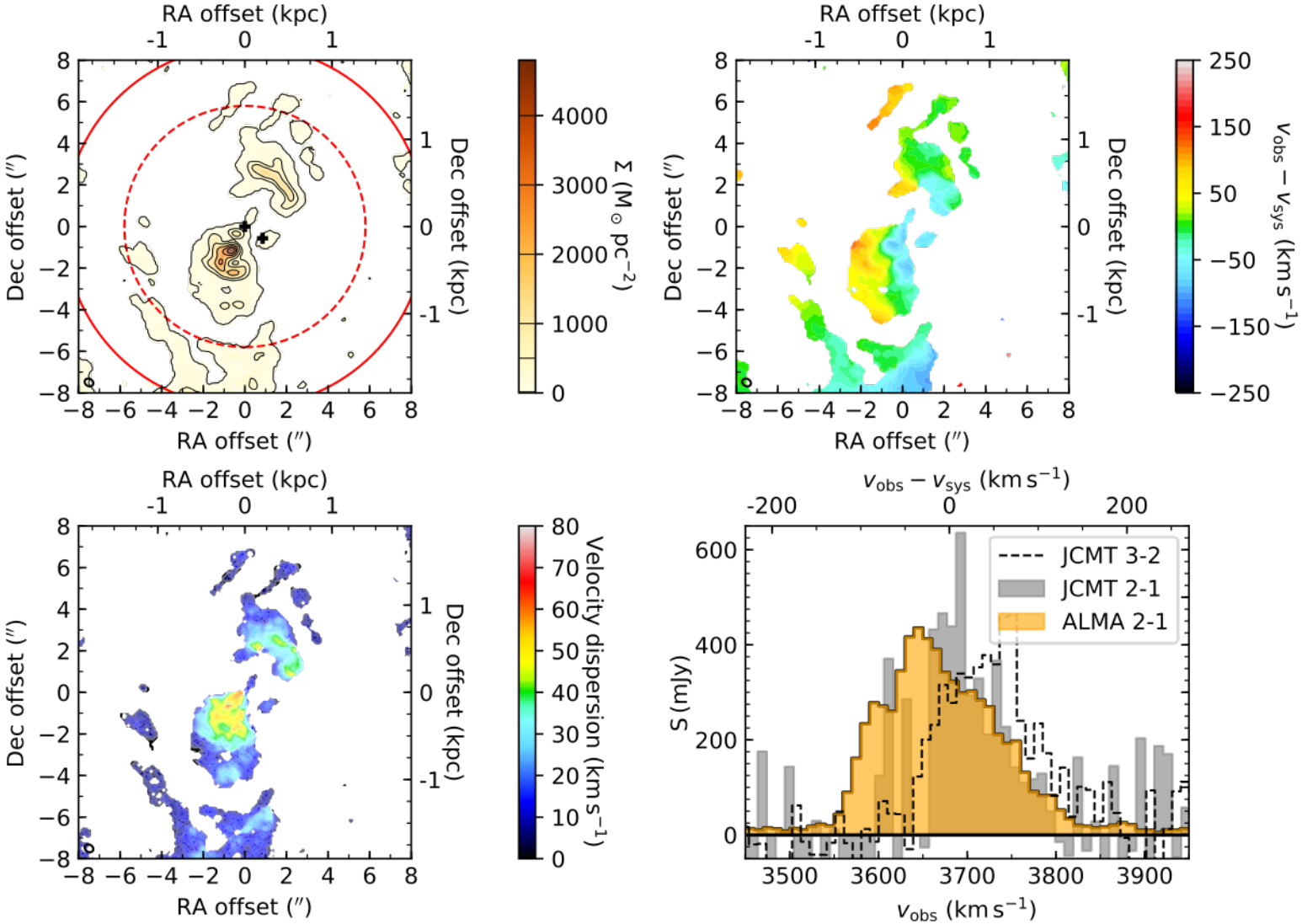

Figure 5.3: Moment maps of the ^{12}CO(2-1) emission of NGC 3393, from our ALMA observations, centered on the nuclear continuum source. **Top-left:** Molecular gas surface density, assuming a CO-to-H_2 conversion factor $\alpha_{CO} = 4.3\,M_\odot\,(K\,km\,s^{-1})^{-1}\,pc^{-2}$. Black contours are from the level at which the noise was clipped, $15\,M_\odot\,pc^{-2}$, and then at 500, 1000, 2000, 3000, 4000, and $5000\,M_\odot\,pc^{-2}$. The red circles indicate the JCMT primary beam at CO(2-1) (solid) and CO(3-2) (dashed). Black crosses indicate the positions of the nuclear and SW continuum sources. **Top-right:** Mean line-of-sight velocity. **Bottom-left:** Line-of-sight velocity dispersion. **Bottom-right:** Integrated spectra, synthesised from our ALMA (orange), and JCMT (greyscale) at CO(2-1) and CO(3-2) (dashed black line) observations. In both right panels, v_{obs} is the observed line-of-sight velocity and $v_{sys} = 3680\,km\,s^{-1}$ is the mean systemic velocity. The synthesised beam is shown in the bottom-left corner of each map.

5.3.3 NGC 5765b

NGC 5765b is a late-type spiral galaxy with Seyfert 2 nuclear activity. Central maser emission was originally detected with the Green Bank Telescope as part of the Megamaser Cosmology Project, and monitored over two years, allowing an angular diameter distance of 126 ± 12 Mpc and a central SMBH mass of $4.55 \pm 0.4 \times 10^7$ $M_\odot$ to be measured (Gao et al., 2016). The galaxy has a close companion on the sky, NGC 5765a, at an angular separation of 22″.5. Its distance is unknown but its redshift places it a distance consistent with that of NGC 5765b. NGC 5765a is beyond the ALMA primary beam, and therefore not probed by our observations. A *Hubble Space Telescope* (*HST*) Wide Field Camera 3 (WFC3) F814W image (Figure 5.4) shows that NGC 5765b has a stellar bar, two large-scale rings (at ≈1″.5 and ≈3″.5 radius) and spiral features between these rings (Pjanka et al., 2017).

Our ALMA observations did not detect 1.3 mm continuum emission. The CO(2-1) emission (Figure 5.5) is very strong and shows the characteristic signatures of a bar-driven inflow. The gas is mostly confined to the bar, with the peak gas density tracing the dust lanes (themselves tracing bar-induced shocks). The velocity field similarly shows gas flows along the bar, with the transition to the nuclear region marked by the central kinematically-decoupled disc. The velocity dispersion map shows broad line widths along the spiral arms and in the transition regions, exceeding ≈40 km s^{-1}. Outside these regions, the line widths are not well-sampled by our adopted 10 km s^{-1} channels.

The JCMT spectrum and integrated spectrum synthesised from the ALMA data show good agreement. As the JCMT beam only covers the bar-dominated region, the patchy emission at larger radii detected by ALMA would not have been detected by JCMT, implying that the true fraction of flux resolved out by the interferometer may be a little larger (though this emission is faint).

The presence of significant non-circular motions from kpc-scales to the galactic nucleus due to the bar perturbation implies that the SMBH-dominated region (not spatially resolved by our observations) is likely to be kinematically disturbed. However, our observations show that there is a substantial molecular gas reservoir

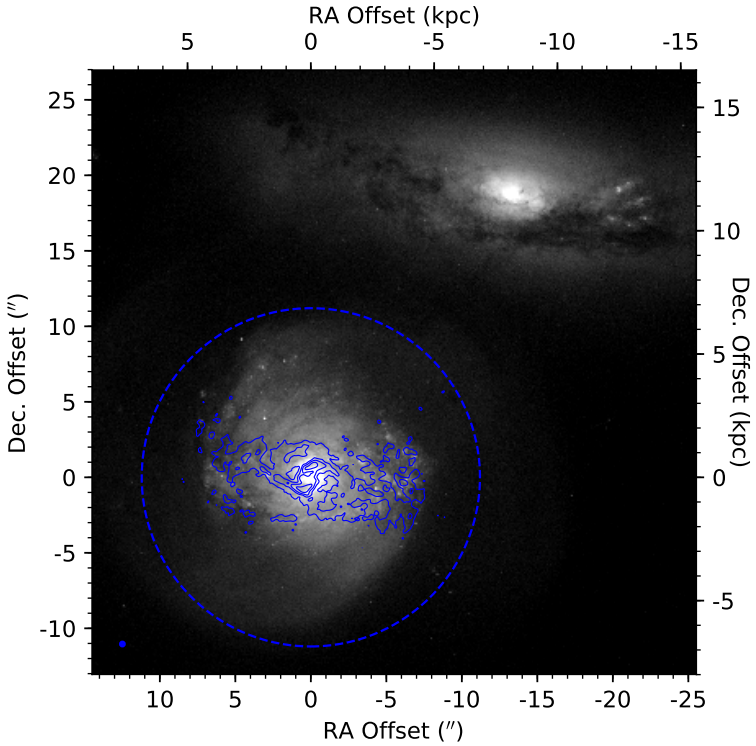

Figure 5.4: Unsharp-masked *HST*/WFC3 F814W image of NGC5765b (bottom-left) and its companion NGC5765a (top-right), overlaid with the ^{12}CO(2-1) emission observed with ALMA (blue contours). The blue dashed circle indicates the full-width at half-maximum of the primary beam of the ALMA 12-m dishes. The synthesised beam is shown in the bottom-left corner.

in the galactic nucleus, and follow-up observations connecting these large-scale motions to the nuclear region are feasible. Unfortunately, reaching the extremely small predicted sphere of influence (only $0\farcs01$), though possible would require very long integrations with ALMA ($\approx$270 hours to reach the same 1.2 mJy beam^{-1} sensitivity on a $0\farcs01$ beam), with no certainty that the gas is undisturbed (or even still present) at this scale. NGC 5765b was therefore not selected for further follow-up observations.

Nevertheless, the large-scale molecular gas kinematics are themselves of interest, and are an exceptional example of the power of ALMA to study bar-driven non-circular motions and gas inflows. Higher-resolution observations (although not sufficient to resolve $R_{\rm SoI}$) would allow us to constrain the role of molecular gas in feeding the central active galactic nucleus (AGN). While such a study is beyond the scope of this thesis, we discuss its potential further in Section 6.4.3.

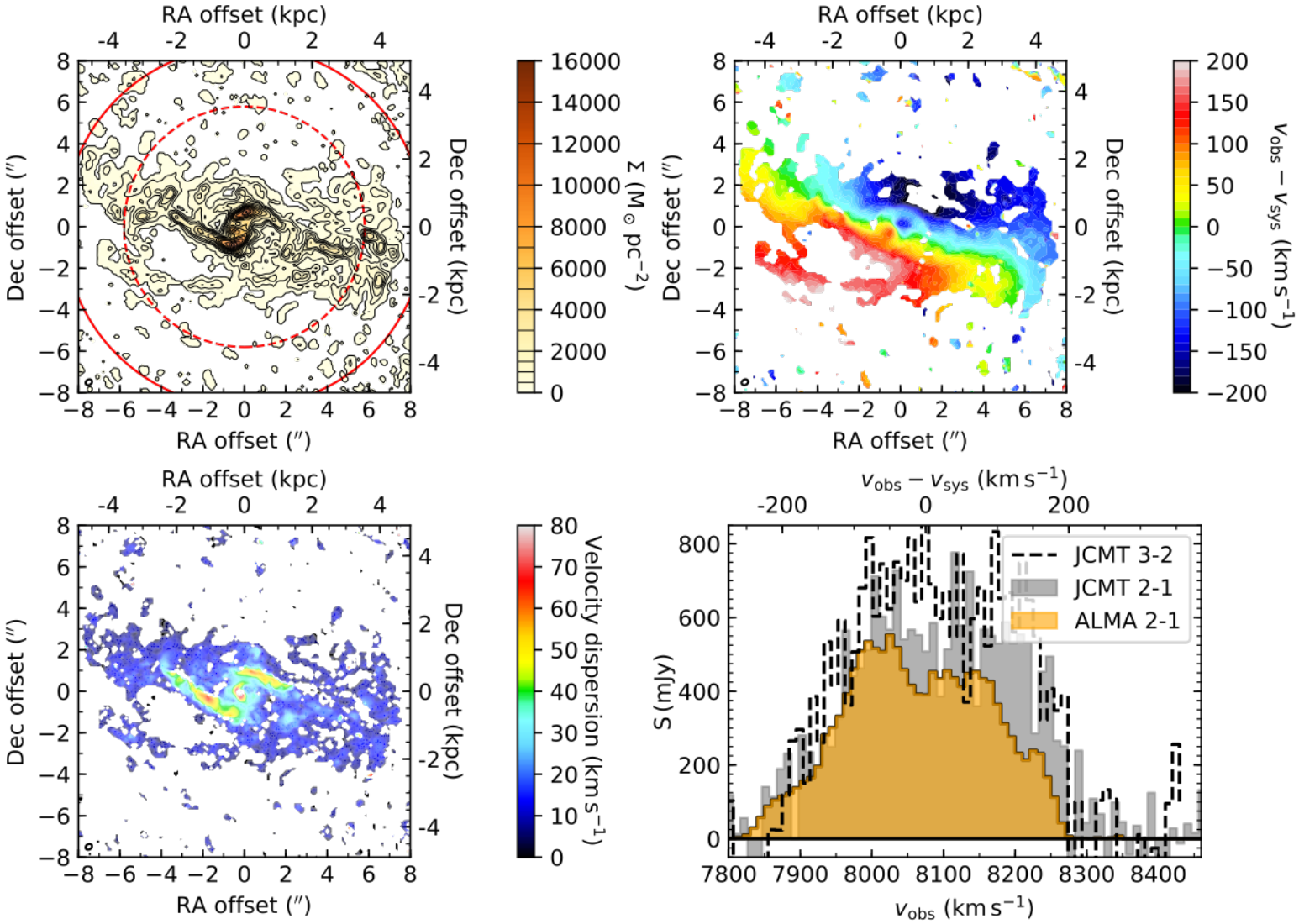

Figure 5.5: Moment maps of the ^{12}CO(2-1) emission of NGC 5765b, from our ALMA observations. **Top-left:** Molecular gas surface density, assuming a CO-to-H_2 conversion factor $\alpha_{CO} = 4.3\,M_\odot\,(K\,km\,s^{-1})^{-1}\,pc^{-2}$. Black contours are from the level at which the noise was clipped, $15\,M_\odot\,pc^{-2}$, at $500\,M_\odot\,pc^{-2}$ increments from 500 to $2000\,M_\odot\,pc^{-2}$, then at $1000\,M_\odot\,pc^{-2}$ increments up to $8000\,M_\odot\,pc^{-2}$, and finally at $2000\,M_\odot\,pc^{-2}$ increments up to $16\,000\,M_\odot\,pc^{-2}$. The red circles indicate the JCMT primary beam at CO(2-1) (solid) and CO(3-2) (dashed). **Top-right:** Mean line-of-sight velocity. **Bottom-left:** Line-of-sight velocity dispersion. **Bottom-right:** Integrated spectra, synthesised from our ALMA (orange), and JCMT CO(2-1) (greyscale) and CO(3-2) (dashed black line) observations. In both right panels, v_{obs} is the observed line-of-sight velocity and $v_{sys} = 8075\,km\,s^{-1}$ is the mean systemic velocity of the galaxy. The synthesised beam is shown in the bottom-left corner of each map.

5.4 NGC 4501

One of the advantages of using molecular gas kinematics for SMBH mass measurements is that the same method can be used in both early- and late-type galaxies. However, spiral galaxies are more challenging as their molecular gas kinematics exhibit complicated features, such as non-circular motions driven by non-axisymmetric perturbations to the potential, and turbulent motions driven by, for example, feedback from star formation. NGC 4501 (M88) was observed as part of our sub-sample of late-type galaxies (LTGs), but was found to suffer precisely this problem. As one of the most massive spirals in the Virgo cluster it has been extensively studied previously (over 750 papers listed on NED), but never in CO at the exceptional resolutions attained by our ALMA observations.

The CO(1-0) transition was observed with the Nobeyama Millimeter Array at 1.″8 (144 pc) resolution (Onodera et al., 2004). These observations showed that the molecular gas is distributed in two components: an outer spiral and a concentrated nuclear region from which it extends. The CO gas in the nuclear region was spatially-resolved into two peaks which exhibit slight non-circular motions. Mazzalay et al. (2013) observed this region using the Spectrograph for Integral-field Observations in the Near Infrared (SINFONI) on the Very Large Telescope. The warm H_2 emission is concentrated in north-west and south-east arms and a central peak. Although the stellar kinematics appear to show regular rotation, the H_2 indicate deviations from this rotation. Mazzalay et al. (2014) fit a thin disc model to the stellar kinematics and subtracted this model from the H_2 velocity field to determine the velocity residuals. These residuals indicate that the north-west arm is offset by $\approx$80 km s^{-1} from the underlying rotation (Figure 14 of Mazzalay et al. 2014). The south-east arm is consistent with the stellar rotation, and the velocity dispersion map shows no deviations corresponding to the north-west arm. It was therefore suggested that this feature is a gas filament with a peculiar motion relative to the galactic disc (Mazzalay et al., 2013, 2014).

Our ALMA observations (Table 5.3; Figure 5.6) confirm the CO emission is concentrated in the nuclear region, with an outer patchy ring/spiral matching

that found by Onodera et al. (2004). The exceptional spatial resolution achieved by our observations in this object (≈3 pc) dramatically outperforms these earlier observations, allowing us to unravel the structure of the nuclear region. The north-west arc identified by Mazzalay et al. (2014) is particularly prominent in CO, and the south-eastern feature is more extended in CO than in H_2. These features distort the velocity field and warp the zero-velocity curve (i.e. the systemic velocity isovelocity contour), but they do not necessarily originate in a geometrically warped disc. The velocity dispersion map shows enhanced dispersions throughout the nuclear region (≈40 km s^{-1} compared to ≈10 km s^{-1} in the outer parts), but no significant systemic additional enhancement associated with these features. Modelling the streaming motions of these features is beyond the scope of this thesis, but our data on this object provide an exciting opportunity for further study.

Stellar kinematics have been used to measure a SMBH mass of $M_{\rm BH} = 2.0 \pm 0.4 \times 10^7$ M$_\odot$ (Saglia et al., 2016), yielding a predicted sphere of influence of 3.5 pc (assuming $\sigma_* = 157$ km s^{-1}; Saglia et al. 2016). Our ALMA observations therefore (just) resolve this spatial scale, at which the predicted projected circular velocity is 161 km s^{-1}. However, we do not detect molecular gas moving at this velocity, and larger-scale non-circular motions imply that the argument made in Chapter 2 (that central gas velocities should be enhanced above those expected from the stars alone) cannot be invoked.

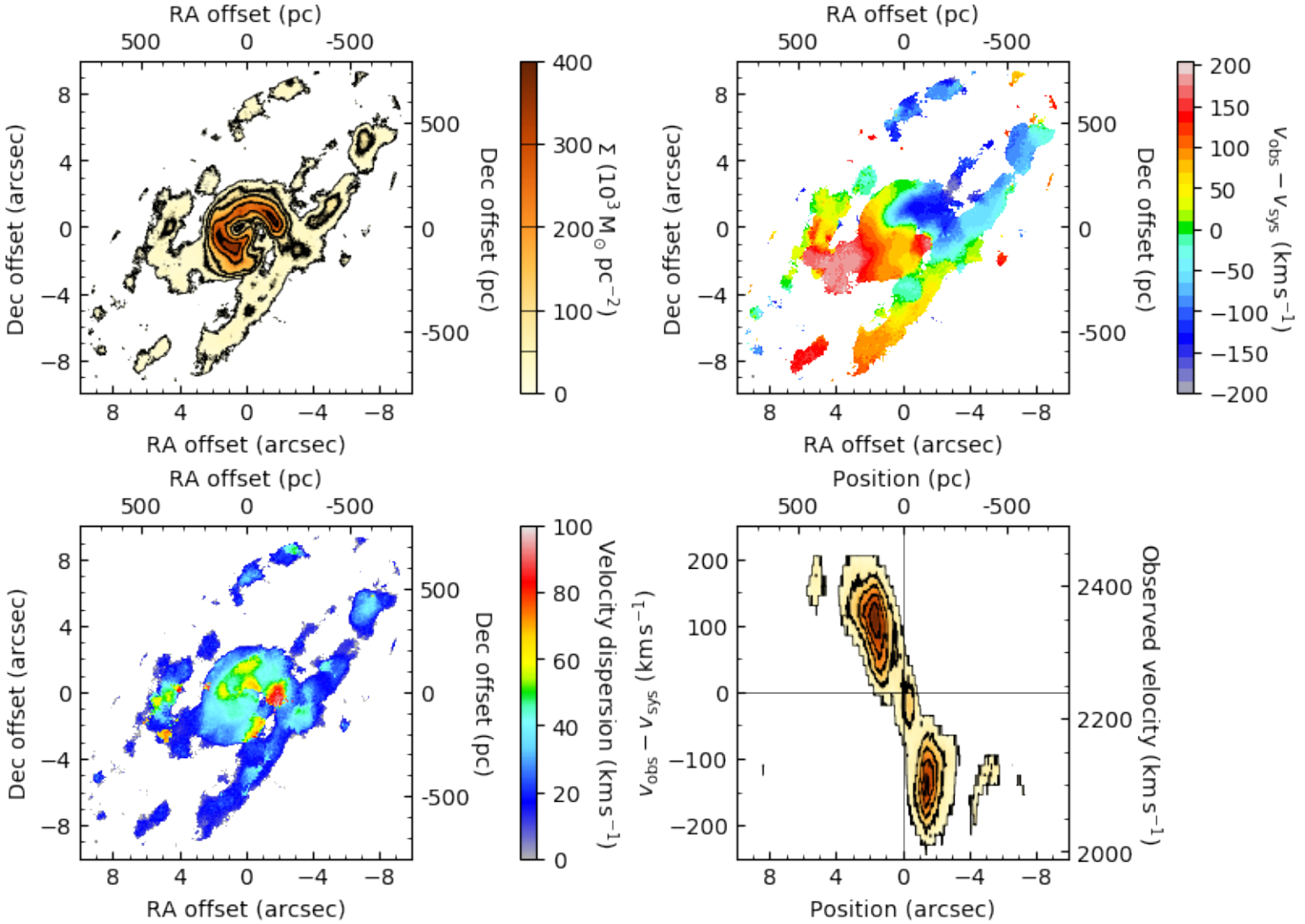

Figure 5.6: Moment maps of the ^{12}CO(2-1) emission of NGC 4501, from our ALMA observations. **Top-left:** Molecular gas surface density, assuming a CO-to-H_2 conversion factor $\alpha_{CO} = 4.3\,M_\odot\,(K\,km\,s^{-1})^{-1}\,pc^{-2}$. Black contours are from the level at which the noise was clipped, $15\,M_\odot\,pc^{-2}$, and then at 50 000, 100 000, 200 000, and 300 000 $M_\odot\,pc^{-2}$. **Top-right:** Mean line-of-sight velocity. **Bottom-left:** Line-of-sight velocity dispersion. **Bottom-right:** Kinematic major-axis position-velocity diagram. In both right panels, v_{obs} is the observed line-of-sight velocity and $v_{sys} = 2240\,km\,s^{-1}$ is the mean systemic velocity of the galaxy. The (extremely small) synthesised beam is shown in the bottom-left corner of each map.

5.5 High-mass SMBH candidates

At the highest galaxy masses, the $M_{\rm BH}-\sigma_*$ relation appears to break, deviating toward higher SMBH masses at a fixed σ_* (see e.g. Figure 1.1). This appears to be the result of the known saturation in σ_* at high galaxy masses/luminosities (seen for instance in the Faber-Jackson relation; Faber & Jackson 1976; Davies et al. 1983; Oegerle & Hoessel 1991a; Matković & Guzmán 2005; Cappellari et al. 2013b), since the $M_{\rm BH}-M_{\rm Bulge}$ relation does not appear to similarly break (e.g. Lauer et al., 2007; Kormendy & Bender, 2013). This phenomena has been explained by evolutionary models in which the largest elliptical galaxies undergo a series of dissipationless (dry) major mergers, growing their central SMBHs without further increasing σ_* (in contrast to the wet mergers common at lower galaxy masses that simultaneously increase σ_*; Volonteri et al. 2003; Hilz et al. 2012; Kormendy & Bender 2013).

Additional SMBH masses that independently probe this region are required to confirm that the $M_{\rm BH}-\sigma_*$ relation indeed saturates at high σ_*, and to exclude the known bias towards detecting the largest $M_{\rm BH}$ at any given σ_*. A high-mass sub-sample of WISDOM galaxies was therefore selected, using stellar velocity dispersions (either observed or inferred from the fundamental plane) to estimate the SMBH masses and spheres of influence. We thus successfully proposed ALMA observations of nine galaxies in programmes 2017.1.00904.S and 2018.1.00397.S. Some observations were obtained in 2017-2018, mostly short baseline tracks, with the remainder delivered in late 2019. We have already described the results for NGC 7052 in Chapter 3. ALMA observations of NGC 612 were intended to provide long baselines to supplement the earlier low-resolution observations of Ruffa et al. (2019a) and are not discussed here. The preliminary results from the other seven galaxies are discussed below.

The properties of the ^{12}CO(2-1) data cubes and 1.3 mm continuum images are listed in Table 5.5. Nuclear continuum emission was detected in six of the seven galaxies and fit using the `CASA` task `imfit`. The results are also listed in Table 5.5.

Table 5.5: High-mass sub-sample galaxy image properties.

Galaxy property:	Frl 49	Frl 1146	Mrk 567
Morphology	Sa	Sc	Sc
Systemic velocity ($\mathrm{km\,s^{-1}}$)	5870	9140	9400
Distance (Mpc)	88 ± 6	140 ± 10	140 ± 10
Velocity dispersion ($\mathrm{km\,s^{-1}}$)	$(700)^1$	$(370)^1$	$(370)^1$
Continuum image property:			
Image size (px)	512×512	512×512	2048×2048
Pixel scale ($''$/px)	0.02	0.05	0.03
Robust weighting	0.5	0.5	0.5
Sensitivity ($\mu\mathrm{Jy\,beam^{-1}}$)	41	27	36
Synthesised beam ($''$)	0.17×0.13	0.28×0.26	0.14×0.13
Continuum source property:			
Right ascension (J2000)	$18^{\mathrm{h}}36^{\mathrm{m}}58\overset{\mathrm{s}}{.}234 \pm 0\overset{\mathrm{s}}{.}001$	$08^{\mathrm{h}}38^{\mathrm{m}}30\overset{\mathrm{s}}{.}774 \pm 0\overset{\mathrm{s}}{.}001$	–
Declination (J2000)	$-59°24'08\overset{''}{.}29 \pm 0\overset{''}{.}01$	$-35°59'33\overset{''}{.}32 \pm 0\overset{''}{.}01$	–
Deconvolved size (milliarcsec)	$(275 \pm 30) \times (211 \pm 25)$	$(263 \pm 59) \times (154 \pm 75)$	–
Integrated flux (mJy)	2.4 ± 0.2	0.70 ± 0.09	$<0.1^2$
CO(2-1) cube property:			
Spatial size (px)	1024×1024	1024×1024	2048×2048
Pixel scale ($''$/px)	0.02	0.05	0.03
Robust weighting	0.5	Natural	0.5
Sensitivity ($\mathrm{mJy\,beam^{-1}}$)	0.8	0.4	1.0
Synthesised beam ($''$)	0.22×0.16	0.38×0.34	0.16×0.12
Velocity range ($\mathrm{km\,s^{-1}}$)	5500 – 6385	8850 – 9510	9100 – 9685
Channel width ($\mathrm{km\,s^{-1}}$)	15	15	15
CO(2-1) property:			
Integrated flux ($\mathrm{Jy\,km\,s^{-1}}$)	169.9 ± 0.2	18.9 ± 0.3	136 ± 2
Molecular gas mass ($\log[M_{\mathrm{mol}}/\mathrm{M}_\odot]$)	10.14 ± 0.08	9.59 ± 0.06	10.44 ± 0.06
Disc diameter ($''$)	7.4×3.7	–	7.8×5.3
Disc diameter (pc)	3160×1580	–	5300×3600
Disc inclination ($°$)	60	–	47

Table 5.5: (continued) High-mass sub-sample galaxy image properties.

Galaxy property:	NGC 3862	NGC 4061	NGC 4261
Morphology	E	E	E
Systemic velocity ($\mathrm{km\,s^{-1}}$)	6350	7150	2200
Distance (Mpc)	84.6 ± 8.5	107.2	30
Velocity dispersion ($\mathrm{km\,s^{-1}}$)	265 ± 15	270 ± 20	260 ± 13
Continuum image property:			
Image size (px)	512×512	512×512	512×512
Pixel scale ($''$/px)	0.02	0.05	0.05
Robust weighting	0.5	0.5	0.5
Sensitivity ($\mu\mathrm{Jy\,beam^{-1}}$)	270[3]	14	2000[3]
Synthesised beam ($''$)	0.13×0.10	0.13×0.10	0.24×0.20
Continuum source property:			
Right ascension (J2000)	$11^{\mathrm{h}}45^{\mathrm{m}}05\overset{\mathrm{s}}{.}00887 \pm 0\overset{\mathrm{s}}{.}00016$	$12^{\mathrm{h}}04^{\mathrm{m}}01\overset{\mathrm{s}}{.}461 \pm 0\overset{\mathrm{s}}{.}001$	$12^{\mathrm{h}}19^{\mathrm{m}}23\overset{\mathrm{s}}{.}2158 \pm 0\overset{\mathrm{s}}{.}0004$
Declination (J2000)	$+19°36'22\overset{''}{.}744 \pm 0\overset{''}{.}002$	$+20°13'56\overset{''}{.}36 \pm 0\overset{''}{.}01$	$+5°49'29\overset{''}{.}696 \pm 0\overset{''}{.}005$
Deconvolved size (milliarcsec)	$(54 \pm 19) \times (32 \pm 19)$	$(340 \pm 43) \times (327 \pm 43)$	$(240 \pm 26) \times (163 \pm 27)$
Integrated flux (mJy)	51.7 ± 3.5	3.71 ± 0.37	332 ± 21
CO(2-1) cube property:			
Spatial size (px)	512×512	512×512	512×512
Pixel scale ($''$/px)	0.05	0.05	0.05
Robust weighting	0.5	0.5	0.5
Sensitivity ($\mathrm{mJy\,beam^{-1}}$)	0.3	0.4	0.3
Synthesised beam ($''$)	0.15×0.11	0.15×0.12	0.27×0.24
Velocity range ($\mathrm{km\,s^{-1}}$)	6100 – 6625	6000 – 8385	1450 – 2935
Channel width ($\mathrm{km\,s^{-1}}$)	15	15	15
CO(2-1) property:			
Integrated flux ($\mathrm{Jy\,km\,s^{-1}}$)	31.74 ± 0.04	66.6 ± 0.3	9.54 ± 0.08
Molecular gas mass ($\log[M_{\mathrm{mol}}/\mathrm{M}_\odot]$)	9.37 ± 0.09	9.90 ± 0.09	7.95 ± 0.09
Disc diameter ($''$)	1.6×1.6	4.4×2.0	2.1×1.4
Disc diameter (pc)	650×650	2070×940	300×200
Disc inclination ($°$)	0	63	48

Table 5.5: (continued) High-mass sub-sample galaxy image properties.

Galaxy property:	NGC 5995
Morphology	Sa
Systemic velocity ($\mathrm{km\,s^{-1}}$)	7430
Distance (Mpc)	113 ± 8
Velocity dispersion ($\mathrm{km\,s^{-1}}$)	(590)[1]
Continuum image property:	
Image size (px)	2048×2048
Pixel scale (″/px)	0.02
Robust	0.5
Sensitivity ($\mu\mathrm{Jy\,beam^{-1}}$)	34
Synthesised beam (″)	0.20×0.16
Continuum source property:	
Right ascension (J2000)	$15^{\mathrm{h}}48^{\mathrm{m}}24\overset{\mathrm{s}}{.}9452 \pm 0\overset{\mathrm{s}}{.}0005$
Declination (J2000)	$-13°45'27\overset{''}{.}255 \pm 0\overset{''}{.}007$
Deconvolved size (milliarcsec)	280×250
Integrated flux (mJy)	1.9 ± 0.2
CO(2-1) cube property:	
Spatial size (px)	2048×2048
Pixel scale (″/px)	0.02
Robust	0.5
Sensitivity ($\mathrm{mJy\,beam^{-1}}$)	0.7
Synthesised beam (″)	0.16×0.13
Velocity range ($\mathrm{km\,s^{-1}}$)	7000 – 8035
Channel width ($\mathrm{km\,s^{-1}}$)	15
CO(2-1) property:	
Integrated flux ($\mathrm{Jy\,km\,s^{-1}}$)	80.4 ± 0.1
Molecular gas mass ($\log[M_{\mathrm{mol}}/\mathrm{M_\odot}]$)	10.033 ± 0.001
Disc diameter (″)	14.9×7.4
Disc diameter (pc)	8160×4050
Disc inclination (°)	60

(1) These velocity dispersions are estimated from the fundamental plane of van den Bosch (2016) and HyperLEDA. (2) This upper limit assumes an unresolved continuum source at 3σ significance. (3) The bright continuum source's side lobes dominate the noise at the edge of the primary beam, so this is an upper limit.

5.5.1 Fairall 49

Fairall 49 (Frl 49; Fairall & Jones, 1991) is a southern galaxy with a bright AGN. *HST* Advanced Camera for Surveys (ACS) images reveal a central spiral leading to a sequence of star-forming knots and a bright nucleus (Muñoz Marín et al., 2007), while earlier *HST* WFPC2 F606W images showed a 'filamentary/wispy' structure (Malkan et al., 1998). Observations with the Parkes radio telescope did not detect maser emission (Greenhill et al., 2002).

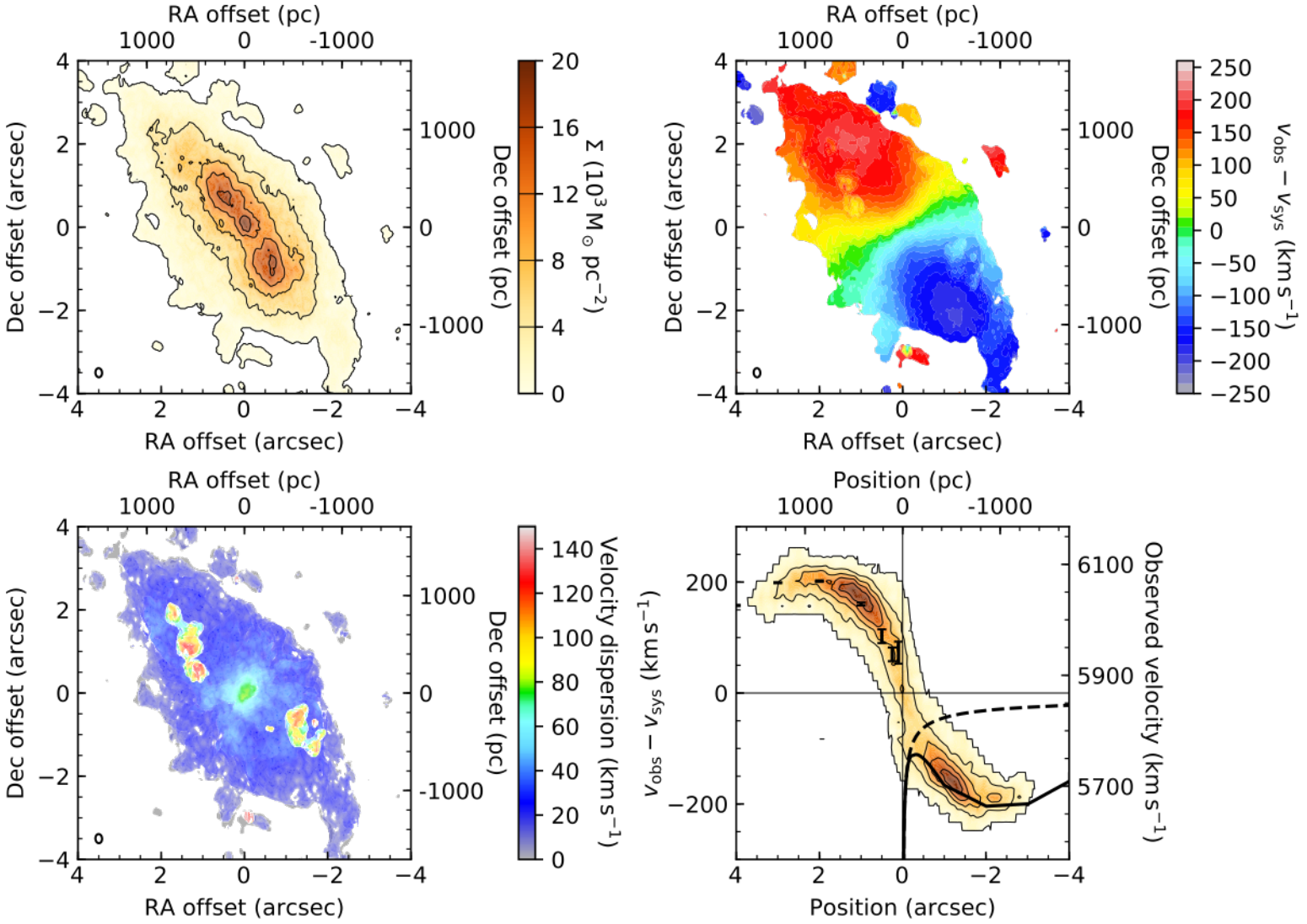

Figure 5.7: Moment maps of the ^{12}CO(2-1) emission of Frl 49, from our ALMA observations. **Top-left:** Molecular gas surface density, assuming a CO-to-H_2 conversion factor $\alpha_{CO} = 4.3\,M_\odot\,(K\,km\,s^{-1})^{-1}\,pc^{-2}$. Black contours are from the level at which the noise was clipped, $15\,M_\odot\,pc^{-2}$, and then at 4000, 8000, 12 000, 16 000 and 20 000 $M_\odot\,pc^{-2}$. **Top-right:** Mean line-of-sight velocity. **Bottom-left:** Line-of-sight velocity dispersion. **Bottom-right:** Kinematic major-axis position-velocity diagram. Black data points with error bars are the mean velocities due to the stars in our four dynamical models. The black dashed curve shows the velocities due to the SMBH alone, while the black solid curve shows the total velocity (i.e. including the SMBH mass). In both right panels, v_{obs} is the observed line-of-sight velocity and $v_{sys} = 5870\,km\,s^{-1}$ is the mean systemic velocity of the galaxy. The synthesised beam is shown in the bottom-left corner of each map.

Our ALMA observations reveal a compact nuclear continuum source and rotating disc of CO (Table 5.5 and Figure 5.7). The velocity dispersion map shows high-dispersion features that appear to correlate with the star-forming regions identified by Muñoz Marín et al. (2007). We do not spatially resolve the predicted SMBH sphere-of-influence. There is no velocity dispersion estimate in the literature, but using the $M_{\rm BH}-\sigma_*$ relation of (McConnell & Ma, 2013) to rewrite $R_{\rm SoI}$ as a function of $M_{\rm BH}$ only, the absence of a Keplerian signature implies an upper-limit on the SMBH mass of $\approx 1.5 \times 10^9\,{\rm M}_\odot$.

The asymmetries in the *HST* optical images, and oversaturation of the nucleus in an archival Near-Infrared Camera and Multi-Object Spectrometer image, imply that a MGE would not be a good model of the observed light (and hence the stellar mass distribution). Therefore our standard approach of parametrising the stellar mass distribution with an MGE is not appropriate. Instead, we entirely bypass the need to specify a stellar mass model and follow Boizelle et al. (2019). We assume that the stellar mass distribution can be purely specified by a circular velocity curve itself parametrised by the velocities at five radii ($r_{\rm inner}$, 1″, 2″, 3″ and 4″); these velocities become free parameters in our `KinMS`/MCMC fit to the full data cube described below. At $r = 0$, the contribution from this stellar component is fixed to be zero, while between these radii the velocities are linearly interpolated. This approach does not assume any specific functional shape for the stellar mass distribution.

We thus fit the entire data cube in a process otherwise identical to that used in Chapters 2 and 3. The circular velocity curve input to `KinMS` is the sum in quadrature of the stellar circular velocity curve described above, and that expected from a point mass/SMBH, this mass also becoming a free parameter. As the stellar contribution to the circular velocity curve is linearly interpolated between fixed radii, the shape of the central potential is effectively determined by the value of $r_{\rm inner}$ (and the rotation velocity at this radius). To explore the impact of this choice on the model (i.e. varying the slope of the central potential), we therefore fit the data cube four times with different values of $r_{\rm inner}$ ($r_{\rm inner} \in \{0\farcs1, 0\farcs25, 0\farcs5, 1''\}$). In all four models, the resulting best-fitting SMBH mass is consistent within the formal uncertainties.

Marginalising over these four $r_{\rm inner}$ yields $M_{\rm BH} = 3.2^{+6.9}_{-1.5} \times 10^8\,{\rm M}_\odot$ (3σ confidence intervals). As there is no reliable velocity dispersion measurement in the literature, we infer σ_* from our $M_{\rm BH}$ and the $M_{\rm BH}-\sigma_*$ relation of McConnell & Ma (2013) to derive an estimated $R_{\rm SoI}{\approx}30\,{\rm pc}$. As our beam is 60 pc, we thus resolve roughly $2\,R_{\rm SoI}$.

It is worth stressing here the importance of fitting the full data cube, rather than only the observed mean line-of sight velocity field (first moment) or the rotation curve (or trace of the PVD; e.g. Davis et al. 2013b), in cases such as this. If the SMBH sphere of influence is resolved, the SMBH mass is mostly constrained by the mean line-of-sight velocities of all the synthesised beams in which these velocities are enhanced compared to those inferred from the stars alone (e.g. Chapters 2 and 3). On the other hand, if the SMBH sphere of influence is not resolved (by a moderate fraction), only the central beam contains any gas experiencing its dynamical influence. Whether or not a SMBH is present, the mean line-of-sight velocity in this beam will be zero, as gas on one side of the galactic centre cancels gas on the other side. However, the presence of a SMBH will broaden the emission line (which otherwise will be determined by beam-smearing), as high velocity gas in Keplerian rotation close to the SMBH is detected. This will lead to a broad, (potentially bimodal) line profile, whereas in the absence of a SMBH the profile would be narrower (and monomodal, with a peak at the galaxy's systemic velocity). Thus the line profile still contains dynamical information (analogously to the higher-order line-of-sight velocity distribution moments commonly used in analysing stellar dynamics), and we can exploit all this information by fitting the full cube rather than some projection.

Although the stellar mass distribution modelled is allowed to vary almost completely freely to replicate the CO observations, the imposition of $v(r{=}0) = 0$ prevents the model from obviating a central SMBH by constructing an arbitrarily dense nuclear stellar cluster. However, it is not implausible that such a cluster may exist, and thus the SMBH mass estimate obtained by this approach must be treated with extreme caution. Finally, we draw attention to the predicted circular velocity curves in the PVD (bottom-right panel, Figure 5.7). These show that the SMBH

contribution dominates the central parts, but that its mass is not quite large enough to disentangle any Keplerian rotation from the broad envelope at this resolution.

5.5.2 Fairall 1146

The CO emission in Fairall 1146 (Frl 1146; Fairall & Jones, 1991) is faint, so we adopt natural weighting to maximise the signal-to-noise ratio at the expense of angular resolution, yielding a data cube with moments shown in Figure 5.8. This weighting enables us to detect emission from large galactic radii ($R{\approx}5$ kpc), indicative of a ring. The central emission is extended along the major axis, with two bright peaks either side of the kinematic centre. These peaks produce the broad velocity features within $1''$ of the centre in the major-axis PVD. The envelopes of these features decline in velocity toward the galactic centre, indicating that the observations have not detected the SMBH sphere of influence. However, as the synthesised beam is only $0\farcs36$ or $\approx$250 pc, longer baseline follow-up observations should be able to resolve the central structure in more detail, potentially resolving the SMBH sphere of influence. Such observations would likely miss the ring detected here, but the CO core is bright enough to be detected at high angular resolution in a reasonable integration time.

5.5.3 Markarian 567

A *HST* WFPC2/PC F606W image of Markarian 567 (Markaryan & Lipovetskii, 1973) reveals flocculent spiral structures in the nucleus (Malkan et al., 1998). The CO emission detected with ALMA is distributed in a large-scale rotating disc, with central spiral structures matching those in the optical images (Figure 5.9). These spiral structures show increased velocity dispersions and distort the isovelocity contours in the centre of the disc. Although the major-axis PVD appears to peak in velocity slightly within 500 pc (consistent with the position of the CO spiral), there is no evidence of an inner Keplerian feature.

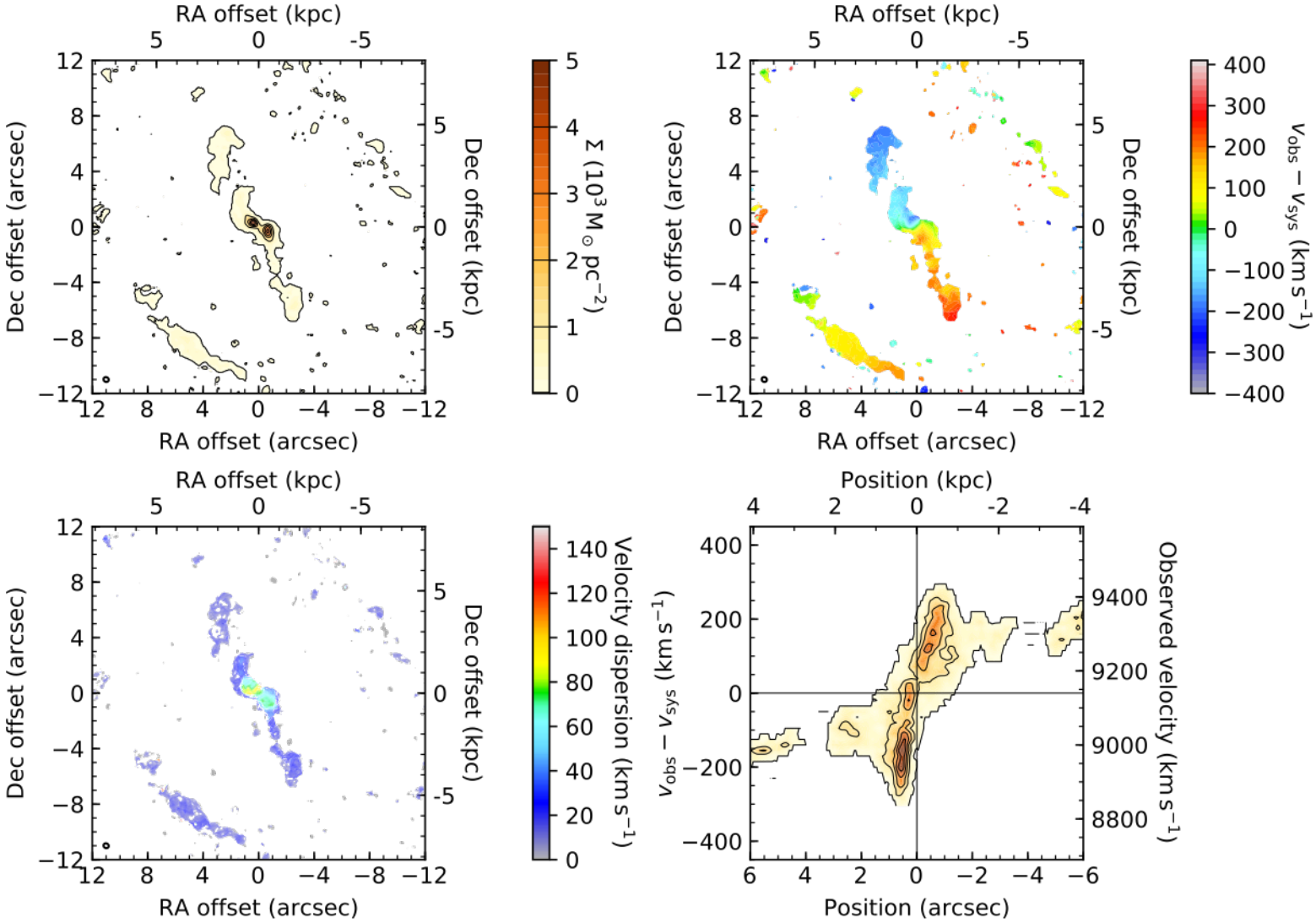

Figure 5.8: Moment maps of the ^{12}CO(2-1) emission of Frl 1146, from our ALMA observations. **Top-left:** Molecular gas surface density, assuming a CO-to-H_2 conversion factor $\alpha_{CO} = 4.3\,M_\odot\,(K\,km\,s^{-1})^{-1}\,pc^{-2}$. Black contours are from the level at which the noise was clipped, $15\,M_\odot\,pc^{-2}$, and then at 1000, 2000, 3000, 4000 and $5000\,M_\odot\,pc^{-2}$. **Top-right:** Mean line-of-sight velocity. **Bottom-left:** Line-of-sight velocity dispersion. **Bottom-right:** Kinematic major-axis position-velocity diagram. In both right panels, v_{obs} is the observed line-of-sight velocity and $v_{sys} = 9140\,km\,s^{-1}$ is the mean systemic velocity of the galaxy. The synthesised beam is shown in the bottom-left corner of each map.

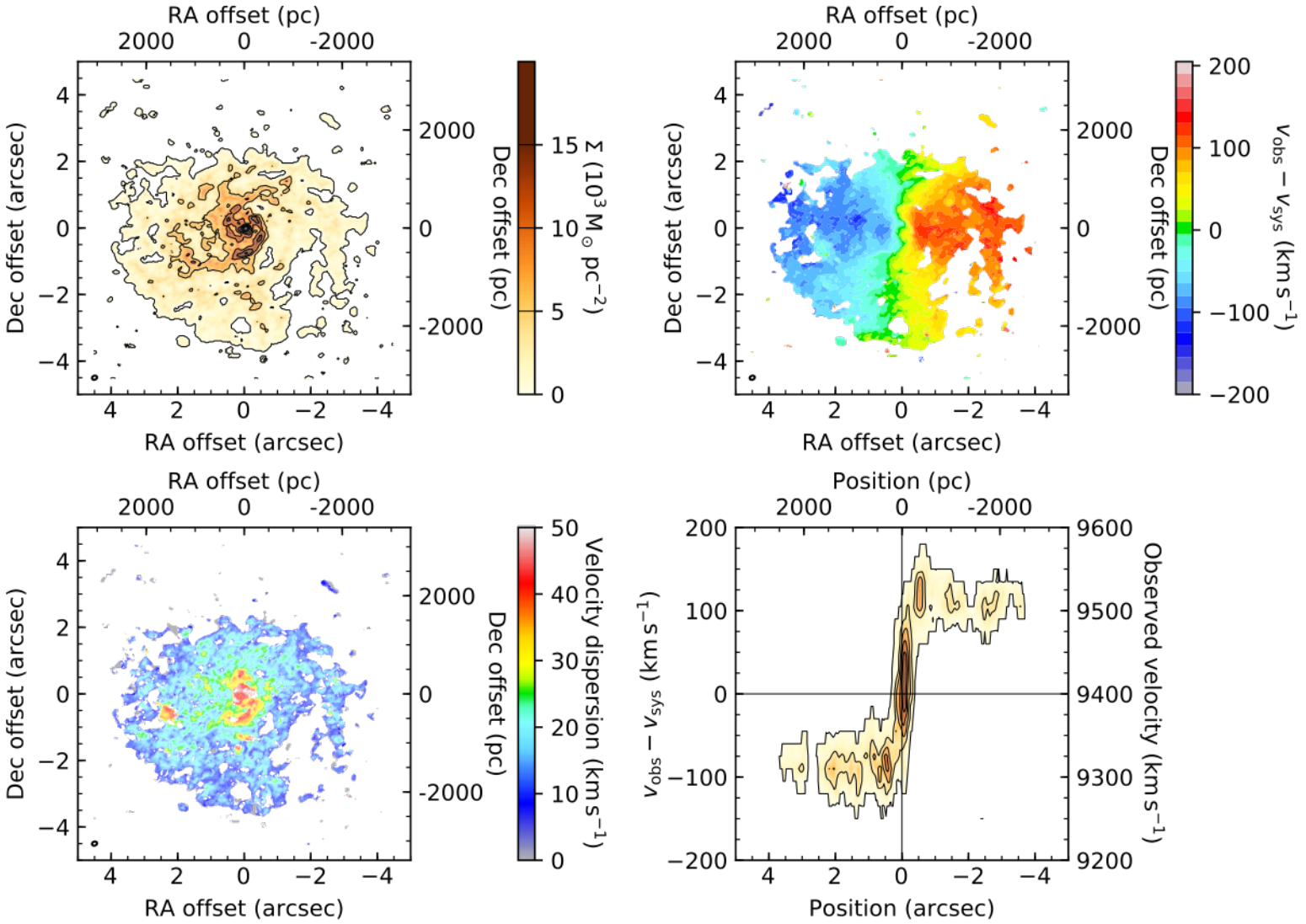

Figure 5.9: Moment maps of the ^{12}CO(2-1) emission of Mrk 567, from our ALMA observations. **Top-left:** Molecular gas surface density, assuming a CO-to-H_2 conversion factor $\alpha_{CO} = 4.3\,M_\odot\,(K\,km\,s^{-1})^{-1}\,pc^{-2}$. Black contours are from the level at which the noise was clipped, $15\,M_\odot\,pc^{-2}$, and then at $5000\,M_\odot\,pc^{-2}$ increments. **Top-right:** Mean line-of-sight velocity. **Bottom-left:** Line-of-sight velocity dispersion. **Bottom-right:** Kinematic major-axis position-velocity diagram. In both right panels, v_{obs} is the observed line-of-sight velocity and $v_{sys} = 9400\,km\,s^{-1}$ is the mean systemic velocity of the galaxy. The synthesised beam is shown in the bottom-left corner of each map.

5.5.4 NGC 3862

NGC 3862 (3C264) is famous for its very bright radio jets, that are even visible in the optical. We adopt a distance of 84.6 ± 8.5 Mpc (van den Bosch, 2016). Earlier Institut de Radioastronomie Millimétrique (IRAM) 30-m telescope observations detected CO emission with a double-horned profile (Lim et al., 2000).

The moment maps from our ALMA data (details in Table 5.5) are shown in Figure 5.10 and indicate a nearly face-on CO disc. Although the disc features a central hole, the PVD indicates that the rotation curve rises with decreasing radius to the smallest radii, consistent with motion around a compact central mass.

Optical images are contaminated by emission from the jet and the central AGN. However, a first-order MGE model can be constructed from an *HST* WFC3/F814W image by masking a 10 pixel (0.″46) wide strip along the jet. The resulting MGE components are listed in Table 5.6. Since the molecular gas disc appears to be at a very low inclination, we circularise the MGE as discussed in Section 2.4.5.

We construct a dynamical model as discussed in Chapters 2 and 3, adopting a `SkySampler` model of the molecular gas distribution, and infer a SMBH mass $M_{\rm BH} = 3.4^{+5.7}_{-1.5} \times 10^9\,{\rm M}_\odot$ and a radially-constant I-band stellar mass-to-light ratio $M/L_I = 3.0^{+4.5}_{-1.5}\,{\rm M}_\odot\,{\rm L}_\odot^{-1}$. The uncertainties are dominated by covariances with the inclination, that is only constrained to $i = 15 \pm 5°$. All quoted uncertainties are at the 3σ level. The best-fitting projected circular velocity curves are overlaid on the PVD in the lower-left panel of Figure 5.10. Although this best-fitting model matches well the observed velocities at the edge of the central hole, it underestimates the gas velocities at the outer edge of the disc, suggesting that a mass-to-light ratio gradient may be present.

Our SMBH mass is marginally larger than the $\approx 1 \times 10^9\,{\rm M}_\odot$ predicted from the $M_{\rm BH}$–σ_* relation (McConnell & Ma 2013; assuming $\sigma_* = 265\,{\rm km\,s^{-1}}$ from HyperLEDA[1]), but it is consistent within the intrinsic scatter of the relation. It is also consistent with the previous upper limit derived from ionised gas kinematics ($M_{\rm BH} < 2.8 \times 10^9\,{\rm M}_\odot$; Beifiori et al. 2009, corrected to our inclination).

[1] http://leda.univ-lyon1.fr

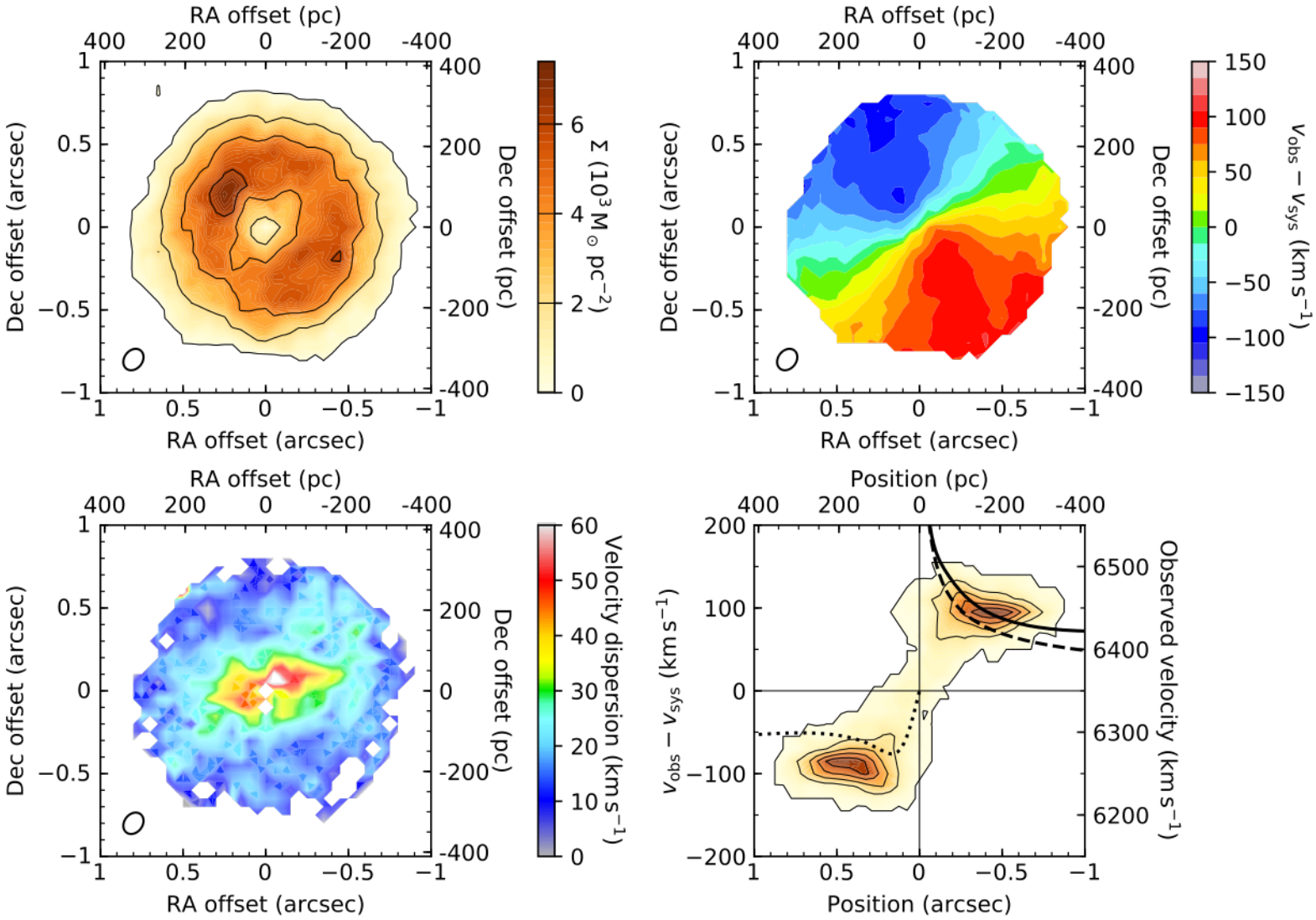

Figure 5.10: Moment maps of the ^{12}CO(2-1) emission of NGC 3862, from our ALMA observations. **Top-left:** Molecular gas surface density, assuming a CO-to-H_2 conversion factor $\alpha_{CO} = 4.3\,M_\odot\,(K\,km\,s^{-1})^{-1}\,pc^{-2}$. Black contours are from the level at which the noise was clipped, $15\,M_\odot\,pc^{-2}$, and then at 2000, 4000 and $6000\,M_\odot\,pc^{-2}$. **Top-right:** Mean line-of-sight velocity. **Bottom-left:** Line-of-sight velocity dispersion. **Bottom-right:** Kinematic major-axis position-velocity diagram. The black lines indicate the projected circular velocities from the SMBH alone (black dashed curve), the stars alone (black dotted curve), and from both together (black solid curve). In both right panels, v_{obs} is the observed line-of-sight velocity and $v_{sys} = 6350\,km\,s^{-1}$ is the mean systemic velocity of the galaxy. The synthesised beam is shown in the bottom-left corner of each map.

Table 5.6: Deconvolved 2D MGE components of NGC 3862 and NGC 4061.

$\log_{10}\left(\frac{I'_j}{\mathrm{L}_{\odot,I}\,\mathrm{pc}^{-2}}\right)$	$\log_{10}\left(\frac{\sigma_j}{\mathrm{arcsec}}\right)$	q'_j	$\log_{10}\left(\frac{I'_j}{\mathrm{L}_{\odot,I}\,\mathrm{pc}^{-2}}\right)$	$\log_{10}\left(\frac{\sigma_j}{\mathrm{arcsec}}\right)$	q'_j
(1)	(2)	(3)	(1)	(2)	(3)
NGC 3862 (*HST* WFC3/UVIS F814W)			NGC 4061 (*HST* WFPC2/PC F814W)		
5.90	−1.71	0.96	4.27	−1.76	0.90
4.96	−1.10	0.95	3.99	−0.48	0.84
3.60	0.13	0.98	3.68	−0.15	0.96
3.06	0.67	1.00	3.30	−0.03	0.76
			3.55	0.38	0.84

Notes: The tables list the central surface brightness (column 1), width (column 2) and axial ratio (column 3) of each de-convolved Gaussian component.

5.5.5 NGC 4061

NGC 4061 (also known as NGC 4055) is an elliptical galaxy with two large-scale radio jets (Jaffe et al., 1986) perpendicular to a central 2.3 kpc diameter regular dust disc. We adopt a distance of 107.2 Mpc from a Hubble flow model (Ma et al., 2014).

The literature reveals significant disagreement on the stellar velocity dispersion of NGC 4061. HyperLEDA lists $477 \pm 27\,\mathrm{km\,s^{-1}}$ (White et al. 1983; standardised to an aperture of 0.595 kpc radius), one of the largest dispersions recorded in the catalogue, suggesting in turn that the SMBH must be one of the most massive. However, Ma et al. (2014) list $270\,\mathrm{km\,s^{-1}}$. The predicted SMBH mass (and hence spheres of influence) are $2 \times 10^{10}\,\mathrm{M}_\odot$ (380 pc or 0.″73) and $1 \times 10^{9}\,\mathrm{M}_\odot$ (60 pc or 0.″12), respectively, using the McConnell & Ma (2013) M_{BH}–σ_* relation.

The Nuker team studied the nuclear region of NGC 4061 using stellar and H α kinematics. Although their observations should have resolved the SMBH sphere of influence predicted from HyperLEDA, no Keplerian motion was detected, and they suggested that the associated velocity dispersion may be erroneous (Pinkney et al., 2005). Initial attempts at modelling these kinematics estimated the SMBH mass to be $\approx 10^9\,\mathrm{M}_\odot$ (Pinkney et al. 2005), but this result was not subsequently published in the refereed literature.

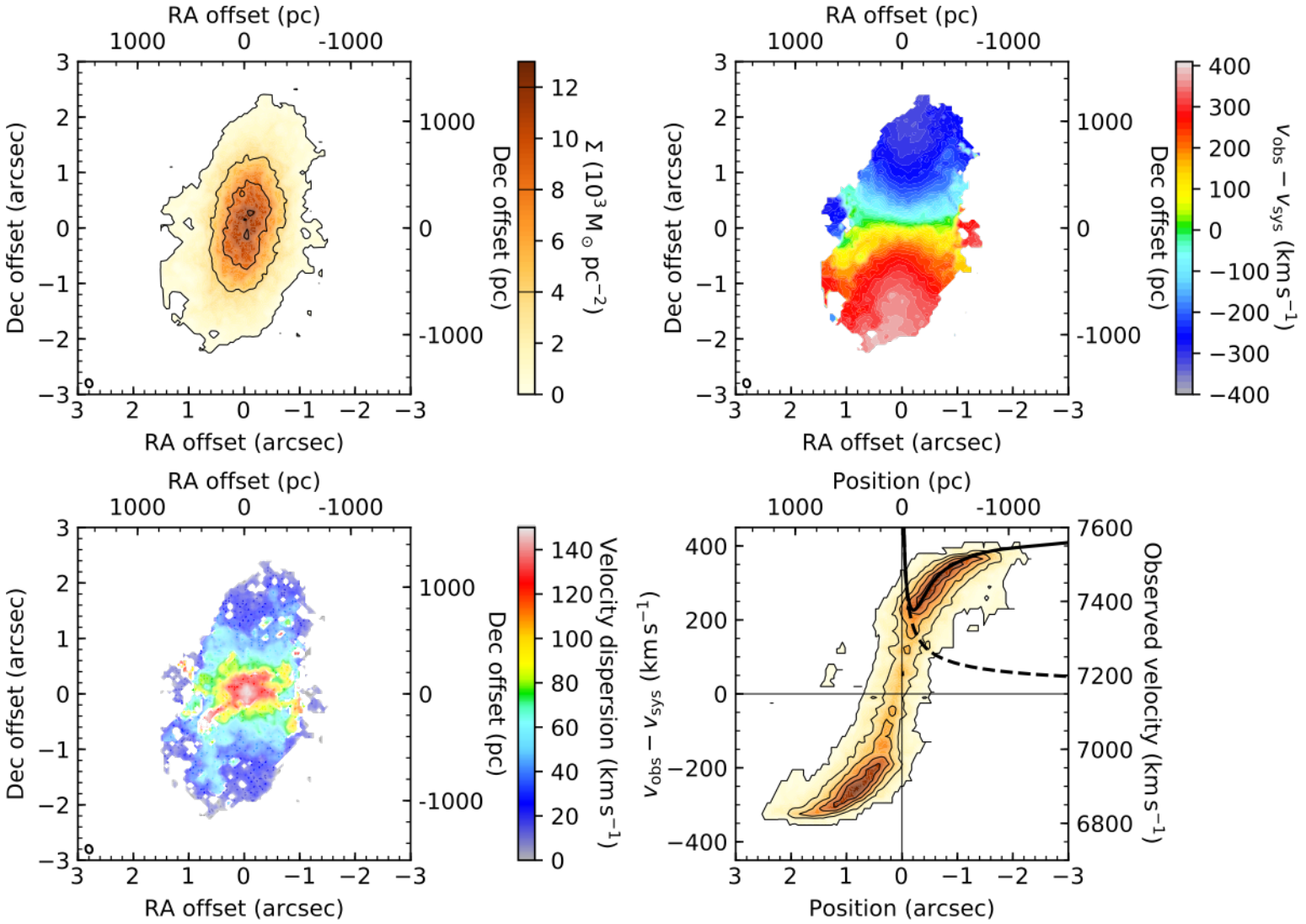

Figure 5.11: Moment maps of the ^{12}CO(2-1) emission of NGC 4061, from our ALMA observations. **Top-left:** Molecular gas surface density, assuming a CO-to-H_2 conversion factor $\alpha_{CO} = 4.3\,M_\odot\,(K\,km\,s^{-1})^{-1}\,pc^{-2}$. Black contours are from the level at which the noise was clipped, $15\,M_\odot\,pc^{-2}$, and then at 4000, 8000 and $12\,000\,M_\odot\,pc^{-2}$. **Top-right:** Mean line-of-sight velocity. **Bottom-left:** Line-of-sight velocity dispersion. **Bottom-right:** Kinematic major-axis position-velocity diagram. The black curves indicate circular motion due to the SMBH only(dashed) and in the total (SMBH and stars; black solid curve) potential. In both right panels, v_{obs} is the observed line-of-sight velocity and $v_{sys} = 7150\,km\,s^{-1}$ is the mean systemic velocity of the galaxy. The synthesised beam is shown in the bottom-left corner of each map.

Our ALMA observations are described in Table 5.5. We detect a nuclear continuum source that we fit with a 2D Gaussian, the properties of which are also listed in Table 5.5. The ^{12}CO(2-1) emission matches the dust disc very well. Small patches of red- and blue-shifted emission along the disc minor axis are consistent with the direction of the radio jets, suggesting that the jets are interacting with the disc.

Our observations do not exhibit central Keplerian rotation, indicating that the SMBH mass must be much smaller than that estimated from HyperLEDA ($\approx 10^{10}\,\mathrm{M}_\odot$). On this basis, a simple upper limit can be derived assuming that the sphere-of-influence is just spatially unresolved by the beam. If we adopt a velocity dispersion of $477\,\mathrm{km\,s^{-1}}$ ($270\,\mathrm{km\,s^{-1}}$), this implies $M_{\mathrm{BH}} \lesssim 3.1 \times 10^9\,\mathrm{M}_\odot$ ($\lesssim 1.0 \times 10^9\,\mathrm{M}_\odot$).

In fact, simple dynamical modelling (following the methods described in Chapters 2 and 3) yields a good constraint on the SMBH mass. We construct a MGE model of a *HST* WFPC2/PC F814W image (masking the foreground side of the dust disc; components listed in Table 5.6), adopt a spatially-constant stellar mass-to-light ratio and CO velocity dispersion, and adopt an exponentially-decaying ^{12}CO(2-1) surface brightness profile. The best-fitting SMBH mass is then $1.1^{+0.4}_{-0.3} \times 10^9\,\mathrm{M}_\odot$, with a stellar mass-to-light ratio of $4.3 \pm 0.3\,\mathrm{M}_\odot/\mathrm{L}_{\odot,I}$. These constraints suggest that the SMBH sphere of influence (assuming $\sigma_* = 270\,\mathrm{km\,s^{-1}}$) is only just spatially unresolved. Further study will be required to determine if this result is robust against a variation of our assumptions.

5.5.6 NGC 4261

NGC 4261 is an elliptical galaxy at a distance of 30 Mpc (Nolthenius, 1993; Ferrarese et al., 1996), hosting a famous dust disc (among the first ones detected in an elliptical galaxy; Jaffe et al., 1993). *HST* *R*-, *V*-, and *I*-band observations show this dust disc to be slightly offset from the optical isophotal centre, suggesting the dust originated externally, while the nuclear emission is also offset from the isophotal centre by about 3 pc, in the direction that would be expected from recoil from the radio jet (Ferrarese et al., 1996).

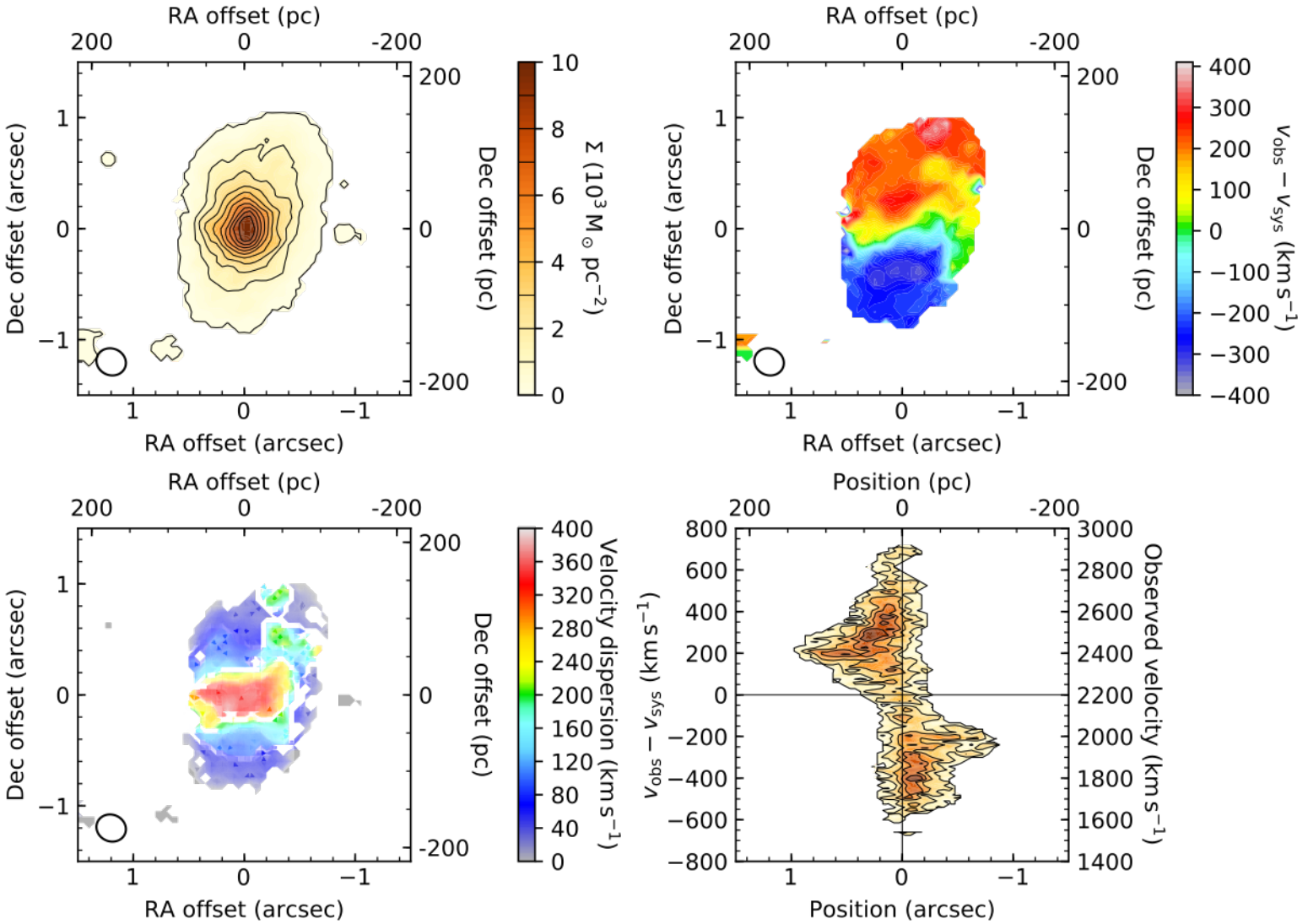

Figure 5.12: Moment maps of the ^{12}CO(2-1) emission of NGC 4261, from our ALMA observations. **Top-left:** Molecular gas surface density, assuming a CO-to-H_2 conversion factor $\alpha_{CO} = 4.3\,M_\odot\,(K\,km\,s^{-1})^{-1}\,pc^{-2}$. Black contours are from the level at which the noise was clipped, $15\,M_\odot\,pc^{-2}$, and then at $1000\,M_\odot\,pc^{-2}$ intervals. **Top-right:** Mean line-of-sight velocity. **Bottom-left:** Line-of-sight velocity dispersion. **Bottom-right:** Kinematic major-axis position-velocity diagram. In both right panels, v_{obs} is the observed line-of-sight velocity and $v_{sys} = 2200\,km\,s^{-1}$ is the mean systemic velocity of the galaxy. The synthesised beam is shown in the bottom-left corner of each map.

HST Faint Object Spectrograph observations of ionised gas at a variety of positions around the nucleus were presented by Ferrarese et al. (1996), and the [N II] emission line kinematics were fit with a Keplerian model to infer a SMBH mass $M_{\rm BH} = 4.9 \pm 1.0 \times 10^8\,{\rm M}_\odot$. The predicted sphere of influence, using this SMBH mass and $\sigma_* = 263 \pm 12\,{\rm km\,s^{-1}}$ (van den Bosch et al., 2016), is $31 \pm 7\,{\rm pc}$ ($0\farcs21 \pm 0\farcs05$). Nuclear maser emission was detected by Wagner (2013), however no attempt has yet been made to follow-up with VLBI to independently measure the SMBH mass.

The presence of a central dust disc, the existing dynamical SMBH mass measurement, and the easily resolvable sphere of influence made this galaxy a suitable target for a molecular gas measurement of the SMBH mass, in spite of an earlier non-detection of CO emission by Okuda et al. (2013). It was thus observed using ALMA by both the WISDOM team and another group (at different spatial resolutions). The data discussed below combine the tracks from both sets of observations.

Although the CO(2-1) emission appears to originate in a disc, the CO kinematics appear to show two distinct rotating components (Figure 5.12): a large-scale disc with a radius of approximately $1''$, and an inner disc of radius $\approx 0\farcs5$. The molecular gas velocity dispersions are large, rising to $\approx 380\,{\rm km\,s^{-1}}$ in the centre. The major-axis PVD does show increasing velocities with decreasing radii, but the high velocity dispersions and complicated kinematics make determining a SMBH mass challenging.

5.5.7 NGC 5995

NGC 5995 is a Seyfert-2 galaxy with large-scale spiral structure revealed by a *HST* WFPC2 F606W image (Malkan et al., 1998). Our CO observations (Table 5.5 and Figure 5.13) show similar spiral structures within an outer ring. The zero-velocity isovelocity contour (green) in the velocity field shows deviations from the minor axis due to this spiral perturbation. Although the kinematic major-axis PVD indicates the CO velocities peak in the nuclear region ($r < 500\,{\rm pc}$), the deviations from circular motion are non-negligible and will require bespoke modelling.

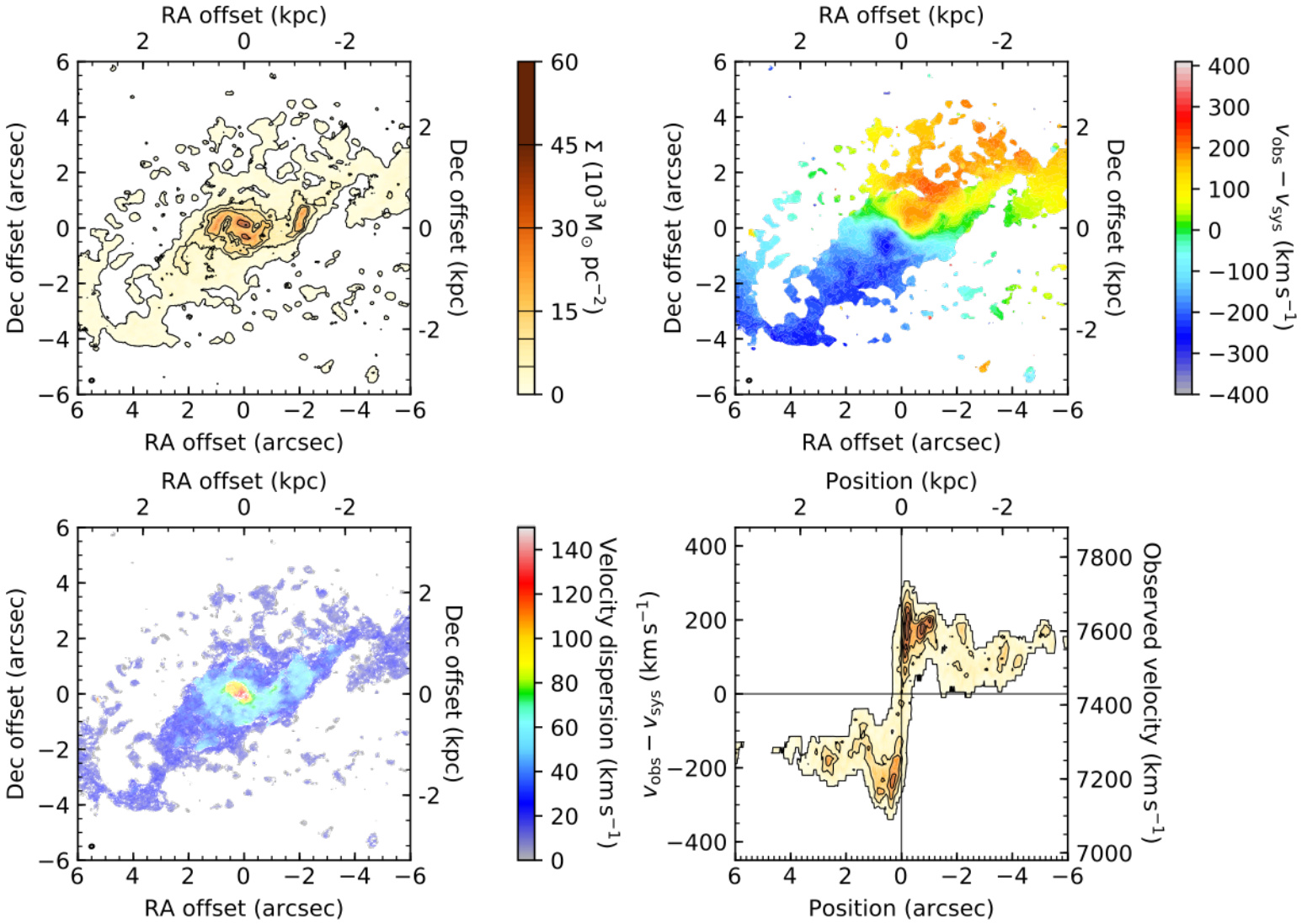

Figure 5.13: Moment maps of the ^{12}CO(2-1) emission of NGC 5995, from our ALMA observations. **Top-left:** Molecular gas surface density, assuming a CO-to-H_2 conversion factor $\alpha_{CO} = 4.3\,M_\odot\,(K\,km\,s^{-1})^{-1}\,pc^{-2}$. Black contours are from the level at which the noise was clipped, $15\,M_\odot\,pc^{-2}$, to $15\,000\,M_\odot\,pc^{-2}$ in $5000\,M_\odot\,pc^{-2}$ intervals, and then to $60\,000\,M_\odot\,pc^{-2}$ in $15\,000\,M_\odot\,pc^{-2}$ intervals. **Top-right:** Mean line-of-sight velocity. **Bottom-left:** Line-of-sight velocity dispersion. **Bottom-right:** Kinematic major-axis position-velocity diagram (PVD). In both right panels, v_{obs} is the observed line-of-sight velocity and $v_{sys} = 7430\,km\,s^{-1}$ is the mean systemic velocity of the galaxy. The synthesised beam is shown in the bottom-left corner of each map.

5.6 Conclusions

The galaxies discussed in this chapter were studied as part of three distinct WISDOM projects. NGC 1194, NGC 3393 and NGC 5765b were all observed as part of a study to establish whether maser galaxies host molecular gas discs suitable for high-resolution observations, themselves aiming to measure their SMBH masses and thereby cross-check the molecular gas method. Unfortunately, none of these three galaxies has such a suitable disc, NGC 1194 being too faint in CO, and NGC 3393 and NGC 5765b both revealing CO kinematics strongly perturbed by non-axisymmetries. NGC 4501 was observed as part of a study targeting spiral galaxies, and it exhibits dramatically-perturbed nuclear molecular gas kinematics.

The remaining seven galaxies were observed as part of a study of galaxies at the high-σ_* end of the $M_{\rm BH}-\sigma_*$ relation. Although their SMBH spheres of influence were not spatially resolved, three of these galaxies (Frl 49, NGC 3862, and NGC 4061) nevertheless exhibit enhanced molecular gas central velocities, allowing their SMBH masses to be estimated via dynamical modelling. Two of these galaxies (Mrk 567 and NGC 5995) exhibit spiral perturbations in the centre and will therefore require more sophisticated modelling. The remaining two galaxies (Frl 1146 and NGC 4261) have high molecular gas velocity dispersions in their nuclear regions, implying that pressure-support is non-negligible. NGC 4261 also appears to harbour two distinct dynamical components.

The observations discussed in this chapter, although not as promising for SMBH mass measurements as the two cases presented in Chapters 2 and 3, indicate the natural next steps in the WISDOM project, which will be discussed further in Section 6.4. They also illustrate the incredible potential of ALMA to unlock the power of molecular gas kinematics observations in a variety of local galaxies, and the opportunity for such observations to illuminate a range of questions regarding the dynamical evolution of galaxies.

6 Conclusions

Contents

6.1 Summary

SMBH masses are now widely known to correlate with a variety of properties of their host galaxies. The tightest correlation among these is the $M_{\rm BH}$–σ_* relation, where σ_* is the stellar velocity dispersion, typically averaged over $1\,R_{\rm e}$. Correlations are also found with the host galaxy bulge mass or luminosity, the central concentration (Sérsic) index, and spiral arm winding angle. Although some authors have claimed to find correlations with the asymptotic velocity at large radii, total mass/luminosity, and halo mass, others have disputed these claims.

These correlations are tighter than would be expected from the simple premise that 'big galaxies contain big black holes', and they are now conventionally interpreted as indicating some form of self-regulating growth process. That a

SMBH, with gravitational influence only on very small spatial scales, could affect the evolution of a galaxy several orders of magnitude larger remains a surprising result.

Multiple physical processes have been proposed to underpin this mutual evolution, principally reflecting the dispute over whether SMBHs grow primarily through secular accretion, episodic accretion, or mergers. AGN feedback is supported by increasingly sophisticated simulations, permitting the SMBH to regulate accretion on small scales and influence the galaxy on large scales, but these correlations are no tighter in active galaxies. That the tightest correlations are with the properties of merger-formed bulges suggests that merger histories are important, yet bulge-less galaxies still exhibit sufficiently tight correlations to imply co-evolution. Further work is required to unravel the relative importance of these mechanisms.

The most reliable SMBH masses are derived from high-spatial resolution observations of dynamical tracers in the SMBH-dominated regions of the potentials. Stars, ionised gas, and masers have regularly been used. However, each of these suffers from significant and mutually exclusive selection effects, implying they can rarely be used to cross-check one another. Moreover, the measurements yielded from each tracer can be biased by different effects.

Molecular gas observations, enabled by the latest millimetre-wave long-baseline interferometers, can help to solve some of these issues. Molecular gas, as traced by CO emission, often appears to remain dynamically cold in the centre of a galaxy, apparently less susceptible to non-gravitational forces than ionised gas.

In Chapter 2, we presented a molecular gas measurement of the SMBH mass in the lenticular galaxy NGC 524. ALMA observations revealed a nearly face-on molecular gas disc, exhibiting regular rotation about a compact central 1.3 mm continuum source. However, this gas disc featured a central hole, implying there is no gas to sample the region dominated by the SMBH. The velocities of the gas molecules on the edge of this hole were nevertheless enhanced compared to those expected from the stars only, indicating the presence of a nuclear mass concentration.

We forward-modelled the CO(2-1) line observations within a Markov Chain Monte Carlo framework. The stellar contribution was estimated with a multi-Gaussian expansion of I-band optical images, multiplied by a spatially-constant mass-to-light ratio. No other mass contribution was significant. The inferred SMBH mass was $4.0^{+3.5}_{-2.0} \times 10^8\,\mathrm{M}_\odot$ and the I-band mass-to-light ratio $5.7^{+3.9}_{-1.9}\,\mathrm{M}_\odot/\mathrm{L}_{\odot,\mathrm{I}}$.

Although the WISDOM team had published SMBH mass measurements previously, our work on NGC 524 introduced several new methods now used in our analyses. Firstly, previous results had unphysically small formal uncertainties, caused by the extremely large number of constraints available when fitting an entire data cube. We thus introduced a rescaled log-likelihood function intended to compensate for this effect, and validated that the new uncertainties are consistent with those estimated via bootstrapping fits to sub-sections of the data cube. Secondly, we introduced the new `SkySampler` tool for modelling clumpy and/or complex gas distributions. This tool extracts the three-dimensional coordinates of a large number of point sources that replicate the observed gas distributions. This avoids the need to introduce very large numbers of uninteresting parameters to model complicated surface brightness distributions. `SkySampler` also trivially allows the use of non-axisymmetric distributions. Although NGC 524 did not require this new tool, we were able to validate that it yields the same SMBH mass. `SkySampler` has subsequently been used with other galaxies (including others presented in this thesis) whose molecular gas distributions cannot be represented by simple axisymmetric functions.

The very low inclination of NGC 524 meant that the SMBH mass uncertainties were dominated by those in the inclination. This effect was so strong that it appeared to over-ride the conservation of total dynamical mass in the 2D marginalisation of the covariance between SMBH mass and stellar mass. We however showed that by fixing the inclination (using information not contained in the ALMA observations), the expected covariances were recovered. The inclination uncertainties were then reintroduced to the SMBH mass and stellar mass-to-light ratio *ex post facto* by Monte-Carlo methods.

The observed gas velocity and velocity dispersion fields revealed a distortion at a radius of $\approx 2\farcs5$. We showed that the enhanced velocity dispersions were consistent with beam-smearing of the distorted velocities. We then decomposed the observed velocity field into its circular harmonics, assuming either a constant inclination and position angle, or a tilted-ring model. The distorted gas velocities could be interpreted as either a position-angle warp or a radially-varying inflow; these two phenomena are degenerate in our observations.

In Chapter 3, we presented ALMA observations of the elliptical galaxy NGC 7052. These detected CO gas in Keplerian rotation around a central compact object, and we were able to measure a SMBH mass $M_{\rm BH} = 2.5 \pm 0.3 \times 10^9\,{\rm M}_\odot$ and a stellar mass-to-light ratio $M/L_I = 3.9 \pm 0.2\,{\rm M}_\odot/{\rm L}_{\odot,{\rm I}}$ using the same methods as for NGC 524. A slight asymmetry in the Keplerian velocity profile was shown to be due to an asymmetry in the galaxy's molecular gas distribution, that `SkySampler` correctly recovered.

Our observations strongly excluded the previous SMBH mass measurement from ionised gas kinematics. We argued that our measurement significantly betters and thus supersedes this, as the ionised gas exhibits high velocity dispersions close to the SMBH that were not accounted for dynamically (leading to an underestimate of the SMBH mass).

Finally, we considered the role that tidal forces play in disrupting molecular clouds. We showed that the gas distribution in NGC 7052 peaks at the radius where the tidal term in the cloud energy budget changes sign. Within this radius, tidal acceleration disrupts rather than confines clouds. If this term is dominant (or, more likely, if the other terms are finely balanced by the self-gravity of the cloud), the disrupted clouds will no longer enable the efficient formation of molecules nor shield these molecules from photo-dissociation. We note, however, that other explanations such as central photo-dissociation by the AGN or the molecular gas being better traced by other CO transitions are of course possible.

In Chapter 4 we presented a correlation between the line width of CO emission spatially-integrated on kiloparsec scales ($\Delta V_{\rm CO}$) and the central SMBH mass.

This work made use of the reasonably large number of dynamical SMBH mass measurements now available in the literature, archival CO observations, and two new programmes of observations.

The correlation is expected as rotating CO discs are typically found on scales similar to those used to measure stellar velocity dispersions. They thus trace the same (star-dominated) component of the potential. Thus, this correlation can be viewed as being analogous to the $M_{\rm BH}-\sigma_*$ relation.

CO spectra were obtained from either single-dish telescopes or short-baseline interferometric observations. The data cubes produced by the latter were spatially integrated within a mask, to synthesise global spectra at very high signal-to-noise ratios. The resulting spectra were fit using a 'Gaussian double-peaked line profile', expected from a regularly-rotating disc. Spectra not exhibiting this profile were excluded from the study, as we concluded that either the molecular gas is kinematically disturbed or the observations do not reach the flat part of the galaxy's rotation curve.

A reasonably tight correlation between CO line width and SMBH mass was obtained, although our $\Delta V_{\rm CO}-\sigma_*$ correlation had larger scatter. Most significantly, the intrinsic scatter of our tightest correlation (using only spatially-resolved CO observations and early-type galaxies) was only 0.6 dex in SMBH mass, larger than the 0.3 dex in the standard $M_{\rm BH}-\sigma_*$ relation, but comparable to the accepted correlations with other host galaxy properties. We therefore proposed that, in the absence of a measurement of σ_*, and in cases where a bulge/disc decomposition is either impossible or too laborious, CO line widths are reasonable proxies of SMBH masses. As a simple demonstration, we used our correlation and the CO line widths from the COLDGASS survey to estimate the SMBH mass function in the local universe, finding that it is consistent with that found using the local AGN luminosity function (assuming a physically-reasonable accretion model).

The limitations of this study are however the extreme heterogeneity of the observations and SMBH mass measurements used. Further limiting the applicability of this result to other galaxies is the need to verify that the CO disc extends

sufficiently far to reach the flat part of the rotation curve in each galaxy, to check that the disc exhibits regular rotation, and to measure the inclination of the disc. These problems are all mitigated by using spatially-resolved observations.

Chapter 5 contains unpublished material on some other galaxies that were imaged but which were not immediately suitable for SMBH mass measurements. Three of these galaxies (NGC 1194, NGC 3393 and NGC 5765b) host megamasers, and were originally intended to cross-check our molecular gas SMBH mass measurements (masers being the only other method capable of resolving equivalent spatial scales). These were the only galaxies we identified suitable for performing such cross-checks. However, the CO emission in NGC 1194 is too faint for higher-resolution follow-up observations to resolve the SMBH sphere of influence to detect emission in reasonable integration times, and the molecular gas in NGC 3393 and NGC 5765b exhibit strong non-circular motions, and in consequence none of these galaxies are suitable for SMBH mass measurements. NGC 4501 similarly exhibits very significant deviations from circular rotation, particularly in the centre of the galaxy. The other seven galaxies were observed as part of our effort to measure SMBH masses at the high end of the σ_* distribution, at which the $M_{\rm BH}-\sigma_*$ appears to saturate. Simple dynamical models allowed SMBH masses to be measured in three of these galaxies (Frl 49, NGC 3862, and NGC 4061), two exhibit central spiral perturbations leading to non-circular motions (Mrk 567 and NGC 5995), and two have high central gas dispersions indicating that disc has non-negligible pressure support (Frl 1146 and NGC 4261).

In the remainder of this Chapter, we will determine the $M_{\rm BH}-\sigma_*$ relation from molecular gas measurements alone, compare molecular gas results to the current 'gold-standard' maser measurements, and propose the next steps for our work.

6.2 Molecular gas $M_{\rm BH}-\sigma_*$ relation

VER the past seven years, SMBH masses have been measured in thirteen galaxies using molecular gas kinematics (see Table 6.1). This homogeneously-measured sample is now sufficiently large to allow us

Table 6.1: SMBH mass measurements using molecular gas kinematics.

Galaxy	Morphology	σ_* ($\mathrm{km\,s^{-1}}$)	$M_{\rm BH}$ ($M_\odot$)	$M_{\rm BH}$ reference
Frl 49	Sa	-	$3.2^{+6.9}_{-1.5} \times 10^8$	Chapter 5
NGC 383	S0	239 ± 16	$4.2^{+0.7}_{-0.7} \times 10^9$	North et al. (2019)
NGC 404	S0	25 ± 5	$5.3^{+1.5}_{-0.6} \times 10^5$	Davis et al. (2020)
NGC 524	S0	220 ± 10	$4.0^{+3.5}_{-2.0} \times 10^8$	Smith et al. (2019), Chapter 2
NGC 1097	Sb	196 ± 5	$1.4^{+0.3}_{-0.2} \times 10^8$	Onishi et al. (2015)
NGC 1332*	S0	330 ± 15	$6.6^{+0.6}_{-0.6} \times 10^8$	Barth et al. (2016a)
NGC 3258*	E1	260 ± 10	$2.30^{+0.02}_{-0.02} \times 10^9$	Boizelle et al. (2019)
NGC 3504*	Sb	120 ± 10	$1.1^{+0.1}_{-0.1} \times 10^7$	Nguyen et al. (2020)
NGC 3665	S0	216 ± 10	$5.8^{+1.5}_{-1.2} \times 10^8$	Onishi et al. (2017)
NGC 3862	E	265 ± 10	$3.4^{+5.7}_{-1.5} \times 10^9$	Chapter 5
NGC 4061	E	270 ± 10	$1.1^{+0.4}_{-0.3} \times 10^9$	Chapter 5
NGC 4429	S0	177 ± 7	$1.5^{+0.2}_{-0.4} \times 10^8$	Davis et al. (2018a)
NGC 4526	S0	222 ± 10	$4.5^{+4.2}_{-3.0} \times 10^8$	Davis et al. (2013b)
NGC 4697	E6	169 ± 7	$1.3^{+0.2}_{-0.2} \times 10^5$	Davis et al. (2017a)
NGC 7052	E	284 ± 12	$2.4^{+0.3}_{-0.3} \times 10^9$	Smith et al. (2021b); Chapter 3

Notes: Galaxies not marked with an asterisk (*) were studied by the WISDOM team. All measurements are based on ALMA observations of CO emission, except NGC 3665 and NGC 4526 (CARMA) and NGC 1097 (HCN emission).

to estimate the $M_{\rm BH}$–σ_* relation using molecular gas measurements only. We use the `HyperFit` package (Robotham & Obreschkow, 2015) via the web interface[1] to fit these data, minimising the scatter orthogonal to the relation and providing an estimated intrinsic scatter. We do not include the dwarf galaxy NGC 404, as its SMBH mass sufficiently departs from the relation defined by the rest of the sample as to have a disproportionate effect on the derived slope.

The best-fitting $M_{\rm BH}$–σ_* relation using only molecular gas measurements is

$$\log\left(\frac{M_{\rm BH}}{\mathrm{M}_\odot}\right) = (8.61 \pm 2.76)\log\left(\frac{\sigma_*}{200\,\mathrm{km\,s^{-1}}}\right) + (8.30 \pm 0.23)\,, \qquad (6.1)$$

with a total scatter of 0.52 dex and an intrinsic scatter of 0.49 ± 0.21 dex, both in the $\log M_{\rm BH}$ direction. Although the intrinsic scatter is slightly larger than that found in other studies, it is consistent with the typical intrinsic scatter (0.3 dex). This inferred $M_{\rm BH}$–σ_* relation is shown in Figure 6.1, along with that found by McConnell & Ma (2013) for reference.

[1] http://hyperfit.icrar.org

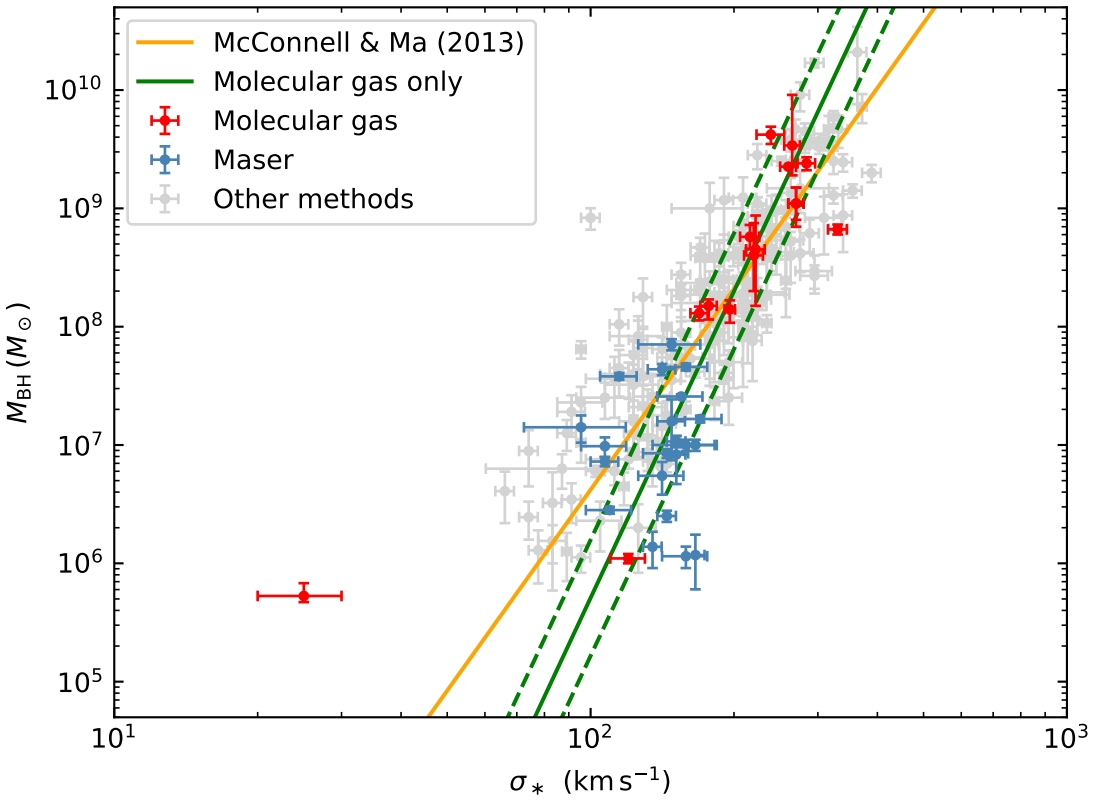

Figure 6.1: $M_{\rm BH}-\sigma_*$ relation from molecular gas measurements only, excluding NGC 404 (green solid line, $\pm1\sigma$ intrinsic scatter indicated by the green dashed lines), and from measurements from all methods (orange solid line; McConnell & Ma 2013). SMBH mass measurements from molecular gas observations are shown by red points, from maser dynamics by blue points, and from other tracers by grey points (Table 6.1 and van den Bosch 2016). Error bars on data points are $\pm3\sigma$, but exclude distance uncertainties.

The inferred $M_{\rm BH}-\sigma_*$ relation is steeper than found by other studies. It is known that the maser measurements (shown in blue in Figure 6.1) are almost all systematically below the canonical $M_{\rm BH}-\sigma_*$ (e.g. Greene et al., 2010, 2016). However, they appear to be consistent with the molecular gas $M_{\rm BH}-\sigma_*$ relation. Since the maser measurements are widely agreed to be the most precise tracers of the SMBH potentials, as they probe radii closer to the SMBHs than other tracers, this consistency is encouraging (although preliminary). A naïve view of this result would be that stellar, ionised gas, and reverberation mapping estimates systematically overestimate SMBH masses. However, it seems more likely that these methods have only traced the most massive SMBH at a given σ_* due to the limited

angular resolutions available (as discussed further in Section 6.4.1.2). Molecular gas measurements of SMBH masses in the $10^6-10^8\,M_\odot$ regime, taking advantage of the higher angular resolutions available from interferometry and thereby potentially tracing the full population, would allow us to test these hypotheses. The slope of our $M_{BH}-\sigma_*$ relation also has relatively large uncertainties. This results from the fact that, with the exception of the dwarf galaxy NGC 404, all the molecular gas measurements are of massive SMBHs ($M_{BH} > 10^8\,M_\odot$), yielding only a small mass range to constrain the slope. If we include NGC 404, in the fit we derive a $M_{BH}-\sigma_*$ relation that is significantly shallower (with a slope of 4.1 ± 0.6), in much better agreement with other studies. It is thus essential to fill in the $10^6-10^8\,M_\odot$ mass range to adequately constrain the slope.

Although the WISDOM survey has observed galaxies across the Hubble sequence, most of our published SMBH mass measurements so far are in early-type galaxies, principally due to the increased complexity of dynamical modelling of non-axisymmetric potentials and/or disturbed gas kinematics. In Chapter 5, we presented observations of several such galaxies, demonstrating that non-circular motions often dominate at very small radii. In principle, at SMBH-dominated spatial scales, the galactic potential should be spherically symmetric, but even these regions can be affected by non-circular motions arising from non-gravitational forces, including e.g. material inflowing from larger radii. It is thus more challenging, though not impossible, to measure SMBH masses with molecular gas in the $10^6-10^8\,M_\odot$ regime. It might, for instance, be possible to use modelling approaches common in stellar dynamics, assuming that the molecular gas is confined to compact cloud structures (rather than a continuous diffuse disc) and is thus collisionless but with significant pressure support (leading to the use of e.g. the Jeans equations).

6.3 Comparing molecular gas to masers

MASER dynamics have long been viewed as the 'gold standard' to trace the potentials around SMBHs. Maser emission can be observed with very long baseline interferometers, resolving spatial scales unachievable

with any other instrument. This means the maser emission can be resolved much closer to the SMBHs than any other tracer, yielding the tightest constraints on the SMBH's masses. In addition, the motions of megamasers can be traced on decadal cadences to yield proper motions, and hence eliminate distance uncertainties. On the other hand, maser emission is very rare and is only found in Seyfert galaxies. In consequence, masers cannot be relied on to provide accurate SMBH masses for many galaxies (even less for an unbiased galaxy sample).

With ALMA, we can achieve angular resolutions of $\approx 0\farcs02$ at ^{12}CO(2-1). Although in principle higher frequencies allow higher resolutions, ALMA does not currently routinely permit the longest baselines to be used at higher frequencies. The limiting resolution is thus approximately constant as a function of frequency.

Figure 6.1 shows that the maser and molecular methods have thus far probed different galaxy populations. However, a simple argument shows that the best molecular gas measurements are now probing the same spatial scales as masers. Assuming a tracer moves in circular motion around a central mass, the balance between gravity and the centrifugal force yields

$$\left(\frac{v}{c}\right) = \left(\frac{2r}{R_{\mathrm{Sch.}}}\right)^{-0.5} \quad , \tag{6.2}$$

where v is the circular velocity reached by a tracer at the smallest radius probed r, c the speed of light, and $R_{\mathrm{Sch.}}$ the SMBH's Schwarzschild radius. Every SMBH mass measurement derived from circular Keplerian motion must, by construction, lie on this function. Figure 6.2 thus shows the smallest resolved radius and maximum central velocity in the observations from which each SMBH mass was derived. NGC 524 (Chapter 2; labelled in Figure 6.2) deviates from this relation as the ALMA observations of NGC 524 do not spatially-resolve the Keplerian motions due to the presence of the central hole in the gas disc. Three molecular gas SMBH mass measurements, in NGC 404 (Davis et al., 2020), NGC 3504 (Nguyen et al., 2020), and NGC 4429 (Davis et al., 2018a), are omitted from the plot due to the large uncertainties on the number of Schwarzschild radii resolved, in turn due to the large uncertainties on their SMBH masses. All three are consistent

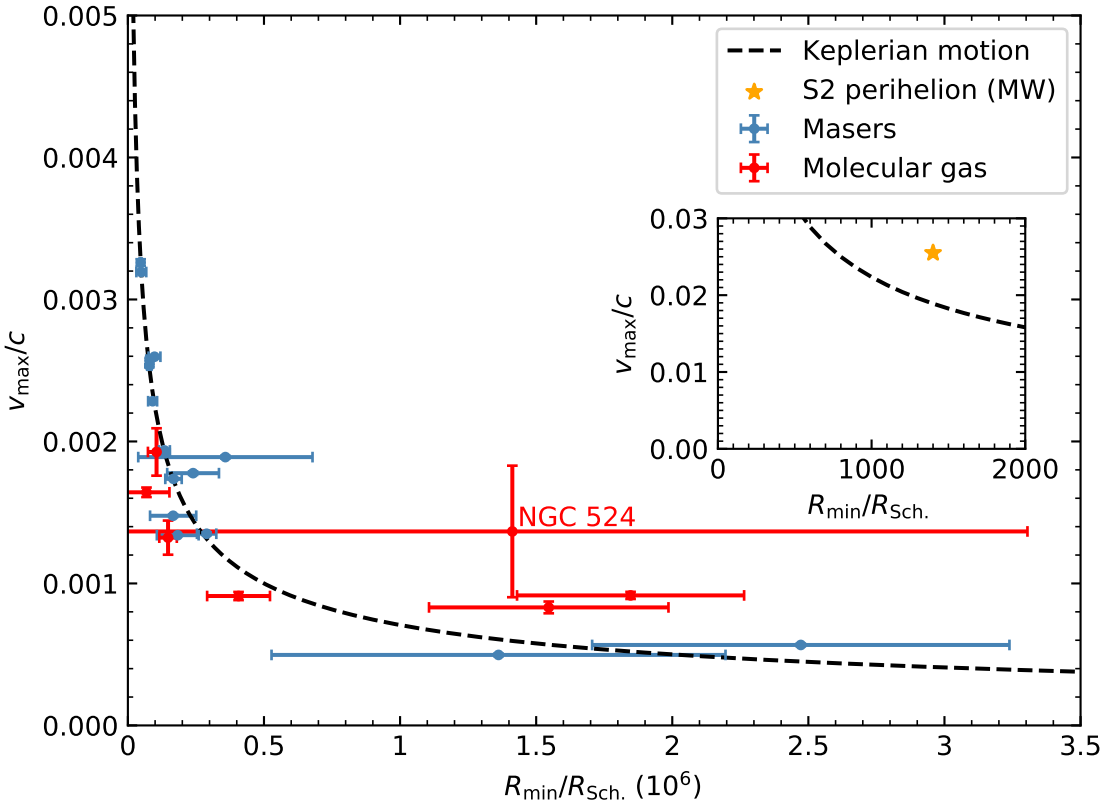

Figure 6.2: Number of Schwarzschild radii resolved using molecular gas (red) and maser (blue) observations as a function of the SMBH masses inferred. If a tracer's motion is circular and Keplerian, each measurement should follow black dashed line (Equation 6.2). The inset panel shows the corresponding quantities for star S2 in the Galactic centre at perihelion (orange star; Gravity Collaboration et al. 2018), that due to its elliptical orbit and relativistic effects departs slightly from the black dashed line. The uncertainties in S2 are smaller than the data point. Maser observations are from Gao et al. (2016, 2017), Greenhill et al. (1997), Herrnstein et al. (2005), Kondratko et al. (2008b), Kuo et al. (2011), Mamyoda et al. (2009), and Zhao et al. (2018). Molecular gas measurements are listed in Table 6.1, but omit NGC 404 and NGC 4429, both of which have very large SMBH mass and hence $R_{min}/R_{Sch.}$ uncertainties. NGC 524 (Chapter 2) is shown, but we do not resolve the Keplerian motions due to the central hole in the gas disc, and the low inclination leads to large uncertainties on both M_{BH} (and hence $R_{min}/R_{Sch.}$) and v_{max}.

with Equation 6.2 within their (large) uncertainties. The preliminary results from Chapter 5 are also omitted.

Although the angular resolution attainable with VLBI observations (≈1 milliarcsec) is better than those attainable with ALMA (10 − 100 milliarcsec), the smaller SMBH masses in the generally farther maser galaxies imply that molecular gas observations resolve comparable numbers of Schwarzschild radii. The highest resolution molecular gas measurement so far, in NGC 383 (North et al., 2019), attained a radius of ≈100 000 $R_{\mathrm{Sch.}}$, well within the typical range of radii resolved in maser galaxies (see Figure 6.2). This shows that molecular gas observations that resolve Keplerian motion should be considered as accurate as maser measurements (especially considering the much larger number of independent measurements in the very inner regions), and using the longest ALMA baselines on the largest SMBH may even outperform masers.

Having said that, the molecular gas observations generally have larger uncertainties, particularly in the scaled radii. The minimum radius probed by a maser is a very well-defined quantity, as the position of the innermost masing (red- or blue-shifted) source is known to very high precision. Extracting this radius from a molecular gas PVD is more challenging as the gas distribution is continuous, and thus the radius attained is not very well defined. The main contributions to the molecular gas velocity uncertainties are from the disc inclinations, but NGC 524 is the only galaxy for which this uncertainty is significant.

6.4 Future work

This thesis has demonstrated the power of molecular gas dynamics, as resolved with the latest interferometers, to explore the centres of galaxies on scales where the galactic potentials are dominated by the SMBHs.

In this section, we consider the key scientific questions of the coming decades in this field, the role that high-resolution molecular gas observations can play to answer them, and anticipate the potential of technical advances.

6.4.1 New SMBH measurements

The relatively small number of published molecular gas-enabled SMBH mass measurements imply that increasing the sample is a pertinent scientific goal in itself. However, there are a few ranges of galaxy parameters that are particularly important to explore better as they pertain to key scientific questions.

6.4.1.1 High-mass SMBHs

This thesis has presented two SMBH mass measurements at the highest mass range of the SMBH mass function. This range is particularly interesting as the stellar velocity dispersions of galaxies appear to saturate as they continue to grow more luminous (e.g. Oegerle & Hoessel, 1991b; Lauer et al., 2007; Nigoche-Netro et al., 2010). This is because the highest mass galaxies principally grow by dry major mergers, thus increasing their stellar luminosities without increasing σ_* in their central parts (e.g. Hilz et al., 2012, 2013; Cappellari et al., 2013b).

This process has implications for SMBH–host galaxy property correlations (e.g. Lauer et al., 2007; Kormendy, 2016). A SMBH that grows principally by secular accretion (mainly of gas, though rare tidal disruption events also allow nearby stars to feed the accretion disc) would no longer grow in gas-poor ETGs, and dry mergers would have minimal effects. This implies that the $M_{\rm BH}-\sigma_*$ relation would be a single power law and the $M_{\rm BH}-L_{\rm bulge}$ relation would saturate. We would thus find no SMBH that exceeds some maximum mass. Conversely, a SMBH that grows principally by mergers would continue to grow, with opposite conclusions.

Although Lauer et al. (2007) suggested that it is the $M_{\rm BH}-\sigma_*$ relation that saturates, rather than the $M_{\rm BH}-L_{\rm bulge}$ relation, there was no dynamical SMBH mass measurement available to test this hypothesis at the time. Direct evidence for a saturated $M_{\rm BH}-\sigma_*$ relation is still provided by only a few SMBH masses ($\approx$7 in McConnell & Ma 2013, all from stellar dynamics), that are all above the power-law predictions. However, we established in Section 1.2 that SMBH mass measurements with dynamical tracers are biased towards the largest SMBHs at any given σ_*. It is thus unclear whether these masses are representative of the

entire SMBH population at large σ_*, or are merely the upper envelope of a broader population consistent with the relation extrapolated from lower σ_*.

My ALMA programmes 2017.1.00904.S and 2018.1.00397.S were specifically designed to probe this region of parameter space, selecting galaxies with predicted $M_{\rm BH} > 10^9\,{\rm M}_\odot$ and with predicted spheres of influence resolvable with ALMA. NGC 7052 (Chapter 3) was the first of these galaxies to be modelled due to its spatially-resolved central Keplerian rotation. Observations of the other galaxies in these programmes were not delivered until late 2019, and initial analyses were presented in Chapter 5. Keplerian rotation was only observed in one galaxy (NGC 3862), although we were able to measure the SMBH masses via the enhanced central velocities in Frl 49 and NGC 4061, although the former lacks an observed σ_* that will be required to place it on the $M_{\rm BH}$–σ_* plane. The lack of Keplerian rotation in the other galaxies suggests that the SMBH masses are smaller than predicted, and it is possible that these data will only yield upper limits (although limits still help to constrain the high-σ_* regime).

6.4.1.2 Spiral galaxies

We mentioned in Section 6.2 that maser-derived SMBH masses appear to be systematically below the canonical $M_{\rm BH}$–σ_* relation. A similar effect is found in the $M_{\rm BH}$–$L_{\rm bulge}$ relation (Läsker et al., 2016). Greene et al. (2016) discussed three possible explanations for this: non-maser measurements trace only the upper edge of a broader distribution of SMBH masses, masers preferentially occur in low-$M_{\rm BH}$ galaxies, or maser measurements systematically select galaxies that are still growing their SMBHs to ultimately reach the $M_{\rm BH}$–σ_* relation.

If masers better trace the true population of SMBHs, then stellar and gas dynamical measurements are systematically missing the low-mass SMBHs. We already know that these observations can only resolve the spheres of influence of the largest black holes at a given distance, so if a low-mass population exists it will have been missed by measurements based on these tracers. Given this, however, a sufficiently large number of maser measurements should yield SMBH masses

as large as those found by other tracers, in addition to the low-mass population. In this scenario, the scatter of the SMBH masses among these galaxies would be larger than that measured for ellipticals. This would accord with the merger-dominated model of SMBH growth, since having experienced very few (if any) mergers in their history, spirals would not yet have converged to the $M_{\rm BH}-\sigma_*$ relation (e.g. Jahnke & Macciò, 2011).

If non-maser measurements do trace the main population of SMBHs, it is likely because the maser-derived SMBH masses constitute a systematically biased sample. We already know that masers are only detected in very few (and only active) galaxies. Maser discs are very rare in massive galaxies, either because their accretion discs are unstable, or because of a shortage of gas to form such discs in the first place. At lower SMBH masses, masers may not be detected either because the presence of central dust and star formation somehow hinders maser formation, or because Eddington-limited accretion is still too faint to be detected (e.g. Greene & Ho, 2007; Reines et al., 2013; van den Bosch et al., 2016). This would imply that masers are only found in a narrow range of SMBH masses, that may be systematically biased low compared to the bulk of the $M_{\rm BH}-\sigma_*$ relation.

Finally, it is possible that the present sample of maser measurements is purely composed of galaxies that, post-merger, have already stabilised in σ_* but which are still growing their SMBHs (through either secular accretion or a future SMBH-SMBH merger; e.g. Grupe & Mathur 2004; Ho et al. 2008; Kim et al. 2008). Greene et al. (2016) however argue that this scenario is highly unlikely, as the timescales for SMBH growth are much shorter than those for bulge assembly (see also Greene et al. 2010).

Molecular gas dynamics offer an exceptional discriminant between these possibilities. ALMA can resolve a $1.4\times10^6\,{\rm M}_\odot$ SMBH up to 10 Mpc and a $4.5\times10^7\,{\rm M}_\odot$ SMBH up to 100 Mpc, and late-type galaxies normally host large molecular gas reservoirs. Notwithstanding the additional complications to model molecular gas dynamics in spiral galaxies (see Section 6.2), a significant number of SMBH mass measurements could be made in this regime. These can resolve spheres of influence

smaller than possible with stellar or gas dynamics, and they are not subject to the active-galaxy biases affecting maser measurements.

6.4.1.3 Dwarf galaxies and intermediate-mass black holes

Very few dynamical SMBH mass measurements in dwarf galaxies have been published to date. These galaxies are likely to have the smallest SMBH masses ($<10^6\,M_\odot$) and they have a strong leverage on the slope of the $M_{BH}-\sigma_*$ relation, as illustrated in Section 6.2. However, as the velocity dispersions of these galaxies are very small, their relative uncertainties are also usually very large, giving individual galaxies low statistical weights.

The principal challenge to measure SMBH masses in dwarf galaxies are the small spheres of influence. Davis (2014) showed that ALMA can only resolve the sphere of influence of a $10^6\,M_\odot$ SMBH if it is nearer than 10 Mpc. Future ALMA upgrades may extend this limit as far as 100 Mpc (see Section 6.4.2), but such upgrades are unlikely before the 2040s.

Nevertheless, a small number of (very local) dwarf galaxies can already be targeted. WISDOM has measured the SMBH mass in the dwarf elliptical galaxy NGC 404 (Davis et al., 2020), using the methods and the `SkySampler` tool presented in Chapters 2 and 3. The Measuring Black Holes Below the Milky Way mass galaxies (MBHBM*) project observed seven such galaxies, finding regularly-rotating molecular gas discs in five, with new higher-resolution ALMA observations due in 2020-21 to spatially-resolve the SMBH spheres of influence. The SMBH mass in the spiral galaxy NGC 3504 has recently been measured from these observations (Nguyen et al., 2020).

The ongoing search for evidence of intermediate-mass black holes (IMBHs; defined for our purposes as black holes with a mass $100-10^5\,M_\odot$) is motivated by the desire to identify the seeds from which the current SMBHs grew (see Section 1.3.3). ALMA observations are unsuited for contributing to this search, as most IMBH are likely to be found outside galactic nuclei and thus searches for them will require large fields of view. However, ALMA may be able to serve for dynamical follow-up

of potential targets, at least for candidates within the Milky Way. Analogous observations of proto-planetary discs (most famously TW Hydra) have resolved physical scales of order 1 AU at a distance of ≈60 pc (e.g. Andrews et al., 2016), and 150 AU at 15 kpc (roughly the size of the Milky Way). At this distance, gas in Keplerian motion around an IMBH of mass $10^5\,M_\odot$ would rotate at ≈750 km s^{-1}. Studies searching for IMBHs close to Sgr A* using ionised (Tsuboi et al., 2019) and molecular gas (e.g. Tokuyama et al., 2019; Takekawa et al., 2019, 2020) dynamics are ongoing and likely to mature over the next few years (Greene et al., 2020).

6.4.1.4 Cross-checking of SMBH masses with multiple techniques

Gas and stellar dynamical measurements dominate the present sample of SMBH mass measurements. However, due to the biases outlined in Section 1.2, very few galaxies satisfy the selection criteria of two, let alone multiple, tracers. When SMBH masses have been measured using multiple techniques, the derived masses often differ substantially, although these differences are also often mitigated by large uncertainties.

Cross-checking SMBH mass measurements with multiple independent tracers is important for three reasons. Firstly, it tests whether the derived masses are robust against varying assumptions. Secondly, it allows us to check for systematic biases between different samples. Thirdly, independent constraints can reduce the uncertainties on the combined measurements.

In principle, high-precision maser measurements would be the preferred method, as argued above (Section 6.3), but the rarity of maser emission means this is not practicable. We have however also shown in Section 6.3 that molecular gas measurements can reach the same spatial scales, and hence could also be suitable. There are a substantial number of suitable molecular gas targets, as the selection criteria are less stringent than those of other tracers. The high spatial resolution attainable with ALMA implies that any SMBH sphere of influence resolved by ground-based or space-based (Hubble) optical images can also be resolved by

ALMA, and large molecular gas reservoirs are common enough so that a reasonable number of targets accessible.

Thus far, for the few molecular gas measurements for which robust measurements using other tracers exist, the derived SMBH masses from the two methods are generally consistent within the uncertainties, although these uncertainties are generally relatively large (typically a factor of 2-3). We attempted to cross-check our molecular gas measurements with maser measurements, and discussed the three galaxies observed in Chapter 5. These three galaxies unfortunately all have kinematically disturbed molecular gas discs, so masses cannot be robustly determined. They are also the only three galaxies both hosting masers, having sufficient CO emission, and for which the SMBH sphere of influence can be resolved with ALMA. Although it is possible that at even higher angular resolution the CO discs of NGC 1194 and NGC 5765b will reveal undisturbed Keplerian motions (as found in NGC 404; Davis et al. 2020), currently we cannot compare our measurements to masers on an object-by-object basis.

Nevertheless, a future ALMA programme targeting a substantial sample of galaxies with stellar and ionised-gas SMBH mass measurements would provide a valuable cross-check linking these two most prolific tracers to ours.

6.4.1.5 Distant universe

Davis (2014) showed that, given sufficient sensitivity, ALMA can spatially resolve the spheres of influence of SMBHs with masses exceeding $10^8\,M_\odot$ at any redshift (see also Section 6.4.2). However, to detect molecular gas at increasingly large distances would require increasingly long integration times. An interferometer is sensitive to given surface brightnesses, not given molecular gas masses. In a static universe, the surface brightness is constant with distance D, as although the flux decreases as D^{-2}, the physical area covered by a given solid angle also increases by D^2. However, in an expanding universe, the surface brightness falls by $(1+z)^4$, dramatically decreasing the perceived surface brightness even by $z = 1$.

A simple estimate of the molecular gas surface density that can be detected in a given integration time is made as follows. We assume the Planck Collaboration et al. (2016) cosmology, and that gas emission along any line of sight is concentrated in a single $15\,\mathrm{km\,s^{-1}}$ channel (roughly the velocity dispersions observed in the molecular gas of WISDOM galaxies). We consider the molecular gas surface density that would be detected with a signal-to-noise of unity by the most extended ALMA configuration, that has an angular resolution of $0\farcs018$ at ^{12}CO(2-1). We further assume the local CO-to-H_2 conversion factor at all redshifts (Carilli & Walter, 2013; Carleton et al., 2017) and a line ratio of unity. The molecular gas surface density then detectable at a given distance and in a given observing time is shown in Figure 6.3.

Typical local galaxies in the WISDOM sample have surface densities in the range $100-20\,000\,\mathrm{M_\odot\,pc^{-1}}$, and these can be detected at $0\farcs1$ resolution in relatively short integration times (see Figure 6.3). However, at higher redshifts the required integration times increase rapidly. The mean molecular gas surface densities found by the PHIBBS survey over $1<z<3$ are no larger than local galaxies. Although attempting to detect high-velocity molecular gas around an SMBH at $z\approx0.2$ is plausible, the same cannot be said for $z\approx1$.

Naturally, at higher redshifts the observed frequency of the CO emission lines will also change. Fortunately, ALMA bands 4 to 7 provide continuous frequency coverage from 125 to 373 GHz (allowing the CO(2-1) line to be observed up to $z=0.84$), and band 3 covers 84 to 116 GHz ($0.98<z<1.74$). Bands 1 and 2, when completed, would further extend coverage to $z<5.5$. Even in the gaps between bands, the other low-J CO lines are accessible.

The ALMA sensitivity limit can be mitigated by exploiting gravitational lensing. Using simulations of strong lenses, Hezaveh et al. (2015) showed that given plausible galaxy density profiles and lens parameters, a 10 hr ALMA observation provides sufficient sensitivity to accurately recover an SMBH mass at $z\approx0.5$.

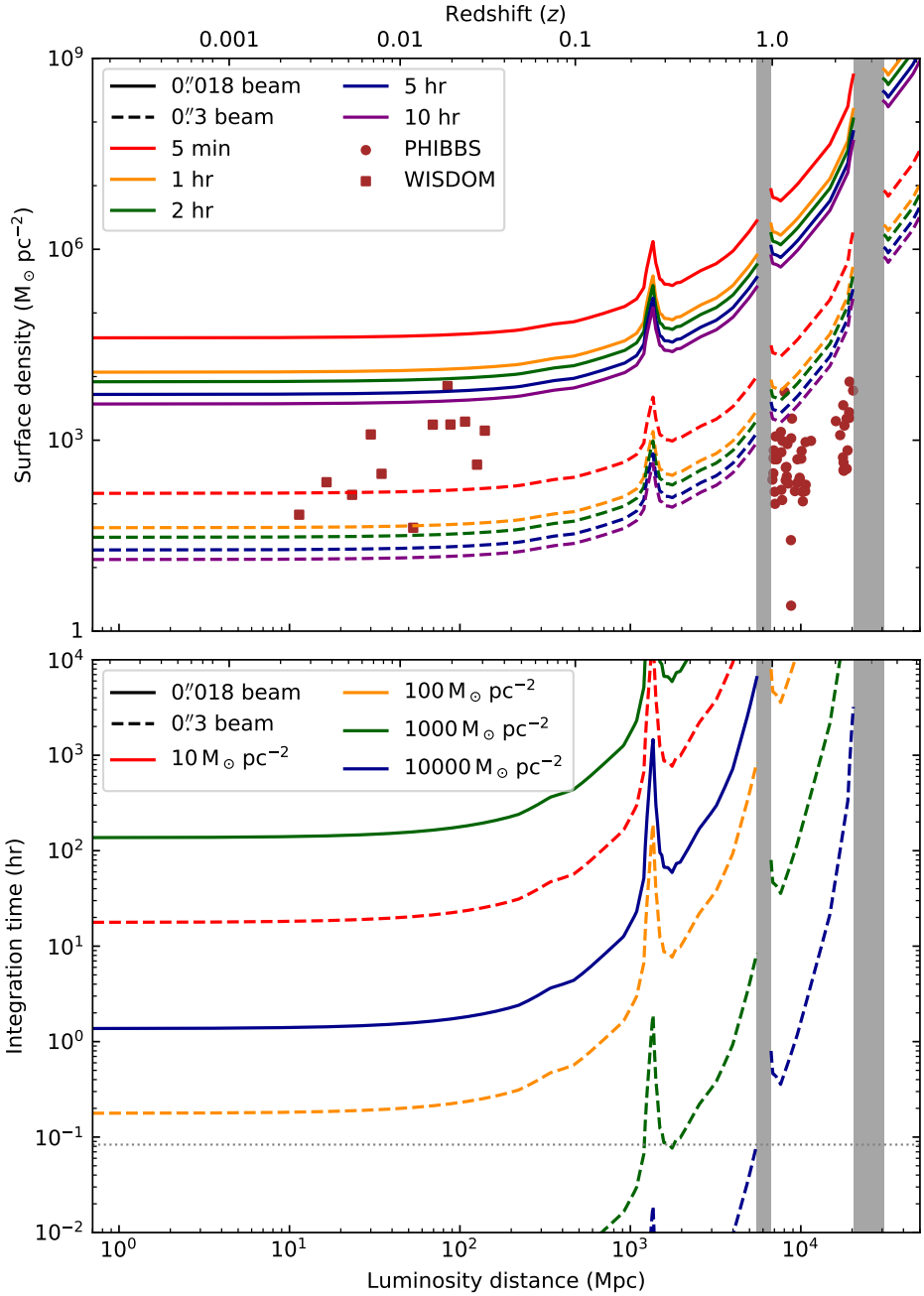

Figure 6.3: Top panel: Molecular gas surface density detectable at various integration times as a function of redshift. **Bottom panel:** Integration time required to detect a given molecular gas surface density as a function of redshift. Both panels show results for the most extended ALMA configuration (solid lines) and an intermediate configuration (dashed lines). Brown points indicate the mean molecular gas surface densities of galaxies in the WISDOM (squares; z<0.1) and PHIBBS (circles; 1<z<3; Tacconi et al. 2013) samples. We assume the use of the ^{12}CO(2-1) emission line, a line ratio of unity, $X_{\rm CO} = 2 \times 10^{20} {\rm mol\,cm^{-2}(K\,km\,s^{-1})^{-1}}$, that emission is confined to a single 15 km s^{-1} channel, and a source at $\delta = 0°$, and a detection at signal-to-noise ratio of unity. Redshifts assume the Planck Collaboration et al. (2016) cosmology. The peaks occur due to the variation of $T_{\rm sys}$ with frequency, while the grey boxes indicate the gaps in frequency coverage between bands 1 and 2 and bands 3 and 4. The dotted horizontal line in the bottom panel is an integration time of 5 min, the minimum allowed by the ALMA observing tool.

6.4.1.6 New modelling tools

The early-type galaxies studied in the WISDOM programme have dynamically cold molecular gas discs ($v/\sigma \gg 1$), with intrinsic velocity dispersions $\sigma \lesssim 20\,\mathrm{km\,s^{-1}}$. However, some of the late-type galaxies (including some shown in Chapter 5) exhibit non-negligible velocity dispersions in the central parts, that exceed the enhanced dispersions expected from beam smearing. Neglecting the dynamical contribution of these random motions would then lead to an underestimate of the SMBH mass, as we have discussed in Section 3.5.4.

An alternative assumption might be that the gas consists of collisionless cloudlets that can be modelled using the Jeans equations. This approach was adopted by Häring-Neumayer et al. (2006) to model [Fe II] emission in Centaurus A (NGC 5128), leading to an SMBH mass that differed by a factor of 3 from that found by assuming instead a dynamically cold thin disc. Although this effect is likely to be smaller in molecular gas, a natural extension of our existing approach would be to calculate the velocities appropriate for individual `KinMS` particles using the Jeans Anisotropic Modelling (JAM) modelling tool (e.g. Cappellari 2008, 2012). This would allow us to explore the impact of varying this assumption, providing an alternative limiting case.

However, this approach alone is insufficient, as the JAM routines are only appropriate for axisymmetric galaxies. At extremely high spatial resolutions, where the potential is dominated by the SMBH, the potential is in fact spherically symmetric. However, as we have already shown in this thesis (e.g. Sections 2.6, 5.5.3 and 5.5.7), non-axisymmetric potentials (and non-gravitational forces) can have a significant influence on the molecular gas dynamics at larger scales. This will require us to either over-resolve the SMBH spheres of influence or introduce models of bars, spiral arms, and other morphological features, potentially dramatically increasing the computational complexity of our forward-modelling processes.

6.4.2 ALMA improvements

Reaching smaller SMBHs and/or galaxies beyond the local universe will require even higher angular resolutions than currently available. In the short term, improvements

to the ALMA calibration pipeline should allow the reclassification of long baselines at high frequencies as 'standard operating modes'. This would enable modest increases of the angular resolutions available by moving to ^{12}CO(3-2) without using the most extended ALMA configurations.

The ALMA development roadmap for the next decade (Carpenter et al., 2019, 2020) proposes three developments relevant to our purposes: increasing the number of antennae, adding even longer baselines, and improving the receivers.

The original ALMA scope included 64 12-m antennae, but only 50 were constructed for cost reasons. Increasing the number of antennae by 14 is possible without further correlator improvements, as the correlator was constructed to be functional with the full array. Most significantly, this would improve the *uv*-plane coverage, particularly in the longest baselines, suppressing side lobes. The number of baselines scales as the square of the number of antennae, so a small increase in the number of antennae can nevertheless be significant. Adding 14 antennae will raise the number of baselines from 1225 to 2016, a 65% increase. These additional baselines will also improve self-calibration. Less significantly, the total array area would increase by a factor of 30%, thereby slightly reducing the time required to attain a required sensitivity. Additional *uv*-plane coverage would improve ALMA images in general, but would specifically help mitigate imaging artefacts at the highest spatial resolutions, as used in the WISDOM project.

The limiting resolution of an interferometer is set by its longest baseline, which for ALMA is currently is 16.2 km. Additional antenna sites beyond the existing array would extend this limit. However, adding a few antennae at long distances adds multiple complications (e.g. Bolatto et al., 2015). First, ALMA currently operates an annual schedule of antenna movements, transporting the dishes between locations (using purpose-built vehicles) to vary the configuration, and hence the attainable resolution and maximum recoverable scale. Significantly longer baselines will require dedicated (fixed) antennae, as it will not be practical to move antennae over such long distances. Second, unlike VLBI observations, ALMA observations are processed by the correlator in real time. Increasing the distances between the antennae and

the correlator will lead to expensive fibre connections, transmission delays that need to be buffered on arrival, or the need to adapt to off-line processing for the longest baselines. Third, longer baselines suffer from decreased phase coherence. Finally, placing individual antennae at large distances from the core of the array will provide poor *uv*-plane coverage. The ALMA 2030 plan (Bolatto et al., 2015) therefore ultimately envisages at least five new antennae on a variety of sites in northern Chile (up to 300 km from the main ALMA site; Kameno et al. 2013), and potentially integrating the single 12-m antenna of the Large Latin-American Millimeter Array (LLAMA; currently under-construction) to provide a ≈180 km baseline (e.g. Bolatto et al., 2015).

Recent tests using a single 24 km baseline between the Operations Support Facility (OSF) and the Array Operations Site (AOS) have demonstrated that the existing fibre connections can provide sufficient fidelity over such distances, and that phase corrections are adequate, although further improvements will be required when all available baselines are used (Carpenter et al., 2020). The ALMA 2030 roadmap envisages constructing $25 - 30$ km baselines, as an intermediate step to 50 km baselines later on.

At 230 GHz, a 24 km baseline (from the AOS to the OSF) yields an angular resolution of $0\farcs011$, and 50 km baselines yields $0\farcs005$. These higher resolutions will enable us to spatially-resolve the spheres of influence of less massive SMBHs in the local universe, or of SMBHs of similar masses at greater distances. Figure 6.4 shows the minimum SMBH mass for which the corresponding sphere of influence can be resolved with the existing ALMA array at a given distance, assuming the stellar velocity dispersion given by the $M_{\rm BH}-\sigma_*$ relation (required to calculate the predicted size of the sphere of influence). The existing SMBH mass measurements are also shown for comparison. We note that a few measurements are not resolvable by ALMA, despite its angular resolution being comparable to or better than that of all other observatories. Some of these are maser measurements, using VLBI observations and hence even longer baselines, while others are estimates from reverberation mapping, that can be made with spatially-unresolved data. Currently, the SMBH

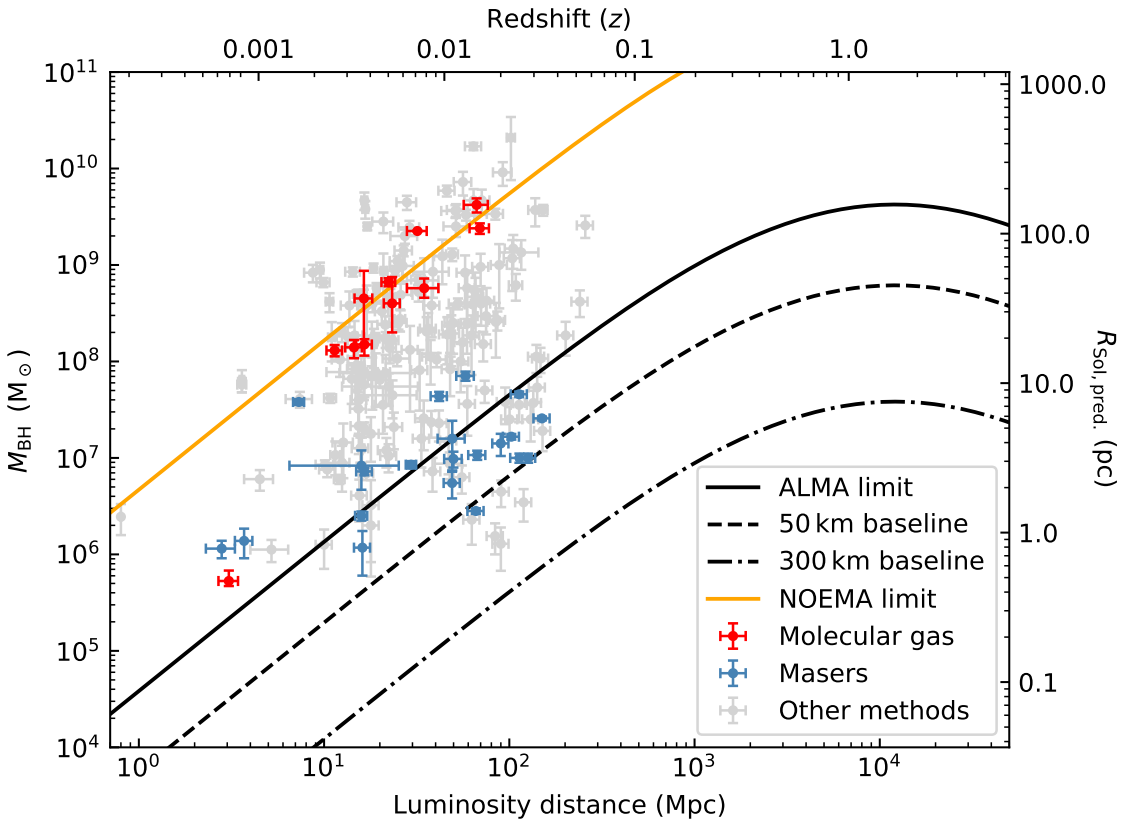

Figure 6.4: Minimum SMBH mass (left-ordinate) and sphere of influence (right-ordinate) that can be spatially-resolved at ^{12}CO(2-1) as a function of the distance to the target, for current ALMA (black solid line), a 50 km baseline (black dashed line), a 300 km baseline (dot-dashed line), and the most extended configuration of NOEMA (orange solid line), all assuming the $M_{BH}-\sigma_*$ relation of McConnell & Ma (2013). Data points with error bars show existing SMBH mass measurements, as compiled by van den Bosch (2016) for masers (blue) and other tracers (grey) and in Table 6.1 for molecular gas (red). Error bars are $\pm3\sigma$, although those in M_{BH} exclude distance uncertainties. Redshifts assume the Planck Collaboration et al. (2016) cosmology.

mass range ($10^6 - 10^{10}\,M_\odot$) can be probed only up to 10 Mpc, and the IMBH mass range ($10^4 - 10^6\,M_\odot$) only for the few nearest objects. Extending ALMA to 50 km baselines would enable SMBH masses to be measured at distances up to 50 Mpc and would allow to properly investigate the IMBH range (see Figure 6.4). By contrast, the largest array in the northern hemisphere offers only 0.″4 resolution at best, and thus can resolve the spheres of influence of only the largest SMBHs at any distance.

Figure 6.4 also shows that the published molecular gas measurements do not push the current ALMA limits. There are three practical and one technical reason for this. First, the early priorities were to measure the easiest SMBHs (i.e. the

largest SMBHs in the most local galaxies) to validate the molecular gas technique and develop the necessary tools. Second, in ALMA Cycles 5-7 (2017-2019) we were allocated only very few of the longest baseline observations requested, and hence the only masses measurable were those with $R_{\rm SoI} \gtrsim 0\farcs1$. Third, even at these distances, smaller SMBHs (mostly in LTGs) have proven harder to model due to the presence of significant non-circular motions (see Chapter 5). Finally, as we go to higher resolutions, the signal is divided over increasingly many synthesised beams. Observing smaller SMBH masses thus becomes more time-intensive. Since ALMA remains oversubscribed by at least a factor of 4 (ALMA Proposal Review Committee, 2017, 2018, 2019), it has been impractical to seek observations of any single target that exceed ≈1.5 hours. This has excluded all but the CO-brightest galaxies, but could be revised in the future.

The third development program is to upgrade the ALMA receivers and backends. The main priority of these projects is to double the bandwidths, not particularly useful to us as the CO emission lines are typically much narrower than the existing bandwidths. However, upgraded receivers are also likely to reduce noise, improving the sensitivity and hence reducing the required integration times. This will decrease the long integrations required at the highest spatial resolutions, that are currently prohibitively expensive.

6.4.3 Secular accretion and AGN fuelling

We discussed in Section 1.3.3 the role of secular accretion to both fuel AGN activity and grow SMBHs. The cold gas phase appears to be a significant source of fuel for both low- and high-excitation radio galaxies (L/HERGs; Hardcastle et al. 2007; Sanders 1981). Observations show that cold gas (and dust) masses are larger in radio-loud than radio-quiet galaxies (e.g. de Koff et al. 2000; Prandoni et al. 2007, 2010), suggesting 'cold-mode' accretion may power these radio jets.

Further recent studies have found cold gas clouds apparently falling towards galactic nuclei (e.g. Tremblay et al. 2016; Maccagni et al. 2018; Rose et al. 2019). ALMA observations of radio galaxies with 100 pc to 1 kpc resolutions are now

being used to investigate AGN fuelling and feedback (Ruffa et al., 2019a,b), radial gas motions providing further evidence of cold gas inflows as a part of the AGN fuelling cycle.

Our ALMA observations of galaxies in the WISDOM sample probe even smaller spatial scales, and several targets exhibit evidence of non-circular (i.e. radial) motions consistent with inflowing material. In this thesis, NGC 524 (Section 2.6), NGC 3393 (Section 5.3.2), NGC 4501 (Section 5.4) and NGC 5765b (Section 5.3.3) all offer the opportunity to further study the mechanisms transporting gas into the central molecular zones. For instance, mass inflow rates over the central kiloparsec have been estimated in a few local galaxies (and in the Milky Way) from analogous kinematic data (e.g. Sormani & Barnes 2019; Querejeta et al. 2016a,b), and similar methods could be applied to the WISDOM data.

6.5 Fin

THIS thesis has demonstrated the potential of interferometric observations of molecular gas within the spheres of influence of extragalactic SMBHs to measure these SMBHs' masses. These measurements will make a major contribution to our understanding of the co-evolution of SMBHs and their host galaxies. The next decade will see substantially more masses measured, and high-resolution molecular gas observations will revolutionise our understanding of gas dynamics in galactic nuclei.

Bibliography

ALMA Proposal Review Committee 2017, ALMA Cycle 5: Selection Statistics. Joint ALMA Observatory, https://almascience.eso.org/documents-and-tools/documents-and-tools/cycle5/alma-cycle5-stats

ALMA Proposal Review Committee 2018, ALMA Cycle 6: Selection Statistics. Joint ALMA Observatory, https://almascience.eso.org/documents-and-tools/documents-and-tools/cycle6/alma-cycle6-stats

ALMA Proposal Review Committee 2019, ALMA Cycle 7: Selection Statistics. Joint ALMA Observatory, https://almascience.eso.org/news/documents-and-tools/cycle7/alma-cycle7-stats

Abbott B. P., et al., 2017a, Phys. Rev. Lett., 118, 221101

Abbott B. P., et al., 2017b, Phys. Rev. Lett., 119, 141101

Abbott B. P., et al., 2017c, ApJ, 851, L35

Alatalo K., et al., 2013, MNRAS, 432, 1796

Allen D. A., Hyland A. R., Hillier D. J., 1990, MNRAS, 244, 706

Alonso-Herrero A., Simpson C., Ward M. J., Wilson A. S., 1998, ApJ, 495, 196

Anderson W., 1929, Zeitschrift fur Physik, 56, 851

Andrae R., 2010, preprint, arXiv:1009.2755

Andrews S. M., et al., 2016, ApJ, 820, L40

Athanassoula E., 1992, MNRAS, 259, 345

Baade W., Zwicky F., 1934, Physical Review, 46, 76

Baldry I. K., et al., 2012, MNRAS, 421, 621

Balick B., Brown R. L., 1974, ApJ, 194, 265

Barlow R. J., 1989, Statistics: a guide to the use of statistical methods in the physical sciences. Manchester physics series, Wiley, Chichester, West Sussex

Barth A. J., Ho L. C., Filippenko A. V., Rix H.-W., Sargent W. L. W., 2001, ApJ, 546, 205

Barth A. J., Martini P., Nelson C. H., Ho L. C., 2003, ApJ, 594, L95

Barth A. J., et al., 2013, ApJ, 769, 128

Barth A. J., Boizelle B. D., Darling J., Baker A. J., Buote D. A., Ho L. C., Walsh J. L., 2016a, ApJ, 822, L28

Barth A. J., Boizelle B. D., Darling J., Baker A. J., Buote D. A., Ho L. C., Walsh J. L., 2016b, ApJ, 822, L28

Barth A. J., Darling J., Baker A. J., Boizelle B. D., Buote D. A., Ho L. C., Walsh J. L., 2016c, ApJ, 823, 51

Baumgartner W. H., Tueller J., Markwardt C. B., Skinner G. K., Barthelmy S., Mushotzky R. F., Evans P. A., Gehrels N., 2013, ApJS, 207, 19

Begelman M. C., Volonteri M., Rees M. J., 2006, MNRAS, 370, 289

Beifiori A., Sarzi M., Corsini E. M., Dalla Bontà E., Pizzella A., Coccato L., Bertola F., 2009, ApJ, 692, 856

Beifiori A., Courteau S., Corsini E. M., Zhu Y., 2012, MNRAS, 419, 2497

Bennert V. N., Treu T., Woo J.-H., Malkan M. A., Le Bris A., Auger M. W., Gallagher S., Blandford R. D., 2010, ApJ, 708, 1507

Benson A. J., Bower R. G., Frenk C. S., Lacey C. G., Baugh C. M., Cole S., 2003, ApJ, 599, 38

Bertram T., Eckart A., Fischer S., Zuther J., Straubmeier C., Wisotzki L., Krips M., 2007, A&A, 470, 571

Binney J., Merrifield M., 1998, Galactic Astronomy. Princeton series in astrophysics, Princeton University Press, Princeton, New Jersey, USA

Binney J., Tremaine S., 2008, Galactic Dynamics: Second Edition. Princeton series in astrophysics, Princeton University Press, Princeton, New Jersey, USA

Blais-Ouellette S., Amram P., Carignan C., Swaters R., 2004, A&A, 420, 147

Blandford R. D., McKee C. F., 1982, ApJ, 255, 419

Boizelle B. D., Barth A. J., Darling J., Baker A. J., Buote D. A., Ho L. C., Walsh J. L., 2017, ApJ, 845, 170

Boizelle B. D., Barth A. J., Walsh J. L., Buote D. A., Baker A. J., Darling J., Ho L. C., 2019, ApJ, 881, 10

Bolatto A. D., et al., 2015, ASAC recommendations for ALMA 2030. ALMA Science Advisory Committee, http://www.eso.org/sci/facilities/alma/developmentstudies/ALMA2030-Reports.pdf

Bolton C. T., 1972, Nature, 235, 271

Bolton C. T., 1975, ApJ, 200, 269

Bosma A., van der Hulst J. M., Sullivan W. T. I., 1977, A&A, 57, 373

Bower R. G., Benson A. J., Malbon R., Helly J. C., Frenk C. S., Baugh C. M., Cole S., Lacey C. G., 2006, MNRAS, 370, 645

Braatz J. A., Wilson A. S., Henkel C., 1996, ApJS, 106, 51

Braatz J., Greenhill L., Moran J., Wilson A., Herrnstein J., 1997, in American Astronomical Society Meeting Abstracts. p. 104.02

Burbidge E. M., Burbidge G. R., Prendergast K. H., 1959, ApJ, 130, 739

Campitiello S., Celotti A., Ghisellini G., Sbarrato T., 2020, A&A, 640, A39

Canzian B., 1993, ApJ, 414, 487

Capetti A., Celotti A., 1999, MNRAS, 304, 434

Capetti A., Trussoni E., Celotti A., Feretti L., Chiaberge M., 2000, MNRAS, 318, 493

Capetti A., Celotti A., Chiaberge M., de Ruiter H. R., Fanti R., Morganti R., Parma P., 2002, A&A, 383, 104

Cappellari M., 2002, MNRAS, 333, 400

Cappellari M., 2008, MNRAS, 390, 71

Cappellari M., 2012, preprint, arXiv:1211.7009

Cappellari M., McDermid R. M., 2005, Classical and Quantum Gravity, 22, S347

Cappellari M., Verolme E. K., van der Marel R. P., Verdoes Kleijn G. A., Illingworth G. D., Franx M., Carollo C. M., de Zeeuw P. T., 2002, ApJ, 578, 787

Cappellari M., et al., 2006, MNRAS, 366, 1126

Cappellari M., et al., 2009, ApJ, 704, L34

Cappellari M., et al., 2013a, MNRAS, 432, 1709

Cappellari M., et al., 2013b, MNRAS, 432, 1862

Carilli C. L., Walter F., 2013, ARA&A, 51, 105

Carleton T., et al., 2017, MNRAS, 467, 4886

Carpenter J., Iono D., Testi L., Whyborn N., Wootten A., Evans N., 2019, preprint, arXiv:1902.02856

Carpenter J., Iono D., Kemper F., Wootten A., 2020, preprint, arXiv:2001.11076

Carter B., 1971, Phys. Rev. Lett., 26, 331

Casares J., 2007, in Karas V., Matt G., eds, IAU Symposium Vol. 238, Black Holes from Stars to Galaxies – Across the Range of Masses. pp 3–12 arXiv:astro-ph/0612312, doi:10.1017/S1743921307004590

Casasola V., Hunt L. K., Combes F., García-Burillo S., Neri R., 2011, A&A, 527, A92

Catinella B., et al., 2018, MNRAS, 476, 875

Cattaneo A., Haehnelt M. G., Rees M. J., 1999, MNRAS, 308, 77

Chandrasekhar S., 1931, MNRAS, 91, 456

Chandrasekhar S., 1935, MNRAS, 95, 207

Choi E., Ostriker J. P., Naab T., Somerville R. S., Hirschmann M., Núñez A., Hu C.-Y., Oser L., 2017, ApJ, 844, 31

Clavel J., et al., 1991, ApJ, 366, 64

Collin S., Kawaguchi T., Peterson B. M., Vestergaard M., 2006, A&A, 456, 75

Combes F., 2000, in Hammer F., Thuan T. X., Cayatte V., Guiderdoni B., Thanh Van J. T., eds, Building Galaxies; from the Primordial Universe to the Present. p. 413 arXiv:astro-ph/9904031

Combes F., 2008, in Bureau M., Athanassoula E., Barbuy B., eds, IAU Symposium Vol. 245, Formation and Evolution of Galaxy Bulges. pp 151–160 arXiv:0709.0091, doi:10.1017/S1743921308017535

Combes F., Young L. M., Bureau M., 2007, MNRAS, 377, 1795

Combes F., et al., 2019, A&A, 623, A79

Condon J. J., Frayer D. T., Broderick J. J., 1991, AJ, 101, 362

Cooke A. J., Baldwin J. A., Ferland G. J., Netzer H., Wilson A. S., 2000, ApJS, 129, 517

Courteau S., et al., 2014, Reviews of Modern Physics, 86, 47

Cresci G., et al., 2009, ApJ, 697, 115

Cretton N., van den Bosch F. C., 1999, ApJ, 514, 704

Cretton N., de Zeeuw P. T., van der Marel R. P., Rix H.-W., 1999, ApJS, 124, 383

Crocker A. F., Bureau M., Young L. M., Combes F., 2008, MNRAS, 386, 1811

Crocker A. F., Jeong H., Komugi S., Combes F., Bureau M., Young L. M., Yi S., 2009, MNRAS, 393, 1255

Crocker A. F., Bureau M., Young L. M., Combes F., 2011, MNRAS, 410, 1197

Croton D. J., et al., 2006, MNRAS, 365, 11

Curran S. J., Johansson L. E. B., Rydbeck G., Booth R. S., 1998, A&A, 338, 863

Czerny B., Hryniewicz K., 2011, A&A, 525, L8

Dalcanton J. J., et al., 2012, ApJS, 200, 18

Dame T. M., 2011, preprint, arXiv:1101.1499

Davies R. L., Efstathiou G., Fall S. M., Illingworth G., Schechter P. L., 1983, ApJ, 266, 41

Davies M. B., Miller M. C., Bellovary J. M., 2011, ApJ, 740, L42

Davis T. A., 2014, MNRAS, 443, 911

Davis T. A., McDermid R. M., 2017, MNRAS, 464, 453

Davis T. A., et al., 2011, MNRAS, 414, 968

Davis T. A., et al., 2013a, MNRAS, 429, 534

Davis T. A., Bureau M., Cappellari M., Sarzi M., Blitz L., 2013b, Nature, 494, 328

Davis T. A., Greene J., Ma C.-P., Pand ya V., Blakeslee J. P., McConnell N., Thomas J., 2016, MNRAS, 455, 214

Davis T. A., Bureau M., Onishi K., Cappellari M., Iguchi S., Sarzi M., 2017a, MNRAS, 468, 4675

Davis B. L., Graham A. W., Seigar M. S., 2017b, MNRAS, 471, 2187

Davis T. A., et al., 2018a, MNRAS, 473, 3818

Davis B. L., Graham A. W., Cameron E., 2018b, ApJ, 869, 113

Davis T. A., Greene J. E., Ma C.-P., Blakeslee J. P., Dawson J. M., Pandya V., Veale M., Zabel N., 2019a, MNRAS, 486, 1404

Davis B. L., Graham A. W., Cameron E., 2019b, ApJ, 873, 85

Davis B. L., Graham A. W., Combes F., 2019c, The Astrophysical Journal, 877, 64

Davis T. A., et al., 2020, MNRAS, 496, 4061

Devecchi B., Volonteri M., 2009, ApJ, 694, 302

Di Matteo T., Springel V., Hernquist L., 2005, Nature, 433, 604

Dickey J. M., Kazes I., 1992, ApJ, 393, 530

Dietrich M., et al., 1993, ApJ, 408, 416

Donato D., Sambruna R. M., Gliozzi M., 2004, ApJ, 617, 915

Doroshenko V. T., Sergeev S. G., Pronik V. I., 2008, Astronomy Reports, 52, 442

Douchin F., Haensel P., 2001, A&A, 380, 151

Dressler A., Richstone D. O., 1988, ApJ, 324, 701

Droste J., 1917, Proceedings of the Royal Academy of Amsterdam, 19, 197

Dyson F. J., Lenard A., 1967, Journal of Mathematical Physics, 8, 423

Eddington A. S., 1916, MNRAS, 77, 16

Eddington A. S., 1924, Nature, 113, 192

Ehrenfest P., 1959, Collected scientific papers. North-Holland Pub. Co. ; Interscience Publishers, Amsterdam : New York

Einstein A., 1905, Annalen der Physik, 322, 891

Einstein A., 1916, Annalen der Physik, 354, 769

Emsellem E., Monnet G., Bacon R., 1994, A&A, 285, 723

Emsellem E., et al., 2007, MNRAS, 379, 401

Emsellem E., et al., 2011, MNRAS, 414, 888

Evans A. S., Mazzarella J. M., Surace J. A., Frayer D. T., Iwasawa K., Sanders D. B., 2005, ApJS, 159, 197

Event Horizon Telescope Collaboration et al., 2019a, ApJ, 875, L1

Event Horizon Telescope Collaboration et al., 2019b, ApJ, 875, L2

Event Horizon Telescope Collaboration et al., 2019c, ApJ, 875, L3

Event Horizon Telescope Collaboration et al., 2019d, ApJ, 875, L4

Event Horizon Telescope Collaboration et al., 2019e, ApJ, 875, L5

Event Horizon Telescope Collaboration et al., 2019f, ApJ, 875, L6

Fabbiano G., Wang J., Elvis M., Risaliti G., 2011, Nature, 477, 431

Faber S. M., Jackson R. E., 1976, ApJ, 204, 668

Faber S. M., et al., 1997, AJ, 114, 1771

Fabian A. C., 2012, ARA&A, 50, 455

Fairall A. P., Jones A., 1991, Southern redshifts catalogue & plots, 5th edn. Department of Astronomy, University of Cape Town

Fanti C., Fanti R., Gioia I. M., Lari C., Parma P., Ulrich M. H., 1977, A&AS, 29, 279

Faraday M., 1846, The London, Edinburgh, and Dublin Philosophical Magazine and Journal of Science, 28, 345

Fedorova E., Vasylenko A., Hnatyk B. I., Zhdanov V. I., 2016, Astronomische Nachrichten, 337, 96

Ferrarese L., 2002, ApJ, 578, 90

Ferrarese L., Ford H., 2005, Space Sci. Rev., 116, 523

Ferrarese L., Merritt D., 2000, ApJ, 539, L9

Ferrarese L., Ford H. C., Jaffe W., 1996, ApJ, 470, 444

Ferrarese L., et al., 2006, ApJ, 644, L21

Filho M. E., Fraternali F., Markoff S., Nagar N. M., Barthel P. D., Ho L. C., Yuan F., 2004, A&A, 418, 429

Finkelstein D., 1958, Phys. Rev., 110, 965

Finlez C., Nagar N. M., Storchi-Bergmann T., Schnorr-Müller A., Riffel R. A., Lena D., Mundell C. G., Elvis M. S., 2018, MNRAS, 479, 3892

Ford H. C., Butcher H., 1979, ApJS, 41, 147

Ford H. C., et al., 1994, ApJ, 435, L27

Forrest W. J., Shure M. A., Pipher J. L., Woodward C. E., 1987, in Backer D. C., ed., American Institute of Physics Conference Series Vol. 155, The Galactic Center. pp 153–156, doi:10.1063/1.36414

Freedman W. L., et al., 2001, ApJ, 553, 47

Gao F., et al., 2016, ApJ, 817, 128

Gao F., et al., 2017, ApJ, 834, 52

Gaskell C. M., 1988, ApJ, 325, 114

Gaskell C. M., 1996, ApJ, 464, L107

Gebhardt K., et al., 2000, ApJ, 539, L13

Gebhardt K., Adams J., Richstone D., Lauer T. R., Faber S. M., Gültekin K., Murphy J., Tremaine S., 2011, ApJ, 729, 119

Genzel R., Eckart A., 1999, in Falcke H., Cotera A., Duschl W. J., Melia F., Rieke M. J., eds, Astronomical Society of the Pacific Conference Series Vol. 186, The Central Parsecs of the Galaxy. p. 3

Genzel R., Watson D. M., Crawford M. K., Townes C. H., 1985, ApJ, 297, 766

Genzel R., Thatte N., Krabbe A., Kroker H., Tacconi-Garman L. E., 1996, ApJ, 472, 153

Genzel R., Pichon C., Eckart A., Gerhard O. E., Ott T., 2000, MNRAS, 317, 348

Ghez A. M., Klein B. L., Morris M., Becklin E. E., 1998, ApJ, 509, 678

Ghez A. M., Morris M., Becklin E. E., Tanner A., Kremenek T., 2000, Nature, 407, 349

Ghez A. M., et al., 2003, ApJ, 586, L127

Ghez A. M., Salim S., Hornstein S. D., Tanner A., Lu J. R., Morris M., Becklin E. E., Duchêne G., 2005, ApJ, 620, 744

Ghez A. M., et al., 2008, ApJ, 689, 1044

Gillessen S., Eisenhauer F., Trippe S., Alexand er T., Genzel R., Martins F., Ott T., 2009, ApJ, 692, 1075

Goodman J., Lee H. M., 1989, ApJ, 337, 84

Goulding A. D., et al., 2016, ApJ, 826, 167

Graham A. W., 2008, Publ. Astron. Soc. Australia, 25, 167

Graham A. W., 2016, in Laurikainen E., Peletier R., Gadotti D., eds, Astrophysics and Space Science Library Vol. 418, Galactic Bulges. p. 263 arXiv:1501.02937, doi:10.1007/978-3-319-19378-6_11

Graham A. W., Driver S. P., 2007, ApJ, 655, 77

Graham A. W., Erwin P., Caon N., Trujillo I., 2001, ApJ, 563, L11

Gravity Collaboration et al., 2018, A&A, 615, L15

Greene J. E., Ho L. C., 2007, ApJ, 667, 131

Greene J. E., et al., 2010, ApJ, 721, 26

Greene J. E., Seth A., Lyubenova M., Walsh J., van de Ven G., Läsker R., 2014, ApJ, 788, 145

Greene J. E., et al., 2016, ApJ, 826, L32

Greene J. E., Strader J., Ho L. C., 2020, ARA&A, 58, 257

Greenhill L. J., Henkel C., Becker R., Wilson T. L., Wouterloot J. G. A., 1995, A&A, 304, 21

Greenhill L. J., Moran J. M., Herrnstein J. R., 1997, ApJ, 481, L23

Greenhill L. J., et al., 2002, ApJ, 565, 836

Greenhill L. J., Kondratko P. T., Lovell J. E. J., Kuiper T. B. H., Moran J. M., Jauncey D. L., Baines G. P., 2003a, ApJ, 582, L11

Greenhill L. J., et al., 2003b, ApJ, 590, 162

Grupe D., Mathur S., 2004, ApJ, 606, L41

Gültekin K., et al., 2009a, ApJ, 695, 1577

Gültekin K., et al., 2009b, ApJ, 698, 198

Haller J. W., Rieke M. J., Rieke G. H., Tamblyn P., Close L., Melia F., 1996, ApJ, 456, 194

Hardcastle M. J., Evans D. A., Croston J. H., 2007, MNRAS, 376, 1849

Hargrave P. J., Ryle M., 1974, MNRAS, 166, 305

Häring N., Rix H.-W., 2004, ApJ, 604, L89

Häring-Neumayer N., Cappellari M., Rix H. W., Hartung M., Prieto M. A., Meisenheimer K., Lenzen R., 2006, ApJ, 643, 226

Harms R. J., et al., 1994, ApJ, 435, L35

Heckman T. M., Blitz L., Wilson A. S., Armus L., Miley G. K., 1989, ApJ, 342, 735

Helfer T. T., Thornley M. D., Regan M. W., Wong T., Sheth K., Vogel S. N., Blitz L., Bock D. C. J., 2003, ApJS, 145, 259

Hernquist L., 1989, Nature, 340, 687

Herrnstein J. R., Moran J. M., Greenhill L. J., Trotter A. S., 2005, ApJ, 629, 719

Hezaveh Y. D., Marshall P. J., Blandford R. D., 2015, ApJ, 799, L22

Hilz M., Naab T., Ostriker J. P., Thomas J., Burkert A., Jesseit R., 2012, MNRAS, 425, 3119

Hilz M., Naab T., Ostriker J. P., 2013, MNRAS, 429, 2924

Hirschmann M., Khochfar S., Burkert A., Naab T., Genel S., Somerville R. S., 2010, MNRAS, 407, 1016

Ho L., 1999, in Chakrabarti S. K., ed., Astrophysics and Space Science Library Vol. 234, Observational Evidence for the Black Holes in the Universe. p. 157, doi:10.1007/978-94-011-4750-7_11

Ho L. C., 2007a, ApJ, 668, 94

Ho L. C., 2007b, ApJ, 669, 821

Ho L. C., Darling J., Greene J. E., 2008, ApJ, 681, 128

Högbom J. A., 1974, A&AS, 15, 417

Hopkins P. F., Hernquist L., Cox T. J., Robertson B., Krause E., 2007, ApJ, 669, 45

Hovatta T., et al., 2014, AJ, 147, 143

Israel W., 1967, Physical Review, 164, 1776

Israel W., 1968, Communications in Mathematical Physics, 8, 245

Jaffe W., Gavazzi G., Valentijn E., 1986, AJ, 91, 199

Jaffe W., Ford H. C., Ferrarese L., van den Bosch F., O'Connell R. W., 1993, Nature, 364, 213

Jahnke K., Macciò A. V., 2011, ApJ, 734, 92

Jahnke K., et al., 2009, ApJ, 706, L215

Jansky K. G., 1933a, Proc. I.R.E., 21, 1387

Jansky K. G., 1933b, Popular Astronomy, 41, 548

Jansky K. G., 1933c, Nature, 132, 66

Jeans J. H., 1915, MNRAS, 76, 70

Jeans J. H., 1922, MNRAS, 82, 122

Jeter B., Broderick A. E., McNamara B. R., 2019, ApJ, 882, 82

Jungwiert B., Combes F., Axon D. J., 1997, A&AS, 125, 479

Kameno S., Nakai N., Honma M., 2013, in Kawabe R., Kuno N., Yamamoto S., eds, Astronomical Society of the Pacific Conference Series Vol. 476, New Trends in Radio Astronomy in the ALMA Era: The 30th Anniversary of Nobeyama Radio Observatory. p. 409

Kaspi S., Smith P. S., Netzer H., Maoz D., Jannuzi B. T., Giveon U., 2000, ApJ, 533, 631

Kelly B. C., Merloni A., 2012, Advances in Astronomy, 2012, 970858

Kerr R. P., 1963, Phys. Rev. Lett., 11, 237

Kim M., Ho L. C., Peng C. Y., Barth A. J., Im M., Martini P., Nelson C. H., 2008, ApJ, 687, 767

Kirchhoff G., 1857, Annalen der Physik, 178, 529

Kollatschny W., Ulbrich K., Zetzl M., Kaspi S., Haas M., 2014, A&A, 566, A106

Kondratko P. T., et al., 2006, ApJ, 638, 100

Kondratko P. T., Greenhill L. J., Moran J. M., 2008a, ApJ, 678, 87

Kondratko P. T., Greenhill L. J., Moran J. M., 2008b, ApJ, 678, 87

Kormendy J., 1988a, ApJ, 325, 128

Kormendy J., 1988b, ApJ, 335, 40

Kormendy J., 2016, in Laurikainen E., Peletier R., Gadotti D., eds, Astrophysics and Space Science Library Vol. 418, Galactic Bulges. p. 431, doi:10.1007/978-3-319-19378-6_16

Kormendy J., Bender R., 2011, Nature, 469, 377

Kormendy J., Bender R., 2013, ApJ, 769, L5

Kormendy J., Gebhardt K., 2001, in Wheeler J. C., Martel H., eds, American Institute of Physics Conference Series Vol. 586, 20th Texas Symposium on relativistic astrophysics. pp 363–381 arXiv:astro-ph/0105230, doi:10.1063/1.1419581

Kormendy J., Ho L. C., 2013, Annual Review of Astronomy and Astrophysics, 51, 511

Kormendy J., Richstone D., 1995, ARA&A, 33, 581

Kormendy J., Bender R., Cornell M. E., 2011, Nature, 469, 374

Koss M. J., et al., 2015, ApJ, 807, 149

Kovačević A., Popović L. Č., Shapovalova A. I., Ilić D., Burenkov A. N., Chavushyan V. H., 2014, Advances in Space Research, 54, 1414

Krabbe A., Genzel R., Drapatz S., Rotaciuc V., 1991, ApJ, 382, L19

Krabbe A., et al., 1995, ApJ, 447, L95

Krajnović D., Cappellari M., Emsellem E., McDermid R. M., de Zeeuw P. T., 2005, MNRAS, 357, 1113

Krajnović D., Cappellari M., de Zeeuw P. T., Copin Y., 2006, MNRAS, 366, 787

Krajnović D., McDermid R. M., Cappellari M., Davies R. L., 2009, MNRAS, 399, 1839

Krajnović D., Cappellari M., McDermid R. M., 2018, MNRAS, 473, 5237

Kuo C. Y., et al., 2011, ApJ, 727, 20

Lacy J. H., Baas F., Townes C. H., Geballe T. R., 1979, ApJ, 227, L17

Lacy J. H., Townes C. H., Hollenbach D. J., 1982, ApJ, 262, 120

Laplace P. S., 1796, Exposition du système du monde. Part II. Crapelet, Paris, France

Laplace P. S., 1799, Allgemeine Geographische Ephemeriden, 4, 1

Larson R. B., 1981, MNRAS, 194, 809

Läsker R., Ferrarese L., van de Ven G., Shankar F., 2014, ApJ, 780, 70

Läsker R., Greene J. E., Seth A., van de Ven G., Braatz J. A., Henkel C., Lo K. Y., 2016, ApJ, 825, 3

Lattimer J. M., Prakash M., 2001, ApJ, 550, 426

Lauer T. R., et al., 2007, ApJ, 662, 808

Lavezzi T. E., Dickey J. M., 1997, AJ, 114, 2437

Lemaître G., 1933, Annales de la Société Scientifique de Bruxelles, 53, 51

Lenard A., Dyson F. J., 1968, Journal of Mathematical Physics, 9, 698

Leung G. Y. C., et al., 2018, MNRAS, 477, 254

Levy R. C., et al., 2018, ApJ, 860, 92

Lim J., Leon S., Combes F., Dinh-V-Trung 2000, ApJ, 545, L93

Liu L., et al., 2021, MNRAS, in revision

Lodato G., Bertin G., 2003, A&A, 398, 517

Lynden-Bell D., 1969, Nature, 223, 690

Lynden-Bell D., Rees M. J., 1971, MNRAS, 152, 461

Ma C.-P., Greene J. E., McConnell N., Janish R., Blakeslee J. P., Thomas J., Murphy J. D., 2014, ApJ, 795, 158

Maccagni F. M., Morganti R., Oosterloo T. A., Oonk J. B. R., Emonts B. H. C., 2018, A&A, 614, A42

Macchetto F., Marconi A., Axon D. J., Capetti A., Sparks W., Crane P., 1997, ApJ, 489, 579

Maciejewski W., Teuben P. J., Sparke L. S., Stone J. M., 2002, MNRAS, 329, 502

Madau P., Rees M. J., 2001, ApJ, 551, L27

Magorrian J., et al., 1998, AJ, 115, 2285

Maiolino R., Ruiz M., Rieke G. H., Papadopoulos P., 1997, ApJ, 485, 552

Malkan M. A., Gorjian V., Tam R., 1998, ApJS, 117, 25

Mamyoda K., Nakai N., Yamauchi A., Diamond P., Huré J.-M., 2009, PASJ, 61, 1143

Maoz E., 1998, ApJ, 494, L181

Maoz D., et al., 1993, ApJ, 404, 576

Marconi A., Hunt L. K., 2003, ApJ, 589, L21

Markaryan B. E., Lipovetskii V. A., 1973, Astrophysics, 9, 283

Markwardt C. B., 2009, in Bohlender D. A., Durand D., Dowler P., eds, Astronomical Society of the Pacific Conference Series Vol. 411, Astronomical Data Analysis Software and Systems XVIII. p. 251 arXiv:0902.2850

Martín-Navarro I., Brodie J. P., Romanowsky A. J., Ruiz-Lara T., van de Ven G., 2018, Nature, 553, 307

Martinsson T. P. K., Verheijen M. A. W., Westfall K. B., Bershady M. A., Andersen D. R., Swaters R. A., 2013, A&A, 557, A131

Martynov D. V., et al., 2016, Phys. Rev. D, 93, 112004

Matković A., Guzmán R., 2005, MNRAS, 362, 289

Matsubayashi T., Shinkai H.-a., Ebisuzaki T., 2004, ApJ, 614, 864

Maxwell J. C., 1865, Philosophical Transactions of the Royal Society of London, 155, 459

Mazzalay X., et al., 2013, MNRAS, 428, 2389

Mazzalay X., et al., 2014, MNRAS, 438, 2036

McConnell N. J., Ma C.-P., 2013, ApJ, 764, 184

McMullin J. P., Waters B., Schiebel D., Young W., Golap K., 2007, in Shaw R. A., Hill F., Bell D. J., eds, Astronomical Society of the Pacific Conference Series Vol. 376, Astronomical Data Analysis Software and Systems XVI. p. 127

McNamara B. R., Nulsen P. E. J., 2007, ARA&A, 45, 117

Mejía-Restrepo J. E., Lira P., Netzer H., Trakhtenbrot B., Capellupo D. M., 2018, Nature Astronomy, 2, 63

Memola E., Trinchieri G., Wolter A., Focardi P., Kelm B., 2009, A&A, 497, 359

Merloni A., et al., 2010, ApJ, 708, 137

Meza A., Navarro J. F., Steinmetz M., Eke V. R., 2003, ApJ, 590, 619

Mezcua M., 2017, International Journal of Modern Physics D, 26, 1730021

Michell J., 1784, Philosophical Transactions of the Royal Society of London Series I, 74, 35

Michelson A. A., Morley E. W., 1887, American Journal of Science, 34, 333

Mitzkus M., Cappellari M., Walcher C. J., 2017, MNRAS, 464, 4789

Miyoshi M., Moran J., Herrnstein J., Greenhill L., Nakai N., Diamond P., Inoue M., 1995, Nature, 373, 127

Mo H., van den Bosch F. C., White S., 2010, Galaxy Formation and Evolution. Cambridge University Press, Cambridge, UK

Montgomery C., Orchiston W., Whittingham I., 2009, Journal of Astronomical History and Heritage, 12, 90

Mould J. R., et al., 2000, ApJ, 529, 786

Muñoz Marín V. M., González Delgado R. M., Schmitt H. R., Cid Fernandes R., Pérez E., Storchi-Bergmann T., Heckman T., Leitherer C., 2007, AJ, 134, 648

Mulchaey J. S., Jeltema T. E., 2010, ApJ, 715, L1

Mutlu-Pakdil B., Seigar M. S., Hewitt I. B., Treuthardt P., Berrier J. C., Koval L. E., 2018, MNRAS, 474, 2594

Naab T., Ostriker J. P., 2017, Annual Review of Astronomy and Astrophysics, 55, 59

Nagai H., et al., 2019, ApJ, 883, 193

Narayan R., McClintock J. E., 2013, preprint, arXiv:1312.6698

Nelson C. H., 2000, ApJ, 544, L91

Nelson C. H., Whittle M., 1999, in Merritt D. R., Valluri M., Sellwood J. A., eds, Astronomical Society of the Pacific Conference Series Vol. 182, Galaxy Dynamics - A Rutgers Symposium. p. 53

Newman E. T., Janis A. I., 1965, Journal of Mathematical Physics, 6, 915

Newman E. T., Couch E., Chinnapared K., Exton A., Prakash A., Torrence R., 1965, Journal of Mathematical Physics, 6, 918

Nguyen D. D., et al., 2020, ApJ, 892, 68

Nieto J. L., McClure R., Fletcher J. M., Arnaud J., Bacon R., Bender R., Comte G., Poulain P., 1990, A&A, 235, L17

Nigoche-Netro A., Aguerri J. A. L., Lagos P., Ruelas-Mayorga A., Sánchez L. J., Machado A., 2010, A&A, 516, A96

Noel-Storr J., Baum S. A., Verdoes Kleijn G., van der Marel R. P., O'Dea C. P., de Zeeuw P. T., Carollo C. M., 2003, ApJS, 148, 419

Noel-Storr J., Baum S. A., O'Dea C. P., 2007, ApJ, 663, 71

Nolthenius R., 1993, ApJS, 85, 1

Noordermeer E., Verheijen M. A. W., 2007, MNRAS, 381, 1463

Noordermeer E., van der Hulst J. M., Sancisi R., Swaters R. S., van Albada T. S., 2007, MNRAS, 376, 1513

Nordström G., 1918, Koninklijke Nederlandse Akademie van Wetenschappen Proceedings Series B Physical Sciences, 20, 1238

North E. V., 2020, PhD thesis, Cardiff University

North E. V., et al., 2019, MNRAS, 490, 319

North E. V., et al., 2021, MNRAS, 503, 5179

Nyland K., et al., 2016, MNRAS, 458, 2221

Ocaña Flaquer B., Leon S., Combes F., Lim J., 2010, A&A, 518, A9

Oegerle W. R., Hoessel J. G., 1991a, ApJ, 375, 15

Oegerle W. R., Hoessel J. G., 1991b, ApJ, 375, 15

Okuda T., Iguchi S., Kohno K., 2013, ApJ, 768, 19

Onishi K., Iguchi S., Sheth K., Kohno K., 2015, ApJ, 806, 39

Onishi K., Iguchi S., Davis T. A., Bureau M., Cappellari M., Sarzi M., Blitz L., 2017, MNRAS, 468, 4663

Onodera S., Koda J., Sofue Y., Kohno K., 2004, PASJ, 56, 439

Oosterloo T., et al., 2010, MNRAS, 409, 500

Oppenheimer J. R., Volkoff G. M., 1939, Physical Review, 55, 374

Özel F., Freire P., 2016, ARA&A, 54, 401

Pancoast A., Brewer B. J., Treu T., 2014, MNRAS, 445, 3055

Pandya V., et al., 2017, ApJ, 837, 40

Parma P., de Ruiter H. R., Fanti C., Fanti R., 1986, A&AS, 64, 135

Pastorini G., et al., 2007, A&A, 469, 405

Pauli W., 1940, Phys. Rev., 58, 716

Pauli, W. 1925, Zeitschrift für Physik, 31, 765

Pease F. G., 1918, Proceedings of the National Academy of Science, 4, 21

Peng C. Y., 2007, ApJ, 671, 1098

Penrose R., 1965, Phys. Rev. Lett., 14, 57

Peterson B. M., Horne K., 2004, Astronomische Nachrichten, 325, 248

Peterson B. M., Wandel A., 1999, ApJ, 521, L95

Peterson B. M., et al., 1991, ApJ, 368, 119

Peterson B. M., et al., 2004, ApJ, 613, 682

Pierce M. J., Tully R. B., 1988, ApJ, 330, 579

Pinkney J. C., et al., 2005, in American Astronomical Society Meeting 206 Abstracts. p. 11.17

Pizzella A., Corsini E. M., Dalla Bontà E., Sarzi M., Coccato L., Bertola F., 2005, ApJ, 631, 785

Pjanka P., Greene J. E., Seth A. C., Braatz J. A., Henkel C., Lo F. K. Y., Läsker R., 2017, ApJ, 844, 165

Planck Collaboration et al., 2016, A&A, 594, A13

Prandoni I., Laing R. A., Parma P., de Ruiter H. R., Montenegro-Montes F. M., Wilson T. L., 2007, in Baker A. J., Glenn J., Harris A. I., Mangum J. G., Yun M. S., eds, Astronomical Society of the Pacific Conference Series Vol. 375, From Z-Machines to ALMA: (Sub)Millimeter Spectroscopy of Galaxies. p. 271

Prandoni I., Laing R. A., de Ruiter H. R., Parma P., 2010, A&A, 523, A38

Querejeta M., et al., 2016a, A&A, 588, A33

Querejeta M., et al., 2016b, A&A, 593, A118

Ramakrishnan V., et al., 2019, MNRAS, 487, 444

Reid M. J., Braatz J. A., Condon J. J., Greenhill L. J., Henkel C., Lo K. Y., 2009, ApJ, 695, 287

Reines A. E., Greene J. E., Geha M., 2013, ApJ, 775, 116

Reissner H., 1916, Annalen der Physik, 355, 106

Rhook K. J., Wyithe J. S. B., 2005, MNRAS, 361, 1145

Richstone D., Bower G., Dressler A., 1990, ApJ, 353, 118

Rieke G. H., Rieke M. J., 1988, ApJ, 330, L33

Robotham A. S. G., Obreschkow D., 2015, Publ. Astron. Soc. Australia, 32, e033

Rose T., et al., 2019, MNRAS, 489, 349

Rubin V. C., Ford Jr. W. K., 1970, ApJ, 159, 379

Ruffa I., et al., 2019a, MNRAS, 484, 4239

Ruffa I., et al., 2019b, MNRAS, 489, 3739

Rusli S. P., et al., 2013, AJ, 146, 45

Sabra B. M., Saliba C., Abi Akl M., Chahine G., 2015, ApJ, 803, 5

Saglia R. P., et al., 2016, ApJ, 818, 47

Saintonge A., et al., 2011, MNRAS, 415, 32

Saintonge A., et al., 2017, ApJS, 233, 22

Salcido J., Bower R. G., Theuns T., McAlpine S., Schaller M., Crain R. A., Schaye J., Regan J., 2016, MNRAS, 463, 870

Salgado M., Bonazzola S., Gourgoulhon E., Haensel P., 1994, A&AS, 108, 455

Sanders R. H., 1981, Nature, 294, 427

Sanders D. B., Soifer B. T., Elias J. H., Madore B. F., Matthews K., Neugebauer G., Scoville N. Z., 1988, ApJ, 325, 74

Sargent W. L. W., Young P. J., Boksenberg A., Shortridge K., Lynds C. R., Hartwick F. D. A., 1978, ApJ, 221, 731

Sarzi M., Rix H.-W., Shields J. C., Rudnick G., Ho L. C., McIntosh D. H., Filippenko A. V., Sargent W. L. W., 2001, ApJ, 550, 65

Sarzi M., Rix H.-W., Shields J. C., Ho L. C., Barth A. J., Rudnick G., Filippenko A. V., Sargent W. L. W., 2005, ApJ, 628, 169

Satyapal S., Vega D., Heckman T., O'Halloran B., Dudik R., 2007, ApJ, 663, L9

Satyapal S., Vega D., Dudik R. P., Abel N. P., Heckman T., 2008, ApJ, 677, 926

Savorgnan G. A. D., Graham A. W., 2016, ApJS, 222, 10

Schaye J., et al., 2015, MNRAS, 446, 521

Schinnerer E., Maciejewski W., Scoville N., Moustakas L. A., 2002, ApJ, 575, 826

Schmidt M., 1963, Nature, 197, 1040

Schödel R., Ott T., Genzel R., Eckart A., Mouawad N., Alexander T., 2003, ApJ, 596, 1015

Schoenmakers R. H. M., Franx M., de Zeeuw P. T., 1997, MNRAS, 292, 349

Schulze A., Gebhardt K., 2011, ApJ, 729, 21

Schwarzschild K., 1906, Nachrichten von der Königlichen Gesellschaft der Wissenschaften zu Göttingen. Math.-phys. Klasse, 195, 41

Schwarzschild K., 1916, Abh. Konigl. Preuss. Akad. Wissenschaften Jahre, 1916, 189

Schwarzschild M., 1979, ApJ, 232, 236

Seigar M. S., Bullock J. S., Barth A. J., Ho L. C., 2006, ApJ, 645, 1012

Seigar M. S., Kennefick D., Kennefick J., Lacy C. H. S., 2008, ApJ, 678, L93

Sellgren K., McGinn M. T., Becklin E. E., Hall D. N., 1990, ApJ, 359, 112

Sellwood J. A., Wilkinson A., 1993, Reports on Progress in Physics, 56, 173

Serabyn E., Lacy J. H., 1985, ApJ, 293, 445

Serra P., Oosterloo T., Cappellari M., den Heijer M., Józsa G. I. G., 2016, MNRAS, 460, 1382

Shahbaz T., 1999, Journal of Astrophysics and Astronomy, 20, 197

Shankar F., Weinberg D. H., Miralda-Escudé J., 2009, ApJ, 690, 20

Shankar F., et al., 2016, MNRAS, 460, 3119

Shields G. A., Menezes K. L., Massart C. A., Vand en Bout P., 2006, ApJ, 641, 683

Shklovskii I. S., 1967, AZh, 44, 930

Shlosman I., Frank J., Begelman M. C., 1989, Nature, 338, 45

Sil'chenko O. K., 2000, AJ, 120, 741

Silk J., Mamon G. A., 2012, Research in Astronomy and Astrophysics, 12, 917

Simmons B. D., Smethurst R. J., Lintott C., 2017, MNRAS, 470, 1559

Smith M. D., et al., 2019, MNRAS, 485, 4359

Smith M. D., et al., 2021a, MNRAS, 500, 1933

Smith M. D., et al., 2021b, MNRAS, 503, 5984

Sofue Y., 1992, PASJ, 44, L231

Sofue Y., Rubin V., 2001, ARA&A, 39, 137

Sormani M. C., Barnes A. T., 2019, MNRAS, 484, 1213

Spekkens K., Sellwood J. A., 2007, ApJ, 664, 204

Steger C., 1998, IEEE Transactions on Pattern Analysis and Machine Intelligence, 20, 113

Stoner E., 1929, The London, Edinburgh, and Dublin Philosophical Magazine and Journal of Science, 7, 63

Sun A.-L., Greene J. E., Impellizzeri C. M. V., Kuo C.-Y., Braatz J. A., Tuttle S., 2013, ApJ, 778, 47

Sun J., et al., 2018, ApJ, 860, 172

Sylos Labini F., Benhaiem D., Comerón S., López-Corredoira M., 2019, A&A, 622, A58

Tacconi L. J., et al., 2013, ApJ, 768, 74

Takekawa S., Oka T., Iwata Y., Tsujimoto S., Nomura M., 2019, ApJ, 871, L1

Takekawa S., Oka T., Iwata Y., Tsujimoto S., Nomura M., 2020, ApJ, 890, 167

Tanaka Y., et al., 1995, Nature, 375, 659

Tiley A. L., Bureau M., Saintonge A., Topal S., Davis T. A., Torii K., 2016, MNRAS, 461, 3494

Tiley A. L., et al., 2019, MNRAS, 482, 2166

Toba Y., et al., 2014, ApJ, 788, 45

Tokuyama S., Oka T., Takekawa S., Iwata Y., Tsujimoto S., Yamada M., Furusawa M., Nomura M., 2019, PASJ, 71, S19

Tolman R. C., 1939, Physical Review, 55, 364

Tonry J. L., Dressler A., Blakeslee J. P., Ajhar E. A., Fletcher A. B., Luppino G. A., Metzger M. R., Moore C. B., 2001, ApJ, 546, 681

Toomre A., Toomre J., 1972, ApJ, 178, 623

Topal S., Bureau M., Tiley A. L., Davis T. A., Torii K., 2018, MNRAS, 479, 3319

Trani A. A., Mapelli M., Ballone A., 2018, ApJ, 864, 17

Tremaine S., et al., 2002, ApJ, 574, 740

Tremblay G. R., et al., 2016, Nature, 534, 218

Tsuboi M., Kitamura Y., Tsutsumi T., Miyawaki R., Miyoshi M., Miyazaki A., 2019, PASJ, 71, 105

Tully R. B., Fisher J. R., 1977, A&A, 54, 661

Utomo D., Blitz L., Davis T., Rosolowsky E., Bureau M., Cappellari M., Sarzi M., 2015, ApJ, 803, 16

Vasylenko A. A., Fedorova E. V., Hnatyk B. I., Zhdanov V. I., 2015, Kinematics and Physics of Celestial Bodies, 31, 13

Veale M., Ma C.-P., Greene J. E., Thomas J., Blakeslee J. P., McConnell N., Walsh J. L., Ito J., 2017, MNRAS, 471, 1428

Verdoes Kleijn G. A., van der Marel R. P., Noel-Storr J., 2006, AJ, 131, 1961

Verolme E. K., et al., 2002, MNRAS, 335, 517

Véron-Cetty M. P., Véron P., 2006, A&A, 455, 773

Vogelsberger M., et al., 2014, MNRAS, 444, 1518

Volonteri M., 2010, A&ARv, 18, 279

Volonteri M., Haardt F., Madau P., 2003, ApJ, 582, 559

Wagner J., 2013, A&A, 560, A12

Walsh J. L., Barth A. J., Ho L. C., Sarzi M., 2013, ApJ, 770, 86

Wandel A., Peterson B. M., Malkan M. A., 1999, ApJ, 526, 579

Wang Z., Kenney J. D. P., Ishizuki S., 1992, AJ, 104, 2097

Weber W., Kohlrausch R., 1856, Annalen der Physik, 175, 10

Webster B. L., Murdin P., 1972, Nature, 235, 37

Welch G. A., Sage L. J., 2003, ApJ, 584, 260

Weyl H., 1917, Annalen der Physik, 359, 117

White S. D. M., Huchra J., Latham D., Davis M., 1983, MNRAS, 203, 701

Whitmore B. C., Kirshner R. P., 1981, ApJ, 250, 43

Whitmore B. C., Kirshner R. P., Schechter P. L., 1979, ApJ, 234, 68

Williams M. J., Bureau M., Cappellari M., 2009, MNRAS, 400, 1665

Willmer C. N. A., 2018, ApJS, 236, 47

Willott C. J., McLure R. J., Jarvis M. J., 2003, ApJ, 587, L15

Wollman E. R., Geballe T. R., Lacy J. H., Townes C. H., Rank D. M., 1977, ApJ, 218, L103

Woo J.-H., Yoon Y., Park S., Park D., Kim S. C., 2015, ApJ, 801, 38

Wu X.-B., 2007, ApJ, 657, 177

Yoon I., 2017, MNRAS, 466, 1987

Young P. J., Westphal J. A., Kristian J., Wilson C. P., Landauer F. P., 1978, ApJ, 221, 721

Young J. S., et al., 1995, ApJS, 98, 219

Young L. M., Bureau M., Cappellari M., 2008, ApJ, 676, 317

Young L. M., et al., 2011, MNRAS, 414, 940

Yu L.-M., Bian W.-H., Wang C., Zhao B.-X., Ge X., 2019, MNRAS, 488, 1519

Zabel N., et al., 2019, MNRAS, 483, 2251

Zhao W., et al., 2018, ApJ, 854, 124

Zschaechner L. K., et al., 2016, ApJ, 832, 142

Zwicky F., 1939, Physical Review, 55, 726

Życki P. T., Done C., Smith D. A., 1999a, MNRAS, 305, 231

Życki P. T., Done C., Smith D. A., 1999b, MNRAS, 309, 561

de Koff S., et al., 2000, ApJS, 129, 33

van Albada T. S., Sancisi R., 1986, Philosophical Transactions of the Royal Society of London Series A, 320, 447

van de Ven G., de Zeeuw P. T., van den Bosch R. C. E., 2008, MNRAS, 385, 614

van den Bosch R. C. E., 2016, ApJ, 831, 134

van den Bosch R. C. E., van de Ven G., 2009, MNRAS, 398, 1117

van den Bosch F. C., van der Marel R. P., 1995, MNRAS, 274, 884

van den Bosch R. C. E., Greene J. E., Braatz J. A., Constantin A., Kuo C.-Y., 2016, ApJ, 819, 11

van der Marel R. P., van den Bosch F. C., 1998, AJ, 116, 2220

van der Marel R. P., de Zeeuw P. T., Rix H.-W., Quinlan G. D., 1997, Nature, 385, 610

van der Marel R. P., Cretton N., de Zeeuw P. T., Rix H.-W., 1998, ApJ, 493, 613